EXTREME MEDICINE

MAIN TOPIC:

STUDY OF TOXIC EFFECTS OF XENOBIOTICS AND THEIR BIOTRANSFORMATION PRODUCTS

EXTREME MEDICINE

SCIENTIFIC AND PRACTICAL JOURNAL OF FMBA OF RUSSIA
Frequency of 4 issues per year. Founded in 1999

Indexed in Scopus in 2022 Indexed in RSCI. IF 2021: 0,450 Listed in HAC 08.10.2024 (№ 1668) Open access to archive

Scopus® | НАУЧНАЯ ЭЛЕКТРОННАЯ БИБЛИОТЕКА eLIBRARY.RU | ВЫСШАЯ АТТЕСТАЦИОННАЯ КОМИССИЯ (ВАК) | CYBERLENINKA

МЕДИЦИНА ЭКСТРЕМАЛЬНЫХ СИТУАЦИЙ

НАУЧНО-ПРАКТИЧЕСКИЙ ЖУРНАЛ ФМБА РОССИИ
Периодичность 4 номера в год. Основан в 1999 году

CONTENTS

VOL. 27, NO. 1, 2025

СОДЕРЖАНИЕ

ТОМ 27, № 1, 2025

CONTENTS

VOL. 27, NO. 1, 2025

СОДЕРЖАНИЕ

ТОМ 27, № 1, 2025

ANALYSIS OF FACTORS INFLUENCING APOPTOTIC PROCESSES DURING FORMATION OF LONG-TERM HEALTH EFFECTS OF SEVERE ACUTE POISONING WITH NEUROTROPIC TOXICANTS

Evgeny B. Shustov[1]✉, Margarita V. Melnikova[1], Kristina V. Masterova[1], Vladimir F. Ostrov[1], Ekaterina A. Zolotoverkhaja[1], Larisa G. Kubarskaya[1], Ksenia O. Tanayants[1], Alexander A. Kozlov[1], Yulia O. Sokolova[1], Petr K. Potapov[1,2].

[1] Golikov Research Center of Toxicology, St. Petersburg, Russia

[2] Military Medical Academy, St. Petersburg, Russia

Background. The nervous system damage caused by neurotoxicants is characterized by various morphological changes, manifested mainly by dystrophic and necrotic processes. The key mechanisms of post-intoxication asthenia pathogenesis, determined by the specifics of the toxicant, involve activation of apoptosis, trophic disorder, lipid peroxidation (LPO), neuropeptide regulatory insufficiency, as well as cerebrospinal fluid dynamics disorders.

Objective. Quantification of the contribution of apoptosis, oxidative stress, and neurotrophin regulation processes to the formation of long-term health consequences of severe acute poisoning with neurotropic toxicants.

Material and methods. Experimental studies were performed in male rats. The following toxicants were used: phenylcarbamate (1.6 mg/kg bw), methanol (11.5 g/kg bw), lead acetate (300 mg/kg bw). The period of formation of long-term health effects was 30 days. The level of apoptosis of the brain temporal cortex neurons was evaluated by the TUNEL method. The identification of blood plasma neurospecific proteins was carried out by the ELISA method. Evaluation of LPO and antioxidant system was carried out by standard biochemical methods.

Results. Exposure to the substances caused the signs of toxic effects in rats on days 1–2. The maximum severity of poisoning with phenylcarbamate was on the first day, while the maximum severity of poisoning with methanol and lead acetate was manifested on the second day. By days 5–7, the survived animals showed a normalization in the status regardless of the toxicant. On day 30, violations were detected, the totality of which allowed the survived animals to be divided into subgroups according to the manifestation of functional signs of long-term health effects of acute poisoning.

Conclusions. The formation of long-term health effects of severe acute poisoning with the studied neurotoxicants was shown to be associated with an increase in the number of TUNEL positive neurons and a decrease in the S100 protein serum concentration. Lipid peroxidation in brain tissues during the specified period did not play a significant role in apoptosis activation.

Keywords: psychoorganic syndrome; antioxidant system; apoptosis; neuron-specific proteins; neurotoxicants, late effect of intoxication; lipid peroxidation

УДК 616-099:616-018:616-092.9

АНАЛИЗ ФАКТОРОВ, ВЛИЯЮЩИХ НА ПРОЦЕССЫ АПОПТОЗА В ПЕРИОДЕ ОТДАЛЕННЫХ ПОСЛЕДСТВИЙ ТЯЖЕЛЫХ ОСТРЫХ ОТРАВЛЕНИЙ НЕЙРОТРОПНЫМИ ТОКСИКАНТАМИ

Е.Б. Шустов[1]✉, М.В. Мельникова[1], К.В. Мастерова[1], В.Ф. Остров[1], Е.А. Золотоверхая[1], Л.Г. Кубарская[1], К.О. Танаянц[1], А.А. Козлов[1], Ю.О. Соколова[1], П.К. Потапов[1,2]

[1] Научно-клинический центр токсикологии имени академика С.Н. Голикова Федерального медико-биологического агентства, Санкт-Петербург, Россия

[2] Военно-медицинская академия имени С.М. Кирова, Санкт-Петербург, Россия

Введение. Поражение нервной системы при действии нейротоксикантов характеризуется различными морфологическими изменениями, проявляющимися в основном дистрофическими и некротическими процессами. Ключевыми механизмами патогенеза постинтоксикационной астении, определяющимися спецификой токсиканта, являются активация апоптоза, нарушение трофики, активация перекисного окисления липидов (ПОЛ), недостаточность нейропептидного звена регуляции, нарушения ликвородинамики.

Цель. Количественная оценка вклада процессов апоптоза, оксидативного стресса и нейротрофиновой регуляции в формировании отдаленных последствий тяжелых острых отравлений нейротропными токсикантами.

Материалы и методы. Экспериментальное исследование выполнено на крысах-самцах. В качестве токсикантов использовались: фенилкарбамат (1,6 мг/кг м.т.), метанол (11,5 г/кг м.т.), ацетат свинца (300 мг/кг м.т.). Период формирования отдаленных последствий составил 30 суток. Уровень апоптоза нейронов височной коры головного мозга определяли методом TUNEL. Определение нейроспецифических белков в плазме крови осуществлялось ИФА-методом. Определение показателей ПОЛ и антиоксидантной системы проводили стандартными биохимическими методами.

Результаты. Воздействие веществ вызывало признаки токсического действия у крыс на 1–2-е сутки, причем у фенилкарбамата с максимальной выраженностью в первые, а у метанола и ацетата свинца — на вторые. К 5–7-м суткам у выживших животных (независимо от токсиканта) состояние нормализовалось. На 30-е сутки были выявлены нарушения, совокупность которых позволила разделить выживших животных на подгруппы по уровню сформированности функциональных признаков отдаленных последствий острых отравлений.

Выводы. Показано, что формирование отдаленных последствий тяжелых острых отравлений для исследуемых нейротоксикантов связано с повышением количества TUNEL-позитивных нейронов и снижением концентрации белка S100 в сыворотке. Процессы ПОЛ в тканях мозга в указанные сроки не играли существенной роли в активации апоптоза.

Ключевые слова: психоорганический синдром; антиоксидантная система; апоптоз; нейроспецифические белки; нейротоксиканты; отдаленные последствия отравлений; перекисное окисление липидов

✉ Шустов Евгений Борисович shustov-msk@mail.ru

INTRODUCTION

The long-term period following severe acute poisoning with neurotropic toxicants is characterized by the development of mainly nonspecific manifestations of the psychoorganic syndrome, post-intoxication and cerebrogenic asthenia, toxic polyneuropathies. Toxic damage to the nervous system, as well as to other body tissues, involves various morphological changes at the cellular and tissue levels and is manifested by various dystrophic and necrotic processes [1–2]. The use of light microscopy makes it possible to establish the presence of neuronal apoptosis, which is a consequence of most toxic lesions of the nervous system [3]. Toxic damage to brain tissue is characterized by small foci of necrosis, often elective, in which only individual tissue elements are damaged (some of them remain); such foci are manifested by rarefaction of the neuropil and gliopenia. The morphological basis of the psychoorganic syndrome in neurointoxication consists in the death of neurons and glial cells associated with both the direct toxic effect of xenobiotics and the induction of apoptotic processes [4]. The key mechanisms behind the pathogenesis of post-intoxication asthenia, determined by the specifics of the toxicant, involve activation of apoptosis, trophic disorder, lipid peroxidation (LPO), neuropeptide regulatory insufficiency, and cerebrospinal fluid dynamics disorders. Toxic neuropathies are manifested by segmental demyelination (toxic myelopathy) and axonal degeneration (toxic distal axonopathy).

The nonspecific mechanisms of toxic action characteristic of all neurotropic xenobiotics include inhibition of enzyme activity due to the blockade of sulfhydryl, carboxyl, amino, and other functionally active structural groups in peptides and proteins; formation of oxidative stress with subsequent activation of LPO processes[1]; mitochondrial inhibition; calcium homeostasis disorder; excitotoxicity; proinflammatory cytokine expression, inflammatory process induction in nervous tissue; haptenic modification of proteins with their acquisition of antigenic properties and induction of autoimmune damage mechanisms; inhibition of neurotrophin release, neurogenesis and gliogenesis in combination with suppression of proliferation and differentiation of new neurons and gliocytes; increased permeability of the blood-brain barrier; increased processes of cell apoptosis of the central and peripheral nervous system[2] [5–8].

Taking all the above mentioned into account, a deeper understanding of the long-term health effects of severe acute poisoning with neurotropic toxicants is required. In this connection, the present study aims to assess the quantitative contribution of apoptosis, oxidative stress, and neurotrophin regulation processes to the formation of long-term health consequences of severe acute poisoning with neurotropic toxicants.

MATERIALS AND METHODS

The experimental study involved 53 male outbred rats with a body weight (bw) of 180–220 g (baseline), received from the Kurchatov Institute Research Center — Rappolovo Nursery (Leningrad Region, Russia).

Long-term effects were simulated by a single administration of a neurotropic toxicant to laboratory animals at a dose of LD_{50}. The period of formation of long-term consequences was 30 days. The following were used as toxicants:
- phenylcarbamate, a reversible acetylcholinesterase inhibitor, synthesized in the Golikov Research Center of Toxicology [11];
- methanol (Vecton, Russia), an organic solvent that implements its toxic effect by damaging cell membranes;
- lead acetate (Reahim, Russia), an organic heavy metal salt that suppresses the activity of various enzymes.

Laboratory animals were divided into four groups:
- group 1 or C (Control) ($n = 8$), intragastric administration of 0.5 mL of saline solution;
- group 2 or PC (Phenylcambamate) ($n = 15$), intraperitoneal administration of an 0.1% aqueous solution at a dose of 1.6 mg/kg bw;

---

[1] FMBA Guidelines 12.08-2021 *Clinic, diagnosis and treatment of chronic poisoning (exposure) to neurotoxic substances*. 2021. (In Russ.)
[2] Badalyan AV., Belova MV., Brusin KM. et al. *Medical Toxicology: National guidelines.* M.: GEOTAR-Media, 2014. (In Russ.)

- group 3 or M (Methanol) (n = 15), intragastric administration of a 75% aqueous solution at a dose of 11.5 g/kg bw;
- group 4 or LA (Lead acetate) (n = 15), intraperitoneal administration of a 5% aqueous solution at a dose of 300 mg/kg bw.

The signs of toxic effects identified as a result of observation were evaluated in points according to the scale of signs of intoxication [10]. The dynamics of the animals' body weight, their consumption of feed and water were determined weekly.

To assess the formation of the phase of long-term consequences, neurophysiological testing of animals was performed on days 7, 15, 28 by such tests as open field (VideoMot 2, TSE, Germany), rotating rod (Rota-Rod Treadmills for rats 7700-7750, Ugo Basile, Italy), grip strength (Gripstrengthmeter 303500 series, TSE, Germany), sensory reactions tests (Startle Response System, TSE, Germany), assessment of the conditioned passive avoidance reflex (CPAR) (PACS-30, Columbus Instruments, USA).

On day 28, blood and brain tissue samples were collected from the survived animals (n = 32) for subsequent examination.

The determination of neurospecific proteins (neurospecific enolase NSE, brain neurotrophic factor BDNF, basic myelin protein MBP and calcium-binding protein S100) in animal blood plasma was carried out by enzyme immunoassay using commercial kits (Cloud-Clone Corp., USA) according to the manufacturer's instructions. Indicators of lipid peroxidation (diene conjugates of DC, malonic dialdehyde MDA); the antioxidant system of AOS (reduced glutathione GSH, activity of glutathione transferase GST, glutathione peroxidase GP, superoxide dismutase SOD), as well as energy metabolism (activity of glucose-6-phosphate dehydrogenase G6PDH) were determined in the homogenate of brain tissue, as described in [11].

The activity of apoptotic processes was assessed by determining the number of TUNEL-positive (terminal deoxynucleotidyl transferase dUTP nick end labeling) cells in the temporal cortex of rats. The choice of this area of the cortex was determined by the peculiarities of its cytoarchitectonics (high density of neurons, radial divergence of cortical columns, presence of eight types of interneurons and projections from the auditory, statokinetic, gustatory and olfactory analyzers, thalamus, their high sensitivity to hypoxia, frequent dysplasia and the ability to epileptogenesis). Apoptotic TUNEL cells were counted on 4–5 slices of the studied brain area using a commercial Elabscience® E-CK-A320 kit "TUNEL In Situ Apoptosis Kit (Green, FITC), One-step TUNEL In Situ Apoptosis Kit". Images of brain slices were obtained using a Nikon Eclipse 80i microscope with a Nikon DS-Fi1c color camera at a magnification of ×100 for analysis and ×200 for photographic materials at a resolution of 1280×960 pixels using the NIS-Elements AR 4.20.00 software application. Apoptotic TUNEL cells were counted on 4–5 slices of the studied area of the brain of each animal.

Statistical processing of the experimental data obtained was carried out in the MS EXCEL spreadsheet processor using the Data Analysis application software and the specialized statistical analysis software Statistica v.10. The

methods of frequency, variance, factor, and correlation analysis were used. The significance of differences between the groups was assessed using the rank-sum test (White), the Fisher's exact probability test for frequency analysis, the F-criterion of the analysis-of-variance (ANOVA).

RESULTS

Observation of animals during the acute intoxication period showed that toxic effects signs (according to the sum of points characterizing the features of appearance, muscle tone, motor activity, and reaction to gripping) were detected on 1–2 days, with a rapid normalization of the condition by days 5–7 in the survived animals (Fig. 1).

The clinical picture of acute phenylcarbamate intoxication was dominated by signs of seizures and ataxia. Methanol poisoning led to a decreased muscle tone and motor activity, impaired coordination of movements and posture, decreased sensitivity and reflexes. Under lead acetate intoxication, the enteropathogenic symptom complex, irritation of the peritoneum, impaired motor activity and respiration were observed. At the same time, different toxicants were characterized by a different rate of increase and decrease in the symptoms of intoxication (the fastest and most pronounced manifestation of intoxication, an intensive decrease for phenylcarbamate, a slower decrease for methanol). Lead acetate was characterized by a slower increase in poisoning symptoms, which is associated with the peculiarities of its absorption in the body.

During dynamic observation of animals, no statistically significant differences were found between the control group and the groups of animal survivors of acute intoxication in terms of such indicators as body weight, feed intake, paw grip strength, retention time on a rotating rod, as well as in terms of individual indicators of the neurophysiological techniques used (locomotor activity, emotional lability, aggressiveness, grooming in the open field test; locomotor activity and staying in the illuminated sector during the CPAR test; indicators of reflex response to harsh sound and latency characteristics in the Startle Response System test). Therefore, these indicators were not reflected in the tables and figures following below.

On day 30 of the study, signs of impaired ingestive (feeding and drinking) behavior, reproduction of CPAR,
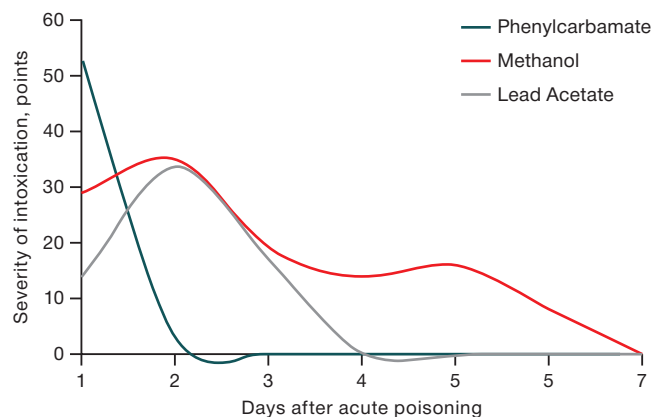
Figure prepared by the authors based on their own data

Fig. 1. Dynamics of intoxication severity after administration of LD_{50} toxicants

coordination of movements, inhibition in polysynaptic reflex circuits, depletion of activation influences were revealed (Table 1). The totality of these signs allowed the animal poisoning survivors to be divided into subgroups according to the level of formation of functional signs of the long-term health consequences of acute poisoning.

Table 1 indicates that early stages after acute intoxication (seven days) were associated with a statistically significant increase in water consumption in animals treated with phenylcarbamate and methanol. Additional water intake is explained by the need to reduce the concentration of the toxicant and accelerate its excretion from the body.

In the methanol exposure group, male rats demonstrated a decrease in search and research activity of 2.8 ± 0.7 units versus 9.2 ± 1.7 units in control animals, which is a manifestation of the direct toxic effect of the substance. The animals also showed disorders in the reproduction of conditioned reflexes in the CPAR test, a post-stress effect in animals from the phenylcarbamate group of 33 ± 13 s versus 4 ± 3 s in the control group, a shortening of the reaction time to a flash of light of 7 ± 1 ms versus 13 ± 3 ms in the control group. The group of animals exposed to methanol demonstrated a decrease in the amplitude of the reaction in response to an electrical stimulus of 46 ± 15

Table 1. Dynamics of neurophysiological parameters in the post-intoxication period

Indicator, test	Group	Days after intoxication			
		7	15	21	28
Water consumption, mL/day #	Control	26.9	25.6	27.5	28.1
	Phenylcarbamate	32.8*	32.2	33.3*	36.8*
	Methanol	32.0*	35.5*	21.1	20.0*
	Lead Acetate	24.0	23.0	21.1	20.0*
Search and research activity, units	Control	9.2 ± 1.7	8.9 ± 1.6	6.0 ± 1.5	4.9 ± 1.0
	Phenylcarbamate	11.4 ± 1.1	10.2 ± 1.2	6.2 ± 1.3	5.6 ± 1.3
	Methanol	$2.8 \pm 0.7*$	$3.1 \pm 0.8*$	4.5 ± 0.4	4.9 ± 1.0
	Lead Acetate	14.6 ± 0.9	12.4 ± 2.0	8.2 ± 2.0	$9.2 \pm 1.2*$
Duration of stay in a dark cell, s	Control	29 ± 15	-	-	4 ± 3
	Phenylcarbamate	$75 \pm 11*$	-	-	$33 \pm 13*$
	Methanol	35 ± 14	-	-	24 ± 13
	Lead Acetate	35 ± 23	-	-	$40 \pm 2.5*$
Treadmill, proportion of completed the test, %	Control	100	100	100	100
	Phenylcarbamate	89	100	78	33
	Methanol	100	0♦	44	44
	Lead Acetate	100	30	70	0♦
Response to sound, amplitude, units	Intact	76 ± 34	123 ± 63		247 ± 113
	Phenylcarbamate	153 ± 72	271 ± 135		303 ± 134
	Methanol	61 ± 39	248 ± 33		159 ± 59
	Lead Acetate	76 ± 31	112 ± 58		79 ± 25
Reaction to light, duration, ms	Control	13 ± 3	9 ± 2		15 ± 2
	Phenylcarbamate	14 ± 2	9 ± 4		16 ± 2
	Methanol	$7 \pm 1*$	9 ± 1		$21 \pm 2*$
	Lead Acetate	20 ± 5	9 ± 4		$31 \pm 2♦$
Response to an electrical stimulus, amplitude, units	Control	224 ± 46	293 ± 111		618 ± 80
	Phenylcarbamate	283 ± 67	358 ± 78		537 ± 145
	Methanol	$46 \pm 15♦$	337 ± 60		$315 \pm 63♦$
	Lead Acetate	202 ± 70	360 ± 140		$221 \pm 74♦$

Table prepared by the authors based on their own data

Notes: the data is presented as the mean value and the standard error of the mean ($M \pm m$); the indicator "water consumption" is presented as the mean group value; "–" — not investigated; statistically significant differences with the control animal group: * — $p < 0.05$; ♦ — $p < 0.01$; • — $p < 0.001$.

units, compared with animals from the control group, 224 ± 46 units. These signs correspond to a prolonged period of acute intoxication pattern.

In the following periods, the severity of the above changes was mostly leveled. At the end point of the study (day 28), the animals from the PC group retained increased water consumption and impaired conditioned reflex reproduction, which had been noted in the early stages after intoxication.

In animals exposed to methanol, the initial increase in water consumption was replaced by its decrease on day 21. Along with this, the early increase in the duration of the reaction to a flash of light and a decrease in the amplitude of the response to an electrical stimulus were leveled by the end of the experiment.

In the group of animals who survived lead acetate poisoning, a decrease in water consumption was noted throughout the observation period with its increase by day 28. These animals also demonstrated disorders of conditioned reflexes reproduction, reactions to light (31 ± 2 ms versus 15 ± 2 ms in the control) and sound, with these indicators being more significant than those in the methanol-exposed group. In addition, these animals were unable to perform a treadmill running test; in the open field test, they showed some fussiness, accompanied by an increased search and research activity.

An analysis of the detected dynamics of toxic effects and neurophysiological indicators revealed signs that are sensitive to the formation of long-term consequences of acute poisoning. These include impaired ingestive behavior and its endocrine regulation (decreased water consumption), impaired conditioned reflex reproduction, increased sensitivity to stress (time spent in a dark chamber in the CPAR test), inability to perform the treadmill running test at a high speed of the tape, inhibition in the polysynaptic pathways (high reaction time light in the TSE Startle Response System test), and insufficiency (exhaustion) of activation effects (low amplitude of the response to an electrical stimulus in the TSE Starter Response System test). Altogether, these signs made it possible to obtain an integral quantitative value of the level of formation of long-term consequences based on a point-based assessment system.

Individual variations in the studied indicators of brain metabolism were noted, with the corresponding data presented in Table 2.

An analysis of the data presented in Table 2 shows a moderate decrease in S100 protein by 30% ($p < 0.05$) in survivors on day 28 after poisoning (the period of formation of long-term consequences of acute poisoning) under the influence of acute phenylcarbamate intoxication.

The group of animals exposed to methanol poisoning showed a statistically significant increase in the activity of SOD by 90% and G-6-FDG by 37%, as well as a statistical tendency to decrease the activity of S100 protein by 27% with an increase in the activity of antioxidant defense enzymes (glutathione transferase and glutathione peroxidase by 20–21%). This observation may be indicative of compensatory processes in brain tissue in the post-intoxication period.

On day 28 after acute intoxication with lead acetate, survived animals demonstrated a statistical tendency to increase the marker of neuronal damage NSE by 94% and a threefold increase in the concentration of LPO final products — DCs — with a decrease in glutathione transferase activity by 10%, reflecting the neurotoxicity of this compound. However, in comparision with other toxicants, lead acetate exposure resulted in a more pronounced, statistically significant decrease in the activity of S100 protein by 46% and MBP by 23%, an increase in the activity of the brain neurotrophic factor BDNF by 42%, as well as a moderate increase in the activity of G-6-FDG by 18%. These indicators manifest a high activity of compensatory and adaptive biochemical mechanisms during this period.

It should be noted that neurospecific proteins detected in blood serum 30 days after acute poisoning proved to be uninformative for detecting and assessing the severity of long-term health effects of intoxication. Only for lead acetate, metabolic signs of neuronal damage and, probably,

Table 2. Indicators of brain metabolism in survived animals on day 28 after acute poisoning with neurotoxicants

Indicator, unit	Control (*n* = 8)	Phenylcarbamate (*n* = 9)	Methanol (*n* = 10)	Lead Acetate (*n* = 5)
NSE, pg/mL	0.71 ± 0.11	0.65 ± 0.07	0.99 ± 0.17	1.38 ± 0.39*
BDNF, ng/mL	1.22 ± 0.12	1.15 ± 0.04	1.30 ± 0.09	1.73 ± 0.11*
MBP, ng/mL	0.06 ± 0.01	0.06 ± 0.01	0.06 ± 0.01	0.05 ± 0.01
S100, ng/mL	0.120 ± 0.011	0.084 ± 0.007*	0.087 ± 0.012	0.064 ± 0.006*
GSH, mmol/L	2.00 ± 0.05	1.95 ± 0.04	1.91 ± 0.04	1.94 ± 0.05
MDA, mmol/L	19.1 ± 1.7	19.2 ± 0.9	22.8 ± 2.3	18.9 ± 1.0
DC, mmol/L	65.3 ± 1.6	98.7 ± 36.0	126.7 ± 52.9	197.2 ± 80.6
GST, U/g of protein	62.7 ± 1.2	57.8 ± 3.5	75.2 ± 6.0	56.2 ± 1.2
GP, U/g of protein	1.45 ± 0.03	1.42 ± 0.08	1.76 ± 0.16	1.40 ± 0.04
G6PDH, U/g of protein	35.8 ± 2.3	38.2 ± 3.2	49.2 ± 5.0*	42.4 ± 2.3
SOD, U/g of protein	21.5 ± 5.3	24.2 ± 5.7	50.0 ± 5.4*	20.5 ± 5.4

Table prepared by the authors using their own data

Note: the data are presented as the mean value and the standard error of the mean ($M \pm m$); statistically significant differences with the group of intact animals: * — $p < 0.05$.
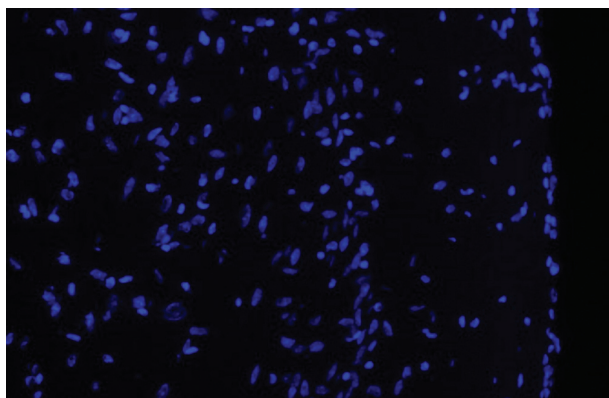
Control, DAPI — nuclear neurons in a cross section, ×200
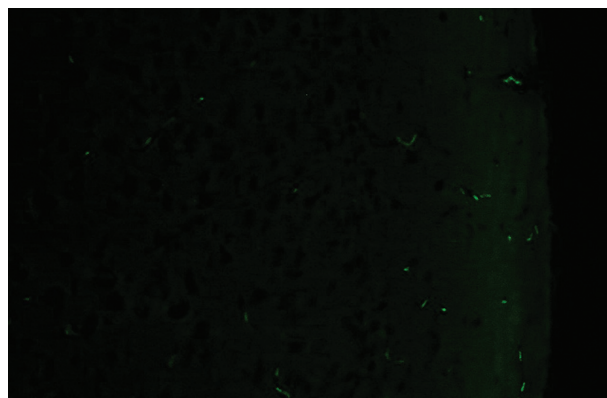
Contol, TUNEL — apoptotic neurons, ×200
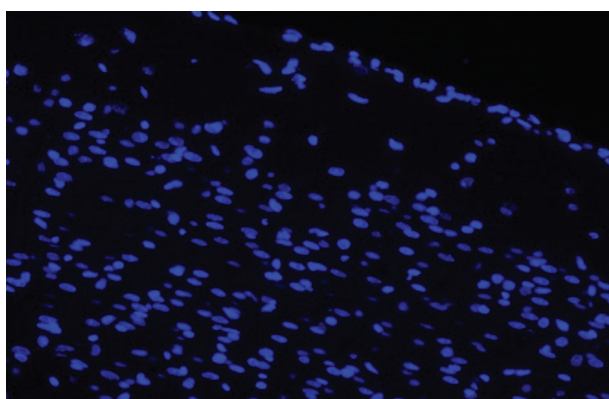
Phenylcarbamate, DAPI — nuclear neurons in a cross section, ×200
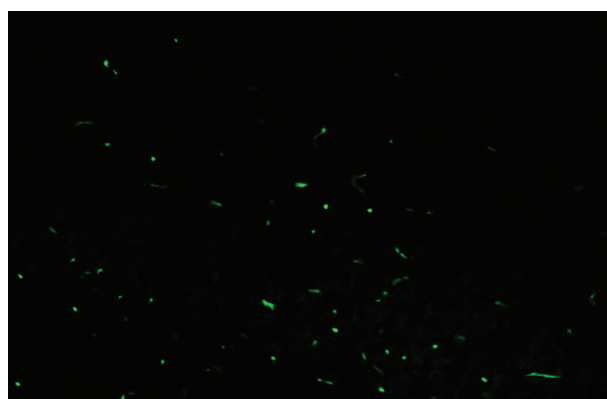
Phenylcarbamate, TUNEL — apoptotic neurons, ×200
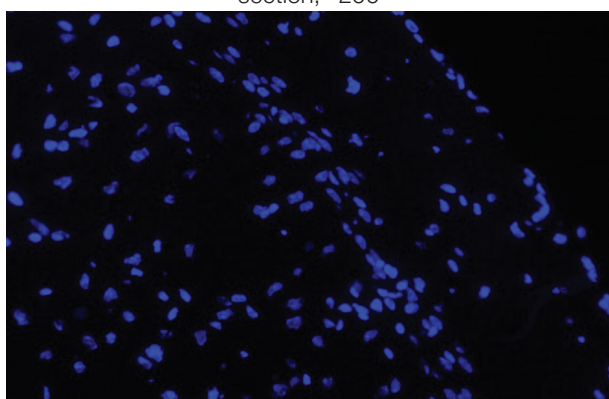
Methanol, DAPI — nuclear neurons in a cross section, ×200
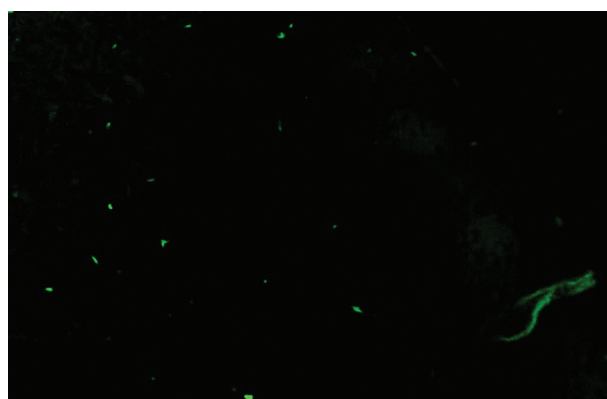
Methanol, TUNEL — apoptotic neurons, ×200
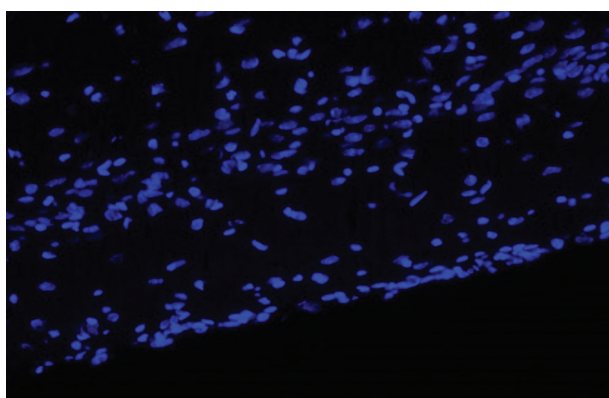
Lead acetate, DAPI — nuclear neurons in a cross section, ×200
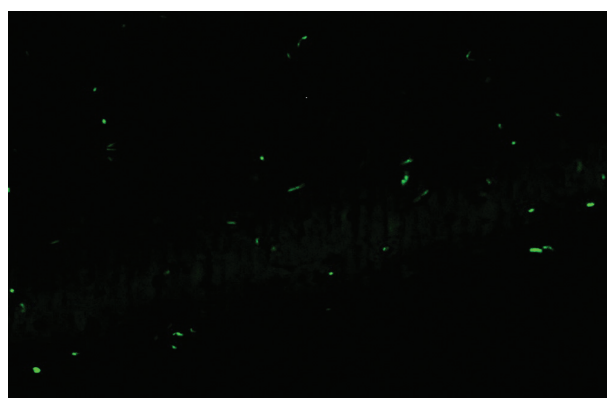
Lead acetate, TUNEL — apoptotic neurons, ×200

Figure prepared by the authors using their own data

Fig. 2. Slice micrographs of the rat brain temporal cortex
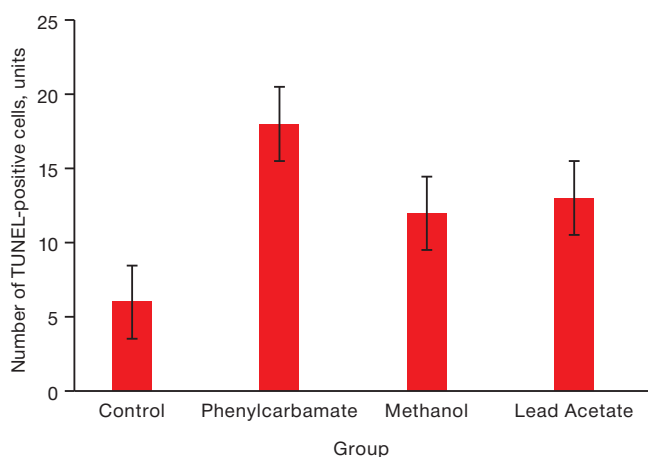
Figure prepared by the authors using their own data

Fig. 3. The activity of apoptotic processes in the cells of the rat brain temporal cortex on day 28 after acute poisoning with neurotoxicants
Note: * $p < 0.05$ — statistically significant differences from the control group
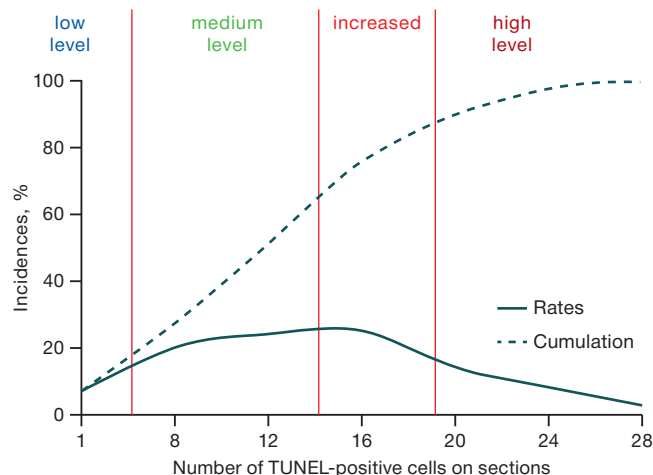
Figure prepared by the authors using their own data

Fig. 4. Frequency distribution curves of the number of TUNEL-positive cells on sections of the rat brain temporal cortex

increased permeability of the blood–brain barrier were found. It is important that lead acetate is characterized by the activation of LPO processes in the setting of a decrease in the activity of the enzymatic link of the antioxidant system. These findings are likely to be correlated with the ability known for heavy metals to inhibit the enzymatic activity of a wide range of enzymes due to binding to thiol groups in the active site.

Figure 2 demonstrates slice micrographs of the rat brain temporal cortex to assess the effect of toxicants on the processes of neuronal apoptosis.

Under almost the same number of blue-colored nuclear neurons on a slice of the cerebral cortex (left photos), the number of apoptotic TUNEL-positive nerve cells in the survived animals significantly increased under the influence of toxicants (green glow, right row of photos, Fig. 2).

Figure 3 presents the results of assessing the activity of apoptotic processes.

The data presented in Fig. 3 shows that all the studied toxicants, regardless of the mechanisms of their toxic effect, increase the number of neurons in the state of apoptosis by 3–4 times, thereby being the inducers of this pathological process.

A variance factor analysis showed that the severity of neuron apoptosis in the rat cerebral cortex is closely related to the formation of long-term consequences of severe acute poisoning with neurotropic toxicants. This indicator is associated with more than 20% of the total variability in the assessment of their formation ($R^2 = 0.47$, $p = 0.034$) in survivor animals. In this regard, the subsequent analysis was focused on assessing the significance of the influence of the studied metabolic factors on the activity level of neuronal apoptosis processes.

It follows from Fig. 3 that, on day 28, a pronounced sharp activation of apoptotic processes was observed in the brain cells of the survived animals, which is more characteristic of phenylcarbamate. The variance factor analysis showed that the controlled factor of intoxication fact determines 64% of the total variability ($p = 5 \times 10^{-8}$) of the apoptosis index. The type of neurotoxicant is even more important in activating apoptosis (72% of the total variation of the trait,

$p = 2 \times 10^{-6}$), while the coefficient of determination for phenylcarbamate equaled D = 0.97 ($p = 5 \times 10^{-13}$), for methanol D = 0.86 ($p = 4 \times 10^{-8}$), for lead acetate D = 0.80 ($p = 4 \times 10^{-5}$).

In order to assess the level of apoptosis activation during the formation of long-term health consequences of acute poisoning, a frequency analysis and S-scaling were performed. To that end, the inflection points on the curves of the statistical distribution of the number of TUNEL-positive cells in slices were determined (Fig. 4), which are the boundaries of the levels of apoptosis activation. If the indicator under study can be characterized as close to a normal statistical distribution, such criterion points on the cumulative curve will be 16% (the boundary of low and medium levels), 66% (the boundary of medium and elevated levels), and 84% (the boundary of elevated and high levels). It is noteworthy that apoptosis induction was more pronounced (by four times) when exposed to phenylcarbamate, while the apoptosis-inducing activity of methanol and lead acetate was weaker (by about 30%).

The boundaries of the ranges (Fig. 4) are as follows: low-level — 6 or fewer TUNEL-positive cells per slice; medium-level — 7–10 cells, elevated — 14–18 cells, high-level — 19 or more cells per slice.

The following structure of apoptosis activation levels was revealed in the experimental groups (Table 3).

Table 3 shows that phenylcarbamate is a strong apoptosis inducer, causing predominantly a high level of its activation, while methanol and lead acetate cause moderate activation of programmed cell death of neurons.

The conducted analysis of the role of individual components of the brain metabolic systems in the activation of apoptotic processes under the action of neurotoxicants found that the studied metabolic parameters do not play a significant role in the process of brain cell apoptosis at the stage of formation of the long-term consequences of severe acute poisoning with neurotropic toxicants. Thus, their coefficients of determination ranged from 0.02 to 0.11, not being statistically significant. For neurospecific proteins, this may probably be due to both the features of toxic brain damage at the tissue level and the timing after acute intoxication, which triggered the activation of apoptosis.

Table 3. Distribution of animals by levels of apoptosis activation under the influence of neurotoxicants

Group	Level of apoptosis activation			
	low	moderate	increased	high
Control	88	12	–	–
Phenylcarbamate (1.6 mg/kg bw)	–	–	33	67
Methanol (11.5 g/kg bw)	–	100	–	–
Lead Acetate (300 mg/kg bw)	–	80	–	20

Table prepared by the authors using their own data

Note: the data is presented in the form of % incidence in the group.

Thus, NSE is known to reach a maximum in cerebrospinal fluid one day after an ischemic or hemorrhagic stroke, decreasing by days 4–5 and being more specific to focal brain damage than diffuse [12–15]. S100 protein also shows typical periods for increasing its concentration, i.e., days 2–7. MBP is a marker of axonal damage and demyelination, which may not have formed by the time of 30 days from the moment of acute intoxication. BDNF is more overexpressed with a lack of neuronal plasticity, and the weak response of this neurotrophin to brain tissue damage is clinically more significant [17–18].

In the group of intact animals, the apoptosis level had no significant correlations with either neurospecific proteins or LPO indicators and the antioxidant system (AOS), being a spontaneous process. In the group of animals exposed to phenylcarbamate intoxication, the apoptosis level was modestly affected by a low level of reduced glutathione ($r = -0.53$). After methanol intoxication, a weak correlation between apoptosis and the content of the main protein myelin ($r = +0.47$) was revealed, most likely reflecting the presence of a common inducing factor for them. After intoxication with lead acetate, the activity of neuronal apoptotic processes was associated with a low activity of glutathione transferase ($r = -0.66$) and SOD ($r = -0.47$). Therefore, the use of activators of these enzymes can be useful in the set of measures for preventing the long-term consequences of poisoning with organic lead derivatives.

NSE in the group of intact animals showed moderate negative associations with the activity of glutathione-dependent AOS enzymes — GST ($r = -0.63$) and GP ($r = -0.57$), i.e., an increase in the content of this marker protein may reflect the weakness of the AOS enzymatic link. At the same time, a positive correlation was found with the level of reduced glutathione ($r = +0.75$). Taken together, these connections may indicate a link between the damage to the bodies of neurons and the disorder of the ability to utilize reduced glutathione in antioxidant defense reactions, since the latter results in a simultaneous increase in its level and a decrease in the activity of utilization enzymes. This pattern is also observed in phenylcarbamate poisoning; however, there is an additional decrease in glucose-6-phosphate dehydrogenase activity ($r = -0.67$) and a positive correlation with S100 protein ($r = +0.70$). Following methanol intoxication, accumulation of utilized reduced glutathione ($r = +0.55$) is also noted; however, this is combined with lower BDNF values ($r = -0.50$). A peculiar pattern of NSE relationships is noted after lead acetate intoxication.

An alternative activation of the expression of either NSE or S100 protein was revealed (with the correlation coefficient between them of $r = -0.81$). Moreover, the low activity of AOS shifts the system toward increasing the level of S100 protein. In lead intoxication, a pronounced positive correlation (almost linear) was found between the level of NSE and the activity of SOD ($r = +0.94$), which implies a single response to lead poisoning. After phenylcarbamate poisoning, this marker negatively correlates with the activity of glutathione-dependent AOS enzymes. In case of methanol poisoning, an increase in the amount of this protein in brain tissues is associated with the accumulation of MDA ($r = +0.61$) and a compensatory substrate increase in SOD activity ($r = +0.57$). A similar correlation between MBR and SOD was also found after lead acetate poisoning ($r = +0.53$).

In phenylcarbamate poisoning, the BDNF level correlated with diene conjugates ($r = +0.61$). After methanol poisoning, it was correlated with a deficiency of reduced glutathione ($r = -0.60$). After lead poisoning, the neuroprotective effects of BDNF were recorded, including a decrease in axonal damage by the S100 protein marker ($r = -0.66$) and an improvement in antioxidant protection (a decrease in diene conjugates ($r = -0.62$), an increase in the activity of glutathione transferase ($r = +0.68$), glutathione peroxidase ($r = +0.61$) and SOD ($r = +0.49$).

Protein S100 in the group of intact animals and in methanol poisoning showed a moderate correlation with SOD ($r = +0.62$). After phenylcarbamate poisoning, it correlates with the level of NSE ($r = +0.70$), which may reflect the process of parallel damage to both neuron bodies and axons. After poisoning with lead acetate, the level of S100 protein increases with insufficiency of the antioxidant system, i.e., low levels of reduced glutathione ($r = -0.51$), GST ($r = -0.61$), and, in particular, GP ($r = -0.84$) and SOD ($r = -0.75$).

With regard to LPO and AOS indicators, a dense cluster of positively correlating activity indicators of glutathione-dependent enzymes (GST and GP) and glucose-6-phosphate dehydrogenase was isolated in the brain tissues of intact animals (correlation coefficients in the range from +0.70 to +0.98). In case of poisoning with phenylcarbamate and methanol, SOD joins this cluster, the density of correlations decreases slightly. At the same time, after poisoning with lead acetate, this cluster disintegrates, glutathione peroxidase becomes the key antioxidant enzyme, and SOD is associated with a moderate correlation with glucose-6-phosphate dehydrogenase.

CONCLUSION

The conducted research showed that the common effects shared by the analyzed toxicants include an increase in the number of neurons dying by apoptosis (most pronounced with phenylcarbamate intoxication) and a decrease in the blood serum level of S100 protein (most pronounced with lead acetate poisoning). Moderate activation of antioxidant protection enzymes was specific for the long-term effects of methanol poisoning, likely as a compensatory reaction against the activation of LPO processes. The long-term effects of lead acetate poisoning in survivor animals were manifested by increased serum levels of NSE and BDNF, decreased protein S100 and MBP, increased levels of diene conjugates with decreased GST activity, and moderate activation of glucose-6-phosphate dehydrogenase. The latter is a key enzyme in the pentose phosphate pathway for the formation of reduced forms of coenzymes for the oxidation of energy metabolism substrates in brain tissues.

It was established that phenylcarbamate exhibits the properties of a strong inducer of apoptosis of cerebral cortex cells, while methanol and lead acetate are inducers with moderate activity.

It should be noted that the calculated coefficients of determination exhibit low or moderate values (for glutathione transferase and glutathione peroxidase). This suggests that neurospecific proteins, lipid peroxidation and antioxidant protection processes do not significantly affect the processes of neuronal apoptosis in survived animals at the stage of formation of long-term health consequences of severe acute poisoning. In this regard, future research should address the effect of metabolic processes in animal brain tissue on the activity of apoptotic processes and the formation of long-term consequences at an earlier stage after acute intoxication with neurotropic toxicants.

References

1. Krasnov VN. Psycho-organic syndrome as a subject of neuropsychiatry. *Doktor.Ru.* 2011;(4):34–42 (In Russ.). EDN: OYYBSX
2. Brendan L. McNeish, Noah Kolb. Toxic Neuropathies. *Continuum (Minneap Minn)*. 2023;29(5):1444–68. https://doi.org/10.1212/CON.0000000000001343
3. Gaikova ON, Kozlov AA, Katretskaya GG, Melnikova MV, Melekhova AS, Bondarenko AA, et al. Morphological characteristics of toxic brain damage. *Extreme medicine*. 2024;26(2):13–19 (In Russ.). https://doi.org/10.47183/mes.2024.025
4. Deev RV, Bilyalov AI, Zhampeisov TM. Modern concepts of cell death. *Genes and Cells.*2018; 13(1):6–19 (In Russ.). https://doi.org/10.23868/201805001
5. Kashuro VA. Dynamics of the content of neurotrophic factors of the brain in experimental coma in rats. *Kazan Medical Journal*. 2013;(94):695–9 (In Russ.). EDN: RSHIDV
6. Kostrova TA. Experimental assessment of changes in neurotrophic and apoptotic factors in the long-term effects of acute severe sodium thiopental poisoning. *Toxicological bulletin*. 2019;(5): 49–53 (In Russ.). https://doi.org/10.36946/0869-7922-2019-5-49-53
7. Luzhnikov EA. The specific features of the development and course of toxicohypoxic encephalopathy in acute poisoning by neurotoxic agents. *Anesthesiology and reanimatology*. 2005;(6):4–8 (In Russ.). EDN: HVKWSV
8. Petrov AN, Voytsekhovich KO, Melekhova AS, Lisitskiy DS, Bel'skaya AV, Mikhaylova MV, Gaykova ON. Problems of diagnostics of neurotoxic disorders — the effects of convulsive substances poisoning. *Bulletin of the Russian Military Medical Academy*. 2017;3(59):211–7 (In Russ.). EDN: ZOWOBD
9. Bespalov AYa, Prokopenko LI, Gorchakova TL, Kozlov VK, Petrov AN, Zaytseva MA, Melekhova AS, Bel'skaya AV, Mel'nikova MV, Ivanov MB, Chigareva SM. Hydrochlorides of substituted 2-[(dimethylamino)methyl] aryl dimethyl carbamates with anticholinesterase activity. Patent of the Russian Federation No. 2754133;2021 (In Russ.).
10. Kapanadze GD, Revyakin AO, Shustov EB. Methodology for evaluating the detoxification system of xenobiotics in laboratory animals. *Biomedicine*. 2017;(3):71–81 (In Russ.). EDN: ZHYWKB
11. Kostrova TA, Batotsyrenova EG, Kashuro VA, Dolgo-Saburov VB, Stepanov SV, Zolotoverhaya EA, et al. Evaluation of biochemical parameters in the brain tissues of rats in the long-term period after severe sodium thiopental poisoning. *Medicine of Extreme Situations*, 2019;21(3):429–35 (In Russ.). EDN: GGIEFQ
12. Maksimova MYu, Ionova VG, Syskina AA, Shabalina AA, Kostyreva MA, Senektutova OA. Neurospecific peptides in the assessment of brain damage in patients with atherothrombotic stroke. *Annals of Clinical and Experimental Neurology*. 2011;5(3):4–10 (In Russ.). EDN: OOKEFR
13. Wunderlich MT, Lins H, Skalej M, Wallesch C-W, Goertler M. Neuron-specific enolase and tau protein as neurobiochemical markers of neuronal damage are related to early clinical course and long-term outcome in acute ischemic stroke. *Clin Neurol Neurosurg.*2006; 108(6):558–63. https://doi.org/10.1016/j.clineuro.2005.12.006
14. Berger RP, Beers SR, Richichi R, Wiesman D, Adelson PD. Serum biomarker concentrations and outcome after pediatric traumatic brain injury. *Journal of Neurotrauma*. 2007;(24):1793–1801. https://doi.org/10.1089/neu.2007.0316
15. Vlasakova K, Tsuchiya T, Garfinkel IN, et al. Performance of biomarkers NF-L, NSE, Tau and GFAP in blood and cerebrospinal fluid in rat for the detection of nervous system injury. *Front Neurosci.* 2024;(17):1285359. https://doi.org/10.3389/fnins.2023.1285359
16. Klimenko AL, Deev AI, Baskakov IS, Bogdanova MN, Zabirova AKh, Mazikina AN. Neurospecific proteins of s100 family and metal-ligand homeostasis in etiopathogenesis of ischemic stroke: a literature review. *Trace elements in medicine*. 2019;20(1):3–13 (In Russ.). https://doi.org/10.19112/2413-6174-2019-20-4-3-13
17. Levchuk LA, Bokhan NA, Ivanova SA. Neurospecific Proteins as Transdiagnostic Markers of Affective Disorders. *Neurochemistry*. 2023;40(1):30–4 (In Russ.). https://doi.org/10.31857/S1027813323010119
18. Lima Giacobbo B, Doorduin J, Klein HC, Dierckx RAJO, Bromberg E, de Vries EFJ. Brain-Derived Neurotrophic Factor in Brain Disorders: Focus on Neuroinflammation. *Mol Neurobiol.* 2019;56(5):3295–3312. https://doi.org/10.1007/s12035-018-1283-6

AUTHORS

Evgeny B. Shustov, Dr. Sci. (Med.),
shustov-msk@mail.ru
https://orcid.org/0000-0001-5895-688X

Kristina V. Masterova
masterova.k.v@toxicology.ru
https://orcid.org/0000-0002-5731-8146

Ekaterina A. Zolotoverkhaja, Cand. Sci. (Biol.)
e.zolotoverkhaja@yandex.ru
https://orcid.org/0000-0002-9708-2596

Ksenia O. Tanayants
tanayantsksenia@yandex.ru
https://orcid.org/0009-0009-7594-0201

Yulia O. Sokolova, Cand. Sci. (Biol.)
yulya_sokolova91@mail.ru
https://orcid.org/0009-0002-8748-8426

Margarita V. Melnikova
melnikova.m.v@toxicology.ru
https://orcid.org/0000-0002-2996-5151

Vladimir F. Ostrov, Cand. Sci. (Biol.)
ostrov.v.f@toxicology.ru
https://orcid.org/0009-0008-1410-806X

Larisa G. Kubarskaya, Cand. Sci. (Biol.),
larkub@yandex.ru
https://orcid.org/0000-0001-7622-0390

Alexander A. Kozlov
Alexandrk0zlov89@yandex.ru
https://orcid.org/0000-0003-4168-0658

Petr K. Potapov, Cand. Sci. (Med.)
forwardspb@mail.ru
https://orcid.org/0000-0002-4602-4468

CC BY 4.0

Check for updates

PHYSICAL AND CHEMICAL CRITERIA FOR HAZARD ASSESSMENT OF CNS-ACTIVE XENOBIOTICS

Denis V. Krivorotov✉, Anatoly I. Nikolaev, Andrey S. Radilov, Vladimir R. Rembovsky, Viktor A. Kuznetsov

Research Institute of Hygiene, Occupational Pathology and Human Ecology, Leningrad region, Russia

Introduction. Forensic medical examinations frequently encounter poorly understood, potentially hazardous psychoactive substances. At the same time, information on the biological activity of such substances may be either fragmentary and contradictory or absent altogether. Therefore, the development of approaches to predicting the health hazard of xenobiotics is an urgent task of emergency medicine.

Objective. To study the relationship between physicochemical properties and the hazard rate of one class of CNS-active substances using the methods of mathematical analysis followed by scientific substantiation of criteria for preliminary hazard assessment of narcotic drugs.

Materials and methods. The study models included the known structures of narcotic analgesics, divided into three groups according to their potential hazard rate. The physicochemical properties of such substances, i.e., molecular weight, polarity, polar surface area, distribution coefficients, and basic dissociation constants were considered as potential hazard factors. Linear discriminant analysis was used to identify the relationship between the physicochemical properties of psychoactive substances and their hazard potential.

Results. The considered example of one class of CNS-active substances confirms the relationship between their hazard rate and the physicochemical properties affecting their redistribution from the central bloodstream to the central nervous system. Physicochemical criteria for predicting the hazard rate of psychoactive substances are proposed. These criteria serve as classification functions that distinguish groups of model substances.

Conclusions. The physicochemical properties of psychoactive substances and the strength of their binding to target receptors equally determine the characteristics of their toxic effect. The formulated classification functions, calculated based on the physicochemical properties of substances, can be used for a preliminary hazard assessment of xenobiotics during their detection in biological samples.

Keywords: xenobiotics; biological samples; narcotic drugs; blood–brain barrier; physicochemical properties; molecular weight; polarity; dissociation constants; distribution coefficients

ФИЗИКО-ХИМИЧЕСКИЕ КРИТЕРИИ ОЦЕНКИ ОПАСНОСТИ ЦНС-АКТИВНЫХ КСЕНОБИОТИКОВ

Д.В. Криворотов✉, А.И. Николаев, А.С. Радилов, В.Р. Рембовский, В.А. Кузнецов

Научно-исследовательский институт гигиены, профпатологии и экологии человека Федерального медико-биологического агентства, Ленинградская область, Россия

Введение. Судебно-медицинская экспертиза часто сталкивается с малоизученными, потенциально опасными психоактивными веществами. При этом информация о биологической активности таких веществ отрывочна и противоречива или вообще отсутствует. Поэтому разработка подходов к прогнозированию опасности ксенобиотиков является актуальной задачей медицины экстремальных ситуаций.

Цель. Изучение взаимосвязи физико-химических свойств и степени опасности представителей одного из классов ЦНС-активных веществ с использованием методов математического анализа и последующим научным обоснованием критериев предварительной оценки опасности наркотических средств.

Материалы и методы. В качестве модельных объектов исследования использовали известные структуры наркотических анальгетиков, разделенные на три группы по степени потенциальной опасности. В качестве факторов потенциальной опасности таких веществ рассматривали их физико-химические свойства, такие как: молекулярная масса, полярность, площадь полярной поверхности, коэффициенты распределения и константы основной диссоциации. Для выявления связи физико-химических свойств и степени опасности психоактивных веществ использовали линейный дискриминантный анализ.

Результаты. На примере представителей одного из классов ЦНС-активных веществ показана связь степени их опасности с физико-химическими свойствами, влияющими на перераспределение таких веществ из центрального кровотока в ткани центральной нервной системы. Для прогнозирования степени опасности психоактивных веществ предложены физико-химические критерии — классификационные функции, достаточно хорошо разделяющие группы модельных веществ между собой.

Выводы. Показали, что физико-химические свойства психоактивных веществ определяют особенности их токсического действия в не меньшей степени, чем сила их связывания с целевыми рецепторами. Сформулированные в работе классификационные функции, рассчитываемые на основании физико-химических свойств веществ, могут быть использованы для предварительной оценки степени опасности ксенобиотиков в ходе их выявления в биологических пробах.

Ключевые слова: ксенобиотики; биологические пробы; наркотические средства; гематоэнцефалический барьер; физико-химические свойства; молекулярная масса; полярность; константы диссоциации; коэффициенты распределения

✉ Криворотов Денис Викторович denis.krivorotov@bk.ru

INTRODUCTION

The forensic medical examination of poisoning cases with psychoactive substances is carried out using targeted analytical methods, such as gas chromatography–mass spectrometry (GC-MS) and liquid chromatography-tandem mass spectrometry (HPLC-MS/MS), to detect known xenobiotics and their metabolites [1]. Untargeted testing using high-resolution liquid chromatography-mass spectrometry (HPLC-HRMS) technologies can be used to identify the chemical structure of new substances appearing in illicit traffic. Substances identified in biological samples can pose a significant threat [2–5]. Although the safety of a particular drug can be measured by determining its therapeutic index, calculated as the ratio of the drug maximum dose that does not exhibit toxicity to the dose that provides the desired effect (LD_{50}/ED_{50}), this approach cannot be used for substances detected during forensic medical examination. In addition, information about the hazardous pharmacological activity of xenobiotics may frequently be either fragmentary and contradictory or absent altogether, for a number of reasons:

- rapid emergence of new psychoactive chemicals that are illegally marketed in the absence of reference materials and methods for their determination in biological and other environments [6];
- legislative restrictions on the research of narcotic drugs with no intended medical use [6];
- insufficient standardization of methods for studying the pharmacological properties of narcotic drugs [7, 8];
- complexity of the interspecific transfer of preclinical research results, leading to an underestimation of the toxicity of narcotic drugs [9];
- impossibility of comparing the biological effects of drugs that are not standardized in terms of purity and isomeric composition [3].

The above reasons hamper the medicobiological assessment of new psychoactive substances, although there has been a growth in the number of cases of illicit trafficking both in Russia and globally [4, 8–10]. In order to be able to predict the potential hazard of CNS-active xenobiotics and other chemical substances, criteria for a straightforward determination of their toxic effect are required.

It is common knowledge that the toxicity of many narcotic analgesics is associated with opioid-induced respiratory depression, which result in the patient's death in the absence of proper treatment [11]. The central generator of breathing patterns in the brainstem is the preBötzinger Complex and the Kolliker–Fuse nucleus. In these areas of the brain, only 70–140 neurons are involved in responding to an increase in carbon dioxide (pCO_2) levels and a decrease in blood oxygenation (pO_2), which is necessary for the reflex mechanism of respiration [12]. Accordingly, the mechanism of regulation of respiratory activity is extremely vulnerable to substances capable of selectively affecting these targets in the brain. It can be assumed that the health hazard of CNS-active xenobiotics, expressed in terms of strength and speed, is mediated, on the one hand, by factors determining the degree of their effect on target receptors in the neurons of these brain regions, and, on the other, by factors determining the transfer of xenobiotics from the central bloodstream to their biological targets in the brain.

The strength of narcotic analgesics is often associated with the inhibition constants of opioid receptors [13]. However, under standardized conditions, morphine and fentanyl, which differ significantly in the strength of their analgesic effects, possess comparable inhibition constants (K_i) of the μ-opioid receptors (MOR) (Table 1) [5, 7].

Upon closer examination, no direct relationship exists between the analgesic activity of opioids and the strength of their binding to the receptor, which was earlier confirmed by numerous examples [14]. Thus, according to Boström et al., oxycodone, which binds to opioid receptors more than 20 times less strongly than morphine (Table 1), exhibits a 1.8-fold greater analgesic activity. This effect can be explained by its higher concentration in the target brain tissues than in the blood. Morphine, on the contrary, has an achievable concentration in the brain of rats several times lower than in the blood [15]. Thus, the binding of small molecules to opioid receptors in most cases is the determining condition for manifestation of analgesic activity, although being not the main factor in the strength and speed of its manifestation (similar to the classical works of N.V. Lazarev on the manifestation of narcotic properties in hydrocarbons (non-electrolytes)) [16]. The hazardous effects of opioid analgesics are also related to their properties, which determine the characteristics of entry into target tissues, organs, and targets in the central nervous system (CNS) through the blood-brain barrier (BBB).

The BBB acts as a filter through which nutrients flow from the bloodstream to the brain and in the opposite direction, while the waste products of the nervous tissue are removed. The BBB protects the brain from microorganisms, toxins, cellular and humoral factors of the immune system, and xenobiotics circulating in the blood. Drugs acting on CNS targets must have the ability to penetrate such a biological barrier. Currently, three main ways of transporting small molecules to brain tissues are being considered, including unidirectional penetration into the brain through passive and facilitated diffusion, due to a concentration gradient of substances and requiring no additional energy; active transport, requiring energy (ATP) for the transport of molecules against a concentration gradient; passive diffusion for moderately lipophilic medications and active

Table 1. Inhibition constants of μ-opioid receptors by some narcotic analgesics

Low-affinity ligands, K_i>100 nM		Morphine-like ligands, K_i=1–100 nM		High-affinity ligands, K_i<1 nM	
medication	K_i (nM) MOR	medication	K_i (nM) MOR	medication	K_i (nM) MOR
tramadol	1248.6	hydrocodone	41.58	butorphanol	0.76
codeine	734.2	oxycodone	25.87	levorphanol	0.41
meperidine	450.1	diphenoxylate	12.37	oxymorphone	0.40
propoxyphene	120.2	alfentanil	7.39	hydromorphone	0.36
pentazocine	117.8	methadone	3.37	buprenorphine	0.21
		nalbuphine	2.11	sufentanil	0.13
		fentanyl	1.34		
		morphine	1.16		

Table prepared by the authors using data from [7]

transport mechanisms for penetration through the BBB of predominantly polar molecules [17, 18].

The membranes separating the cells of the BBB layers act as a channel for the diffusion of organic molecules through the BBB cellular layers. In order to pass through such a channel, a molecule dissolved in the blood must be transformed during a multi-stage physicochemical process of desolvation and charge loss for a non-covalent interaction with the phospholipid bilayer. This process is similar to that of ligand-receptor interaction, although with lower steric requirements. Therefore, for penetration into the brain, small molecules must exhibit a set of specific properties, such as optimal geometric size, ionization properties, flexibility, etc. Thus, lipophilicity is a parameter that correlates well with the analgesic power of anesthetics and analgesics. This parameter, expressed in the form of Log$P$ [16], is now considered as a composite descriptor describing the contribution of steric intermolecular interactions and that of formed hydrogen bonds [17]. Descriptors of hydrogen bond formation are properties of molecules, such as polarizability, polar surface area, the number of donors and acceptors of hydrogen bonds, or heteroatoms capable of their formation. Polar compounds with a high potential for hydrogen bonding, e.g., peptides, cannot easily penetrate the BBB. Polarizability, underlying a number of physical properties of substances, including surface tension and solubility, is characterized by a dipole moment. The polar surface area is defined as the sum of the surfaces of all polar atoms or molecules, primarily oxygen and nitrogen. Medications acting on the CNS possess smaller polar surface areas (PSA) than other classes of drugs, usually no more than 90 A². Molecules with a polar surface area of more than 140 A² do not readily penetrate cell membranes.

Geometric and steric factors expressed by the molecular weight, molecular volume, and flexibility of the molecule, are important for diffusion through biological membranes. For effective penetration through the BBB, the molecular weight should not exceed 400 Da. The molecular volume as a function of the molecular weight and structure takes all the conformations available to the molecule into account. The presence of more than ten rotating connections in structures correlates with a decrease in their bioavailability and CNS activity. The limited

flexibility and compactness of molecules with fewer polar groups on their surface capable of functioning as donors and acceptors of hydrogen bonds is an advantage for substances acting on the CNS; therefore, the parameters describing these properties are significant factors related to the CNS activity of xenobiotics.

Most CNS-active substances have a nitrogen atom capable of ionization in the blood plasma. The resulting charge of the protonated molecule negatively affects its ability to diffuse through the dielectric layers of phospholipid membranes, compared to neutral molecules [18]. However. the presence of a positive charge on the nitrogen atom is considered an important factor for the electrostatic interaction of substances with the key amino acids of target receptors [19]. The molecule ionization degree in the buffer system of the blood and cerebrospinal fluid is a dualistic factor related both to the rate of entry of active molecules into CNS tissues and influencing their ability to bind to CNS targets [20, 21]. Thus, the severity of the toxic effect of CNS-active substances, due to the effectiveness of their entry into the brain, is determined by the sum of physicochemical factors related to their chemical structure. These factors can be experimentally evaluated or calculated.

This work is aimed at studying the relationship between the physicochemical properties of one class of CNS-active substances and their health hazard potential using mathematical analysis. On this basis, criteria for preliminary hazard assessment of narcotic drugs are substantiated.

MATERIALS AND METHODS

Table 2 presents a sample of model objects used in the study selected from the known structures of narcotic analgesics. The objects under consideration were divided into three groups:

1. Group 1 includes narcotic analgesics ever used in medicine [14], taking into account possible side effects during their medical use. These substances are considered as those potentially capable of manifesting health hazard.

2. Group 2 includes narcotic substances not intended for medical use, but purposefully created for illegal human use, taking into account information about cases of mass poisoning with such substances [22]. These substances

are considered as those potentially capable of manifesting high health hazard.

3. Group 3 included highly active drugs, the use of which in medicine requires precautions for their controlled dosing, as well as veterinary and research drugs not intended for human consumption [3, 14]. These substances are considered as those potentially capable of manifesting extremely high health hazard.

The physicochemical properties that can be measured without laborious experiments and reference materials of controlled substances were considered as potential descriptors of the hazard rate of CNS-active xenobiotics (see Table 3). The molecular weight of substances was determined by GC-MS; the distribution constants "octanol/water" and acid-base dissociation correlated with retention times were established by HPLC [21, 23]. In cases where information about the structural formula of a xenobiotic can be found in mass spectrometry databases, computer simulation methods using accessible and reliable calculation algorithms are used to determine its physicochemical properties [24].

The values of the selected physicochemical parameters for the training sample of substances were calculated using the ACD/Percepta software [24]. The methods of descriptive statistics and the method of linear discriminant analysis using the Statistica 6.0 statistical analysis application were used for mathematical data analysis. We previously showed the effectiveness of multidimensional statistics (chemometry) methods, in particular linear discriminant analysis and multiple regression for calculating toxic properties

of refrigerants based on the physicochemical parameters of molecules [25], for assessing the degree of exposure to xenobiotics and noninvasive diagnosis of a number of diseases based on the spectral characteristics of biological samples[1] [26].

DISCUSSION

The generated sample contained 53 anonymized records of the calculated values of the physicochemical properties of the model CNS-active substances described in the literature (Table 2). The structures of the analyzed model preparations were used for calculating the selected physicochemical quantities, the results of which are shown in Table 4.

Table 5 presents the average values of the physicochemical descriptors used to construct regression models and to determine the limits of their applicability.

The average values of the physicochemical quantities presented in Table 5 show that the narcotic substances in Group 2 demonstrate the highest lipophilicity (Log$P$). At the same time, the ratio of the average lipophilicity values of the drug groups in water and blood plasma — Log$P$ and Log$D_{7.4}$ — shows that the lipophilicity of Groups 1 and 2 significantly decreases at physiological pH. Conversely, the highly active substances belonging to Group 3 and having a lower value of the basic ionization constant demonstrate high lipophilicity not only in water, but also in blood plasma. This emphasizes the relationship between lipophilicity and the ability

Table 2. Characteristics of the training sample of model substances

Group	Model objects	Information source	Structures number	Assessment of model objects
1	Medical narcotic analgesics	[7]	17	substances with a hazard risk
2	Non-medical narcotic analgesics	[22]	18	substances with a high hazard risk
3	Highly active narcotic analgesics	[3, 14]	18	substances with an extremely high hazard risk
Total number of training sample structures			53	

Table prepared by the authors using data from [3, 7, 14, and 22]

Table 3. Selected physicochemical descriptors of the hazard level of CNS-active xenobiotics

Parameter designation	Parameter Description	Dimension	Determination possibility
Log$P$ / Log$D_{7.4}$	The partition coefficient of the substance in the octanol–water system reflects the lipophilicity of the substances; the ability to dissolve in fats, lipids, and other media at pH 7.0 (Log$P$) or at physiological pH (Log$D_{7.4}$) during the distribution of substances in the body.	–	HPLC is experimental, by calculation methods
pK$_b$	The basic dissociation constant determines the lipophilicity of ionized molecules.	–	HPLC is experimental, by calculation methods
MW	The molecular weight of the substance reflects the steric factors affecting the distribution of substances in the body.	Da	HPLC-MS is experimental, by calculation methods
TPSA	The topological polar surface area is a calculated parameter, associated with the ability of substances to cross biological membranes	$\mathring{A}^2$ (10^{-16}cm^2)	by calculation methods
Polar	Polarizability — the physical property of substances to acquire an electric or magnetic dipole moment in an external electromagnetic field and associated with the ability of substances to form hydrogen bonds and overcome biological membranes	$\mathring{A}^3$ (10^{-24}cm^3)	by calculation methods

Table prepared by the authors

---

[1] Rembovsky VR, Radilov AS, Dulov SA, Nikolaev AI. Assessment of the degree of exposure to xenobiotics based on the spectral characteristics of water-protein complexes of blood plasma. Methodological recommendations 12.11. Moscow: FMBA; 2012 (In Russ.).

of substances to enter CNS tissues during redistribution in the blood-brain system.

The physicochemical criteria that can be used for hazard assessment of CNS-active substances were established based on paired correlation coefficients between the physicochemical descriptors shown in Table 6. It can be seen that most descriptors are weakly correlated with one another. The strongest correlation is observed between the $LogD_{7.4}$ and $LogP$ values since these are highly

similar parameters in nature. The difference between them is related to the pH values at which they are determined, being due to the degree of ionization of the molecules of substances at these pH values. This is indicated by a rather strong correlation ($R = 0.97$) between the calculated value ($LogD_{7.4} - LogP$) and the pKb value.

A strong correlation is also observed between the values of MW and Polar. This is likely to be due to a proportional increase in the integral polarizability of the molecule,

Table 4. Calculation of physicochemical descriptors

No.	Model object	Group number	Calculated physicochemical descriptors					
			$LogD_{7.4}$	$LogP$	MW	TPSA	Polar	pK_b
1	fentanyl	1	3.32	4.08	336.47	23.55	41.09	8.08
2	buprenorphine	1	3.48	4.45	467.64	62.16	52.07	8.26
3	methadone	1	3.12	4.44	309.44	20.31	38.02	8.70
4	levorphanol	1	1.94	3.21	257.37	23.47	30.49	8.61
5	hydrocodone	1	0.57	1.31	299.36	38.77	32.32	8.06
6	pentazocine	1	3.05	3.79	285.42	23.47	34.96	8.04
7	butorphanol	1	1.96	3.52	327.46	43.7	37.64	8.85
8	propoxyphene	1	3.97	4.85	339.47	29.54	40.58	8.23
9	meperidine	1	1.22	2.44	247.33	29.54	28.25	8.60
10	nalbuphine	1	0.98	2.03	357.44	73.16	38.11	8.35
11	tramadol	1	0.71	2.54	263.37	32.7	30.90	9.24
12	hydromorphone	1	0.53	1.29	285.33	49.77	30.41	8.03
13	codeine	1	0.34	1.21	299.36	41.93	32.84	8.21
14	morphine	1	-0.18	0.69	285.33	52.93	30.93	8.16
15	oxycodone	1	0.16	0.91	315.36	59.00	32.95	8.06
16	diphenoxylate	1	5.42	5.72	452.58	53.33	52.93	7.40
17	oxymorphone	1	0.25	1.00	301.33	70.00	31.03	8.03
18	4-fluorophenyl	2	3.11	3.87	354.46	23.55	41.09	8.07
19	furanyl-fentanyl	2	3.35	4.12	374.47	36.69	44.25	8.08
20	3-methylthiophentanyl	2	2.96	4.09	356.52	51.79	42.32	8.50
21	β-hydroxy-thiophentanyl	2	2.38	2.77	358.49	72.02	41.06	7.58
22	β-hydroxy-fentanyl	2	2.87	3.07	352.47	43.78	41.70	7.15
23	α-methyl-thiophentanyl	2	3.15	4.04	356.52	51.79	42.25	8.23
24	α-methyl-fentanyl	2	2.75	4.09	350.49	23.55	42.89	8.73
25	acetyl-α-methylfentanyl	2	2.56	3.91	336.47	23.55	41.05	8.73
26	3-methylbutyril fentanyl	2	4.21	4.98	364.52	23.55	44.79	8.08
27	remifentanil	2	1.77	1.85	376.44	76.15	40.06	6.70
28	4-methoxy-butyrylfentanyl	2	3.55	4.33	380.52	32.78	45.58	8.10
29	thiofentanyl	2	2.66	3.79	342.49	51.79	40.45	8.50
30	4-fluoro-butyrylfentanyl	2	3.69	4.44	368.48	23.55	42.93	8.07
31	3-methylfentanyl	2	3.36	4.13	350.49	23.55	42.96	8.08
32	acrylic fentanyl	2	2.99	3.75	334.45	23.55	40.98	8.08
33	acetylfentanyl	2	2.98	3.74	322.44	23.55	39.25	8.08
34	alfentanil	2	1.99	2.04	416.51	81.05	46.25	6.53
35	sufentanil (SF)	2	2.91	3.77	386.55	61.02	44.80	8.20
36	pyrrole analog SF No.1	3	2.33	2.55	383.48	54.78	44.16	7.19
37	etorfin	3	2.30	3.09	411.53	62.16	45.51	8.07

Table 4 (continued)

No.	Model object	Group number	Calculated physicochemical descriptors					
			$LogD_{7.4}$	$LogP$	MW	TPSA	Polar	pK_b
38	heterocyclic analogue CF No.1	3	3.05	3.10	506.59	90.47	54.93	6.43
39	heterocyclic analogue SF No.1	3	1.80	2.67	462.58	65.45	53.43	8.20
40	heterocyclic analogue SF No.2	3	3.14	3.26	449.54	70.16	49.87	6.86
41	heterocyclic analogue CF No.2	3	2.93	2.98	463.52	87.23	49.82	6.43
42	heterocyclic analogue SF №3	3	2.59	2.81	435.55	53.09	49.82	7.23
43	гетероцикл. аналог CF No.3	3	2.61	2.70	449.54	70.16	49.77	6.79
44	heterocyclic analogue CF No.4	3	2.53	2.65	483.60	87.23	52.76	6.90
45	pyrrole analog CF No.1	3	0.72	1.16	444.48	142.52	46.55	7.64
46	pyrrole analog SF No.2	3	1.59	2.46	370.48	50.6	43.21	8.20
47	pyrrole analog CF No.2	3	1.91	2.12	384.47	67.67	43.55	7.19
48	heterocyclic analogue CF No.5	3	2.26	2.86	415.55	90.98	45.91	7.86
49	ohmefentanyl	3	3.04	3.24	366.49	43.78	43.57	7.15
50	3-thiophene-CF	3	3.01	3.61	400.53	78.09	44.75	7.86
51	vinyl-CF	3	3.19	3.51	392.49	49.85	45.29	7.44
52	lofentanyl	3	3.96	4.29	408.53	49.85	47.26	7.44
53	carfentanyl (CF)	3	3.17	3.49	394.50	49.85	45.39	7.44

Table prepared by the authors using their own data

Table 5. Descriptor mean values by groups

Substance group	Calculated physicochemical descriptors					
	$LogD_{7.4}$	$LogP$	MW	TPSA	Polar	pK_b
Group 1	1.46	2.49	300.7	40.79	34.04	8.35
Group 2	3.16	4.08	355.6	33.88	42.55	8.25
Group 3	2.51	2.83	414.9	69.86	46.58	7.28
All substances	2.38	3.07	365.0	51.43	41.78	7.86

Table prepared by the authors using their own data

Table 6. Correlation coefficients of physicochemical descriptors

	$LogD_{7.4}$	$LogP$	MW	TPSA	Polar	pK_b	$LogP — LogD_{7.4}$
$LogD_{7.4}$	1.00	0.92	0.36	-0.31	0.58	-0.18	-0.21
$LogP$	0.92	1.00	0.10	-0.52	0.35	0.20	0.18
MW	0.36	0.10	1.00	0.64	0.96	-0.70	-0.68
TPSA	-0.31	-0.52	0.64	1.00	0.43	-0.56	-0.53
Polar	0.58	0.35	0.96	0.43	1.00	-0.60	-0.59
pK_b	-0.18	0.20	-0.70	-0.56	-0.60	1.00	0.97
$LogP — LogD_{7.4}$	-0.21	0.18	-0.68	-0.53	-0.59	0.97	1.00

Table prepared by the authors using their own data

associated with an increase in the number of polarizable fragments with increasing mass. An analysis of the obtained correlations between the physicochemical properties in the training groups of CNS-active substances showed that the values considered, either by themselves or in pairs, do not allow for an unambiguous distribution of substances to one of the three groups of hazardous substances.

A discriminant analysis was used to analyze the entire data set of physicochemical properties of model substances in order to identify their relationship with the degree of their health hazard. Discriminant analysis, as a branch of multidimensional statistical analysis, includes statistical methods for classifying multidimensional observations in a situation where the researcher has a priori so-called

training samples (classification with learning). Discriminant analysis makes it possible to classify an object based on the measurement of various characteristics (features, descriptors), i.e., permitting their assignment to one of several groups (classes). In this study, discriminant analysis was used to determine the differences of aggregates in the mean of a variable (or a linear combination of variables) for subsequent use of this variable or a linear combination of variables as a criterion for the membership of new members to a particular group.

The resulting data set was subjected to a linear discriminant analysis (LDA) procedure with step-by-step inclusion of variables. The grouping variable was the "Group" category, with all other descriptors being used as independent variables. Initially, the data array was divided into two parts: one part was used as a training part to derive a mathematical classification model, while the second part acted as a control part to verify the resulting model. The last three compounds in the list of each group were used as controls.

In the process of LDA with step-by-step inclusion of variables, discriminant functions were determined. At each step, we analyzed all the variables to find the one that made the greatest contribution to the difference between the aggregates. This variable was included in the model at this step, and then the transition to the next step was carried out. The step-by-step variable inclusion mode allowed the minimum of variables to be involved in the analysis. The discriminant functions, expressing the maximum heterogeneity of groups among themselves, were linear combinations of variables optimized such that to discriminate groups among themselves most effectively. Since all discriminant functions were orthogonal, they collectively formed the phase space of discriminant functions, i.e., an n-dimensional Cartesian coordinate system, where n is the number of statistically significant discriminant functions.

The discriminant functions were uniform for the data set involved in LDA; however, the values of the roots of each of the discriminant functions were strictly specific for each substance. The roots of discriminant functions for each substance were calculated by matrix multiplication of a vector of descriptors of this substance by a matrix of coefficients of discriminant functions. Thus, the original data matrix was transformed into a matrix containing values of the roots of discriminant functions instead of descriptors. The values of the roots, unique to each junction, were essentially the coordinates of the points of the corresponding junctions in the phase space of the discriminant functions. The average values of these roots for each group determined the coordinates of the group centers (the so-called group centroids). It was the values of the roots of discriminant functions or the coordinates of objects (substances) in the phase space of discriminant functions that made it possible to classify objects, i.e., to correlate a specific substance with any of the groups by the proximity of a point to the centroid of the group.

The conducted LDA of the training sample of the data matrix with descriptors for three groups of substances produced two statistically significant discriminant functions $dF1$ and $dF2$. These functions were fully descriptive the data array, of which the $dF1$ function describes 88% of the information contained in the data presented in Table 7.

Thus, the obtained discriminant functions are the following linear combinations of descriptor values:

$dF1 = 0{,}051 \times MW + 2.599 \times LogP - 1.943 \times LogD_{7.4} - 0.643 \times Polar - 0.032 \times TPSA + 6.638$

$dF2 = 0.028 \times MW - 1.376 \times LogP - 0.845 \times LogD_{7.4} - 0.359 \times Polar + 7.010$

The standardized coefficients for each descriptor for the $dF1$ function, which are relatively close to each other in absolute value and far from zero, indicate the important contribution of all the considered physicochemical indicators to the discrimination performed by this most statistically significant discriminant function. In principle, the same applies to the $dF2$ function, with the exception for the TPSA (topological area of the polar surface) indicator, which proved to be negligible.

For all model substances from Table 4, including the control ones, the values of the roots of the discriminant functions $dF1$ and $dF2$ were calculated. The root values, unique for each junction, are the coordinates of the points of the corresponding junctions in the phase space of discriminant functions, which is a flat coordinate system with

Table 7. Coefficients of discriminant functions for groups of model xenobiotics

Descriptor	Non-standardized		Standardized	
	$dF1$	$dF2$	$dF1$	$dF2$
MW	0.051	0.028	1.724	0.966
Log$P$	2.599	-1.376	2.190	-1.159
Log$D_{7.4}$	-1.943	0.845	-1.712	0.745
Polar	-0.643	-0.359	-2.329	-1.300
TPSA	-0.032	0.000	-0.611	-0.005
Constant	6.638	7.010	0	0
Eigenval	**4.090**	**0.562**	**4.090**	**0.562**
Cum.Prop	**0.879**	**1.000**	**0.879**	**1.000**

Table prepared by the authors using their own data
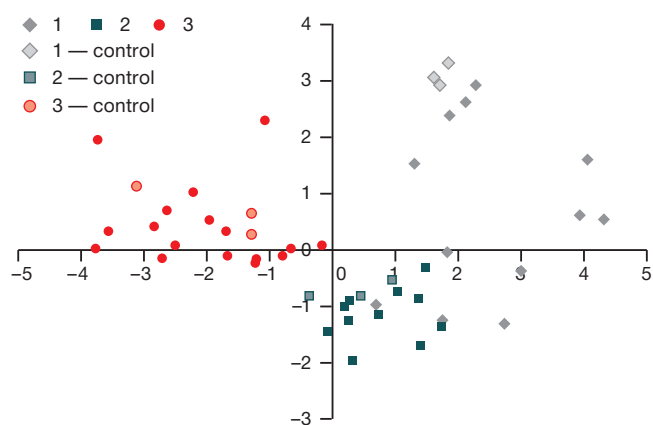
Figure prepared by the authors using their own data

Fig. 1. Roots values of the $dF1$ and $dF2$ discriminant functions for groups 1, 2, and 3 of model chemical xenobiotics, control compounds included

the $dF1$ and $dF2$ axes. Figure 1 demonstrates the location of points corresponding to specific samples of substances from the three groups in the phase space of the $dF1$ and $dF2$ functions.

It can be seen from Fig. 1 that all groups are well separated from each other; all control points were determined in their groups.

For all three groups of model substances, the average values of the roots of the $dF1$ and $dF2$ discriminant functions were found, which are the coordinates of the centroids of the groups in the phase space of the $dF1$ and $dF2$ functions (Tables 8 and 9). The obtained discriminant functions, according to the data of the classification matrix (Table 9), possess a high discriminating power,

allowing a fairly clear division of the groups of substances under consideration among themselves. Table 9 shows the LDA classification results for both the substances in the training sample and for all substances, including the control ones.

In general, the substances were classified correctly, with the exception for substances No. 1, 2, and 8 from Group 1, which were clearly assigned to Group 2 already at the first LDA steps. This proves the validity of the mathematical model developed based on physicochemical properties for classifying substances from the class of opioid analgesics into groups.

Thus, in order to determine whether new compounds not included in the research list belong to one of the three groups, it would be necessary to:
- determine the values of all descriptors;
- calculate the values of the roots of the $dF1$ and $dF2$ discriminant functions corresponding to the coordinates of the point of this connection in the phase space of the $dF1$ and $dF2$ functions;
- select the smallest distance from a given point to the centers of each of the groups (the distance is according to the rules of geometry, i.e., the Pythagorean formula), which will indicate belonging to this group.

It may happen that, when situated relatively far from all the centroids, the determined point will not belong to any of the three groups.

To directly calculate the classification index in order to assign the evaluated compounds to one of the three groups, the CF1-CF3 classification functions can be used to determine which group is most likely to be assigned to a xenobiotic. There are as many classification functions as there are groups:

Table 8. Average values of the roots of the $dF1$ and $dF2$ discriminant functions for groups of model xenobiotics

Substance group	$dF1$	$dF2$
Group 1	2.485±1.225	0.675±1.368
Group 2	0.797±0.716	−1.176±0.485
Group 3	0.797±0.716	0.255±0.809

Table prepared by the authors using their own data

Table 9. Classification matrix obtained for the substances of the training sample and for all substances, control substances included

	Group	% of correct classification	Group 1	Group 2	Group 3
Training sample only	1	75	9	3	0
	2	100	0	11	0
	3	100	0	0	19
	Total	92.9	9	14	19
	Group	% of correct classification	Group 1	Group 2	Group 3
All substances	1	80	12	3	0
	2	100	0	14	0
	3	100	0	0	22
	Total	94.1	12	17	22

Table prepared by the authors using their own data

CF1 = 0.276×MW + 22.406×Log$P$ – 23.622×Log$D_{7.4}$ + 0.906× Polar – 0.160×TPSA – 66.585
CF2 = 0.137×MW + 20.566×Log$P$ – 21.906× Log$D_{7.4}$ + 2.657× Polar – 0.105×TPSA – 88.554
CF3 = 0.034×MW + 11.248×Log$P$ – 15.200×Log$D_{7.4}$ + 3.963× Polar + 0.013×TPSA – 97.835

For each new or known compound, all three functions are calculated, and the compound is assigned to the group for which the classification function is most important.

When new CNS-active substances and xenobiotics are being identified based on the proposed physicochemical criteria, they can be classified into one of three groups: substances with a hazard risk, those with a high hazard risk, and those with an extremely high hazard risk.

The operability of the created mathematical model was assessed using the classification of substances in the training sample. The obtained results of the classification of substances, which differ from the initial classification into groups in the training sample, are shown in Table 10.

According to the results of the conducted classification, a potentially greater hazard was predicted for 9 out of 53 model substances than initially expected. The effectiveness of the proposed model for assessing the potential health hazard of CNS-active substances was demonstrated by the example of propoxyphene. This drug was initially classified as Group 1; however, further analysis clearly allocated it to Group 2, i.e., substances with a high hazard risk. Indeed, since 2009, this drug has been designated as hazardous in a number of countries and discontinued due to the high risk of fatal overdoses and cardiac arrhythmias.[2] Table 10 also shows that certain drugs and substances detected in illicit trafficking may carry certain risks when used uncontrolled, which is consistent with the literature data on their toxic effects [22].

Diphenoxylate and buprenorphine, classified as Groups 2 and 3, respectively, can be considered as pharmacological exceptions. Diphenoxylate is used for gastrointestinal disorders, with its action being directed at opioid receptors located in the intestine. Therefore, the excessively high lipophilicity of diphenoxylate prevents its action on the CNS [23]. Buprenorphine, which belongs to the family of highly active Bentley compounds, is a powerful drug that could be just as dangerous as its related etorphine. Nevertheless, pharmacologically, it exhibits the properties of an opioid receptor agonist, posing no significant threat to human life. The results obtained emphasize that the proposed model based on the physicochemical properties of substances cannot take into account the peculiarities of their effect on CNS targets, such as receptors and enzymes. Hence, false positive and false negative results are possible in the resulting solutions. At the same time, the correct classification of most model compounds into groups according to their hazard potential shows the determining effect of the physicochemical properties of narcotic analgesics on their toxic action.

CONCLUSION

Using the example of representatives of one class of CNS-active substances, we confirmed the relationship between the potential health hazard of narcotic analgesics and their physicochemical properties, which determine the redistribution of such substances from the central bloodstream into the CNS tissues. The molecular weight, lipophilicity, ability to acid-base dissociation, polarity and polarizability of CNS-active substances, as well as their ability to bind to target receptors, equally determine the specific features of their toxic effects. Therefore, these physicochemical properties can serve as criteria for determining the health hazard potential of CNS-active xenobiotics.

The method of linear discriminant analysis with step-by-step inclusion of variables from a training sample of representatives of one class of CNS-active substances (opioid analgesics), divided into three groups according to their hazard level, was used to derive a mathematical model for classifying psychoactive substances based on their physicochemical properties. The model included two

Table 10. Classification of the substances other than the training sample

No.	Model object	Initial group	Calculation of classification functions			Defined group
			CF1	CF2	CF3	
1	fentanyl	1	72.67	75.38	72.13	2
2	buprenorphine	1	117.08	122.51	122.32	2
3	propoxyphene	1	74.24	75.65	69.24	2
4	diphenoxylate	1	97.91	107.42	109.98	3
5	β-hydroxy thiofentanyl	2	64.01	67.06	73.06	3
6	β-hydroxy fentanyl	2	62.37	66.13	70.84	3
7	remifentanil	2	61.15	60.83	68.69	3
8	alfentanil	2	76.10	81.34	93.42	3
9	sufentanil	2	86.61	90.79	91.79	3

Table prepared by the authors using their own data

---

[2] Gandey A. Physicians Say Good Riddance to Worst Drug in History.2011. https://www.medscape.com/viewarticle/736718?src=mp&spon=25&form=fpf (Available from: 16 Jun 2024).

*dF*1 and *dF*2 discriminant functions as linear combinations of the values of physicochemical descriptors, allowing us to satisfactorily divide the considered groups of narcotic analgesics among themselves according to the criterion of potential threat. The CF1-CF3 classification functions were calculated to assign new compounds to a particular group.

The validity of the proposed mathematical model for assessing the potential hazard of CNS-active xenobiotics was confirmed on the example of classifying a training sample of substances. As a result, 44 substances out of 53 were classified correctly. The classification of seven substances was clarified; two substances proved to be pharmacological exceptions.

The calculated classification functions can be easily embedded as formulas in tabular editors or specialized software and databases for automatic classification of new and known compounds. Provided that the quantitative expression of the power and speed of action of opioid analgesics on the body and other parameters of molecules are determined, it becomes possible to conduct a mathematical analysis in order to establish a quantitative relationship between the characteristics of their biological activity and quantitative structure-activity relationship (QSAR). Of significant interest is the applicability of the results obtained in the study to other classes of CNS-active substances.

Undoubtedly, along with perfection of predictive methods, their results require confirmation by conventional toxicological methods. However, the demonstrated possibility of rapid detection of potentially hazardous xenobiotics will be useful for the prevention of mass poisoning when such CNS-active substances enter illicit traffic.

References

1. Zaikina OL. Lodjagin AN. Shilov VV. Gamma-hydroxybutyrate and fentanyl derivatives: chemical and toxicological confirmation of poisoning. *Russian Journal of Forensic Medicine.* 2016;2(2):112–3 (In Russ.).
EDN: YHZMBF
2. Stanley TH. Egan TD. Aken HVan. A Tribute to Dr. Paul A. J. Janssen: Entrepreneur Extraordinaire. Innovative Scientist. and Significant Contributor to Anesthesiology. *Anesth. Analg.* 2008;106(2):451–62.
https://doi.org/10.1213/ane.0b013e3181605add
3. Lindsay CD. Riches JR. Timperley CM. Chemical Warfare Toxicology. Management of Poisoning Chemical Defence Against Fentanyls. *The Royal Society of Chemistry.* 2016;259–313.
https://doi.org/10.1039/9781782628071-00259
4. Sosnov AV. Semchenko FM. Tohmahchi VN. Sosnova AA. et al. Selection criteria of compounds for development of high-potent analgesics and other CNS drugs. *Drug development & registration.* 2018;3(24):42–56 (In Russ.).
EDN: OYVYND
5. Kelly E. Sutcliffe K.. Cavallo D. Ramos-Gonzalez N. Alhosan N. et al. The anomalous pharmacology of fentanyl. *Br J Pharmacol.* 2023;180(7):797-812.
https://doi.org/10.1111/bph.15573
6. Sosnov AV. Golubev SS. Punkevich BS. Sadovnikov SV. Zagrebin EM. et al. Reference standards of active ingredients of potent analgesic drugs. *Drug development & registration.* 2016;1(14):216–23 (In Russ.).
EDN: WBODLX
7. Volpe DA. McMahon Tobin GA. Mellon RD et al. Uniform assessment and ranking of opioid µ receptor binding constants for selected opioid drugs. *Regul Toxicol Pharmacol.* 2011;59(3):385-90.
https://doi.org/10.1016/j.yrtph.2010.12.007
8. Uyba VV. Krivorotov DV. Zabelin MV. Radilov AS. Rembovskiy VR et al. Opioid receptor antagonists. From the present to the future. *Extreme Medicine.* 2018;20(3):371-82 (In Russ.).
EDN: YPHKPZ
9. Skolnick P. Treatment of overdose in the synthetic opioid era. *Pharmacol. Ther.* 2022;233:108019.
https://doi.org/10.1016/j.pharmthera.2021.108019
10. Golovko AI. Ivnitsky Ju.Ju.. Rejniuk VL et al. Reasons for high lethality in overdose of drugs from the group of synthetic opioids *Medline.ru.* 2020;21:141-56 (In Russ).
EDN: CMQERC
11. Hill R. Santhakumar R. Dewey W. Kelly E. Henderson G. Fentanyl depression of respiration: Comparison with heroin and morphine. *Br J Pharmacol.* 2020;177(2):254-66.
https://doi.org/10.1111/bph.14860
12. Bachmutsky I. Wei XP. Kish E. Yackle K. Opioids depress breathing through two small brainstem sites. *Elife.* 2020;19;9:e52694.

13. Vardanyan RS. Hruby VJ. Vardanyan RS. Hruby VJ. Fentanyl-related compounds and derivatives: current status and future prospects for pharmaceutical applications. *Future Med Chem.* 2014;6(4):385–412.
https://doi.org/10.4155/fmc.13.215
14. Bagley JR. Thomas SA. Rudo FG. Spencer HK. Doorley BM et al. New 1-(heterocyclylalkyl)-4-(propionanilido)-4-piperidinyl methyl ester and methylene methyl ether analgesics. *J Med Chem.* 1991;34(2):827–41.
https://doi.org/10.1021/jm00106a051
15. Boström E. Hammarlund-Udenaes M. Simonsson US. Blood-brain barrier transport helps to explain discrepancies in in vivo potency between oxycodone and morphine. *Anesthesiology.* 2008;108(3):495–505.
https://doi.org/10.1097/ALN.0b013e318164cf9e
16. Lazarev NV. Narcotic drugs. Leningrad: *In-t gigieny truda i profzabolevanij Lengorzdravotdela.* 1940 (In Russ.).
17. Raevsky OA. Solodova SL. Raevskaya OE. Mannhold R. Quantitative relationship between the chemicals structure and BBB-crossing ability of organic compounds. *Pharmaceutical Chemistry Journal.* 2012;46(3):3–8 (In Russ.).
https://doi.org/10.30906/0023-1134-2012-46-3-3-8
18. Pajouhesh H. Lenz GR. Medicinal chemical properties of successful central nervous system drugs. *NeuroRx.* 2005;2(4):541-53.
https://doi.org/10.1602/neurorx.2.4.541
19. Noha SM. Schmidhammer H. Spetea M. Molecular docking. molecular dynamics. and structure-activity relationship explorations of 14-oxygenated N-methylmorphinan-6-ones as potent µ-opioid receptor agonists. *ACS Chem Neurosci.* 2017;8(6):1327–37.
https://doi.org/10.1021/acschemneuro.6b00460
20. Sugano K. Kansy M. Artursson P. Avdeef A. Bendels S. et al. Coexistence of passive and carrier-mediated processes in drug transport. *Nat Rev Drug Discov.* 2010;9(8):597–614.
https://doi.org/10.1038/nrd3187
21. Šegan S. Jevtić I. Tosti T. Penjišević J. Šukalović V et al. Determination of lipophilicity and ionization of fentanyl and its 3-substituted analogs by reversed-phase thin-layer chromatography. *J Chromatogr B Analyt Technol Biomed Life Sci.* 2022;1211:123481.
https://doi.org/10.1016/j.jchromb.2022.123481
22. Suzuki J. El-Haddad S. A review: Fentanyl and non-pharmaceutical fentanyls. *Drug Alcohol Depend.* 2017;171:107–16.
https://doi.org/10.1016/j.drugalcdep.2016.11.033
23. Krivorotov DV. Kochura DM. Dulov SA. Radilov AS. Experimental comparing of lipophilicity of opioid antagonists. *Toxicological Review.* 2022;30(3):149–57 (In Russ.).
https://doi.org/10.47470/0869-7922-2022-30-3-149-157

https://doi.org/10.7554/eLife.52694

24. Janicka M. Janicka M. Sztanke M. Sztanke K. Reversed-phase liquid chromatography with octadecylsilyl. immobilized artificial membrane and cholesterol columns in correlation studies with in silico biological descriptors of newly synthesized antiproliferative and analgesic active compounds. *J Chromatogr A.* 2013;1318:92–101.
https://doi.org/10.1016/j.chroma.2013.09.060

25. Nikolaev AI. Shkaeva IE. Solnceva SA. Nikulina OS. Calculation of the toxic properties of halogenated hydrocarbons of normal structure according to the physico-chemical parameters of the molecule. *Russian Chemical Industry.* 2019;96(4):205–11 (In Russ.).
EDN: TOOJXY

26. Nikolaev AI. Antonova IN. Donskaja OS. Vladimirova LG. LC-spectra analysis algorithm for non-invasive diagnostics by oropharyngeal washout samples. *Medical alphabet.* 2019;4(35):23–7 (In Russ).
https://doi.org/10.33667/2078-5631-2019-4-35(410)-23-27

AUTHORS

Denis V. Krivorotov, Cand. Sci. (Chem.)
https://orcid.org/0000-0002-6077-2534
denhome@bk.ru

Anatoly I. Nikolaev, Cand. Sci. (Chem.)
https://orcid.org/0009-0007-1405-8683
ainikolaev1956@gmail.com

Andrey S. Radilov, Dr. Sci. (Med.), Professor
https://orcid.org/0000-0003-0776-7434
a.radilov@icloud.com

Vladimir R. Rembovsky, Dr. Sci. (Med.), Professor
niigpech@rihophe.site

Viktor A. Kuznetsov, Cand. Sci. (Chem.),
niigpech@rihophe.site

A NEW ONE-POT TECHNIQUE FOR OBTAINING POTENTIAL INDAPAMIDE METABOLITES BY OXIDATION AND CONJUGATION ON MALDI TARGET

Olga A. Keltsieva[1,2], Anna A. Afanasyeva[1], Semyon K. Ilyushonok[2,3], Alexey S. Gladchuk[1,2,3], Alexander N. Arseniev[2], Alexander S. Frolov[2], Vladimir N. Babakov[3], Konstantin A. Krasnov[1✉], Ekaterina P. Podolskaya[2]

[1] Golikov Research Center of Toxicology, St. Petersburg, Russia

[2] Institute of Analytical Instrumentation RAS, St. Petersburg, Russia

[3] Research Institute of Hygiene, Occupational Pathology and Human Ecology, Leningrad region, Russia

Introduction. Metabolic activation of xenobiotics, including pharma drugs, is considered to be one of the main mechanisms for the development of idiosyncratic reactions. Accordingly, the potential bioactivation of a xenobiotic should be carefully evaluated in the early stages of drug development. In this regard, the search for new rapid and effective screening techniques for reactive metabolites of xenobiotics presents particular interest.

Objective. Development of a new technique for modeling the processes of xenobiotic biotransformation *in vitro* to identify potential metabolites of indapamide.

Materials and methods. Non-enzymatic instrumental methods, such as electrochemical oxidation (ECO) and photocatalytic oxidation (PCO) in volume, were used as comparison methods. The second phase of metabolism was modeled by incubating the oxidation products of indapamide with a trapping agent (glutathione, GSH). The oxidation products, as well as their conjugates with GSH, were then analyzed by high-performance liquid chromatography–tandem mass spectrometry (HPLC–MS/MS). The developed one-pot technique for metabolism modeling is based on a UV-induced PCO of a xenobiotic in the presence of GSH on the surface of a target functionalized with titanium dioxide followed by detection of the products by matrix-assisted laser desorption/ionization mass spectrometry (MALDI).

Results. In use of ECO resulted in the detection of 5 metabolites and 3 adducts with GSH, while the use of PCO in the volume allowed detection of 7 metabolites and 1 adduct with GSH. The new one-pot technique detected 8 adducts with GSH. In addition to the detection of a number of known indapamide metabolites and their conjugates with GSH, a total of 4 previously unstudied metabolites and adducts with GSH were each detected for indapamide by the three methods.

Conclusions. In comparison with ECO and PCO in volume, the proposed analytical technique for modeling indapamide metabolism showed its higher informativity combined with simplicity and rapidity, which makes it a promising candidate for use in preclinical studies of drugs in predicting the metabolism and toxicity of pharmaceutical objects, as well as in studying the biotransformation processes of various xenobiotics.

Keywords: indapamide; MALDI mass spectrometric analysis; adducts; electrochemical oxidation; glutathione; photocatalytic oxidation; xenobiotics; reactive metabolites

УДК 615.9

НОВАЯ ONE-POT МЕТОДИКА ПОЛУЧЕНИЯ ПОТЕНЦИАЛЬНЫХ МЕТАБОЛИТОВ ИНДАПАМИДА ПУТЕМ ОКИСЛЕНИЯ-КОНЪЮГАЦИИ НА МАЛДИ-МИШЕНИ

О.А. Кельциева[1,2], А.А. Афанасьева[1], С.К. Ильюшонок[2,3], А.С. Гладчук[1,2,3], А.Н. Арсеньев[2], А.С. Фролов[2], В.Н. Бабаков[3], К.А. Краснов[1✉], Е.П. Подольская[2]

[1] Научно-клинический центр токсикологии имени академика С. Н. Голикова Федерального медико-биологического агентства, Санкт-Петербург, Россия

[2] Институт аналитического приборостроения Российской академии наук, Санкт-Петербург, Россия

[3] Научно-исследовательский институт гигиены, профпатологии и экологии человека Федерального медико-биологического агентства, Ленинградская обл., Россия

Введение. Метаболическая активация ксенобиотиков, в том числе лекарственных средств, считается одним из основных механизмов развития идиосинкразических реакций. Соответственно, потенциальная биоактивация ксенобиотика должна быть тщательно оценена на ранних этапах разработки лекарств. В связи с этим поиск новых быстрых и эффективных методик скрининга реакционноспособных метаболитов ксенобиотиков является актуальным.

Цель. Разработка новой методики моделирования процессов биотрансформации ксенобиотиков *in vitro* для выявления потенциальных метаболитов индапамида.

Материалы и методы. В качестве методов сравнения были выбраны такие неферментативные инструментальные методы, как электрохимическое окисление (ЭХО) и фотокаталитическое окисление (ФКО) в объеме. Моделирование второй фазы метаболизма осуществлялось путем инкубации продуктов окисления индапамида с улавливающим агентом (глутатион, GSH). Продукты окисления, а также их конъюгаты с GSH затем анализировали методом высокоэффективной жидкостной хроматографии с тандемной масс-спектрометрией. В основе новой one-pot методики

моделирования метаболизма лежит проведение УФ-индуцированного ФКО ксенобиотика в присутствии GSH на функционализированной диокси-дом титана поверхности мишени с последующей регистрацией продуктов с помощью масс-спектрометрии с матрично-активированной лазерной десорбцией/ионизацией.

Результаты. В случае ЭХО было обнаружено 5 метаболитов и 3 аддукта с GSH, а при использовании ФКО в объеме было выявлено 7 метаболитов и 1 аддукт с GSH. При использовании новой one-pot методики было найдено 8 аддуктов с GSH. Помимо ряда выявленных известных метаболитов индапамида и их конъюгатов с GSH, в совокупности тремя методами для индапамида было зафиксировано по 4 ранее не изученных метаболита и аддукта с GSH.

Выводы. По сравнению с ЭХО и ФКО в объеме предложенный аналитический подход к моделированию метаболизма индапамида показал более высокую информативность в сочетании с простотой и экспрессностью, что делает его перспективным для использования в доклинических исследованиях лекарственных препаратов при прогнозировании метаболизма и токсичности объектов фармацевтической разработки, а также при изучении процессов биотрансформации различных ксенобиотиков.

Ключевые слова: индапамид, МАЛДИ масс-спектрометрический анализ, аддукты, электрохимическое окисление, глутатион, фотокаталитическое окисление, ксенобиотики, реактивные метаболиты

INTRODUCTION

Indapamide (IPM), which is a sulfonamide derivative of the indole series, is considered as one of the most effective diuretics used in hypertension and congestive heart failure.[1] IPM, the structure of which is shown in Fig. 1, is a halogen-containing compound with the molecular formula of $C_{16}H_{16}ClN_3O_3S$ (m/z [M-H]- 364.05).

The use of IPM can be accompanied by a number of side effects, including such hypersensitivity reactions as rash and photosensitivity [2–4]. The occurrence of idiosyncratic reactions to chemical compounds foreign to the body (xenobiotics) is largely determined by their metabolic biotransformation.[2] Due to its active metabolization in the human body, IPM represents an interesting object for studying its biotransformation products, the identification of which can be very useful for tracking the mechanisms of skin reactions and other manifestations of individual intolerance to drugs and xenobiotics.

Xenobiotic transformations in the body occur through the following three phases. The first phase involves chemical transformations under the action of redox or hydrolytic enzymes with the formation of primary metabolites, as a rule, enriched in polar functional groups. This increases the hydrophilicity of the molecules, making them more efficiently eliminated from the body [5]. During the second phase, primary metabolites can enter into conjugation reactions with endogenous molecules, forming stable (covalent) adducts [6]. During the third phase, metabolic products are eliminated from the body, which usually occurs with the participation of transport proteins [7].

It should be noted that short-living xenobiotic metabolites pose a significant hazard to the body, since they react with proteins due to their high reactivity, thereby disrupting their functional activity. Direct detection of reactive metabolites in the body is not an easy task; however, their indirect determination through adducts with biomolecules is possible. In comparison with free metabolites, such adducts (conjugates) are more informative biomarkers of the effect of an exogenous compound on the body due to a longer stay in the body [8]. Reduced glutathione (GSH), a tripeptide of key importance for protecting cells from toxic damage by xenobiotics is of the most important conjugating agents in the body [9]. During the metabolism of xenobiotics, GSH reacts with substrates, such as epoxides, halides, and active unsaturated compounds, followed by excretion of the as-formed adducts from the body in bile or urine [10]. In this regard, GSH is used in model experiments as a low-molecular trap for detecting reactive products of xenobiotic metabolism. Such studies are an important stage in pharmaceutical research, allowing the toxicity and safety of a potential drug to be predicted [11].

Biochemical methods using cells or subcellular fractions are conventionally applied to model the metabolism of xenobiotics. The latter include liver microsomes containing
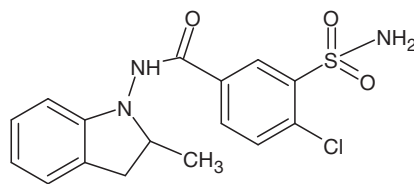
Figure prepared by the authors using data from [1]
Fig. 1. Structural formula of indapamide

1   Mashkovskij MD. Drugs. Moscow: Novaya Volna; 2024 (In Russ).
2   Granik VG. Metabolism of exogenous compounds. Drugs and other xenobiotics. Moscow: Vuzovskaya kniga; 2015 (In Russ).

enzymes of the first phase of metabolism (cytochrome P450), cytosol enriched with enzymes of the second phase (transferases), or fraction S9 containing a complete set of metabolic enzymes of the I and II phases of xenobiotic biotransformation [5, 12, 13]. However, biochemical methods possess a number of disadvantages, including low productivity, high labor costs, difficulty in isolating individual metabolites from biological matrices, etc.

In this regard, alternative approaches to modeling metabolism based on non-enzymatic instrumental methods that require no biological matrices and minimize the time and cost of research are increasingly attracting attention [14]. Among them are electrochemical oxidation (ECO) [15] and photocatalytic oxidation (PCO) [16].

In the ECO method, the oxidation of xenobiotics is carried out in an electrochemical reactor, where reactive oxygen species perform the function of an oxidizer [17, 18]. The coupling of an electrochemical cell with a mass spectrometer [19] or a chromato-mass spectrometer [20] makes it possible to register ECO products in real time. This method is capable of simulating not only the first, but also the second phase of metabolism provided that, after ECO, trapping agents such as GSH or cysteine are treated [21]. The study by Shono T. et al. [22] used the example of N-dealkylation of imipramine and diazepam to demonstrate that ECO provides a higher yield of metabolites compared to the microsomal fraction.

In another method of metabolic modeling, PCO, the oxidation reactions of xenobiotics are initiated under the action of light radiation in the presence of catalysts [23]. Titanium dioxide (TiO_2) is one of the most actively used photocatalysts due to its optical and photochemical properties, as well as its low cost [24]. In addition, Ruokolainen M. et al. [25] showed that the photocatalytic oxidation induced by ultraviolet radiation in a suspension of titanium dioxide (UV/TiO_2-PCO) simulates more reactions of the first phase of metabolism occurring in human liver microsomes than ECO or the Fenton reaction.

Despite the emergence of new approaches to modeling the biotransformation of xenobiotics, the study of metabolism continue to be a challenging and labor-consuming task. In this regard, the development of a simpler and more effective technique for obtaining and identifying xenobiotic metabolites appears to be highly relevant.

In this study, we set out to propose a technique for modeling xenobiotic biotransformation processes *in vitro* to identify potential indapamide metabolites.

MATERIALS AND METHODS

Electrochemical oxidation of indapamide and production of adducts with glutathione

When developing an ECO IPM technique, we relied on the data obtained in [26] using a similar system for ECO. 10 mg of IPM substance (analytical standard; Merck, Germany) was placed in a 15 mL tube followed by addition of 10 mL of methanol (HPLC grade; Merck, Germany); the mixture was intensively stirred using a vortex-type BR-2000 Vortexer (Bio-Rad, USA) until the substance dissolved. To obtain a working solution of IPM, a stock solution (1 mg/mL

in methanol) was diluted with 75% (vol/vol) aqueous acetonitrile (HPLC grade; Merck, Germany) with the addition of ammonium formate (10 mM; pH 7.4; purity 97%; Merck, Germany) to a concentration of 50 μg/mL.

A three-electrode μ-PrepCell™ electrochemical cell (volume 0.7 μL, electrolyte layer 50 μm, working electrode — Glassy carbon) as part of the ROXY™ EC system (Antec, the Netherlands) was pre-rinsed with 5 mL of distilled water using a Harvard automatic syringe pump (702212B, Harvard Apparatus, USA) with a flow rate of 100 μL/min. Subsequently, 5 mL of 50% (v/v) aqueous acetonitrile solution was passed through the cell at a flow rate of 100 μL/min.

To perform an ECO, 100 μL of an IPM working solution was passed through the cell at a rate of 15 μL/min. Electrolysis was performed at 37°C and a constant voltage of 2.4 V. The products of IPM oxidation were collected in a microsample; the metabolite solution was diluted fivefold with deionized water and placed in vials for subsequent HPLC–MS/MS analysis.

In the study of adducts with GSH (purity > 98%; Merck, Germany), the solution passed through an electrochemical cell was collected in a tube containing 100 μL of an aqueous solution of GSH (1 mg/mL) and incubated for 1h at a temperature of 37°C. The resulting mixture with GSH was then diluted 25 times with deionized water and transferred to vials for subsequent analysis by high performance liquid chromatography with tandem mass spectrometry (HPLC–MS/MS).

Ultraviolet-induced photocatalytic oxidation of indapamide in the presence of titanium dioxide nanoparticles in a microsample and preparation of adducts with glutathione

When developing an UV/TiO_2-PCO IPM technique, we relied on the previously proposed approach described in [27]. 10 mg of the IPM substance was placed in a 1.5 mL tube followed by addition of 1 mL of methanol; the solution was intensively mixed using a vortex-type BR-2000 Vortexer until dissolution of the substance. To obtain a working solution, an IPM stock solution (10 mg/mL in methanol) was diluted with deionized water to a concentration of 1 mg/mL.

10 mg of TiO_2 titanium dioxide nanoparticles (ratio of polymorphic modifications of anatases: rutile = 80/20; Plasmotherm, Russia) and 2 mL of deionized water were added to a 2 mL microsample followed by placing the suspension in an ultrasound bath for 10 min. The resulting suspension (5 mg/mL) was used immediately after preparation.

12.5 μL of IPM solution (1 mg/mL in 10% (vol.) aqueous methanol), 12.5 μL of TiO_2 suspension (5 mg/mL), and 150 μL of deionized water were added to a 0.2 mL microsample. Subsequently, the open microsample was placed in a plastic holder and covered with a laboratory-made panel for ultraviolet irradiation (LEDs BL-L522VC (λ_{max} = 405 nm; Betlux Electronics, China) mounted on a non-conductive substrate) and held for 30 min. When searching for GSH adducts, 5 μL of an aqueous GSH solution (5 mg/mL) was added to the suspension after irradiation and incubated for 1 h at a temperature of 37°C.

Costar® Spin-X® centrifuge filters were used to purify TiO$_2$ (pore size — 0.22 µm, nylon membrane; Corning, USA). 150 µL of suspension with IPM oxidation products and 150 µL of deionized water were added to the filter, after which they were centrifuged for 5 min at 10,000 g using a MiniSpin centrifuge (Eppendorf, Germany). The filtrate was transferred to another microsample followed by addition of 300 µL of acetonitrile with 0.1% (v/v) formic acid (98% purity; Merck, Germany) to the used filter and centrifuged again for 5 min at 10,000 g. This filtrate was combined with the previously obtained filtrate and evaporated using a SpeedVac centrifuge evaporator (Eppendorf, Germany). 5% (vol/vol) aqueous acetonitrile with 0.1% (vol/vol) formic acid was added to the precipitate to a final GSH concentration of 20 µg/mL; the resulting solution was then placed in a vial for subsequent HPLC–MS/MS analysis.

Ultraviolet-induced photocatalytic oxidation of indapamide in the presence of titanium dioxide nanoparticles and production of adducts with glutathione on the surface of a MALDI target

A polished stainless steel MALDI target was used as the substrate. 2 µL of TiO$_2$ suspension (2 mg/mL) was applied onto the surface of the MALDI target cells and dried at room temperature.

Target cells functionalized with TiO$_2$ were applied:
- 10 µL of deionized water (control);
- 9 µL of deionized water and 1 µL of GSH aqueous solution (100 µg/mL) (control);
- 7 µL of deionized water, 2 µL of IPM solution (50 µg/mL) and 1 µL of GSH solution (100 µg/mL) (determination of GSH adducts with oxidation products).

The target with the deposited samples was covered with the previously described panel for ultraviolet irradiation and irradiated for 30 min. After completion of irradiation, 1 µL was taken from each drop and transferred to an adjacent cell, after which 1 µL of solution (20 mg/mL in 80% (vol/vol) aqueous acetonitrile with 0.1% (vol/vol) trifluoroacetic acid (purity 99%; Merck, Germany) was added) 2,5-dihyroxybenzoic acid matrices (DHB; Bruker Daltonik GmbH, Germany). The target was dried at room temperature before analysis by MALDI mass spectrometry.

Analysis of indapamide oxidation products and their adducts with glutathione by high performance liquid chromatography with tandem mass spectrometry

HPLC–MS/MS analysis was conducted using an analytical system consisting of an Agilent 1290 Infinity liquid chromatograph (Agilent Technologies, USA) and an Amazon ETD ion trap mass spectrometer (Bruker Daltonik GmbH, Germany) with an electrospray ion source. Experimental data was recorded and processed using the Data Analysis 5.0 software package (Bruker Daltonik GmbH, Germany).

Chromatographic separation was carried out under the following conditions: column — zorbrax Eclipse Plus C18 Rapid Resolution High Definition (2.1 × 150 mm, 1.8 microns; Agilent Technologies, USA); temperature column — 40°C; flow rate of the mobile phase — 200 µL/min; volume of the injected sample — 5 µL; A phase — 0.1% (vol/vol) aqueous formic acid solution; B phase — 0.1% (vol/vol) formic acid solution in 90% (vol/vol) in aqueous acetonitrile; elution mode — gradient: 5% B (0–2 min), 5–60% B (2–30 min), 60% B (30–31 min), 60–50% B (31–32 min), 5% B (32–37 min).

Mass spectrometric analysis was performed under the following operating conditions of the mass spectrometer: capillary voltage — 4.5 kV; nebulizer pressure — 2.2 bar; drying gas — nitrogen; drying gas flow rate — 9 L/min; drying gas temperature — 280°C; operating mode — Auto MS/MS; scanning mode — Auto MS/MS; range m/z — 100–1000; moving average — disabled; frequency of spectra — 4 Hz; type of fragmentation — dissociation activated by collisions; gas for collisions — helium; number of precursor ions — 3; isolation window of the precursor ion — 3.5 m/z. IPM metabolites were analyzed in the negative ion registration mode; GSH adducts were analyzed in the positive ion registration mode. The mass spectrometer was calibrated using a 1 m sodium formate solution (97% purity; Merck, Germany) in 90% (vol/vol) aqueous isopropanol (HPLC grade; Merck, Germany).

MALDI mass spectrometric analysis

Mass spectrometric analysis of reactive metabolites of IPM and their adducts with GSH was performed by an UltrafleXtreme tandem time-of-flight mass spectrometer (Bruker Daltonik GmbH, Germany) equipped with an Nd:YAG laser (λ = 355 nm) using the facilities of the resource center "Development of Molecular and Cellular Technologies", St. Petersburg State University Science Park.

Mass spectra were recorded in the reflection mode with positive ion detection at the following operating parameters of the mass spectrometer: range m/z — 300–1100; voltage at the first source — 19.0 kV; voltage at the second source — 16.8 kV; voltage at the lenses — 7.0 kV; voltage at the first reflector — 20.5 kV; voltage at the second reflector — 10.5 kV; the delay of pulsed ion extraction — 90 ns. To obtain one spectrum, 10,000 laser irradiation acts were used with a laser power of 60% and an irradiation frequency of 2000 Hz. The flexControl and flexAnalysis software applications (Bruker Daltonik GmbH, Germany) were used to register and interpret the mass spectra.

Tandem mass spectrometric analysis was performed in the laser-induced dissociation mode at the following operating parameters of the mass spectrometer: the precursor ion selector window — 2 m/z; voltage at the first source — 7.6 kV; voltage at the second source — 6.9 kV; voltage at the lenses — 3.5 kV; voltage at the first reflector — 29.4 kV; voltage at the second reflector — 14.1 kV; LIFT 1 (19.0 kV); LIFT 2 (3.2 kV); pulse ion extraction delay — 90 ns.

The mass spectrometer was calibrated using a Peptide calibration standard II calibration mixture (Bruker Daltonik GmbH, Germany).

RESULTS AND DISCUSSION

At the first stage of the study of IPM metabolism, two of the most common non-enzymatic approaches for the

production of xenobiotic oxidation products *in vitro* were compared: electrochemical oxidation (ECO) and UV-induced photocatalytic oxidation in the presence of titanium dioxide nanoparticles (UV/TiO$_2$-PCO). According to the literature data [28], five metabolites (M1–M5) are known for IPM, each of which is capable of reacting with GSH. The selection of GSH as a trapping agent is due to its important role in the metabolism of xenobiotics in the human body (it is one of the main biomolecules involved in the binding of reactive products of xenobiotic metabolism), as well as its ability to enter into conjugation reactions with molecules containing quinoid-type groups (the presence of such groups is characteristic of a number of IPM metabolites).

The scheme of the experiment using ECO is shown in Fig. 2A.

Oxidation was carried out using the Roxy Exceed electrochemical system equipped with a μ-PrepCell electrochemical reactor. Part of the reaction mixture was then selected for subsequent analysis; the remaining part was mixed with a GSH solution and incubated during 1 h at 37°C.

According to the results of HPLC–MS/MS analysis, the presence of 3 known metabolites of IPM (M1, M4, M5), as well as 2 metabolites with m/z 381.93 (PM2) and m/z 429.96 (PM6), which had not been previously described in the literature, was revealed. The corresponding data are presented in Fig. 3A. In addition, the HPLC–MS/MS analysis of the incubation mixture of oxidation products of IPM and GSH revealed 3 signals, which, by the presence of an isotopic distribution characteristic of compounds containing a chlorine atom and the results of tandem mass spectrometric analysis, were attributed to

GSH adducts with 2 known (M2, M4) and 1 undetected (PM7) metabolites of IPM. The corresponding data are presented in Fig. 3B. Information on the detected ECO IPM products, as well as GSH adducts, is presented in Table 1.

Thus, the ECO method makes it possible to obtain IPM metabolites, but it has a number of disadvantages.:
- The inability to perform multiple experiments simultaneously;
- The need to clean the electrochemical cell after each use;
- High consumption of reagents and studied xenobiotics.

Taking into account the above, we stated that modeling of the metabolism of xenobiotics using the ECO method is lengthy and costly.

At the next stage of the study, we modeled the processes of IPM metabolism using the UV/TiO$_2$-PCO method. The scheme of UV/TiO$_2$-PCO is shown in Fig. 2B. At the first stage, a tube with an incubation mixture (an aqueous suspension of TiO$_2$ nanoparticles containing IPM) was irradiated with UV radiation. Following irradiation, GSH was added to the tube and the procedure for conjugation of the trapping agent with UV/TiO$_2$ products was performed. In total, the stages of oxidation and conjugation lasted for 90 min, similar to the case of ECO. However, the advantage of UV/TiO$_2$-PCO consists in the possibility of conducting several experiments in parallel, thus saving time significantly when selecting oxidation conditions. In general, compared to ECO, the UV/TiO$_2$-PCO method is more economical in terms of the cost of both reagents and test substances. However, for further HPLC–MS/MS analysis, it becomes necessary to carry out sample
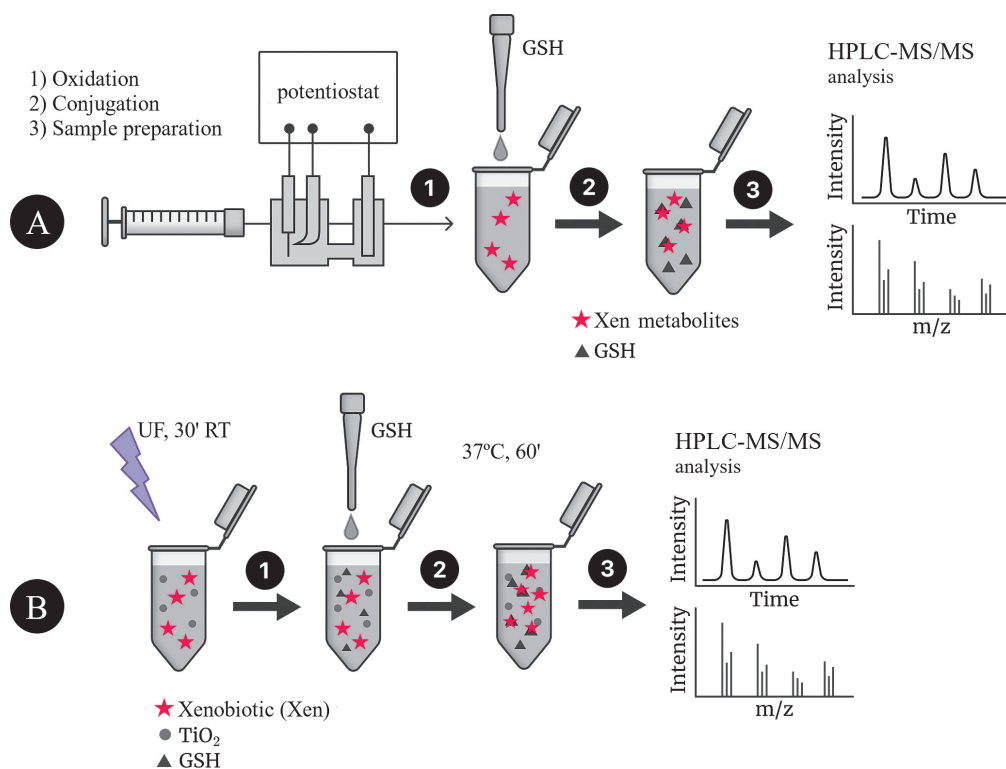
Figure prepared by the authors using their own data

Fig. 2. Algorithm for obtaining xenobiotic oxidation products by ECO (A) or UV/TiO$_2$-PKO (B) followed by conjugation with GSH and HPLC–MS/MS analysis (using IPM as an example)
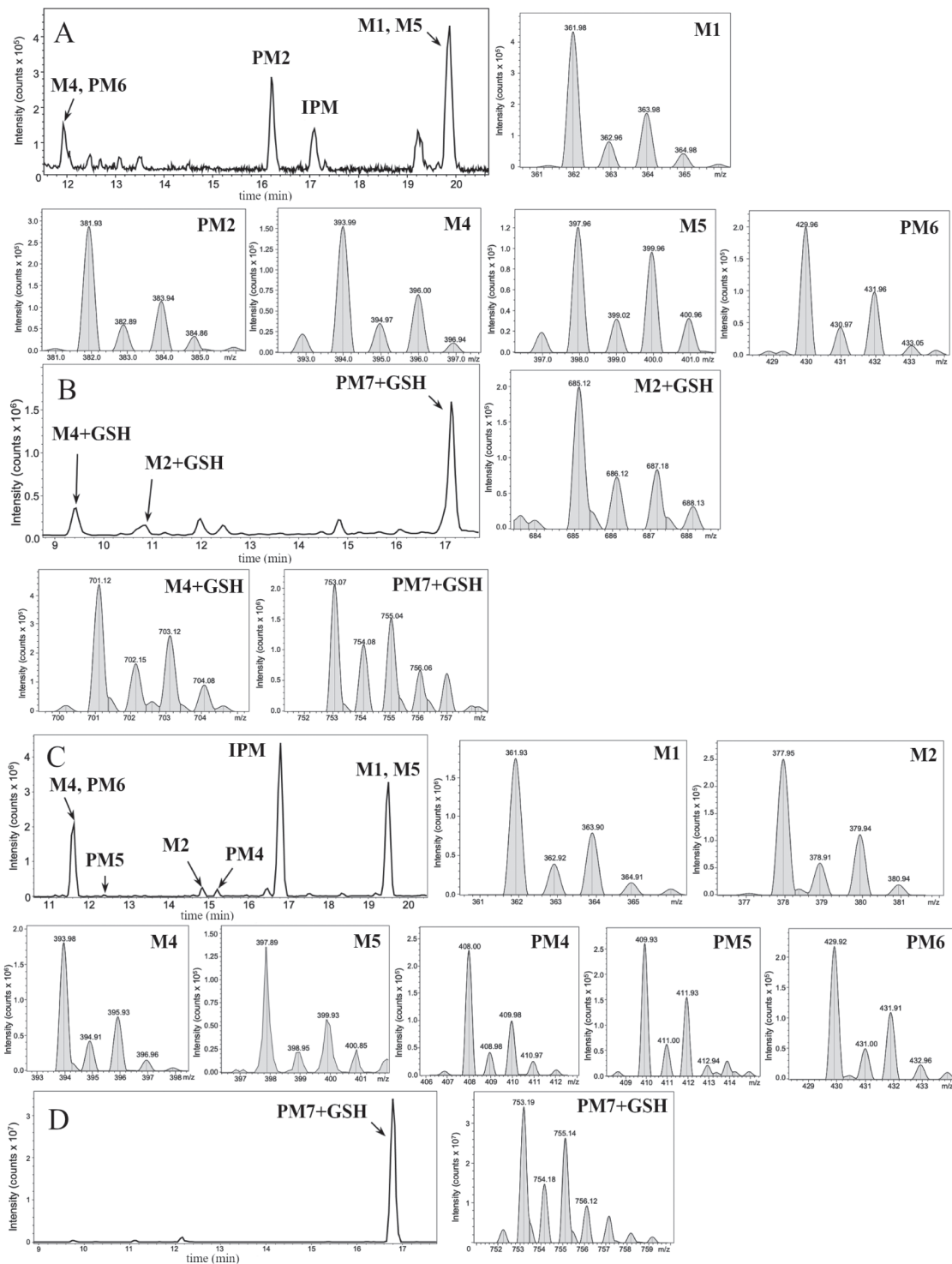
Figure prepared by the authors using their own data

Fig. 3. Mass chromatograms of IPM metabolites obtained by ECO (A) and their adducts with GSH (B), as well as those obtained by UV/TiO$_2$-PCO (C) and their adducts with GSH (D)

Note: the figure shows mass spectra fragments indicating the detected IPM metabolites and their adducts with GSH.

preparation, including the removal of titanium dioxide particles in order to avoid their entry into the chromatographic system.

According to the results of HPLC-MS/MS analysis of UV/TiO$_2$-PCO products of IPM (Fig. 3B), the formation of 4 known IPM metabolites (M1, M2, M4, M5), as well as 3 previously undescribed metabolites with m/z 408.00 (PM4), m/z 409.93 (PM5) and m/z 429.92 (PM6) was detected. It

should be noted that the M2 metabolite, as well as the putative PM4 and PM5 metabolites, were not detected using the ECO method.

When analyzing the products of GSH interaction with IPM metabolites, only one signal was recorded, which, by the presence of a characteristic isotopic distribution and the results of tandem mass spectrometric analysis, was attributed to the GSH adduct with the potential metabolite

Table 1. Molecular weights and probable structures of IPM metabolites and their m/z adducts with GSH, detected by three methods
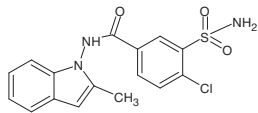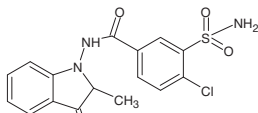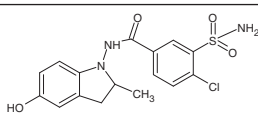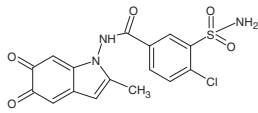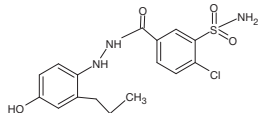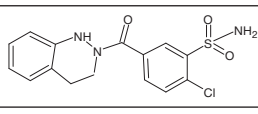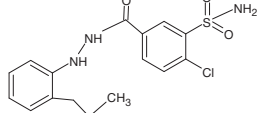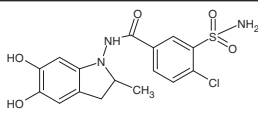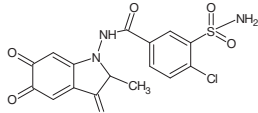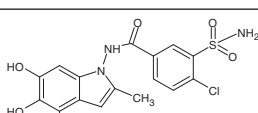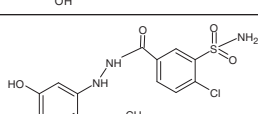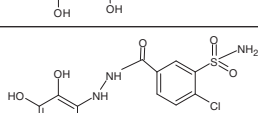
Me-tabo-lite	Structural formula	Biotransformation modeling methods				
		ECO		UF/TiO$_2$-PKO		UF/TiO$_2$-PKO/MM
		m/z of metabo-lite [M-H]⁻	m/z of adduct with GSH [M+H]⁺	m/z of metabo-lite [M-H]⁻	m/z of adduct with GSH [M+H]⁺	m/z of adduct with GSH [M+H]⁺
M1		361.98	-	361.93	-	669.10 671.10
M2		(378)	685.12	377.95	-	685.09
M3		(380)	-	-	-	687.11
M4		393.99	701.12	393.98	-	701.09
M5		397.96	-	397.89	-	705.09
PM1		-	-	-	-	657.09
PM2		381.93	-	-	-	-
PM3		-	-	-	-	703.10
PM4		-	-	408.00	-	-
PM5		-	-	409.93	-	-
PM6		429.96	-	429.92	-	-
PM7		-	753.07	-	753.19	-

Table prepared by the authors using their own data

Note: the values of the m/z metabolites described in the literature but not detected in the experiments performed are shown in parentheses; UV/TiO$_2$-PCO/MM — UV/TiO$_2$-PCO on the MALDI target.

PM7 (Fig. 3G). PM7-GSH became the only detected adduct, while 3 adducts were identified by the ECO method.

The results obtained by ECO and UV/TiO$_2$-PCO methods for IPM are generally comparable. However, both methods have a number of disadvantages that make them individually rather labor- and time-consuming. Therefore, a number of challenges must be overcome when developing a more efficient screening technique for reactive metabolites of xenobiotics. These include the following points.

1. Time consumption. Most of the time spent is consumed by conjugation (1 h) and HPLC–MS analysis (~40 min).

2. Labor cost. Removal of TiO$_2$ particles at UV/TiO$_2$-TCO or flushing of the electrochemical cell after each xenobiotic.

3. Step-by-step oxidation and conjugation can lead to the loss of short-lived metabolites.

4. Possibilities of conducting several experiments in parallel are limited.

5. High consumption of reagents and test substances.

Therefore, further work was aimed at developing a technique for modeling IPM metabolism, in which the listed disadvantages would be eliminated or significantly reduced.

Matrix-activated laser desorption/ionization (MALDI) mass spectrometry is widely used among the methods for determining xenobiotic metabolites and their adducts. This method is characterized by its rapidity and high productivity, since the analysis procedure includes the stage of applying all the necessary samples onto a single solid substrate (target), followed by recording the analyte signals without additional sample preparation.

We established that if a xenobiotic with the addition of a trapping agent (GSH) is applied onto a target MALDI cell functionalized with TiO$_2$, the reactive metabolites formed during UV/TiO$_2$-PCO can bind to the thiol group of the peptide in situ. Subsequent MS analysis allows detection of short-lived oxidation products in the form of adducts. On this basis, an algorithm for conducting UV/TiO$_2$-PCO IPM on a MALDI target (UV/TiO$_2$-VCO/M) was proposed, shown in Fig. 4.

To select an optimal oxidation duration, adducts were searched following 1, 5, 10, 20, and 30 min of UV irradiation. The obtained mass spectra are shown in Fig. 5.

The results of mass spectrometric analysis that after 5 min of irradiation showed the absence of detected signals of GSH adducts with IPM metabolites. At 10 min of UV/TiO$_2$-PCO, three signals were detected, one of which (m/z 687.12) belongs to the conjugation product of GSH with the known metabolite of IPM (M3), and the other (m/z 703.11) can be attributed to the adduct of GSH with the previously unexplored metabolic product of IPM (PM3). For samples taken after 20 min of irradiation, an increase in the intensity of the above signals was observed in the mass spectra.

The most complete information about GSH adducts with IPM metabolites was provided by the mass spectrum corresponding to the exposure of samples to UV radiation for 30 min. In addition to the previously identified conjugation products, signals with values of m/z 669.10, 685.09, 701.09, and 705.10 were detected, corresponding to adducts with known IPM metabolites (M1, M2, M4, M5), as

well as a signal with m/z 657.09 belonging to an adduct with a potential PM1 metabolite. Information about the identified adducts is presented in Table 1. It should be noted that, from our point of view, the metabolites M3, PM1, and PM3 deserve particular attention from in terms of their potential hazard to the body. These metabolites were registered only as adducts with GSH, and only by the UV/TiO$_2$-PCO/MM method under in situ conjugation conditions, which indicates their high reactivity.

In contrast to the ECO and UV/TiO$_2$-PCO techniques, in this case, a significant number of signals attributed to GSH adducts with IPM oxidation products were detected in the mass spectra, as shown in the diagram (Fig. 6), which allows us to conclude that the proposed approach shows promise.

Together, four previously unexplored metabolites were identified by three methods for IPM (m/z [M-H]- 381,93; 408,00; 409,93; 429,96) and the adduct with GSH (m/z [M+H]+ 657,09; 671,10; 703,10; 753,19).

It should be noted that the non-enzymatic methods of modeling the biotransformation of xenobiotics (ECO, UV/TiO$_2$-PCO) considered in this paper cannot act as a full-fledged alternative to classical biological systems (microsomal or S9 fractions of the liver, primary hepatocytes, etc.), since each of the methods cannot fully reproduce the full set of enzymatic reactions occurring during the first phase of metabolism. At the same time, these instrumental approaches make it possible to rapidly and affordably obtain
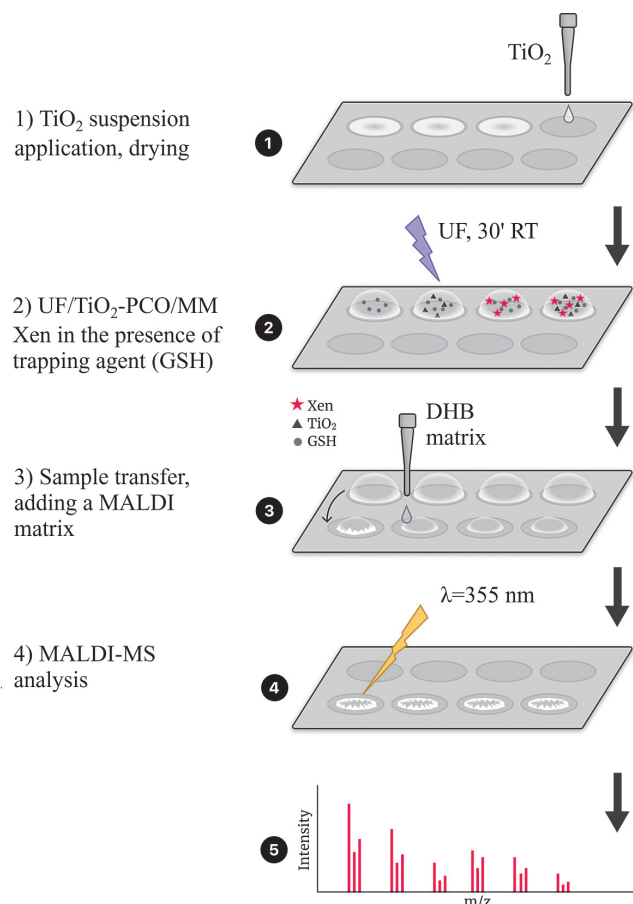
Figure prepared by the authors using their own data

Fig. 4. Algorithm for obtaining IPM metabolites and their adducts with GSH by UV/TiO$_2$-PCO/MM method
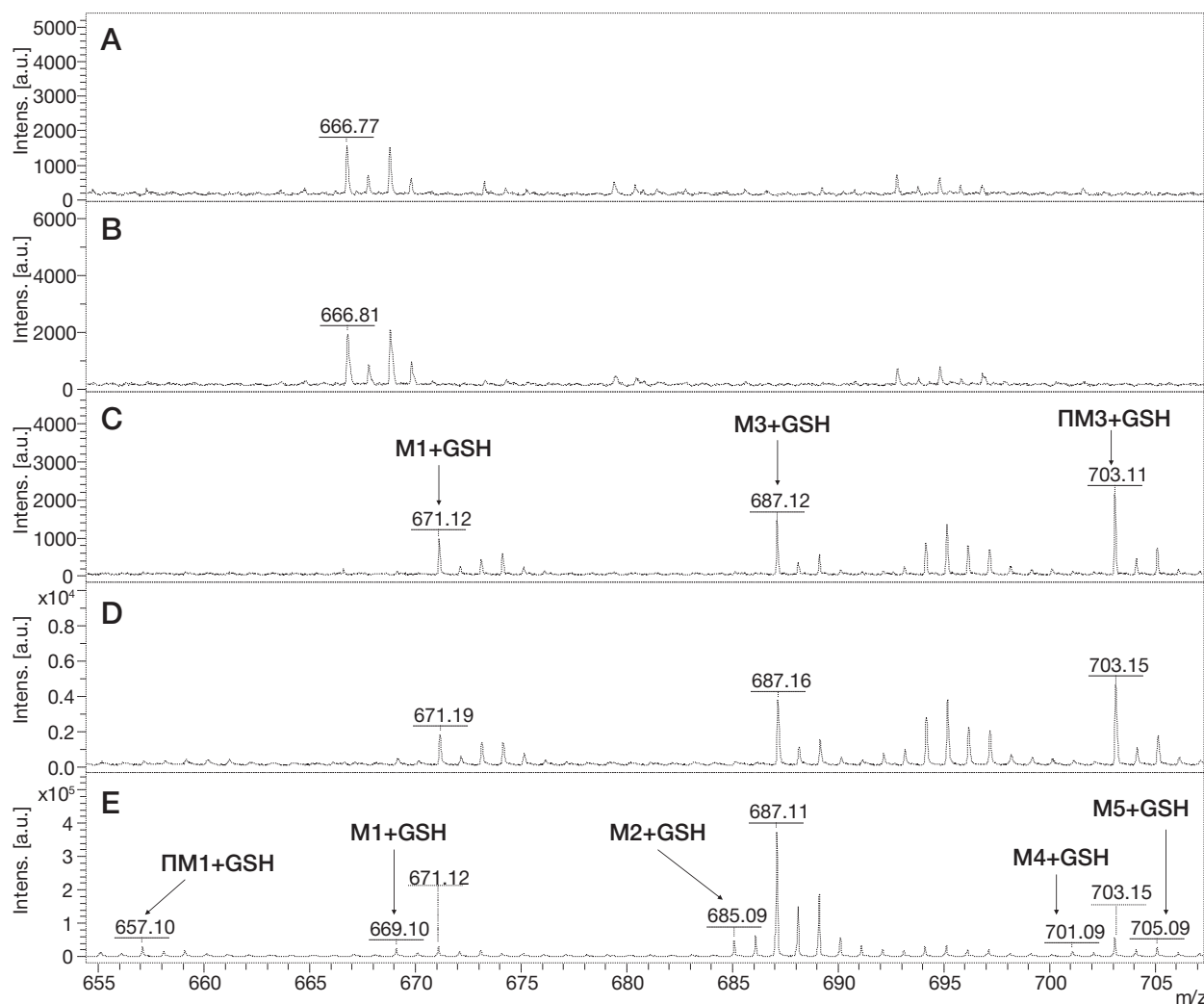
Figure prepared by the authors using their own data

Fig. 5. MALDI mass spectra of GSH adducts with IPM metabolites during UV/TiO2-PCO/MM under UV irradiation of the incubation mixture for 0 min (A), 5 min (B), 10 min (C), 20 min (D), and 30 min (E)

oxidation products in a pure solution without the need for a laborious purification process from the biological matrix, which is particularly important when conducting screening studies of the potential toxicity of xenobiotics.
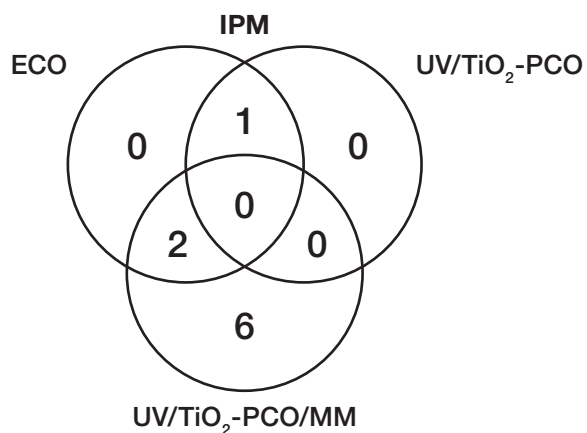
Figure prepared by the authors using their own data

Fig. 6. Numerical comparison of the detected GSH adducts with IPM oxidation products obtained by three different methods

CONCLUSION

In this study, we investigated potential IPM metabolites obtained using non-enzymatic methods for modeling the processes of the first phase of xenobiotic biotransformation, such as ECO and UV/TiO$_2$-PCO in volume. Simulation of the second phase of metabolism was carried out by incubation of indapamide oxidation products with a trapping agent (GSH).

According to the results of HPLC–MS/MS analysis of metabolites and their conjugates with GSH, 5 metabolites and 3 adducts with GSH were detected in the case of ECO. The use of UV/TiO$_2$-PCO in volume resulted in detection of 7 metabolites and 1 adduct with GSH. In addition, a new *in vitro* technique for the detection of reactive xenobiotic metabolites was developed. This technique is based on UV/TiO$_2$-PCO in the presence of a trapping agent (GSH) on the surface of a MALDI target functionalized with titanium dioxide, followed by MALDI mass spectrometric analysis of oxidation products and their conjugates. It was confirmed that the developed technique for detecting reactive metabolites of xenobiotics in the case of IPM surpasses the conventional

approaches both in terms of performance and informativeness, allowing the detection of a larger number of potentially dangerous metabolites (8 adducts with glutathione were detected).

References

1. Wojnarowska Z, Grzybowska K, Hawelek L, Dulski M, Wrzalik R, Gruszka I et al. Molecular dynamics, physical stability and solubility advantage from amorphous indapamide drug. *Mol Pharm*. 2013;10(10):3612–27.
    https://doi.org/10.1021/mp400116q
2. Sanz-Muñoz C, Martínez-Morán C, Torrero-Antón MV, Miranda-Romero A. Indapamide-Associated Stevens-Johnson Syndrome. *Actas Dermosifiliogr*. 2008;99(4):321-2.
3. Mourad SS, Barary MA, El-Yazbi AF. Sensitive "release-on-demand" fluorescent genosensors for probing DNA damage induced by commonly used cardiovascular drugs: Comparative study. *Int J Biol Macromol*. 2024;269(1):131821.
    https://doi.org/10.1016/j.ijbiomac.2024.131821
4. Rutherford T, Sinclair R. Photo-onycholysis due to indapamide. *Australas J Dermatol*. 2007;48(1):35–6.
5. Liu L, Cui H, Huang Y, Hao Y, Zhou Y, Wan Y. Molecular docking and *in vitro* evaluations reveal the role of human cytochrome P450 3A4 in the cross-coupling metabolism of phenolic xenobiotics. *Environ Res*. 2023;220:115256.
    https://doi.org/10.1016/j.envres.2023.115256
6. Shang J, Coe KJ, Lim HK, Chen L, Khatri BB, Salter R et al. Application of Covalent Binding Body Burden in the HμREL Human Hepatocyte Coculture Model for Reactivity Risk Assessment of Metabolically Low Turnover Drugs. *Chem Res Toxicol*. 2024;37(4):540–4.
    https://doi.org/10.1021/acs.chemrestox.4c00046
7. Norman BH. Drug Induced Liver Injury (DILI). Mechanisms and Medicinal Chemistry Avoidance/Mitigation Strategies. *J Med Chem*. 2020;63(20):11397–419.
    https://doi.org/10.1021/acs.jmedchem.0c00524
8. Savelyeva EI, Koryagina NL, Orlova OI. Determination of toxic substances adducts with biomolecules as biomarkers of the exposure/effect. Medicine of Extreme Situations. 2018;20(S3):451–63 (In Russ).
    EDN: YPHKSL
9. Gasmi A, Nasreen A, Lenchyk L, Lysiuk R, Peana M, Shapovalova N et al. An Update on Glutathione's Biosynthesis, Metabolism, Functions, and Medicinal Purposes. *Curr Med Chem*. 2024;31(29):4579–601.
    https://doi.org/10.2174/0109298673251025230919105818
10. Gupta PK. *Fundamentals of Toxicology*: *Essential Concepts and Applications*. New York: Academic Press; 2016.
11. Pognan F, Beilmann M, Boonen HCM, Czich A, Dear G, Hewitt P et al. The evolving role of investigative toxicology in the pharmaceutical industry. *Nat Rev Drug Discov*. 2023;22(4):317–35.
    https://doi.org/10.1038/s41573-022-00633-x
12. Medina D, Omanakuttan B, Nguyen R, Alwarsh E, Walgama C. Electrochemical Probing of Human Liver Subcellular S9 Fractions for Drug Metabolite Synthesis. *Metabolites*. 2024;14(8):429.
    https://doi.org/10.3390/metabo14080429
13. Peeters L, Vervliet P, Foubert K, Hermans N, Pieters L, Covaci A. A comparative study on the *in vitro* biotransformation of medicagenic acid using human liver microsomes and S9 fractions. *Chem Biol Interact*. 2020;328:109192.
    https://doi.org/10.1016/j.cbi.2020.109192
14. Sun H, Scott DO. Structure-based Drug Metabolism Predictions for Drug Design. *Chem Biol Drug Des*. 2010;7(5):3–17.
    https://doi.org/10.1111/j.1747-0285.2009.00899.x
15. Faber H, Vogel M, Karst U. Electrochemistry/mass spectrometry as a tool in metabolism studies. *Anal Chim Acta*. 2014;8(34):9–21.
    https://doi.org/10.1016/j.aca.2014.05.017
16. Gawlik M, Skibiński R, Trawiński J, Komsta Ł. Photocatalysis com-
bined with chromatographic methods as a new promising tool in drug metabolism studies. *Acta Chromatogr*. 2018;30(1):1–8.
    https://doi.org/10.1556/1326.2016.00202
17. Álvarez-Lueje A, Pérez M, Zapata C. Electrochemical Methods for the *In Vitro* Assessment of Drug Metabolism. Topics on Drug Metabolism. *InTech*. 2012;
    https://doi.org/10.5772/28647
18. Nikzad N, Rafiee M. Electrochemical study of drug metabolism. *Curr Opin Electrochem*. 2024;44:101446.
    https://doi.org/10.1016/j.coelec.2024.101446
19. Mielczarek P, Smoluch M, Kotlinska JH, Labuz K, Gotszalk T, Babij M et al. Electrochemical generation of selegiline metabolites coupled to mass spectrometry. *J Chromatogr A*. 2015;1389:96–103.
    https://doi.org/10.1016/j.chroma.2015.02.049
20. Lohmann W, Hayen H, Karst U. Covalent protein modification by reactive drug metabolites using online electrochemistry/liquid chromatography/mass spectrometry. *Anal Chem*. 2008;80:9714–9.
    https://doi.org/10.1021/ac801699g
21. Bussy U, Chung-Davidson YW, Li K, Li W. Phase I and phase II reductive metabolism simulation of nitro aromatic xenobiotics with electrochemistry coupled with high resolution mass spectrometry. *Anal Bioanal Chem*. 2014;406(28):7253-60.
    https://doi.org/10.1007/s00216-014-8171-3
22. Shono T, Toda T, Oshino N. Preparation of N-dealkylated drug metabolites by electrochemical simulation of biotransformation. Drug Metab Dispos. 1981;9:481–2.
    https://doi.org/10.1007/s00216-014-8171-3
23. Gawlik M, Trawiński J, Skibiński R. Photocatalysis as a tool for *in vitro* drug metabolism simulation: multivariate comparison of twelve metal oxides on a set of twenty model drugs. *Catalysts*. 2020;10:26.
    https://doi.org/10.3390/catal10010026
24. Ruokolainen M, Valkonen M, Sikanen TM, Kotiaho T, Kostiainen R. Imitation of phase I oxidative metabolism of anabolic steroids by titanium dioxide photocatalysis. *Eur J Pharm Sci*. 2014;65:45–55.
    https://doi.org/10.1016/j.ejps.2014.08.009
25. Ruokolainen M, Gul T, Permentier H, Sikanen T, Kostiainen R, Kotiaho T. Comparison of TiO$_2$ photocatalysis, electrochemically assisted Fenton reaction and direct electrochemistry for simulation of phase I metabolism reactions of drugs. *Eur J Pharm Sci*. 2016;83:36–44.
    https://doi.org/10.1016/j.ejps.2015.12.012
26. Faber H, Melles D, Brauckmann C, Wehe CA, Wentker K, Karst U. Simulation of the oxidative metabolism of diclofenac by electrochemistry/(liquid chromatography/)mass spectrometry. *Anal Bioanal Chem*. 2012;403:345–54.
    https://doi.org/10.1007/s00216-011-5665-0
27. Gladchuk AS, Gorbunov AY, Keltsieva OA, Ilyushonok SK, Babakov VN, Shilovskikh VV et al. Coating of a MALDI target with metal oxide nanoparticles by droplet-free electrospraying — a versatile tool for in situ enrichment of human globin adducts of halogen-containing drug metabolites. *Microchem J*. 2023;191:108708.
    https://doi.org/10.1016/j.microc.2023.108708
28. Sun H, Moore C, Dansette PM, Kumar S, Halpert JR, Yost GS. Dehydrogenation of the indoline-containing drug 4-chloro-N-(2-methyl-1-indolinyl)-3-sulfamoylbenzamide (indapamide) by CYP3A4: correlation with in silico predictions. *Drug Metab Dispos*. 2009;37(3):672–84.
    https://doi.org/10.1124/dmd.108.022707

AUTHORS

Olga A. Keltsieva
https://orcid.org/0000-0002-4069-0355
keltcieva@gmail.com

Anna A. Afanasyeva
afanasyeva.a.a.2000@yandex.ru

Semyon K. Ilyushonok
https://orcid.org/0000-0003-1672-4583
ilsemen21@mail.ru

Alexey S. Gladchuk, Cand. Sci. (Tech.)
https://orcid.org/0000-0002-4411-2069
aleglad24@gmail.com

Alexander N. Arseniev
star2361@mail.ru

Alexander S. Frolov
Alexander.S.Frolov@gmail.com

Vladimir N. Babakov, Cand. Sci. (Biol.)
vbabakov@gmail.com

Konstantin A. Krasnov, Dr. Sci. (Chem.)
https://orcid.org/0000-0003-1503-2243
krasnov_tox@mail.ru

Ekaterina P. Podolskaya, Dr. Sci. (Tech.)
ek.podolskaya@gmail.com

CC BY 4.0

Check for updates

HEAT TRANSFER BY EVAPORATION DETERMINES THE EFFECT OF NASAL PHENAZEPAM ON THERMAL STRESS IN RATS

Jury Ju. Ivnitsky✉, Olga A. Vakunenkova, Konstantyn A. Krasnov, Semion S. Gaft, Natalja V. Lapina

Golikov Research Center of Toxicology, St. Petersburg, Russia

Introduction. Thermal stress is an increase in body temperature due to the predominance of heat received from outside or released during metabolism over heat losses by the body. Heat production can be regulated using benzodiazepines in doses unattainable with a single intramuscular injection of their officinal preparations. In this study, this limitation is overcome using a prototype of the Phenazepam nasal spray (PNS) preparation, containing 170 mg of phenazepam in 1 mL of a non-aqueous solution.

Objective. Experimental assessment of the PNS effect on the metabolic rate and thermal balance in thermal stress.

Materials and methods. The effect of a single 10 µL PNS intranasal instillation on the external respiration intensity, oxygen consumption, as well as 10 µL PNS intranasal instillations at 0.5 h intervals on the dynamics of rectal temperature, body weight, and lethality in rats at an air temperature of 40 °C was studied.

Results. PNS instillations reduced oxygen consumption by an amount sufficient to decrease body temperature by 0.3 °C in 0.5 h. PNS administration declined the rate of body temperature rise when placing rats in restrainers at an air temperature of 40 °C; however, PNS administration accelerated body temperature rise and increased lethality when placing rats in cages. Due to PNS, moisture loss by rats in cages decreased, judged by the dynamics of body weight.

Conclusions. The study confirmed the prospects of PNS as a pharmacotherapy for heat stroke at a high relative humidity, exposure to insulating skin protectors, or with immersion hyperthermia. The possibility of the aggravating effect of PNS on human thermal stress in the absence of physical obstacles to heat transfer by evaporation requires additional verification.

Keywords: hyperthermia; survival; evaporation; elevated air temperature; body temperature; heat stress; heat loss; heat production; metabolic rate; phenazepam nasal spray

ТЕПЛООТДАЧА ИСПАРЕНИЕМ ОПРЕДЕЛЯЕТ ЗНАК ВЛИЯНИЯ НАЗАЛЬНОГО ФЕНАЗЕПАМА НА ТЕПЛОВОЙ СТРЕСС У КРЫС

Ю.Ю. Ивницкий✉, О.А. Вакуненкова, К.А. Краснов, С.С. Гафт, Н.В. Лапина

Научно-клинический центр токсикологии имени академика С.Н. Голикова Федерального медико-биологического агентства, Санкт-Петербург, Россия

Введение. Тепловой стресс — рост температуры тела вследствие преобладания теплоты, поступившей извне и освободившейся при метаболизме, над теплоотдачей. Коррекция теплопродукции возможна с использованием бензодиазепинов в дозах, недостижимых при однократном внутримышечном введении их официнальных препаратов. Это ограничение преодолено с помощью прототипа препарата «Феназепам спрей назальный» (ФСН), содержащего 170 мг феназепама в 1 мл неводного раствора.

Цель. Экспериментальная оценка влияния ФСН на уровень метаболизма и тепловой баланс при тепловом стрессе.

Материалы и методы. Изучено влияние однократной интраназальной инстилляции ФСН в объеме 10 мкл на интенсивность внешнего дыхания, потребление кислорода, а также повторных интраназальных введений ФСН 170 мг/мл в объеме по 10 мкл с интервалом 0,5 ч на динамику ректальной температуры, массы тела и летальность крыс при температуре воздуха 40 °C.

Результаты. Инстилляция ФСН снижала потребление кислорода на величину, достаточную для уменьшения на 0,3 °C температуры тела за 0,5 ч. Введение ФСН замедляло повышение температуры тела у крыс, размещенных в рестрейнерах при температуре воздуха 40 °C, но ускоряло рост температуры и способствовало повышению летальности при размещении крыс в вольерах. Под влиянием ФСН потеря влаги крысами, находившимися в вольерах, судя по динамике массы тела, уменьшалась.

Выводы. Результаты работы указывают на перспективность ФСН в качестве средства фармакотерапии теплового удара при высокой относительной влажности, пребывании в изолирующих средствах защиты кожи или при иммерсионной гипертермии. Требует проверки возможность усугубляющего влияния ФСН на тепловой стресс у человека при отсутствии физических препятствий для теплоотдачи испарением.

Ключевые слова: гипертермия; выживаемость; испарение; повышенная температура воздуха; температура тела; тепловой стресс; теплоотдача; теплопродукция; уровень метаболизма; феназепам спрей назальный

✉ Ивницкий Юрий Юрьевич neugierig@mail.ru

INTRODUCTION

Thermal (heat) stress is an increase in the core body temperature, when the algebraic sum of thermal energy received from outside and released in metabolic processes exceeds that of thermal energy lost by evaporation, radiation, convection, and heat conduction. The totality of the most severe clinical manifestations of heat stress, referred to as heat stroke [1], is a critical condition with a mortality rate of 27% [2]. Not only children and elderly people are at increased risk of heat stroke, but also the economically active population, whose activities are associated with physical exertion or work in conditions that impede heat transfer. These include, e.g., military personnel, police officers, firefighters, hot shop workers, and athletes.

The basic principle of first aid in heat stroke management consists in a rapid reduction of body temperature. The current standard of emergency medical care[1] recommend physiotherapeutic means for promoting heat transfer, such as cooling liquids and applications. Medications include saline solutions, nonsteroidal anti-inflammatory drugs (NSAID), and diazepam. Based upon the daily or course dose of 10 mg, diazepam can be prescribed in a single dose of 5 mg as a sedative. The current literature lacks data on the effect of diazepam used in this mode on the thermal state of the body. However, parenteral administration of benzodiazepines in doses of more than 20 mg, similar to those used to relieve seizures of chemical etiology [3], is likely to produce the required effect.

Intramuscular administration of benzodiazepines at the prehospital stage, commonly applied for the purpose of relieving convulsive syndrome, is a forced alternative to their intravenous administration, which is problematic in the setting of seizures. Due to the low water solubility of pharmaceutical substances of the benzodiazepine group, their concentration in official injectable medicines (sibazone, midazolam) does not exceed 5 mg/mL. Therefore, simultaneous delivery of benzodiazepines into the human body in doses of more than 20 mg requires intramuscular administration of such medicines in volumes of more than 4 mL, which is rarely possible. We previously proposed an approach to overcoming this limitation based on the use of a non-aqueous solution of benzodiazepine [4] and its nasal dosage form [5]. A prototype of the Phenazepam Nasal Spray medicine (PNS) was created, containing 170 mg of phenazepam in 1 mL. With a double insufflation of 140 μL of PNS into each nasal passage, the dose of phenazepam exceeded the highest single doses of diazepam or midazolam administered as official injectable medicines by 4.8 and 6.4 times, respectively. The need for such doses was determined by the initial requirement for PNS as a means of relieving convulsive syndrome of chemical etiology. However, an increase in drug dose offers the possibility of phenazepam exhibiting other pharmacological properties, potentially beneficial in conditions of heat stress. In this regard, the fact that benzodiazepines reduce oxygen consumption by both the brain [6] and the body as a whole [7] deserves attention. The associated decrease in heat production could delay the increase in body temperature in conditions conducive to overheating of the body, thereby increasing tolerance against heat stress. However, the opposite effect, i.e., violation of behavioral patterns aimed at stimulating heat transfer, must not be neglected. In rats, whose skin, excluding the plantar surface of the extremities, is devoid of sweat glands, hypothetically grooming with saliva applied to the coat and its subsequent evaporation is a thermoregulatory reaction similar to sweating in humans [8].

This study aims to experimentally evaluate the effect of PNS on the metabolic rate and heat balance during heat stress.

MATERIALS AND METHODS

The study was conducted using outbred albino male rats (191–210 g) purchased from the Rappolovo Branch of the Kurchatov Institute Research Center. The animals were receiving standard rat food and drinking water ad libitum. Two series of experiments were conducted.

In the first series of experiments, 16 animals were used, eight individuals in each group (control, experiment). Changes in the intensity of respiratory function and oxygen consumption by the body were studied after a single intranasal instillation of isotonic 0.9% and sodium chloride solution in control animals and PNS 170 mg/mL in a volume of 10 μL (5 μL in each nasal passage) in animals from the experimental group, which corresponds to an average dose of the phenazepam® pharmaceutical substance 8.5 mg/kg and bioequivalent to a dose of 100 mg (four insufflations of 140 μL of PNS) for humans. Variable volume dispensers were used to administer the solutions. The acute toxicity of PNS at this dose was characterized

---

[1] Order of the Ministry of Health of the Russian Federation No. 1115n. Standard of emergency medical care for heat and sunstroke; 12/20/2012.

based on the data from a preclinical study of its prototype, in which intranasal administration of PNS to rats at a 20-fold higher dose (five times 40 μL with an interval of 10 min) did not cause animal death. Body oxygen consumption was determined in a Miropolsky apparatus with a 2L respirometric chamber, to which the animals were accustomed for 2 min before the onset of each measurement. The intensity of body oxygen consumption QO_2, mL/(kg×min), was found from the equation:

$$Q_{O_2} = V \times F / (m \times \Delta t), \tag{1}$$

wherein V — the volume of manometric liquid entering the burette, mL; F — the coefficient for reducing the oxygen volume to normal conditions; m — body weight, kg; Δt — time spent by a rat in a sealed chamber, min.

The measurement duration was 3 min under its absolute error of 0.1 mL (≤ 2% of the V value). The animals were not fixed, they were freely located in the respirometric chamber. At this time, their respiratory rate was calculated (min^{-1}). The measurements were carried out with an interval of 10 min.

The second series of experiments studied the effect of PSN on the dynamics of rectal temperature, body weight, and mortality of rats housed in a thermal chamber in conditions that allowed (placement in enclosures) or excluded (placement in restrainers) grooming. Four randomized groups were formed: two control groups and two experimental groups with 12–14 individuals in each:

Group 1 ($n = 14$) — intranasal administration of 0.9% sodium chloride solution in a volume of 10 μL; animal husbandry;

Group 2 ($n = 14$) — intranasal injection of PSN 170 mg/mL in a volume of 10 μL; keeping animals in an aviary;

Group 3 ($n = 12$) — intranasal administration of 0.9% sodium chloride solution in a volume of 10 μL; animal husbandry in restrainers;

Group 4 ($n = 12$) — intranasal administration of 0.9% PSN solution 170 mg/mL in a volume of 10 μL; animal husbandry in restrainers.

The medications were instilled 5 μL into each nasal passage before the animals were placed in a thermal chamber, followed by instillation every half hour. The number of instillations depended on the life span of the animals and ranged from two to seven; the total dose of phenazepam ranged from 17 mg/kg to 59.5 mg/kg.

Immediately after the administration of the medications, the animals (three individuals from each group at a time) were placed in a thermal chamber. The size of the restrainers did not interfere with breathing movements, but excluded grooming. The climatic conditions that contributed to overheating of the body were modeled in a BMT Stericell SC 111 ECO thermal chamber (Czech Republic) with a volume of 111 L and exhaust ventilation of 5 m³/h. The air temperature was 40 ± 1°C, the relative humidity of 46% was maintained automatically. The thermal balance of the body was assessed by the dynamics of rectal temperature, which was measured at 30 min intervals with an electric thermometer equipped with a sensor for rats RET-2

(WPI, China); the tip of the thermometer was inserted into the rectum to a depth of 3 cm. The body loss of moisture was assessed by changes in body weight measured at half-hour intervals.

The results were presented as an average value and its error ($M \pm m$). The Shapiro–Wilk criterion was used to check the normality of the distribution. A multidimensional analysis of variance was performed to assess the effect of thermal conditions and injected substances on the recorded quantitative indicators. In cases where any factor showed a significant influence, a one-dimensional analysis of variance was performed. In cases of experimental plans with repeated measurements, models with mixed effects were used. The intergroup comparison of averages was performed using priori linear contrasts or posteriori Tukey tests. To identify intergroup differences in survival functions, the Gehan generalised Wilcoxon test was used. The frequency of alternative traits occurrence was determined by the Fisher exact test. The critical significance level of a was assumed to be 0.05.

RESULTS

In the first series of experiments, 2–3 min after a single intranasal instillation of PNS 170 mg/mL 10 μL, the motor activity of the rats decreased; the animals looked inhibited. The results of studying the effect of PNS on oxygen consumption and external respiration are shown in Fig. 1.

Figure 1 shows that 10 min after the use of PNS, oxygen consumption by animals of the experimental group decreased by 33%, and the respiratory rate decreased by 32% compared to the control group. The gas exchange efficiency of external respiration, estimated by oxygen consumption per respiratory cycle, did not change significantly. In the following 20 min, oxygen consumption in rats treated intranasally with a single dose of PNS remained 9–20% lower than in the control, although levelling out. Thus, the duration of the hypometabolic effect of a single PNS instillation was at least half an hour.

The second series of experiments, when studying the effect of PNS 170 mg/mL in a volume of 10 μL on the state of thermal metabolism in rats, found that animal staying in a thermal chamber led to a statistically significant increase in their rectal temperature. In animals placed in restrainers, the temperature increased by 5.5 ± 0.3°C within an hour versus 3.3 ± 0.3°C in animals freely housed in enclosures. At the same time, the use of PNS accelerated the increase in body temperature by 15% in rats housed in enclosures, although slowing it down by 11% in those kept in restrainers (Fig. 2a). When placed in enclosures, the animals that received saline solution showed active grooming, which was not the case with those receiving PNS. About 120 min after being placed in enclosures, the body loss of moisture estimated by weight loss due to the use of PNS was 1% less of the initial body weight than in the control (Fig. 2b). The life expectancy of rats in enclosures was longer than in restrainers. When placed in enclosures, the use of PNS reduced life expectancy; when placed in restrainers, life expectancy tended to increase (Fig. 2c).
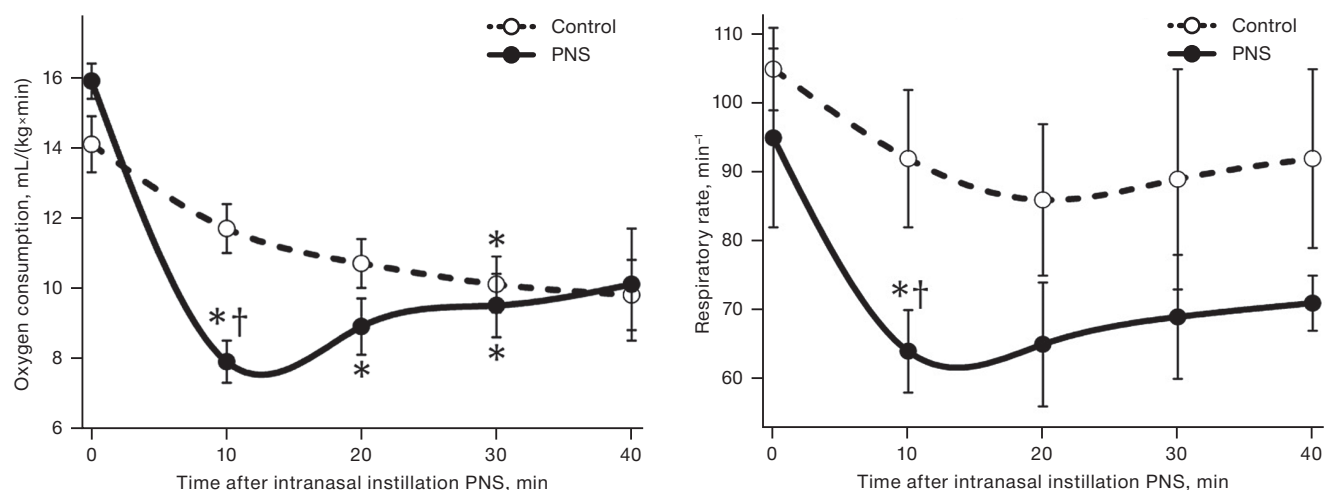
Figure prepared by the authors based on their own data

Fig. 1. Dynamics of oxygen consumption (left) and respiratory rate (right) in male rats after a single intranasal instillation of PNS
Note: the data is presented as mean and the standard error of the mean ($M \pm m$); * — statistically significant difference from the baseline; † — statistically significant difference from the control group.
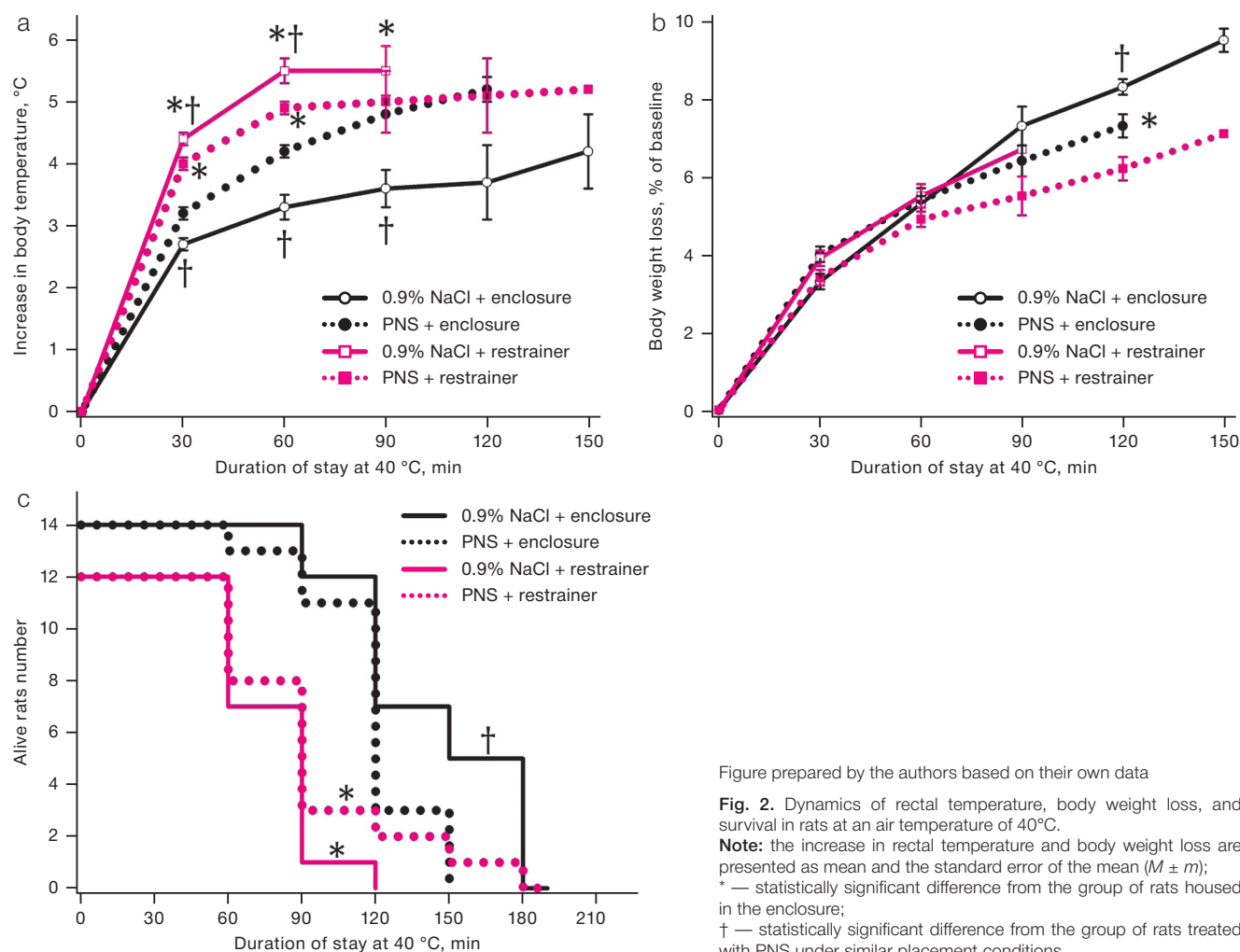
Figure prepared by the authors based on their own data

Fig. 2. Dynamics of rectal temperature, body weight loss, and survival in rats at an air temperature of 40°C.
Note: the increase in rectal temperature and body weight loss are presented as mean and the standard error of the mean ($M \pm m$);
* — statistically significant difference from the group of rats housed in the enclosure;
† — statistically significant difference from the group of rats treated with PNS under similar placement conditions.

DISCUSSION

With a single instillation of 10 µL of PNS, the phenazepam dose for rats was 8.5 mg/kg bw, which is bioequivalent to 100 mg for an adult human. This was five times higher than the highest single intravenous dose of diazepam 20 mg, which reduced human oxygen consumption by 8% [9]. Therefore, the fourfold greater hypometabolic effect of PNS observed in this study was due to the benzodiazepine dose, which, when extrapolated to humans, was five times

higher than the highest single dose. The duration of this effect was close to half an hour, which indicates the need for repeated PNS prescriptions to achieve a longer hypometabolic effect.

As follows from the increase in body temperature, staying in a heat chamber caused thermal stress in the rats. Due to the impossibility of grooming, the distribution of moisture (presumably saliva) over the coat, and, therefore, the loss of heat by evaporation, was hampered in rats placed in restrainers. This made the heat transfer conditions comparable for animals placed in restrainers that received intranasal instillations of PNS or a sodium chloride solution. Therefore, the probable reason for the decrease in thermal stress in rats housed in restrainers, in the setting of PNS, was a decrease in heat production, rather than an increase in heat transfer.

The decrease in heat production in the animals that received PNS before being placed in a thermal chamber was assessed using the caloric equivalent of oxygen, which is close to 21 J/mL in the case of a carbohydrate-dominated diet [10]. During 30 min after PNS instillation, oxygen consumption by animals was on average 2.06 mL/(kg×min) lower than in the control, which corresponds to 1294 J/kg of lower heat production. When the specific heat of biological tissues and water are close to 4187 cal/(kg×°C), this could decrease by 0.3°C the accumulation of body temperature over the following 30 minutes after placing the rats in a thermal chamber, which was observed in the present work. Thus, when the air temperature was elevated and moisture could not evaporate from most of the body surface, the introduction of PNS slowed down the formation of thermal stress in rats, reducing heat production. In order to extrapolate these data to humans, it seems relevant to study the effect of PNS on body temperature under the conditions that prevent heat transfer by evaporation, i.e., at high relative humidity [11], exposure to insulating skin protectors [12], or with immersion hyperthermia [13]. The ability of diazepam, administered intravenously in doses of 10 or 20 mg, to reduce human body temperature [14] allows us to expect its decrease even when using PNS.

An optimal relative humidity and a sufficient rate of air exchange in the thermal chamber favored heat loss by evaporation of moisture by rats who had the opportunity to apply it to the surface of the body. Therefore, when they were placed in aviaries, body temperature rose more slowly than that in restrainers. However, the introduction of PNS smoothed out this difference: the medicine accelerated the increase in body temperature. Following 120 min of being placed in enclosures, body weight loss, mainly due to evaporation of water, was 10 g/kg less with PNS instillation than with the introduction of saline solution. Under the specific heat of water vaporization of 2260 J/g, this corresponded to the accumulation of 22,600 J/kg more heat in the body of animals than in the control. Under the specific heat capacity of biological tissues close to 4187 J/(kg×°C), this energy was sufficient to increase body temperature by 5.4°C. In fact, in rats that received PNS, it was only 2°C higher than in the control. This indicates the influence of oppositely directed factors on the body temperature of rats who received PNS, including a decrease in heat transfer

and the decrease in heat production shown above. As can be seen, in animals that had no physical obstacles to moistening the body surface, the effect of PNS on heat transfer prevailed over its effect on heat production.

Adverse pharmacological effects of benzodiazepines could play a certain role in reducing the survival rate of rats that received PNS before being freely placed in a thermal chamber, including an uncoupling effect on oxidative phosphorylation [15], reduction of blood pressure, heart rate and coronary blood flow [16]. However, the main mechanism of the PNS-induced decrease in survival in conditions of free location in a thermal chamber was the aggravation of thermal stress. This is indicated by the fact that 90 min after being placed in a thermal chamber, the body temperature of 43°C, corresponding to the threshold of irreversible damage to biological tissues [17], was reached in 21% and 71% of animals treated with saline solution and PNS, respectively ($p < 0.05$). Extrapolation of these data to humans is difficult due to the presence of sweat glands on the entire surface of the skin, which ensures heat transfer by evaporation even against the background of physical inactivity. At the same time, impaired heat transfer is not excluded in humans due to reports of antagonism of benzodiazepines to muscarinic receptors [18], which requires consideration of climatic conditions when developing recommendations for the use of PNS.

The results obtained indicate the possibility of mitigating thermal stress with the use of PNS at high relative humidity, exposure to insulating skin protectors, or immersion hyperthermia. Such an opportunity becomes particularly valuable with continued heat exposure or the unavailability of physical means of cooling the body at the pre-hospital stage of assistance to victims.

CONCLUSIONS

1. A single intranasal instillation of phenazepam in rats at a dose of 8.5 mg/kg bw, which is bioequivalent to 100 mg for an adult human, reduced the body oxygen consumption by an amount sufficient to reduce the 0.3°C increase in body temperature over 30 min of exposure to an air temperature of 40°C. The duration of the hypometabolic effect of a single instillation of the nasal preparation of phenazepam (PNS) was at least half an hour, which ensured this effect in animals receiving the drug with a half-hour interval.

2. At an air temperature of 40°C and in the absence of conditions for evaporation of moisture from the body surface, the administration of PNS to rats reduced heat stress, decreasing heat production and increasing rectal temperature by 0.3°C in 30 min.

3. The open arrangement of rats at an air temperature of 40°C in enclosures, which did not create obstacles to heat transfer by evaporation of saliva applied to the coat, was accompanied by a slower increase in body temperature and a lower mortality than when animals were placed in restrainers.

4. The instillation of PNS contributed to an increase in body temperature and mortality in rats housed in enclosures at an air temperature of 40°C. The main mechanism of these effects was a decrease in heat transfer by evaporation due to the suppression by PNS of

a species-specific thermoregulatory reflex, i.e., application of saliva to the coat.

5. PNS is a promising means of pharmacotherapy for heat stroke at high relative humidity, exposure to insulating skin protectors, or immersion hyperthermia. The possibility of the aggravating effect of PNS on human thermal stress in a hot climate with unhindered heat transfer by evaporation needs to be verified.

References

1. Cramer MN, Gagnon D, Laitano O, Crandall C. Human temperature regulation under heat stress in health, disease, and injury. *Physiol. Rev*. 2022;102(4):1907–89.
https://doi.org/10.1152/physrev.00047.2021
2. Garcia CK, Renteria LI, Leite-Santos G, Leon LR, Laitano O. Exertional heat stroke: pathophysiology and risk factors. *BMJ Ved*. 2022;1(1):e000239.
https://doi.org/10.1136/bmjmed-2022-000239
3. Kryukov EV, ed. *Military field therapy*. St. Petersburg: GEOTAR-Media LLC, 2023 (In Russ.).
4. KrasnovKA, Ivnitsky Yu Yu, Vakunenkova OA, Reinyuk VL. A pharmaceutical composition for the elimination of convulsive syndrome based on nicetamide and benzodiazepine group drugs. Patent of the Russian Federation No. 2801050;2023 (In Russ.).
5. Ivnitsky Yu Yu, Reinyuk VL, Krasnova, Krasnova AA, Shataeva KV. Requirements for first aid medications for convulsive syndrome of chemical etiology (literature review). *Military Medical Journal*. 2022;343(3):18–23 (In Russ.).
https://doi.org/10.52424/00269050_2022_343_3_18
6. Fleiscer JE, Milde JH, Moyer TP, Michenfelder JD. Cerebral effects of high-dose midazolam and subsequent reversal with Ro 14-1788 in dogs. *Anesthesiol*. 1988;68(2):234–42.
https://doi.org/10.1097/00000542-198802000-00010
7. Hostler D, Northington WE, Callaway CW. High-dose diazepam facilitates core cooling during cold saline infusion in healthy volunteers. *Appl. Physiol. Nutr. Metab*.2009;4(4):582–6.
https://doi.org/10.1139/H09-011
8. Attah AT, Negrón-Moreno PN, Amigo-Duran M, Zhang L, Kenngott M, Brecht M. et al. Sensory cues, behavior and fur-based drying in the rat wetness response. *Sci Rep*.2024;14(1):24550
https://doi.org/10.1038/s41598-024-74900-9
9. Griffe O, Griffe H, du Cailar J. Effects of diazepam on oxygen consumption. *Ann. Aneshesiol. Fr*. 1979;20(1):37–40.
10. Simbirtsev GS. The regulatory effect of carbon dioxide on oxygen consumption in athletes developing endurance in the light of a mathematical analysis of the production of aerobic oxidation energy. *Sports medicine: science and practice.*
2019;9(3):12–24 (In Russ.).
https://doi.org/10.17238/ISSN2223-2524.2019.3.12
11. Wolf ST, Bernard TE, Kenney WL. Heat exposure limits for young unacclimatized males and females at low and high humidity. *J. Occup. Environ. Hyg*. 2022;19(7):415–24.
https://doi.org/10.1080/15459624.2022.2076859
12. Zhao Y, Su M, Meng X, Liu J, Wang F. Thermophysiological and perceptual responses of amateur healthcare workers: impacts of ambient condition, inner-garment insulation and personal cooling strategy. *Int. J. Environ. Res. Public Health*. 2022;20(1):612.
https://doi.org/10.3390/ijerph20010612
13. Kim AI, Shustov E B, Zaitseva IP, Lemeshchenko AV. Pathophysiological mechanisms of adverse interaction of hypoxia and temperature factors in relation to physical performance. *Pat. Physiol. Experiment. Terap.* 2022;66(4):94–106 (In Russ.).
https://doi.org/0.25557/0031-2991.2022.04.94-106
14. Hostler D, Northington WE, Callaway CW. High-dose diazepam facilitates core cooling during cold saline infusion in healthy volunteers. *Appl. Physiol.Nutr. Metab*. 2009.34(4):582–86.
https://doi.org/10.1139/H09-011
15. Jeso F, Truscello A, Martinotti G, di Jeso B, Magnani B, Martinotti A. Effect of diazepam on mitochondrial respiration. *C. R. Seances. Soc. Biol. Fil*.1990;184(1):37–40.
16. Shintani R, Ichinomiya T, Tashiro K, Miyazaki Y, Tanaka T, Kaneko S, et al. Comparison of hemodynamic effects of remimazolam and midazolam during anesthesia induction in patiemts undergoing cardiovascular surgery: a single-center retrospective and exploratory study. *Cureus*. 2024;16(10):e72032.
https://doi.org/10.7759/cureus.72032
17. Yarmolenko PS, Moon EJ, London C, Manzoor A, Hochman DW, Viglianti L, Dewhirst MW. Thresholds for thermal damage to normal tissues: an update. *Int. J. Hyperthermia*. 2011;27(4):320–43.
https://doi.org/10.3109/02656736.2010.534527
18. Hiroshi K, Naoko T, Mitsuru K, Mostofa J, Asuka I, Nagata K, et al. An autopsy case of heatstroke under the influence of psychotropic drugs. *Soud. Lek*. 2020;65(4):76–8.

AUTHORS

Jury Ju. Ivnitsky, Dr. Sci. (Med.), Professor
https://orcid.org/0000-0002-1057-5356
neugierig@mail.ru

Olga A. Vakunenkova
https://orcid.org/0009-0005-9665-9866
volga-2303@yandex.ru

Konstantyn A. Krasnov, Dr. Sci. (Chem.)
https://orcid.org/0000-0003-1503-2243
krasnov_tox@mail.ru

Semion S. Gaft, Cand. Sci. (Chem.)
https://orcid.org/0009-0008-5092-8161
sgaft@yandex.ru

Natalja V. Lapina, Cand. Sci. (Med.)
https://orcid.org/0000-0002-3418-1095
lapina2005@inbox.ru

CC BY 4.0

Check for updates

IMMUNE RESPONSE AGAINST EPSTEIN-BARR VIRUS AS AN ETIOLOGIC FACTOR AND THERAPEUTIC TARGET FOR MULTIPLE SCLEROSIS

Vladimir S. Rogovskii[1,2✉], Anna D. Kukushkina[2,3], Alexey N. Boyko[1,2]

[1] Federal Center of Brain Research and Neurotechnologies, Moscow, Russia

[2] Pirogov Russian National Research Medical University, Moscow, Russia

[3] Zhadkevich municipal clinical hospital, Moscow, Russia

Introduction. The etiology of multiple sclerosis (MS) remains unknown. According to the current consensus, susceptibility to MS is due to an elaborate interaction between genetic predisposition and multifactorial environmental factors, including vitamin D deficiency, smoking, inflammatory diet, psychoemotional stress, and infections. With regard to the infectious component, for decades, MS has been associated with a prior infection with the Epstein-Barr virus (EBV). However, it remains unclear why only a limited proportion of the numerous EBV-infected population develop MS.

Objective. To discuss the factors of interaction between the immune system and EBV that predispose to the development of MS, as well as to analyze the possibilities of their use as therapeutic targets for the prevention and treatment of MS.

Discussion. The results of a recent large epidemiologic study have provided new evidence for the association between EBV and MS. It has also been shown that cross-reacting antibodies to myelin sheath antigens can be detected in the blood of patients with EBV. However, most patients with EBV do not develop MS. This is probably due to the elimination of autoreactive cells. Natural killer (NK) cells play a particularly important role in this process. In MS, NK-mediated elimination of autoreactive B cells may be impaired. In this regard, an add-on therapy of MS aimed at controlling EBV-induced autoimmune responses appears promising.

Conclusions. Reduced cytotoxic activity of NK cells against cells that show cross-reactivity to EBV antigens and components of the myelin sheath is among the factors of interaction of the immune system with EBV that contribute to MS development. As an add-on therapy for MS, it may be reasonable to use agents that reduce the presence of EBV in the organism and have a favorable safety profile (e.g., curcumin and quercetin). The search for agents that can improve immunological control of autoreactive cells is also promising. Such agents may include compounds that are capable of enhancing the activity of NK cells, for instance, urolithin A, curcumin, and alloferon.

Keywords: multiple sclerosis; Epstein-Barr virus; autoreactive cells; natural killer cells; NK cells; polyphenols; curcumin

УДК 616.8

ИММУННЫЙ ОТВЕТ НА ВИРУС ЭПШТЕЙНА-БАРР КАК ЭТИОЛОГИЧЕСКИЙ ФАКТОР И ТЕРАПЕВТИЧЕСКАЯ МИШЕНЬ ПРИ РАССЕЯННОМ СКЛЕРОЗЕ

В.С. Роговский[1,2✉], А.Д. Кукушкина[2,3], А.Н. Бойко[1,2]

[1] Федеральный центр мозга и нейротехнологий Федерального медико-биологического агентства, Москва, Россия

[2] Российский национальный исследовательский медицинский университет им. Н.И. Пирогова, Москва, Россия

[3] Городская клиническая больница имени М.Е. Жадкевича Департамента здравоохранения города Москвы, Москва, Россия

Введение. Этиология рассеянного склероза (РС) остается неизвестной. Современное консенсусное мнение заключается в том, что восприимчивость к РС обусловлена комплексным взаимодействием между генетической предрасположенностью и многофакторным влиянием внешней среды, включая такие факторы, как недостаток витамина D, курение, приверженность воспалительной диете, инфекции, психоэмоциональный стресс. Что касается инфекционного компонента, на протяжении десятилетий РС ассоциировался с предшествующей инфекцией, вызываемой вирусом Эпштейна-Барр (ВЭБ). Однако вопрос о том, почему лишь небольшая доля популяции, инфицированной ВЭБ, заболевает РС, остается открытым.

Цель. Определение факторов взаимодействия иммунитета с ВЭБ, предрасполагающих к развитию РС, а также анализ возможностей их использования в качестве терапевтической мишени для профилактики и терапии данного заболевания.

Обсуждение. Результаты недавнего крупного эпидемиологического исследования привнесли новые доводы в пользу связи ВЭБ и РС. Было показано, что в крови носителей ВЭБ можно обнаружить антитела, перекрестно-специфичные к антигенам миелиновой оболочки. Несмотря на это, у большинства носителей ВЭБ РС не развивается. Вероятной причиной является своевременное удаление аутореактивных клеток. Особо важную роль в этом процессе играют NK-клетки. При РС нарушаются процессы NK-опосредованной элиминации аутореактивных В-клеток. В этой связи перспективна дополнительная терапия РС, направленная на контроль аутоиммунных реакций, вызванных ВЭБ.

Выводы. Среди факторов взаимодействия иммунной системы с ВЭБ, способствующих развитию РС, следует отметить сниженную цитотоксическую активность NK-клеток против клеток, проявляющих перекрестную реактивность к антигенам ВЭБ и компонентам миелиновой оболочки. В качестве дополнительной терапии РС может быть обоснованным применение средств, способных снижать представленность ВЭБ в организме и обладающих благоприятным профилем безопасности, в частности куркумина и кверцетина. Также перспективен поиск средств, способных усиливать иммунологический контроль над аутореактивными клетками. К таким средствам могут относиться соединения, способные усиливать активность NK-клеток, в частности уролитин А, куркумин, аллоферон.

Ключевые слова: рассеянный склероз; вирус Эпштейна-Барр; аутореактивные клетки; естественные киллеры; NK-клетки; полифенолы; куркумин

✉ Роговский Владимир Станиславович qwer555@mail.ru

INTRODUCTION

Multiple sclerosis (MS) is a chronic autoimmune inflammatory demyelinating disease of the central nervous system (CNS) of unknown etiology. The development of MS is associated with an elaborate interaction between a genetic predisposition and multifactorial environmental factors, including psychoemotional stress, vitamin D deficiency, smoking, changes in the microbiota, and infections [1–3]. Among the infectious component of the etiology and pathogenesis of MS, the association of MS with the Epstein-Barr virus (EBV) can be singled out. About 100% of MS patients are seropositive for EBV [4]. However, while this relationship has been known for a long time, only a small proportion among 90% of the adult population chronically infected with the EBV virus develop MS [1, 2].

Despite its usually subclinical activity, EBV is associated with various tumor and autoimmune diseases. EBV exhibits a fairly profound effect on the immune system, being the most common causative agent of infectious mononucleosis, as well as some fatal lymphoproliferative diseases in immunosuppressive conditions. An increasing amount of data is emerging on EBV infection as a major risk factor in the development of a number of autoimmune diseases, in particular MS [5, 6]. Therefore, it appears relevant to elucidate those features of the immune response against EBV that trigger the subsequent development of MS.

In this work, we set out to determine factors in the interaction of immunity with EBV that predispose to MS development, as well as to analyze the possibilities of their use as a therapeutic target in the prevention and treatment of this disease.

MATERIALS AND METHODS

The search for, systematic analysis, and review of scientific literature was carried out in electronic bibliographic databases in the Russian (eLibrary) and English (PubMed) languages. The search queries included the following keywords: multiple sclerosis, Epstein-Barr virus, autoreactive cells, natural killer cells, NK cells, polyphenols, curcumin. The search depth was 10 years. The inclusion criterion was the availability of data on the results of cohort studies, randomized controlled trials, and preclinical studies.

RESULTS AND DISCUSSION

Epstein-Barr virus in the etiology and pathogenesis of multiple sclerosis

The presence of a close relationship between EBV and MS has been discussed for a number of years, based on data on an increased risk of MS developing after infectious mononucleosis (in the form of symptomatic primary EBV infection) and in patients with high titers of antibodies to specific EBV antigens [7]. The results of a recent extensive epidemiological study by Bjornevik et al. [8] have provided new arguments in favor of the connection between EBV and MS. The hypothesis that MS is caused by EBV was tested in a cohort of more than 10 million young people. According to the results of the study, the risk of MS increased 32-fold after infection with EBV. However, infection with other viruses did not lead to an increased risk of MS, including cytomegalovirus (CMV), which is transmitted in a similar way. The levels of serum light chains of neurofilaments (an indicator of axonal degeneration, one of the diagnostic MS markers) increased only after the production of antibodies to EBV antigens. The authors argue that these results cannot be explained by any known risk factor for MS and may imply that EBV is the leading cause of MS.

The consequences of EBV infection vary, depending on age and genetic factors. The risk of developing infectious mononucleosis and MS is likely to grow when primary EBV infection occurs after the age of 10. At this age, the negative selection of autoreactive T cells slows down and the cell-mediated response of Th-1 cells reaches its peak. Most people are diagnosed with MS between the ages of 20 and 50, several years after becoming infected with EBV. The EBV persistence increases the survival of memory B cells and causes long-term changes in the cytokine response of the host [5, 6].

Nevertheless, the question concerning why only a small proportion of numerous EBV carriers develop MS remains to be elucidated. Moreover, it remains unclear how EBV is involved in the etiology and/or pathogenesis of MS. When answering the second question, literature data offers two main hypotheses [9]. Firstly, persistent infection and re-reactivation of the virus can serve as a stimulus for chronic inflammation inside and outside the nervous system, either directly or by creating a long-term pool of pro-inflammatory B lymphocytes. Secondly, autoimmune reactions can be caused by molecular mimicry of antigens common to EBV proteins and CNS antigens, which was shown, in particular,

for the glial cell adhesion molecule (GlialCAM), the main protein of myelin, and others [9]. It has been mentioned above that the relationship between MS and EBV has been established for quite a long time; however, more evidence has recently emerged to support the second of the above hypotheses.

Role of NK cells in providing immune tolerance in the presence of autoimmunity to CNS antigens

The regulatory role of natural killer (NK) cells was described more than 20 years ago [10]. In recent years, new evidence of the possible role of NK cells in immunological tolerance and their protective value against various autoimmune diseases, including MS, has emerged. In the context of immune regulatory properties, special attention is paid to CD56^{bright} NK cells, which play an important role in controlling the T cell response and maintaining homeostasis. This subpopulation of NK cells owes its name to the high surface expression of CD56 (nerve cell adhesion molecule), being also characterized by the expression of CD16^{dim} and the NKG2A inhibitory receptor and, at the same time, the absence of expression of immunoglobulin-like receptors of killer cell immunoglobulin-like receptors (KIR). CD56^{bright} NK cells possess reduced cytotoxicity compared to CD56^{dim} NK cells, which renders them regulatory. It was shown that therapy with various multiple sclerosis disease-modifying medications (MSDMM) increases the relative number of NK cells, as well as NK-mediated immune regulatory functions [11].

CD56^{bright} NK cells express receptors for various cytokines, such as interleukin (IL)-12, IL-15, and IL-18, which are produced by activated antigen-presenting cells. The response to these cytokines can cause proliferation of CD56^{bright} NK cells and their production of a number of cytokines, including IFN-γ, IL-13, and GM-CSF (granulocyte-macrophage colony-stimulating factor), as well as regulatory IL-10 [10, 11].

According to literature data [12, 13], not only CD56^{bright} NK cells mediate immune regulatory functions. Thus, the association of CMV-induced expansion of NKG2C$^+$ NK cells with a lower risk of disability progression in MS was described, suggesting the influence of these cells on the clinical course of the disease. NKG2C$^+$ human NK cells are part of the CD56^{dim} population, which mediates cytotoxicity and cytokine production when interacting with target cells either directly or indirectly by antibody-dependent cellular cytotoxicity (in this case, the interaction of IgG with CD16A on NK cells).

According to a recent study by Ding et al. [14], immunosuppressive therapy or MSDMM therapy lead to a significant increase in the ratio of CD56^{dim} NK cells to circulating follicular T helper cells. This ratio made it possible to significantly differentiate patients with recurrent MS from healthy individuals and patients in remission. The authors assumed that this ratio may become a new predictor of disease activity and evaluation of treatment effectiveness.

In 2024, Dal et al. [15] showed that a lower relative content of NK cells three months after anti-CD20 therapy (rituximab and ocrelizumab) correlates with the presence of disease activity six months after therapy, which corresponds to the possible protective role of NK cells in MS.

Also, compared with the baseline values, anti-CD20 antibody therapy led to an absolute and relative decrease in B-lymphocyte levels and an increase in absolute and relative NK cell levels three and five months after therapy.

Control mechanisms of cross-activated immune cells to Epstein-Barr virus antigens

In healthy donors with antibodies to the nuclear antigen of the Epstein-Barr virus (EBNA$_{386-405}$) and in patients with MS, their cross-reactivity against the myelin sheath antigen GlialCAM$_{370-389}$ (glial cell adhesion molecule) has been shown. Moreover, this cross-reactivity is capable of eliciting an immune response in both MS patients and healthy donors [9, 16].

In this regard, Vietzen et al. conducted an extensive search for differences in the immune response to EBV antigens in MS patients and healthy donors. The cohorts of 270 EBNA-1 seropositive MS patients and 270 EBNA-1 seropositive healthy donors were analyzed, compared by sex, age, and time since seroconversion to EBV antigens and the onset of infectious mononucleosis. All MS patients had high levels of antibodies to EBNA$_{386-405}$. Among the group of healthy donors, some had low levels of antibodies to EBNA$_{386-405}$ (EBNA^{low} group, 162 people), while some had high levels (EBNA^{high} group, 108 people). It is noteworthy that both MS patients and healthy EBNA^{high} donors showed significantly higher levels of EBNA$_{386-405}$-specific immune cells, in particular plasma CD4$^+$T cells and CD8$^+$T cells, compared to the EBNA^{low} group [17]. Thus, healthy donors from the EBNA^{high} group also have immunological prerequisites for autoimmune damage to the myelin sheath. However, this does not happen, probably due to the presence of protective factors that prevent an autoimmune response.

The results of Vietzen et al. suggest that one of the important factors preventing MS development consists in the destruction of autoimmune GlialCAM$_{370-389}$-specific cells by cytotoxic NK cell reactions. At the same time, in patients with MS, the effectiveness of this process is reduced. Thus, this study revealed a number of differences between the group of MS patients with antibodies to GlialCAM$_{370-389}$ and healthy EBV carriers who also have antibodies to GlialCAM$_{370-389}$. In particular, healthy EBV carriers with autoantibodies to GlialCAM$_{370-389}$ showed a significantly higher representation of NK cells of the NKG2D$^+$ type (NKG2D$^+$ NK cells) with a highly active homozygous genotype — NKG2D$^{HNK/HNK}$. In the population of healthy carriers of autoantibodies to GlialCAM$_{370-389}$, the rate of highly active NKG2D$^+$ NK cells was about five times higher than in that of carriers of autoantibodies to GlialCAM$_{370-389}$ suffering from MS. The level of NKG2C$^+$ NK cells in the control groups was also significantly higher than in patients with MS [17].

In MS patients, autoreactive cells are likely to avoid regulatory and cytotoxic immune reactions effectively by inhibiting NK cells. One of the mechanisms behind this inhibition is an increase in the presence of HLA-E on the surface of B cells, which is induced by certain types of EBV. Normally, HLA-E, bound to normal peptides from HLA class I, signals NK cells that the cell has not been altered and does not need to be eliminated [18]. However, in MS, this mechanism

can become overly active, preventing NK-mediated elimination of autoreactive B cells. HLA-E can play an important role in the immune evasion of EBV-infected cells from natural killers: binding of HLA-E to NKG2A+ on NK cells is known to inhibit their function [19].

HLA-E is stabilized by a peptide derived from the Epstein-Barr virus latent membrane protein 1 (LMP-1), expressed in latently infected EBV cells [20]. LMP-1 is a polymorphic peptide: different variants of EBV may have different variants of LMP-1. It was found that certain variants of LMP-1 (GGDPHLPTL and GGDPPLPTL) led to a stable increase in the level of HLA-E on the surface of B cells specific to GlialCAM$_{370-389}$. It has been shown that almost all MS patients are carriers of the above-mentioned EBV variants that increase HLA-E expression. Increased EBV reactivation and subsequent IL-27 expression correlate with increased HLA-E expression and inhibition of NKG2A+ effector cells in MS patients [17]. IL-27 is a member of the IL-12 family, which is important in the pathogenesis of autoimmune disorders [21]. The NKG2A receptor is one of the inhibitory receptors of NK cells [22].

According to Vietzen et al., the factors associated with a high risk of MS in EBV carriers comprise a low or absent NKG2C+ NK cell response (OR 41.3), variants GGDPHLPTL and GGDPPLPTL of the LMP-1 peptide in EBV (OR 39.6), a low-active NKG2D^{LNK} genotype (OR 8.9) and HLA-E*01:01 (OR 4.3). At the same time, the combination of three or more risk factors leads to an increased risk of MS in carriers of autoreactive antibodies to the EBV nuclear antigen by about 180 times. In addition, infection with EBV with the risky LMP variant in combination with the HLA-E*01:01 genotype increases the risk of developing MS by about 260 times [17]. The importance of NK cells in the removal of autoreactive cells has been confirmed in other studies. It is worth noting that the data on the role of a certain decrease in NK activity in the MS pathogenesis are consistent with the understanding of psychoemotional stress being one of the most important risk factors in the MS etiology. The NK cell function is particularly impaired by psychoemotional stress [23, 24].

Prospects for add-on MS therapy aimed at controlling Epstein-Barr virus-induced immune cross-reactions

In connection with the description of possible immunological mechanisms that ensure protection against MS development in the presence of autoantibodies to CNS antigens, it appears relevant to analyze possible prevention and therapy options aimed at strengthening these mechanisms. These options can be broadly divided into those aimed at enhancing immune regulatory reactions that ensure the autoreactive cells removal, as well as those aimed directly at reducing the EBV level in the body. Further, we will consider the properties of a number of medications offered as an additional MS therapy from these standpoints.

Possibilities for reducing the presence of EBV in the body

EBV infection plays a central role in terms of triggering disruption of immune tolerance mechanisms. However, to date, antiviral medications or vaccines for the treatment and prevention of this infection have not yet been developed. Therefore, it seems promising to search for various compounds aimed at controlling EBV-induced immune cross-reactions. Regarding possible medications for add-on MS therapy with a favorable safety profile, it is of interest that various compounds of natural origin, especially polyphenols and terpenoids such as curcumin, epigallocatechin gallate, resveratrol, moronic acid and andrografolide, exhibit antiviral activity against EBV [25].

Some biologically active compounds isolated from medicinal plants inhibit the early stages of EBV infection. Quercetin, a polyphenolic compound isolated, in particular, from licorice root, prevents the recognition of EBV receptors and, consequently, blocks the penetration of EBV into cells [26]. Another study showed the ability of quercetin to suppress the expression of EBNA-1 and LMP-2, which may help reduce cross-reactions to EBV antigens [27].

A significant antiviral effect of curcumin has been shown, in particular against herpes simplex type 1 and type 2 viruses, CMV, Kaposi's sarcoma-associated herpesvirus, EBV, and bovine herpesvirus 1. The mechanisms of antiviral effects of curcumin are related to its ability to interfere with a number of cellular and molecular processes that are necessary for the expression and replication of viral genes. Curcumin (10 μM) increases the proportion of the plasma membrane accepting the conformation of the lipid raft, which confirms the evidence that curcumin can modulate the lipid bilayer [28]. Lipid rafts are dynamic ensembles of proteins and lipids that float freely in the liquid disordered bilayer of cell membranes, being also capable of agglomerating into large ordered platforms. These structures are important for regulating various membrane functions in eukaryotic cells [29]. Curcumin suppresses the proliferation of human nasopharyngeal carcinoma cells associated with EBV by inhibiting the expression of nuclear antigen 1 of the Epstein-Barr virus. Thus, the 50% inhibitory concentrations of curcumin were 12.4 μM and 3.3 μM for 24-h and 48-h curcumin treatment, respectively [30].

It is worth noting that the above compounds exhibit antiviral activity in in vitro studies in relatively high concentrations: as a rule, several μM/L or more, which is many times higher than their plasma concentrations. In recent years, a number of clinical reports have appeared on ways to increase the bioavailability of lipophilic compounds, such as the use of various nanoforms, liposomal forms, micellar forms, as well as combinations of various substances. In particular, the use of micellar forms of curcumin has made it possible to achieve plasma levels of this compound comparable to its concentrations in in vitro studies [31, 32].

Medications aimed at enhancing immune responses that ensure the removal of autoreactive cells

As noted above, protection against the development of MS in individuals with autoreactive antibodies is largely mediated by the activation of the effector link of immunity against autoreactive cells. This includes certain subpopulations of NK cells and CD8+T cells. Agents with a mild immune stimulating effect may be promising for enhancing immune regulatory reactions that ensure the removal of

autoreactive cells. Thus, the effect of a number of MSDMM is associated with increased NK activity. In particular, in patients receiving dimethyl fumarate (MSDMM 1st line), the total number of lymphocytes decreased depending on the time of exposure. The number of NK cells showed a heterogeneous trend, eventually increasing by about 86% following two years of treatment [33]. However, it should be noted that the use of highly active agents for the purpose of immunomodulation and increased NK activity, such as antibody therapy, may be associated with a number of side effects. The latter may result in cessation of the use of already approved agents [34].

The medications with a favorable safety profile, having immunotropic and neuroprotective effects and suitable for additional therapy of MS, include compounds capable of exhibiting an immune stimulating effect. Thus, urolitin A (a polyphenolic metabolite of the intestinal microbiota) not only has an anti-inflammatory effect against chronic inflammation, but also enhances the persistence and effector functions of CD8$^+$ cytotoxic T lymphocytes, as well as the activity of NK cells [35–37].

Quercetin, the abovementioned polyphenol, increased the proportion of NK cells in in vivo experiments when administered to mice at a dose of 1 mg/kg every 2 days for 30 days without affecting the populations of T and B cells. Also, due to binding to the MYH9 protein (the main component of the cytoskeleton, which plays an important role in the preservation and maintenance of the functionality of hematopoietic stem cells), this polyphenol increased the number and stimulated the maturation of NK cells [38]. However, there are studies where taking polyphenols did not have a significant effect on NK activity. Thus, taking 500–1000 mg of quercetin had no significant effect on NK cell activity in healthy adult women [39]. Perhaps similar results may be related to the previously mentioned low bioavailability of polyphenols.

Quercetin, like many other polyphenols, is found in various products of natural origin (such as grape seeds, onions, garlic, tea, and others). For example, fresh onions contain about 30-45 mg/100 g of quercetin and 4.5 mg/100 g of kaempferol [40]. Due to the low bioavailability of polyphenols, as already noted above, it may be promising to use their combinations with other substances capable of increasing their total bioavailability. From this point of view, the use of natural extracts containing a range of active substances can be effective in enhancing the resulting bioavailability. Thus, the ability of various plant extracts to enhance the activity of NK cells has been shown [41].

According to the results of a recent randomized, double-blind, placebo-controlled trial, the use of onion peel extract (1000 mg of extract per day for 8 weeks) improves NK cell activity in patients with moderate symptoms of upper respiratory tract diseases without any significant side effects [42]. These clinical results are consistent with those obtained in vitro, according to which incubation of peripheral blood mononuclear cells (PBMC) with onion extracts (*Allium cepa*) led to a significant increase in the rate of CD16$^+$ NK cells [43]. Oral administration of a combined extract of *Sargassum coreanum* (at dosages of 30 mg/kg, 100 mg/kg or 300 mg/kg for 4 weeks) and *Curcuma longa*

(5 mg/kg, 4 weeks) to rats also caused an increase in NK cell activity [44].

Focaccetti et al. obtained promising results from an in vitro use of a combination of curcumin and resveratrol. In a human PBMC culture, the combination of these polyphenols (at concentrations of 5 µM), on the one hand, increased the production of IL-10 by regulatory T cells. On the other hand, this combination enhanced the activity of NK cells by increasing and decreasing the regulation of activating and inhibitory receptors, respectively, as well as increasing the level of CD68 expression on monocytes/macrophages [45].

The use of curcumin as an add-on MS therapy is being actively studied, including via clinical trials. To date, a number of clinical studies have reported the efficacy of an add-on curcumin MS therapy, especially when using forms with increased bioavailability [46-48].

Alloferon, an antimicrobial cytokine-like peptide, is also capable of stimulating NK activity and increasing NKG2D production in NK cells, while possessing anti-inflammatory properties. This renders alloferon a promising research object for add-on MS therapy [49, 50].

CONCLUSION

The results obtained in recent years indicate the important role of the immune response to EBV in the etiology and pathogenesis of MS. It seems likely that the removal of autoreactive cells, cross-reactive to EBV antigens, using cytotoxic CD8$^+$ T cells, and NK cells in particular, is one of the main mechanisms preventing the development of autoimmune CNS lesions in MS. A number of risk factors associated with the immune response to EBV have been identified, which may increase the likelihood of developing MS. These risk factors include the following: low or absent NKG2C$^+$ NK cell response, variants GGDPHLPTL and GGDPPLPTL of the LMP-1 peptide in EBV, low-activity genotype NKG2D^{LNK} and HLA-E*01:01. These findings create opportunities for the emergence of new approaches to the prevention and treatment of MS. Thus, the use of certain components of the immune response to EBV, such as NK cell activity, may be promising as a therapeutic target.

Agents with a favorable safety profile for add-on MS therapy may be suitable for these purposes. The efficacy of these medications, especially those of natural origin, may be due to a combination of antiviral, anti-inflammatory, and immune-stimulating activities aimed at enhancing immunological mechanisms capable of eliminating autoreactive cells.

Many of these products are characterized by low bioavailability, which can be enhanced by modern biotechnological methods, e.g., creation of micellar molds. At the same time, the introduction of such tools into clinical practice is hampered by the lack of respective clinical data. Further comprehensive clinical studies of complementary MS therapies are needed, both in combination with classical MSDMM and as monotherapy in patients who, for various reasons, receive no specific pathogenetic therapy.

References

1. Wong Y, Meehan MT, Burrows SR, Doolan DL,Miles JJ. Estimating the global burden of Epstein-Barr virus-related cancers. *J Cancer Res Clin Oncol*. 2022;148(1):31–46.
https://doi.org/10.1007/s00432-021-03824-y

2. Laderach F,Munz C. Epstein Barr Virus Exploits Genetic Susceptibility to Increase Multiple Sclerosis Risk. *Microorganisms*. 2021;9(11).
https://doi.org/10.3390/microorganisms9112191

2. Hatami A, Ahmadi-Khorram M, Keykhaei F, Esfehani AJ,Nematy M. Association Between the Risk of Multiple Sclerosis and Dietary Proinflammatory/Anti-Inflammatory Food Intake and Dietary Diversity: A Case-Control Study. *Clin Nutr Res*. 2024;13(1):61–73.
https://doi.org/10.7762/cnr.2024.13.1.61

4. Lehikoinen J, Nurmi K, Ainola M, Clancy J, Nieminen JK, Jansson L, et al. Epstein-Barr Virus in the Cerebrospinal Fluid and Blood Compartments of Patients With Multiple Sclerosis and Controls. *Neurol Neuroimmunol Neuroinflamm*. 2024;11(3):e200226.
https://doi.org/10.1212/NXI.0000000000200226

5. Soldan SS,Lieberman PM. Epstein-Barr virus and multiple sclerosis. *Nat Rev Microbiol*. 2023;21(1):51–64.
https://doi.org/10.1038/s41579-022-00770-5

6. Xu Y, Hiyoshi A, Smith KA, Piehl F, Olsson T, Fall K, et al. Association of Infectious Mononucleosis in Childhood and Adolescence With Risk for a Subsequent Multiple Sclerosis Diagnosis Among Siblings. *JAMA Netw Open*. 2021;4(10):e2124932.
https://doi.org/10.1001/jamanetworkopen.2021.24932

7. Bjornevik K, Munz C, Cohen JI, Ascherio A. Epstein-Barr virus as a leading cause of multiple sclerosis: mechanisms and implications. *Nat Rev Neurol*. 2023;19(3):160–71.
https://doi.org/10.1038/s41582-023-00775-5

8. Bjornevik K, Cortese M, Healy BC, Kuhle J, Mina MJ, Leng Y, et al. Longitudinal analysis reveals high prevalence of Epstein-Barr virus associated with multiple sclerosis. *Science*. 2022;375(6578):296–301.
https://doi.org/10.1126/science.abj8222

9. Rommer P, Puchhammer-Stöckl E, Lassmann H, Berger T, Vietzen H. Ineffective control of Epstein–Barr virus infection is seen in MS: What is next? *Clinical and Translational Medicine*. 2024;14(2):e1596.
https://doi.org/10.1002/ctm2.1596

10. Cooper MA, Fehniger TA, Turner SC, Chen KS, Ghaheri BA, Ghayur T, et al. Human natural killer cells: a unique innate immunoregulatory role for the CD56^{bright} subset. *Blood*. 2001;97(10):3146–51.
https://doi.org/10.1182/blood.V97.10.3146

11. Gross CC, Schulte-Mecklenbeck A, Wiendl H, Marcenaro E, Kerlero de Rosbo N, Uccelli A, et al. Regulatory Functions of Natural Killer Cells in Multiple Sclerosis. *Front Immunol*. 2016;7:606.
https://doi.org/10.3389/fimmu.2016.00606

12. Moreira A, Alari-Pahissa E, Munteis E, Vera A, Zabalza A, Llop M, et al. Adaptive Features of Natural Killer Cells in Multiple Sclerosis. *Front Immunol*. 2019;10:2403.
https://doi.org/10.3389/fimmu.2019.02403

13. Martinez-Rodriguez JE, Cobo-Calvo A, Villar LM, Munteis E, Blanco Y, Rasal R, et al. Adaptive natural killer cell response to cytomegalovirus and disability progression in multiple sclerosis. *Mult Scler*. 2016;22(6):741–52.
https://doi.org/10.1177/1352458515601215

14. Ding J, Yan X, Zhao C, Zhao D, Jia Y, Ren K, et al. The ratio of circulating CD56(dim) NK cells to follicular T helper cells as a promising predictor for disease activity of relapsing-remitting multiple sclerosis. *Heliyon*. 2024;10(10):e31533.
https://doi.org/10.1016/j.heliyon.2024.e31533

15. Dal Bello S, Lorenzut S, Saccomano E, Tereshko Y, Gigli GL, Pucillo CE, et al. NK Cell Levels Correlate with Disease Activity in Patients with Multiple Sclerosis on Ocrelizumab/Rituximab Therapy. *Pharmaceuticals (Basel)*. 2024;17(2):150.
https://doi.org/10.3390/ph17020150

16. Xie C, Sun C, Zeng MS. Navigating Epstein-Barr virus autoimmunity: role of NK cells and T cells in multiple sclerosis. *Signal Transduct Target Ther*. 2024;9(1):48.
https://doi.org/10.1038/s41392-024-01774-8

17. Vietzen H, Berger SM, Kühner LM, Furlano PL, Bsteh G, Berger T, et al. Ineffective control of Epstein-Barr-virus-induced autoimmunity increases the risk for multiple sclerosis. *Cell*. 2023;186(26):5705-5718.e13.
https://doi.org/10.1016/j.cell.2023.11.015

18. Huisman BD, Guan N, Ruckert T, Garner L, Singh NK, McMichael AJ, et al. High-throughput characterization of HLA-E-presented CD94/NKG2x ligands reveals peptides which modulate NK cell activation. *Nat Commun*. 2023;14(1):4809.
https://doi.org/10.1038/s41467-023-40220-1

19. Fisher JG, Doyle ADP, Graham LV, Khakoo SI,Blunt MD. Disruption of the NKG2A:HLA-E Immune Checkpoint Axis to Enhance NK Cell Activation against Cancer. *Vaccines (Basel)*. 2022;10(12).
https://doi.org/10.3390/vaccines10121993

20. Mbiribindi B, Pena JK, Arvedson MP, Moreno Romero C, McCarthy SR, Hatton OL. Epstein-Barr virus peptides derived from latent cycle proteins alter NKG2A$^+$ NK cell effector function. *Sci Rep*. 2020; 10(1):19973.
https://doi.org/10.1038/s41598-020-76344-3

21. Meka RR, Venkatesha SH, Dudics S, Acharya B, Moudgil KD. IL-27-induced modulation of autoimmunity and its therapeutic potential. *Autoimmun Rev*. 2015;14(12):1131–41.
https://doi.org/10.1016/j.autrev.2015.08.001

22. Yu H, Li C, Wang X, Duan J, Yang N, Xie L, et al. Techniques and Strategies for Potential Protein Target Discovery and Active Pharmaceutical Molecule Screening in a Pandemic. *J Proteome Res*. 2020;19(11):4242–58.
https://doi.org/10.1021/acs.jproteome.0c00372

23. Fernandes SB, Patil ND, Meriaux S, Theresine M, Muller CP, Leenen FAD, et al. Unbiased Screening Identifies Functional Differences in NK Cells After Early Life Psychosocial Stress. *Front Immunol*. 2021;12:674532.
https://doi.org/10.3389/fimmu.2021.674532

24. Wyman PA, Moynihan J, Eberly S, Cox C, Cross W, Jin X, et al. Association of family stress with natural killer cell activity and the frequency of illnesses in children. *Arch Pediatr Adolesc Med*. 2007;161(3):228–34.
https://doi.org/10.1001/archpedi.161.3.228

25. Eladwy RA, Vu HT, Shah R, Li CG, Chang D,Bhuyan DJ. The Fight against the Carcinogenic Epstein-Barr Virus: Gut Microbiota, Natural Medicines, and Beyond. *Int J Mol Sci*. 2023; 24(2).
https://doi.org/10.3390/ijms24021716

26. Lee M, Son M, Ryu E, Shin YS, Kim JG, Kang BW, et al. Quercetin-induced apoptosis prevents EBV infection. *Oncotarget*. 2015;6(14):12603–24.
https://doi.org/10.18632/oncotarget.3687

27. Lee HH, Lee S, Shin YS, Cho M, Kang H,Cho H. Anti-Cancer Effect of Quercetin in Xenograft Models with EBV-Associated Human Gastric Carcinoma. *Molecules*. 2016;21(10):21101286
https://doi.org/10.3390/molecules21101286

28. Zhu L, Ding X, Zhang D, Yuan C, Wang J, Ndegwa E, et al. Curcumin inhibits bovine herpesvirus type 1 entry into MDBK cells. *Acta Virol*. 2015;59(3):221–7.
https://doi.org/10.4149/av_2015_03_221

29. Simons K,Ehehalt R. Cholesterol, lipid rafts, and disease. *J Clin Invest*. 2002;110(5):597–603.
https://doi.org/10.1172/JCI16390

30. Liu L, Yang J, Ji W, Wang C. Curcumin Inhibits Proliferation of Epstein-Barr Virus-Associated Human Nasopharyngeal Carcinoma Cells by Inhibiting EBV Nuclear Antigen 1 Expression. *Biomed Res Int*. 2019;2019:8592921.
https://doi.org/10.1155/2019/8592921

31. Grafeneder J, Derhaschnig U, Eskandary F, Buchtele N, Sus N, Frank J, et al. Micellar Curcumin: Pharmacokinetics and Effects on Inflammation Markers and PCSK-9 Concentrations in Healthy Subjects in a Double-Blind, Randomized, Active-Controlled, Crossover Trial. *Mol Nutr Food Res*. 2022;66(22):e2200139.
https://doi.org/10.1002/mnfr.202200139

32. Gayathri K, Bhaskaran M, Selvam C,Thilagavathi R. Nano for-

mulation approaches for curcumin delivery- a review. *Journal of Drug Delivery Science and Technology*. 2023;82:104326.
https://doi.org/10.1016/j.jddst.2023.104326

33. Marastoni D, Buriani A, Pisani AI, Crescenzo F, Zuco C, Fortinguerra S, et al. Increased NK Cell Count in Multiple Sclerosis Patients Treated With Dimethyl Fumarate: A 2-Year Longitudinal Study. *Front Immunol*. 2019;10:1666.
https://doi.org/10.3389/fimmu.2019.01666

34. Rommer PS, Berger K, Ellenberger D, Fneish F, Simbrich A, Stahmann A, et al. Management of MS Patients Treated With Daclizumab — a Case Series of 267 Patients. *Front Neurol*. 2020;11:996.
https://doi.org/10.3389/fneur.2020.00996

35. Ma S, Wu Q, Wu W, Tian Y, Zhang J, Chen C, et al. Urolithin A Hijacks ERK1/2-ULK1 Cascade to Improve CD8(+) T Cell Fitness for Antitumor Immunity. *Adv Sci (Weinh)*. 2024;11(18):e2310065.
https://doi.org/10.1002/advs.202310065

36. Rogovskii VS, Matyushin AI,Shimanovskii NL. Urolithin A influences cytokine production by various cancer cell lines. *Pharmaceutical Chemistry Journal*. 2023;57(4):17–21.
https://doi.org/10.30906/0023-1134-2023-57-4-17-21

37. Rogovskii V, Murugin VV, Vorobyev N, Popov S, Sturov N, Krasheninnikov A, et al. Urolithin A increases the natural killer activity of PBMCs in patients with prostate cancer. *Front Pharmacol*. 2024;15:1503317.
https://doi.org/10.3389/fphar.2024.1503317

38. Su T, Shen H, He M, Yang S, Gong X, Huang C, et al. Quercetin promotes the proportion and maturation of NK cells by binding to MYH9 and improves cognitive functions in aged mice. *Immun Ageing*. 2024;21(1):29.
https://doi.org/10.1186/s12979-024-00436-1

39. Heinz SA, Henson DA, Nieman DC, Austin MD,Jin F. A 12-week supplementation with quercetin does not affect natural killer cell activity, granulocyte oxidative burst activity or granulocyte phagocytosis in female human subjects. *Br J Nutr*. 2010;104(6):849–57.
https://doi.org/10.1017/S000711451000156X

40. Savitha S, Bhatkar N, Chakraborty S,Thorat BN. Onion quercetin: As immune boosters, extraction, and effect of dehydration. *Food Bioscience*. 2021;44:101457.
https://doi.org/10.1016/j.fbio.2021.101457

41. Shabsoug B, Khalil R,Abuharfeil N. Enhancement of natural killer cell activity *in vitro* against human tumor cells by some plants from Jordan. *J Immunotoxicol*. 2008;5(3):279–85.
https://doi.org/10.1080/15376510802312027

42. Cho H, Kim S, Lee SH,Park Y. Effect of onion (Allium cepa L.) peel extract on natural killer cell and cytokines in a randomized, double-blind, placebo-controlled trial. *Nutr Res Pract*. 2024;18(1):33–45.
https://doi.org/10.4162/nrp.2024.18.1.33

43. Lisanti A, Formica V, Ianni F, Albertini B, Marinozzi M, Sardella R, et al. Antioxidant activity of phenolic extracts from different cultivars of Italian onion (Allium cepa) and relative human immune cell proliferative induction. *Pharm Biol*. 2016; 54(5):799–806.
https://doi.org/10.3109/13880209.2015.1080733

44. Park YM, Lee HY, Shin DY, Kim SH, Yoo Y, Kim MJ, et al. Augmentation of NK-cell activity and immunity by combined natural polyphenols and saccharides *in vitro* and *in vivo*. *Int J Biol Macromol*. 2024;268(Pt 2):131908.
https://doi.org/10.1016/j.ijbiomac.2024.131908

45. Focaccetti C, Palumbo C, Benvenuto M, Carrano R, Melaiu O, Nardozi D, et al. The Combination of Bioavailable Concentrations of Curcumin and Resveratrol Shapes Immune Responses While Retaining the Ability to Reduce Cancer Cell Survival. *Int J Mol Sci*. 2023;25(1).
https://doi.org/10.3390/ijms25010232

46. Petracca M, Quarantelli M, Moccia M, Vacca G, Satelliti B, D'Ambrosio G, et al. ProspeCtive study to evaluate efficacy, safety and tOlerability of dietary supplemeNT of Curcumin (BCM95) in subjects with Active relapsing MultIple Sclerosis treated with subcutaNeous Interferon beta 1a 44 mcg TIW (CONTAIN): A randomized, controlled trial. *Mult Scler Relat Disord*. 2021;56:103274.
https://doi.org/10.1016/j.msard.2021.103274

47. Dolati S, Ahmadi M, Rikhtegar R, Babaloo Z, Ayromlou H, Aghebati-Maleki L, et al. Changes in Th17 cells function after nanocurcumin use to treat multiple sclerosis. *Int Immunopharmacol*. 2018;61:74–81.
https://doi.org/10.1016/j.intimp.2018.05.018

48. Kukushkina A, Rogovskii V, Ponevezhskaya E, Lysogorskaia E, Boyko A. Curcumin as an add-on therapy for multiple sclerosis in patients receiving interferon-beta therapy. *Neurology, Neuropsychiatry, Psychosomatics*. 2024;(16):4–10.
https://doi.org/10.14412/2074-2711-2024-2S-4-10

49. Appiah C, Chen S, Pori AI, Retyunskiy V, Tzeng C, Zhao Y. Study of alloferon, a novel immunomodulatory antimicrobial peptide (AMP), and its analogues. *Front Pharmacol*. 2024;15:1359261.
https://doi.org/10.3389/fphar.2024.1359261

50. Zhang X, Retyunskiy V, Qiao S, Zhao Y,Tzeng CM. Alloferon-1 ameliorates acute inflammatory responses in lambda-carrageenan-induced paw edema in mice. *Sci Rep*. 2022;12(1):16689.
https://doi.org/10.1038/s41598-022-20648-z

AUTHORS

Vladimir S. Rogovskii, Cand. Sci. (Med.)
https://orcid.org/0000-0002-3682-6571
qwer555@mail.ru

Anna D. Kukushkina
https://orcid.org/0000-0001-9964-8103
dr_kukushanna@mail.ru

Alexey N. Boyko, Dr. Sci. (Med.)
https://orcid.org/0000-0002-2975-4151
boiko.a@fccps.ru

LABORATORY MARKERS OF ENDOTHELIAL DESTRUCTION AND HEMOSTASIS ACTIVATION IN PATIENTS WITH ACUTE CEREBROVASCULAR ACCIDENT AND COVID-19

Olga V. Lyang[1,2✉], Mikhail A. Soldatov[1], Leonid V. Klimov[1], Tatiana V. Kiseleva[1,3], Nataliya A. Marskaya[1], Nikolay A. Shamalov[1]

[1] Federal Center of Brain Research and Neurotechnologies, Moscow, Russia

[2] Patrice Lumumba Peoples' Friendship University of Russia, Moscow, Russia

[3] Research Institute for Healthcare Organization and Medical Management of Moscow Healthcare Department, Moscow, Russia

Introduction. The severity of endothelial destruction in patients with the new COVID-19 new coronavirus infection may be correlated with the risk of developing acute cerebrovascular accident (ACVA).

Objective. To study the role of hemostasis system activation markers and vascular wall damage markers in the development of stroke in patients with the new coronavirus infection.

Materials and methods. The study included 38 patients with the new coronavirus infection and ACVA and 40 patients with the new coronavirus infection without ACVA. All patients were tested for antibodies to β2-glycoprotein, antibodies to cardiolipin, plasminogen activator inhibitor type 1 (PAI-1), α2-antiplasmin, intercellular adhesion molecule type 1 (ICAM-1), von Willebrand factor, and homocysteine.

Results. No statistically significant differences were found between the groups in terms of antiphospholipid antibody levels; however, increased antibodies to β2-glycoprotein relative to the reference interval were more frequent in the group without ACVA. Significant differences in PAI-1 levels were found between the group with ACVA and the comparison group ($p < 0.001$), with the PAI-1 concentration being 1.6 times higher in the comparison group. No significant differences were observed between the groups in terms of α2-antiplasmin, ICAM-1, and von Willebrand factor levels. Significant differences for homocysteine were found between the ACVA group and the comparison group ($p < 0.001$), with the concentration in the comparison group being 1.8 times higher.

Conclusions. The development of acute cerebrovascular accident in patients with lower concentrations of homocysteine and PAI-1 may be explained by weaker compensatory mechanisms aimed at repairing of the vascular wall and harmonization of interaction of hemostasis system links, which eventually led to vascular wall damage.

Keywords: ischemic stroke; hemorrhagic stroke; coronavirus; homocysteine; antiphospholipid antibodies; plasminogen activator inhibitor type 1

ЛАБОРАТОРНЫЕ МАРКЕРЫ ЭНДОТЕЛИАЛЬНОЙ ДЕСТРУКЦИИ И АКТИВАЦИИ ГЕМОСТАЗА У ПАЦИЕНТОВ С ИНСУЛЬТОМ И COVID-19

О.В. Лянг[1,2✉], М.А. Солдатов[1], Л.В. Климов[1], Т.В. Киселева[1,3], Н.А. Марская[1], Н.А. Шамалов[1]

[1] Федеральный центр мозга и нейротехнологий Федерального медико-биологического агентства, Москва, Россия

[2] Российский университет дружбы народов им. Патриса Лумумбы (РУДН), Москва, Россия

[3] Научно-исследовательский институт организации здравоохранения и медицинского менеджмента Департамента здравоохранения города Москвы, Москва, Россия

Введение. Выраженность эндотелиальной деструкции у пациентов с COVID-19 может быть взаимосвязана с риском развития острого нарушения мозгового кровообращения.

Цель. Изучение роли маркеров активации системы гемостаза и повреждения сосудистой стенки в развитии острого нарушения мозгового кровообращения (ОНМК) у пациентов с новой коронавирусной инфекцией.

Материалы и методы. В исследование были включены 38 пациентов с новой коронавирусной инфекцией и ОНМК и 40 пациентов с новой коронавирусной инфекцией без ОНМК. Всем пациентам определяли: антитела к бета-2 гликопротеину, антитела к кардиолипину, ингибитор активатора плазминогена 1-го типа (ИАП-1), α2-антиплазмин, молекулу межклеточной адгезии 1-го типа (ICAM-1), фактор Виллебранда, гомоцистеин.

Результаты. По уровню антифосфолипидных антител не было выявлено статистически значимых различий между группами, однако повышенные относительно референтного интервала антитела к бета-2 гликопротеину чаще встречались в группе без ОНМК. По уровню ИАП-1 были выявлены значимые различия между группой с ОНМК и группой сравнения ($p < 0,001$), в группе сравнения концентрация ИАП-1 была в 1,6 раза выше. По уровню α2-антиплазмина, ICAM-1 и фактора Виллебранда значимых различий между группами выявлено не было. Статистически значимые различия по гомоцистеину были выявлены между группой с ОНМК и группой сравнения ($p < 0,001$), концентрация в группе сравнения была в 1,8 раза выше.

Выводы. Развитие ОНМК у пациентов с более низкими концентрациями гомоцистеина и ИАП-1, вероятно, можно объяснить более слабыми компенсаторными механизмами, направленными на репарацию сосудистой стенки и гармонизацию взаимодействия звеньев системы гемостаза, что в конечном счете приводит к повреждению сосудистой стенки.

Ключевые слова: ишемический инсульт; геморрагический инсульт; коронавирус; гомоцистеин; антифосфолипидные антитела; ингибитор активатора плазминогена

INTRODUCTION

The new coronavirus infection (COVID-19) is an acute infectious disease caused by the SARS-CoV-2 strain of coronavirus. Although coronaviruses basically lack neurotropicity, they are capable of affecting the nervous system and disrupting its functions. One of the action mechanisms is respiratory hypoxia accompanying severe coronavirus pneumonia [1]. Another damage mechanism is the cytokine storm, which causes an increase in the pro-inflammatory cytokine level and activation of T-lymphocytes, macrophages, and endothelial cells. Vascular wall permeability increases, the complement system is activated, and blood coagulation properties increase [2]. COVID-19 was shown to develop overexpression of plasminogen activator inhibitor-1 (PAI-1) and thrombin-activated fibrinolysis inhibitor, thus leading to suppression of fibrinolysis and an even greater tendency to hypercoagulation [3].

The role of antiphospholipid antibodies (antibodies to cardiolipin and to β2–glycoprotein) in the pathogenesis of hemostasis system activation was described in previous research. These antibodies activate endothelial cells, monocytes, neutrophils, and platelets, resulting in the transformation of the anticoagulant surface of the endothelium into a procoagulant form [4]. The literature also describes the relationship between the formation of antiphospholipid antibodies as a result of infection and the development of ischemic stroke [5]. According to observations, endotheliopathy is observed in most patients. Markers of endothelial condition, inflammation, and coagulation such as IL-6, TNF-α, von Willebrand Factor (VWF), tissue factor, tissue factor inhibitor, D-dimer, thrombin-antithrombin complex, platelet factor P4, thromboglobulin, P-selectin, and platelet adhesion are significantly increased in mild to moderate COVID-19 [6].

Endothelial wall damage and hemostasis system activation caused by the SARS-COV-2 virus may be the cause of acute vascular events, such as hemorrhagic and ischemic stroke. Moreover, the probability of their development increases in patients with an increased risk of vascular disorders of the brain with upon the onset of the new coronavirus infection [7]. According to the TARGET-VIP hospital registry (Moscow), the incidence of acute cerebrovascular accident (ACVA) in the setting of the coronavirus infection was 0.8%, compared to 2.4% reported by foreign authors [8, 9]. The role of COVID-19 as a risk factor for ischemic brain damage was confirmed by data from the Regional Vascular Center (Botkin Hospital, Moscow). Thus, the number of ischemic stroke cases increased by 2.2–6.1% during the pandemic, while the proportion of hemorrhagic strokes and transient ischemic attacks decreased [10].

Thus, the severity of endothelial destruction and the accompanying activation of the hemostasis system towards hypercoagulation in patients with the new coronavirus infection may be correlated with the development of acute cerebrovascular accident. A number of laboratory markers characterizing the state of the endothelium and the hemostatic system in ischemic stroke have been studied. Thus, an extended meta-analysis showed that an increase in the inhibitor of plasminogen activator type 1 (PAI-1), which regulates the intensity of fibrinolysis in plasma, is associated with death, myocardial infarction, or acute cerebrovascular accident [11]. At the same time, it remains unclear whether PAI-1 is just a risk marker or an etiological cause of a vascular event [12]. The α2-antiplasmin acute phase protein, which inhibits the main enzyme of fibrinolysis plasmin, increases damage to the brain and the blood–brain barrier during acute ischemia by activating matrix metalloproteinases. Experiments showed that therapeutic inactivation of α2-antiplasmin reduces microvascular thrombosis, ischemic damage, and cerebral edema [13]. The Inter-Cellular Adhesion Molecule Type 1 (ICAM-1) expressed on the endothelium is significantly increased in stroke patients, reflecting damage to the blood–brain barrier [11]. The endothelial glycoprotein, von Willebrand factor, is involved in platelet adhesion at the vascular wall damage site. It was shown that elevated levels of von Willebrand factor are associated with the development of primary or recurrent stroke, as well as with fatal stroke [14, 15]. Homocysteine, a metabolite of the methionine and cysteine amino acids, is a marker of vascular wall damage and activation of the hemostatic system. This is one of the most studied biomarkers in stroke: hyperhomocysteinemia is associated with the risk of developing cardiovascular diseases, being a predictor of the severity of neurological symptoms in stroke and poor functional recovery [16–18]. Antibodies to β2-glycoprotein and cardiolipin are autoantibodies to phospholipids, which are markers of antiphospholipid syndrome, which is based

on vasculopathy associated with non-inflammatory and/or thrombotic vascular damage. In old age, the prevalence of positive antiphospholipid antibodies can reach 68% [19]. It was shown that these antibodies can participate in the pathogenesis of ischemic stroke, with their levels being positively correlated with the risk of stroke [20, 21].

In this work, we study the role of markers of hemostasis system activation and vascular wall damage in the development of acute cerebrovascular accident in patients with the new coronavirus infection.

MATERIALS AND METHODS

A total of 78 patients participated in the study, including 35 women and 43 men. The patients were divided into two groups: the study group included 38 patients with the new coronavirus infection and ACVA who were admitted to the Federal Center of Brain Research and Neurotechnologies and the Mukhin Hospital in Moscow, of whom four patients developed hemorrhagic stroke (HS) during hospitalization and 34 developed ischemic stroke (IS). Thus, the group of patients with ACVA was divided into two subgroups: patients with IS and patients with HS. The comparison group comprised 40 patients with the new coronavirus infection without ACVA, who were admitted to the Federal Center of Brain Research and Neurotechnologies.

Group 1 (n = 38) — patients with the new coronavirus infection + ACVA;

Group 1.1 (n = 4) — patients with the new coronavirus infection+ ACVA (HS);

Group 1.2 (n = 34) — patients with the new coronavirus infection+ ACVA (IS);

Group 2 (n = 40) — patients with the new coronavirus infection.

The average age of patients with HI was 70.9 ± 8.0 years; patients with IS — 72.0 ± 7.3 years; the comparison group — 58.2 ± 16.7 years. The criteria for inclusion of patients in the study were age over 18 years, detection of SARS-CoV2 RNA by PCR, clinical signs of pneumonia (body temperature above 38.5°C, respiratory rate above 22 per min, shortness of breath during physical exertion, saturation less than 95% in the air), pneumonia signs in the chest organs confirmed by computed tomography. All participants signed a voluntary informed consent to participate in the study.

Arterial hypertension (64%), chronic heart failure (39%), chronic kidney disease (25%), and diabetes mellitus (21%) prevailed among the concomitant diseases in the general sample. The stroke severity at admission according to the National Institutes of Health Stroke Scale (NIHSS) in the study group was 10.4 ± 5.7 points (13.8 ± 7.6 points in patients with HS; 9.9 ± 5.3 points in patients with IS). The distribution of pathogenetic variants of ischemic stroke was as follows: atherothrombotic — 5 patients (14.7%), cardioembolic — 11 patients (32.4%), lacunar — 2 patients (5.9%), unspecified — 16 patients (47.1%). At the beginning of hospitalization, in 52.6% of patients, the lung damage severity was established at the CT-1 level (77.5% in the comparison group; 29.4% in patients with IS; there were no patients with HS and CT-1). At the same time, grade 1 respiratory failure was detected in 70.5% of patients: in 85.0% of patients

from the comparison group; in 58.8% of patients with IS, in 25.0% of patients with HS. The average hospital stay of patients in the study group was 11.0 ± 4.7 days. Hospital mortality was 5.2% (2 patients), caused by ischemic stroke; the immediate cause of death was cerebral edema. Upon discharge, the median on the Rehabilitation Routing Scale (RRS) was 4.0 (Q 3.0–4.3) points, on the modified Rankin scale — 3.0 (Q 3.0–3.3) points. The neurological symptoms severity according to NIHSS was 8.9 ± 7.2 points. The groups were representative in terms of concomitant diseases and severity of coronavirus infection.

Taking into account their biological role, antibodies to β2-glycoprotein, antibodies to cardiolipin, plasminogen activator inhibitor type 1 (PAI-1), α2-antiplasmin, intercellular adhesion molecule type 1 (ICAM-1), von Willebrand factor, homocysteine were selected for the study.

Venous blood in a volume of 5 mL was collected during the first hospital day in tubes with coagulation activator and separation gel (VACUTEST KIMA, Italy). About 30 min after blood collection, the tubes were centrifuged for 15 min at 1500 g on an ELMI CM-6MT centrifuge; the blood serum was aliquoted and frozen at –70 °C. Further, total antibodies to β2-glycoprotein (Euroimmun, Germany), total antibodies to cardiolipin (Euroimmun, Germany), type 1 plasminogen activator inhibitor (PAI-1) (ABclonal, China), a2-antiplasmin (ABclonal, China) were determined by enzyme immunoassay (ELISA) in serum; intercellular adhesion molecule type 1 (ICAM-1) (ABclonal, China), von Willebrand factor (VWF) (ABclonal, China), homocysteine (ABclonal, China) were determined on an Infinite F50 enzyme microplate automatic immunoassay analyzer using a Shellab GI2-2 laboratory incubator, a Titramax 101 platform vibrating shaker and a HydroFlex microplate flushing analyzer.

For each set of the reagents, a calibration curve was constructed based on measuring the optical density of standard solutions. The conversion of optical density into concentration in serum samples was carried out using the software installed in the Infinite F50 analyzer, taking the calibration data into account.

Statistical data processing was carried out using the SPSS 25.0, Microsoft Excel 2016 software packages. Descriptive statistics of continuous quantitative data after analysis of the normality of distribution are presented as the mean (M) and standard deviation for a normal distribution, or as the median (Md) and values of 25% of the lower and 75% of the upper quartiles using the sign Q [25–75%] for an abnormal distribution. The normal distribution was assumed to have a criterion for distinguishing the Kolmogorov–Smirnov type from a theoretically normal distribution of more than 0.05. Analytical statistics were performed using the Student's t-test for quantitative data with a normal distribution or the Wilcoxon, Mann–Whitney rank/sign sum test for quantitative data with a distribution other than normal. The probability value of $p < 0.05$ demonstrated statistical significance.

RESULTS AND DISCUSSION

The assessment of distribution normality of laboratory marker values showed that most of the markers did not have a normal distribution across a set of factors. As a result,

nonparametric analysis methods were used. Limitations on the choice of statistical methods were also associated with the limited number of patients in the HS subgroup. It should be noted that the objectives of the study did not include calculation of reference intervals, which reagent manufacturers propose to calculate for each laboratory independently through their own sampling. The results of laboratory measurements are shown in the Table.

No statistically significant differences were observed in the level of antiphospholipid antibodies between the groups. At the same time, antibodies to β2-glycoprotein were completely absent (not detected by ELISA) in 16 patients (42%) and antibodies to cardiolipin in 34 patients (89%). In the comparison group, 12 (30%) patients had no antibodies to β2-glycoprotein and 32 (80%) patients had no antibodies to cardiolipin. In 10 (26%) patients from the ACVA group and in 15 (38%) patients from the comparison group, the concentration of antibodies to β2-glycoprotein was higher than the reference range specified in the kit instructions (10 RU/mL), i.e., increased concentrations were more often observed in the comparison group. Elevated concentrations of antibodies to cardiolipin relative to the reference range (more than 10 RU/mL) were much less common: in 1 (2.6%) patient from the ACVA group and in 1 (2.5%) patient from the comparison group. β2-glycoprotein is a serum cofactor, having anticoagulant activity in vivo. Antibodies to β2-glycoprotein, in addition to directly suppressing activity, induce the expression of E-selectin on the membrane of endothelial cells and the secretion of proinflammatory cytokines and prostaglandin E2, which can lead to endothelial damage and activation of the hemostasis system towards hypercoagulation.[1] A single measured increase in the concentration of antiphospholipid antibodies in some patients does not yet indicate the development of antiphospholipid syndrome, although supporting the data of other authors

that the appearance of antiphospholipid antibodies is associated with the viral infection caused by SARS-CoV-2 [22].

According to the PAI-1 level, statistically significant differences were found between the group with ACVA and the comparison group ($p < 0.001$), as well as between the group with IS and the comparison group ($p < 0.001$). In the comparison group, the concentration of PAI-1 was 1.6 times higher than in patients with ACVA. The lower levels of PAI-1 in the ACVA group are likely to be due to the activation of fibrinolysis processes, which are triggered after a thrombotic vascular event, and suppression of blood antifibrinolytic activity.

No statistically significant differences were observed between the groups in terms of α2-antiplasmin, ICAM-1, and von Willebrand factor. At the same time, attention should be drawn to the tendency towards a higher level of the ICAM-1 endothelial molecule in patients with ACVA, which may be caused by damage to the blood–brain barrier due to stroke.

The results of measuring homocysteine in the studied groups turned out to be unexpected. Since the units of measurement from the kit instructions — ng/mL — were used to determine the concentration of homocysteine, and the kit itself was intended strictly for scientific use, we did not compare the level of homocysteine in the studied groups with the generally accepted threshold level[2] of 11.4 μmol/L. The calculation of our own reference interval was not part of the objectives of our study. Statistically significant differences were found between the group with ACVA and the comparison group ($p < 0.001$), the group with IS and the comparison group ($p < 0.001$), as well as between the group with HS and the comparison group ($p < 0.05$). The concentration in the comparison group was 1.8 times higher than in the group with ACVA, although the concentration of homocysteine tends to increase with age

Table. Laboratory parameters measured in patients of the main group and the comparison group

Laboratory parameter	Patients with Acute Cerebrovascular Accident (ACVA)			Comparison group $n = 40$
	Total patients of the ACVA group (HS+IS) $n = 38$	Patients with IS $n = 34$	Patients with HS $n = 4$	
Antibodies to β2-glycoprotein, RU/mL	5.0 [0.0–11.0]	6.8 [0.0–11.5]	0.0 [0.0–9.0]	7.2 [0.0–14.5]
Antibodies to cardiolipin, IU/mL	0.0 [0.0–0.0]	0.0 [0.0–0.0]	0.0 [0.0–0.0]	0.0 [0.0–0.0]
PAI-1, pg/mL	332* [157–456]	318* [152–456]	362 [321–528]	543 [354–773]
α2-antiplasmin, pg/mL	43 [19–90]	49 [19–90]	26 [21–44]	40 [27–81]
ICAM-1, pg/mL	45 [9–45]	37 [9–45]	45 [15–45]	15 [5–45]
von Willebrand factor, ng/mL	91 [110–138]	114 [91–140]	95 [87–122]	116 [77–131]
Homocysteine, ng/mL	22* [16–31]	22* [16–32]	24• [16–31]	39 [33–45]

Table prepared by the authors using their own data

Note: Data are presented as the median (Md) values of the lower and upper quartiles of Q [25%–75%]; statistical significance of differences with the comparison group: * $p < 0.001$; • $p < 0.05$.

---

1. Kudrja AA. Determination of antibodies to cardiolipin and β2-glycoprotein-I. Gomel: *GU RNPC RMiJeCh*; 2020 (In Russ.).
2. Tietz clinical guide to laboratory tests. Moscow: Labora; 2013.

due to a decrease in renal excretory function, and the age of patients with ACVA was higher than in the comparison group. We expected to obtain the opposite results, taking into account the damaging effect of homocysteine on endothelial cells, its suppressive effect on the natural anti-coagulant antithrombin III, direct neurotoxic effect on brain neurons [23] and, consequently, the creation of prerequisites for the development of vascular events. However, the results obtained forced us to take a fresh look at the pathogenesis of ACVA in coronavirus infection.

Thus, the results obtained confirm the data that the new coronavirus infection can induce the formation of antiphospholipid autoantibodies, which were detected in more than half of the studied patients. Such patients should be further monitored and examined to exclude the development of antiphospholipid syndrome and thrombotic complications. Suppression of the antifibrinolytic link in patients with ACVA, manifested by a decrease in the concentration of PAI-1, may be a consequence of a compensatory increase in fibrinolysis in response to a thrombotic event that led to a stroke. Higher levels of homocysteine in patients with

coronavirus infection without ACVA probably indicate an initially higher protective potential of the endothelial wall and the hemostatic system, which reduces the risk of developing ACVA in such patients. However, this assumption requires further elucidation.

CONCLUSION

The development of ACVA in patients with lower concentrations of homocysteine and PAI-1 may probably be explained by weaker compensatory mechanisms aimed at repairing the vascular wall and harmonizing the interaction of hemostasis system links, which ultimately leads to damage to the vascular wall. A more accurate understanding of the molecular mechanisms of stroke in coronavirus infection will be possible provided an extended panel of laboratory biomarkers and an increased patient cohort. Studying the mechanism of formation of antiphospholipid antibodies in the setting of the new coronavirus infection is another undoubtedly urgent task in the light of preventing thrombotic complications.

References

1. Dinkin M, Gao V, Kahan J et al. COVID-19 presenting with ophthalmoparesis from cranial nerve palsy. *Neurology.* 2020;95(5):221–3.
https://doi.org/10.1212/WNL.0000000000009700

2. Mehta P, McAuley DF, Brown M et al. COVID-19: consider cytokine storm syndromes and immunosuppression. *Lancet.* 2020;395(10229):1033–4.
https://doi.org/10.1016/S0140-6736(20)30628-0

3. Zuo Y, Warnock M, Harbaugh A et al. Plasma tissue plasminogen activator and plasminogen activator inhibitor-1 in hospitalized COVID-19 patients. *Sci Rep.* 2021;11(1):1580.
https://doi.org/10.1038/s41598-020-80010-z

4. Pavoni V, Gianesello L, Horton A. Antiphospholipid antibodies in critically ill COVID-19 patients with thromboembolism: cause of disease or epiphenomenon? *J Thromb Thrombolysis.* 2021;52(2):542–52.
https://doi.org/10.1007/s11239-021-02470-y

5. Zhang Y, Xiao M, Zhang S et al. Coagulopathy and Antiphospholipid Antibodies in Patients with Covid-19. *N Engl J Med.* 2020;382(17):e38.
https://doi.org/10.1056/NEJMc2007575

6. Golubeva MG. Role of P-Selectin in the Development of Hemostasis Disorders in COVID-19. *Biology Bulletin Reviews.* 2022;142(2):175–83 (In Russ.).
https://doi.org/10.31857/S004213242202003X

7. Scherbak SG, Golota AS, Kamilova TA et al. Neurological manifestations in patients with new coronavirus infection COVID-19. *Physical and Rehabilitation Medicine, Medical Rehabilitation.* 2022;4(3):154–180 (In Russ.).
https://doi.org/10.36425/rehab109952

8. Lukyanov MM, Andreenko EYu, Martsevich SYu et al. Two-year outcomes in patients after hospitalization for COVID-19: data from the TARGET-VIP registry. *Cardiovascular Therapy and Prevention.* 2023;22(10):3757 (In Russ.).
https://doi.org/10.15829/1728-8800-2023-3757

9. Wong-Chew RM, Rodríguez Cabrera EX, Rodríguez Valdez CA et al. Symptom cluster analysis of long COVID-19 in patients discharged from the temporary COVID-19 Hospital in Mexico City. *Ther Adv Infect Dis*. 2022;9:20499361211069264.
https://doi.org/10.1177/20499361211069264

10. Komarova AG, Ploskireva AA, Litvinenko AS et al. Evolution of the structure of cerebrovascular accidents with COVID-19. *Pharmacology & Pharmacotherapy*. 2022;(5):74–8 (In Russ.).
https://doi.org/10.46393/27132129_2022_5_74

11. Fang C, Lou B, Zhou J, et al. Blood biomarkers in ischemic stroke: Role of biomarkers in differentiation of clinical phenotype. *European Journal of Inflammation*. 2018;16:1–10.
https://doi.org/10.1177/2058739218780058

12. Jung RG, Motazedian P, Ramirez FD, et al. Association between plasminogen activator inhibitor-1 and cardiovascular events: a systematic review and meta-analysis. *Thromb J*. 2018;16:12.
https://doi.org/10.1186/s12959-018-0166-4

13. Reed GL, Houng AK, Singh S, Wang D. α2-Antiplasmin: New Insights and Opportunities for Ischemic Stroke. *Semin Thromb Hemost*. 2017;43(2):191–9.
https://doi.org/10.1055/s-0036-1585077

14. Buchtele N, Schwameis M, Gilbert JC, et al. Targeting von Willebrand Factor in Ischaemic Stroke: Focus on Clinical Evidence. *Thromb Haemost*. 2018;118(6):959–78.
https://doi.org/10.1055/s-0038-1648251

15. Kawano T, Gon Y, Sakaguchi M, et al. Von Willebrand Factor Antigen Levels Predict Poor Outcomes in Patients With Stroke and Cancer: Findings From the Multicenter, Prospective, Observational SCAN Study. *J Am Heart Assoc*. 2024;13(3):e032284.
https://doi.org/10.1161/JAHA.123.032284

16. Lu SS, Xie J, Su CQ, et al. Plasma homocysteine levels and intracranial plaque characteristics: association and clinical relevance in ischemic stroke. *BMC Neurol*. 2018;18(1):200.
https://doi.org/10.1186/s12883-018-1203-4

17. Fan YL, Zhan R, Dong YF, et al. Significant interaction of hypertension and homocysteine on neurological severity in first-ever ischemic stroke patients. *J Am Soc Hypertens*. 2018;12(7):534–41.
https://doi.org/10.1016/j.jash.2018.03.011

18. Markišić M, Pavlović AM, Pavlović DM. The Impact of Homocysteine, Vitamin B12, and Vitamin D Levels on Functional Outcome after First-Ever Ischaemic Stroke. *Biomed Res Int*. 2017;2017:5489057.
https://doi.org/10.1155/2017/5489057

19. Bidenko MA, Kaljagin AN, Novohatko OI. Antiphospholipid syndrome as a cause of stroke. *Siberian Scientific Medical Journal*. 2007;6:87–90 (In Russ.).

20. Cojocaru IM, Cojocaru M, Muşuroi C, Botezat M. Study of anti-cardiolipin and anti-β2-glycoprotein I antibodies in patients with ischemic stroke. *Rom J Intern Med*. 2003;41(2):189–204. PMID: 15526503

21. Dong S, Pei B, Xie W, et al. Anticardiolipin antibody and

anti-β2 glycoprotein I antibody are potential risk markers of ischaemic stroke in Chinese adults. *Rheumatology (Oxford)*. 2020;59(8):1834–41.
https://doi.org/10.1093/rheumatology/kez551

22. Polushin YuS, Gavrilova EG, Shlyk IV, Lapin SV, Tkachenko OYu. Catastrophic antiphospholipid COVID-19 syndrome. *Messenger*

of anesthesiology and resuscitation. 2021;18(1):17–26 (In Russ.). https://doi.org/10.21292/2078-5658-2021-18-1-17-26

23. Zobova DA, Kozlov SA. The role of homocysteine in pathogenesis of certain diseases. Izvestija vuzov. Povolzhskij region. *Medical Sciences*. 2016;3(39):132–44 (In Russ.).
https://doi.org/10.21685/2072-3032-2016-3-15

AUTHORS

Olga V. Lyang, Dr. Sci. (Med.)
https://orcid.org/0000-0002-1023-5490
lyang@fccps.ru

Mikhail A. Soldatov
https://orcid.org/0000-0002-5294-5706
soldatov1477@gmail.com

Leonid V. Klimov, Cand. Sci. (Med.)
https://orcid.org/0000-0003-1314-3388
dr.klimov@mail.ru

Tatiana V. Kiseleva
https://orcid.org/0000-0003-4913-351X
tatiana-kis17@yandex.ru

Nataliya A. Marskaya
https://orcid.org/0000-0002-0789-4823
marskaya@fccps.ru

Nikolay A. Shamalov, Dr. Sci. (Med.)
https://orcid.org/0000-0001-6250-0762
shamalov@fccps.ru

SCHIZOPHRENIA AND NEUROINFLAMMATION: PATHOGENETIC AND THERAPEUTIC ASPECTS

Dmitry A. Chugunov[1,2], Andrey A. Shmilovich[2], Daria V. Nikolaeva[1,2], Tamara V. Yashina[1,2], Mariya R. Larina[2], Vladimir S. Rogovsky[1,2], Anastasia A. Sviridova[1✉]

[1] Federal Center of Brain Research and Neurotechnologies of the Federal Medical and Biological Agency, Moscow, Russia

[2] Pirogov Russian National Research Medical University, Moscow, Russia

Introduction. Schizophrenia is a complex mental disorder with heterogeneous symptoms, including psychotic, negative, cognitive, affective, and psychomotor symptoms. Although the pathogenesis of schizophrenia is mainly associated with neurotransmitter imbalance, recent studies have suggested the importance of neuroinflammation in the pathogenesis of this disease.

Objective. To study the involvement of neuroinflammation in the pathogenesis of schizophrenia and a prognostic assessment of the potential anti-inflammatory effect of antipsychotic medications.

Discussion. Current data indicate a significant role of neuroinflammation in the development and course of schizophrenia. At the initial stages of its development, the number of lymphocytes and the level of some proinflammatory cytokines (IL-1, IL-6, TNF-α, IL-1β) increase, which can be decreased by antipsychotic therapy. Studies involving experimental models of maternal immune activation (MIA) and data obtained by immunohistochemical and PET studies confirm an abnormal activation of microglia, indicating the involvement of innate immune cells. Adaptive immune response cells can also play a significant role in the development of neuroinflammation in schizophrenia. Thus, an increased level of Th17 cells and an increase in the production of proinflammatory cytokines, correlating with the disease severity, were revealed. The role of neurotransmitters in modulating the immune-inflammatory response is discussed. Available data suggest that the participation of dopamine in the schizophrenia pathogenesis can be mediated by its immunomodulatory effect. The role of neuroinflammation in schizophrenia is also indicated by the clinical effectiveness of anti-inflammatory treatment in this disease. On the other hand, the immunomodulatory effect of antipsychotics has been established, which, at least in part, may mediate their clinical effectiveness in schizophrenia.

Conclusions. Given the importance of neuroinflammation in the schizophrenia pathogenesis, further studies into both the anti-inflammatory properties of antipsychotics and the effects of anti-inflammatory drugs in schizophrenia are promising in order to further optimize the treatment of this disease.

Keywords: schizophrenia; inflammation; neuroimmune interactions; antipsychotics; neuroleptics; dopamine

УДК 616.89

ШИЗОФРЕНИЯ И НЕЙРОВОСПАЛЕНИЕ: ПАТОГЕНЕТИЧЕСКИЕ И ТЕРАПЕВТИЧЕСКИЕ АСПЕКТЫ

Д.А. Чугунов[1,2], А.А. Шмилович[2], Д.В. Николаева[1,2], Т.В. Яшина[1,2], М.Р. Ларина[2], В.С. Роговский[1,2], А.А. Свиридова[1✉]

[1] Федеральный центр мозга и нейротехнологий Федерального медико-биологического агентства, Москва, Россия

[2] Российский национальный исследовательский медицинский университет имени Н.И. Пирогова, Москва, Россия

Введение. Шизофрения — это сложное психическое расстройство с гетерогенной симптоматикой, включающей в себя психотические, негативные, когнитивные, аффективные и психомоторные симптомы. Несмотря на то что патогенез шизофрении главным образом связывают с дисбалансом нейротрансмиттеров, исследования последних лет указывают на большое значение нейровоспаления в патогенезе этого заболевания.

Цель. Изучение роли нейровоспаления в патогенезе шизофрении с оценкой вовлечения клеток врожденного, адаптивного иммунного ответа и функционирования гематоэнцефалического барьера (ГЭБ) в возникновении заболевания, а также прогностическая оценка противовоспалительного эффекта антипсихотических средств при шизофрении.

Обсуждение. Современные данные свидетельствуют о значительной роли нейровоспаления в развитии и течении шизофрении. На начальных этапах заболевания повышается количество лимфоцитов, а также уровень нескольких провоспалительных цитокинов (ИЛ-1, ИЛ-6, ФНО-α, ИЛ-1β), которые могут снижаться на фоне антипсихотической терапии. Исследования на экспериментальной модели материнской иммунной активации (МИА) и данные иммуногистохимических и ПЭТ-исследований подтверждают аномальную активацию микроглии, что указывает на вовлечение клеток врожденного иммунитета. Клетки адаптивного иммунного ответа также могут играть существенную роль в развитии нейровоспаления при шизофрении (выявлено повышенное содержание Th17-клеток и увеличение продукции провоспалительных цитокинов, коррелирующих с тяжестью заболевания). Обсуждается роль нейромедиаторов в модуляции иммуновоспалительного ответа. Существующие данные позволяют предположить, что участие дофамина в патогенезе шизофрении может быть опосредовано его иммуномодулирующим эффектом. На роль нейровоспаления при шизофрении также указывает клиническая эффективность применения противовоспалительного лечения при данном заболевании. С другой стороны, установлен иммуномодулирующий эффект антипсихотиков, который, по крайней мере частично, может опосредовать их клиническую эффективность при шизофрении.

Выводы. Ввиду значимости нейровоспаления в патогенезе шизофрении перспективны дальнейшие исследования как противовоспалительных свойств антипсихотиков, так и клинической эффективности противовоспалительных препаратов при шизофрении с целью дальнейшей рационализации терапии данного заболевания.

Ключевые слова: шизофрения; воспаление; нейроиммунные взаимодействия; антипсихотики; нейролептики; дофамин

INTRODUCTION

Schizophrenia is a progressive mental illness with heterogeneous symptoms, including productive, negative, affective, cognitive, and psychomotor symptoms. This disease has a continuous or paroxysmal course, leading to specific personality changes in the form of mental disintegration, autism, thinking disorders, emotional-volitional and cognitive decline [1].

Schizophrenia is the most complex and socially significant problem in modern psychiatry, which is determined by its widespread prevalence, constant tendency to disease progression, and, in the absence of adequate treatment, severe disability of patients, mainly young people who are active in social and labor activities [2]. According to the World Health Organization, in the 15–44 age group, schizophrenia ranks eights among the leading causes of disability worldwide. At the same time, patients with schizophrenia lose an average of 15 years of their life expectancy, mainly due to suicide (suicide risk from 5 to 10%), as well as due to the presence of concomitant diseases, including substance abuse with a prevalence rate of up to 41% [3]. In addition, disordered lifestyle, unhealthy diet, lack of physical activity, and side effects of antipsychotic therapy contribute to an increase in the incidence of metabolic syndrome, as well as cardiovascular and pulmonary diseases [4]. Among mental disorders, schizophrenia is the largest socioeconomic burden, accounting for about 54.5% of the total number of mental disorders, with this number having doubled in recent years [5]. Thus, the treatment of patients with schizophrenia is one of the most urgent tasks of practical psychiatry.

According to the classical understanding, the pathogenesis of schizophrenia is based on a disorder of the metabolism of biogenic amines, especially dopamine, whose receptors are a key target for drugs of pathogenetic therapy of the disease (antipsychotics). In particular, most antipsychotics used in the treatment of schizophrenia are predominantly antagonists of dopamine receptors of the D2 group (D2-, D3-, D4-receptors). However, despite the relief of a number of clinical symptoms, antipsychotic drugs are not capable of significantly slowing down the progression of the disease, which suggests additional pathogenetic mechanisms of schizophrenia [6].

Thus, recent studies have shown that along with impaired functioning of neurotransmitters, neuroinflammation can also be an essential factor in the schizophrenia pathogenesis [6, 7]. It has been shown that at the initial stages of schizophrenia, the number of lymphocytes and the level of certain pro-inflammatory cytokines increases: interleukin-1 (IL-1), IL-6, tumor necrosis factor α (TNF-α) and others, which may decrease against the background of antipsychotic therapy [8]. The higher incidence of autoimmune diseases of the central nervous system (CNS) in patients with schizophrenia also supports the involvement of neuroinflammation in the pathogenesis of schizophrenia [9, 10]. Common mechanisms for these diseases include activation of microglia, increased production of pro-inflammatory cytokines, and disruption of the blood–brain barrier (BBB) [10].

In this article, we study the role of neuroinflammation in the schizophrenia pathogenesis with an assessment of the involvement of cells of the innate, adaptive immune response and functioning of the BBB in the disease development, as well as a prognostic assessment of the anti-inflammatory effect of antipsychotics in schizophrenia.

MATERIALS AND METHODS

The search for relevant scientific publications was conducted in electronic bibliographic databases in both the Russian (eLibrary, CyberLeninka) and English (Web of Science, Scopus, PubMed) languages. The search queries included the words: schizophrenia, inflammation, neuroimmune interactions, antipsychotics, antipsychotics, dopamine. The search depth was 10 years. The inclusion criteria were the availability of data on the results of cohort studies, randomized controlled trials, and preclinical studies.

RESULTS AND DISCUSSION

Role of innate immune response in the development of neuroinflammation in schizophrenia

For a long time, the development of an immune response in the CNS was considered unlikely, which was associated with the isolation of the CNS from the immune system through the BBB, as well as the lack of lymphatic drainage and other mechanisms of natural immunological tolerance (the "immunoprivileged" status of the CNS) [11]. However, recent knowledge indicates the presence of resident immune cells in the CNS, as well as the ways in which the CNS communicates with the deep cervical lymph nodes through the lymph vessels of the dura mater and the lymphatic system. In addition, the ability of cells of both the innate and adaptive immune responses to migrate to the CNS from the periphery has been established. Therefore, research into the role of neuroinflammation in

the pathogenesis of various diseases of the CNS is increasingly attracting attention [12].

Among the cells of the innate immune response in the context of neuroinflammation, microglia — resident macrophages of the CNS — attract the most attention. It has been shown that microglia are able to participate both in the development of neuroinflammation by producing pro-inflammatory cytokines and inducing Th17 and Th1 immune responses (M1 microglia), and maintaining immunological tolerance by producing anti-inflammatory factors and inducing regulatory T cells (Treg) (M2 microglia) [6].

Microglial changes in schizophrenia have been described mainly on experimental models of schizophrenia in animals, MIA, which are reproduced by injecting pregnant rodents with agonists of the innate immune response receptors (in particular, toll-like receptors — TLR-3 and TLR-4). Adult offspring of such rodents develop neuroanatomical, neurochemical, and behavioral changes, some of which correspond to those in schizophrenia (hyperactivity of the dopaminergic system, enlargement of the ventricles of the brain, behavioral and cognitive impairments) [13,14].

In particular, an increase in mobility, density, and the ability of microglia to produce cytokines in MIA induced by the TLR-4 lipopolysaccharide (LPS) agonist has been shown [13]. In addition, the pro-inflammatory functions of microglia in MIA are increased when MIA is induced by the administration of a TLR-3 agonist (polyinosinic:polycytidylic (PolyI:C) [14]. The results of research studies obtained thus far indicate the pro-inflammatory profile of microglia in adolescence with MIA.

In addition, the involvement of microglia in the pathogenesis of schizophrenia is evidenced by the association between suppression of its functions and a decrease in the severity of symptoms of the disease in the setting of anti-inflammatory therapy, in particular minocycline, which has a modulating effect on microglia [15].

Data on abnormal microglial activation, shown in several postmortem immunohistochemical studies and *in vivo* positron emission tomography (PET) studies in patients with schizophrenia, are contradictory [16, 17]. Additional ambiguity during postmortem immunohistochemical examination may be caused by the actual effect of long-term antipsychotic therapy on microglial activation, which is confirmed by PET data [18,19]. At the same time, PET studies in people with an ultra-high risk of developing schizophrenia or in patients with schizophrenia who have not received pathogenetic therapy still remain ambiguous. Thus, according to some studies, a decrease or absence of an increase in the binding of the translocator protein (TSPO, a marker of microglial activation in vivo) has been shown, which indicates a decrease in microglial activation [20, 21]. However, some studies have indicated, on the contrary, an increase in the binding of this ligand throughout the gray matter [22].

The first psychotic episode of schizophrenia is associated with a decrease in the concentration of IL-10 and IL-4 anti-inflammatory cytokines; conversely, the concentration of pro-inflammatory cytokines such as IL-6 and TNF-α, increases [23, 24]. According to Halstead et al., the concentrations of IL-1β, IL-1 receptor antagonist (IL-1RA), soluble IL-2 receptor (sIL-2R), IL-6, IL-8, IL-10, TNF-α, and C-reactive protein increased in peripheral blood (plasma/serum) of schizophrenia patients compared to the control group. The levels of IL-2 and interferon-γ (IFN-γ) were significantly higher in the acute episode of schizophrenia, whereas, in the chronic form, the levels of IL-4, IL-12, and IFN-γ were significantly reduced [25]. A meta-analysis of studies into the cytokine level in cerebrospinal fluid showed similar data, i.e., an increase in IL-1β, IL-6, and IL-8 in patients with schizophrenia [26].

In addition, increased production of IL-8 and IL-1β by LPS-stimulated peripheral blood mononuclear cells (PBMCs) in patients with schizophrenia was observed, confirming the role of innate immune response cells in the pathogenesis of schizophrenia [27]. These data are also consistent with the assessment of mRNA expression levels of proinflammatory cytokines (IL-6, IL-8, and TNF-α) in the PBMCs of patients with schizophrenia [28]. In addition, it was found that the blood serum of patients with schizophrenia who did not receive pathogenetic therapy is able to activate microglia in vitro [29].

The potential role of perivascular macrophages in the pathogenesis of schizophrenia has been reported. In particular, immunohistochemical staining of the frontal lobe of the brain of patients with schizophrenia revealed an increased level of CD163+-macrophages [30, 31].

In addition, patients with schizophrenia have an increased number of M1- and M2-monocytes circulating in the peripheral blood, which have pro- and anti-inflammatory functions, respectively. It is important that, along with disease progression, the ratio of such functional types of monocytes may change. Thus, the predominance of M1 monocytes at an early stage of the disease is replaced by the predominance of M2 monocytes at a later stage [32]. The involvement of proinflammatory M1 monocytes in the pathogenesis of schizophrenia was confirmed by data from other studies [33]. Moreover, an increase in the level of soluble CD14 (a marker of monocytes) in the blood of people who subsequently developed schizophrenia has been reported; this suggests activation of monocytes as an early predictor of the disease [34].

Along with the abovementioned, an increase in the production of IL-1β, IL-6, and TNF-α by stimulated monocytes of patients with schizophrenia was found in comparison with healthy donors *in vitro* [35, 36]. In addition, an increase in the level of chemokines (CL2, CCL4, CL22) necessary for the migration of monocytes, including through endothelial barriers, including the BBB, was found in the blood serum of patients with schizophrenia [37].

Role of the adaptive immune response in the development of neuroinflammation in schizophrenia

Recent studies have shown that along with the innate immune response, adaptive immune response cells can also play a significant role in the development of neuroinflammation in schizophrenia. It was found that during an acute episode of schizophrenia, the number of activated T cells in the central nervous system increases. The relationship between the risk of developing schizophrenia and the level of NK cells, T helper cells (CD4+ T cells), and B lymphocytes was also discussed [38].

Among the cells of the adaptive immune response, presumably involved in the pathogenesis of schizophrenia, type 17 T helper cells (Th17 cells) attract particular attention. Th17 cells differentiate from naive T cells or memory T cells with the participation of IL-6 cytokines, transforming growth factor-β (TRF-β), IL-1β, and IL-23. Th17 cells produce proinflammatory IL-17, IL-21, IL-22 cytokines, granulocytic and granulocyte-macrophage colony stimulating factors (G-CSF or GM-CSF). As a rule, the Th17-type immune response is of a pronounced inflammatory nature. The involvement of these cells in the pathogenesis of autoimmune and neuroinflammatory diseases was emphasized in [39]. The importance of Th17 cells in the development of neuroinflammation is mainly attributed to their ability to migrate to the CNS through the BBB. It was established that C-C chemokine receptor 6 (CCR6; CD196) is a distinctive receptor of Th17 cells, due to which Th17 cells are able to penetrate the BBB. The CCR6 chemokine receptor binds to the corresponding CCL20 ligand, which is expressed on endothelial barriers, including the BBB. An additional factor contributing to the migration of Th17 cells to the CNS may be the destabilizing effect of IL-17 (a key product of Th17 cells) on the BBB permeability. The role of neuroinflammation and Th17 cells in the pathogenesis of schizophrenia has become a focus of research relatively recently. It is believed that the immunopathogenesis of schizophrenia may be based on a chronic inflammatory process supported by the interaction of Th17 cells and microglia activated by IL-17 [39].

A number of studies have found that patients with schizophrenia have a higher level of circulating Th17 cells, as well as IL-17-producing CD4+ T cells, compared with the group of healthy donors [40]. Zheng et al. showed that the number of CD4+ T lymphocytes in the peripheral blood of patients with schizophrenia in the acute phase in the absence of pathogenetic therapy is higher than in the control group [41]. Activation of Th17 cells in patients with the first episode of schizophrenia was also reported. In addition, BBB disorders, brain infiltration by T cells, and activation of microglia were shown in such patients. During the first episode of schizophrenia, changes in the distribution of T-cell subpopulations in the cerebrospinal fluid (CSF) and higher T-lymphocyte densities in the hippocampus of patients were noted [42]. Having penetrated into the CNS, Th17 cells produce pro-inflammatory IL-17 and IL-22 cytokines, leading to neuroinflammation and neurodegeneration [39]. These data are also consistent with the observed increased concentrations of IL-17, IL-22, IL-6, and IL-23 in the blood plasma of patients with schizophrenia compared with the group of healthy donors [43]. Elevated plasma levels of IL-17, TRF-β, and IL-23 (cytokines necessary for Th17 cell differentiation) in patients with schizophrenia correlate with the severity of the disease, aggressive behavior, and apathy [44]. In addition, increased production of IL-6, IL-17A, TNF-α was found in the culture of peripheral blood mononuclear cells (PBMCs) of patients with schizophrenia compared with healthy donors [45].

The malfunction of T-regulatory cells (Treg) that have an anti-inflammatory effect and prevent autoimmune neuroinflammation was revealed. In the absence of pathogenetic treatment, patients with schizophrenia showed a decrease in the number of circulating Tregs, as well as a decrease in the expression of the *Foxp3* gene in these cells, which determines their suppressive properties [45].

Immunomodulatory effects of biogenic amines and antipsychotics in schizophrenia

The leading theory behind the pathogenesis of schizophrenia is associated with a metabolism disorder of biogenic amines, dopamine in particular, whose receptors are one of the key targets for pathogenetic therapy of this disease. Due to the growing interest in the role of neuroinflammation in the schizophrenia pathogenesis, dopamine involvement in neuroimmunomodulation is attracting particular attention. It has become common knowledge that biogenic amines, whose receptors are expressed by cells of both the nervous and immune systems, are direct mediators of neuroimmune interaction. Drugs acting on these receptors are considered as potential neuroimmunomodulators [46, 47].

Dopamine is among the most studied neurotransmitters with immune effects. It can be assumed that dopamine involvement in the schizophrenia pathogenesis, at least partially, may be mediated by its immunomodulatory effect. Dopamine receptors are known to be expressed by T and B lymphocytes, macrophages, monocytes, eosinophils, neutrophils, dendritic cells, NK cells, and microglia.

Research found that the percentage of CD8+ T cells expressing the D2-dopamine receptor (CD8+D2R+ T cells) is increased in patients with schizophrenia compared to that in healthy donors, while the percentage of CD4+D2R+ T cells, on the contrary, is reduced. In addition, a positive relationship was revealed between the scores on the BPRS (Brief Psychiatric Rating Scale) and PANSS (Positive and Negative Syndrome Scale) scales with the number of CD8+D2R+ T cells [48].

The effect of pathogenetic therapy drugs on immune cell functions in schizophrenia has also been shown. Thus, the patients with schizophrenia with a metabolic syndrome treated with second-generation antipsychotics (SGAs) (risperidone, olanzapine, quetiapine, and aripiprazole) demonstrated an increase in the levels of a number of pro-inflammatory cytokines, such as IFN-α2, IL-1α and IL-7, after six weeks of therapy. At the same time, IFN-γ, IL-1β, IL-12p40, IL-17A, IL-6, and TNF-α levels were reduced in patients without a metabolic syndrome [49].

A 28-day treatment of schizophrenia with aripiprazole revealed a significant decrease in the levels of C-reactive protein, insulin, IL-1β, IL-6, TNF-α, sTNF-R1, IL-12, IL-23, IL-1RA, TRF-β1, IL-4, IFN-γ, as well as a significant increase in IL-10 [50].

Of the individual drugs used as monotherapy in patients with the first episode of psychosis, risperidone was associated with statistically significant activation of 11 immune system genes, including cytokines and cytokine receptors, pattern-recognizing receptors (TLR-1, TLR-2, TLR-6) and molecules involved in apoptosis (FAS). It should be noted that risperidone exhibited strong immunomodulatory properties, affecting mainly the components of innate immunity in this category of patients, whereas the observed effects of quetiapine and olanzapine were only insignificant [51].

SGA risperidone has also been shown to reduce the level of the chemotactic cytokine monocyte chemotactic protein-1 (MCP-1), which may indicate some anti-inflammatory effect [52]. A detailed literature review of the immune effects of SGA provides evidence that most of these drugs cause leukopenia, lymphopenia, neutropenia, thrombocytopenia, and agranulocytosis, while reducing the levels of pro-inflammatory cytokines (TNF-α, IL-4, IL-6, IL-8, IL-10, IL-12, IL-17, IL-21, IL-23) and C-reactive protein in patients with schizophrenic spectrum disorders [53].

Regarding the possibility of chronic inflammation in patients with schizophrenia, it is worth noting that plasma levels of IL-6 and its soluble receptor (IL-6R) are significantly higher in patients with schizophrenia, although decreasing after treatment with antipsychotics [54]. All first-generation antipsychotics (FGAs), especially chlorpromazine and haloperidol, reduce IL-6 and IL-6R levels in patients with schizophrenia. A meta-analysis of the use of antipsychotics in the treatment of the first psychotic episode in schizophrenia showed antipsychotic therapy to be associated with a decrease in the concentration of proinflammatory IL-1β, IL-6, IFN-γ, TNF-α cytokines, as well as anti-inflammatory IL-4, IL-10 cytokines. On the other hand, the levels of pro-inflammatory IL-2 and IL-17 remain unchanged [55].

In patients with schizophrenia, all antipsychotics show a clear effect on Treg. Tregs are elevated in the blood of patients with schizophrenia who receive stable therapy. At the same time, a negative correlation was found between Treg cells and negative symptoms [56]. A decrease in the level of Th17 cells was shown in the group of patients with the first episode of schizophrenia after a four-week course of treatment with risperidone. In addition, a significant positive relationship was found between the rate of changes in the total PANSS score and those in the percentage of Th17 cells. However, it remains unclear whether these results were related to risperidone treatment or the natural course of the disease, since the study did not include a placebo control group [40]. However, in a later study, in 113 patients who had not previously taken antipsychotics (or had taken them for less than two weeks in their entire lives), and who had had symptoms of schizophrenia no more than five years prior to the study, risperidone therapy did not cause significant changes in IL-17 in the blood [57].

In another study, the effect of antipsychotic drugs on the expression of *STAT3* and *RORC* genes involved in the development and differentiation of Th17 cells was studied in 27 patients with schizophrenia who had not previously taken antipsychotics. In addition, the effect of antipsychotic drugs in plasma was evaluated at the level of five cytokines associated with Th17 cells. A significant decrease in *STAT3* gene expression and levels of IL-1β, IL-6, and IL-17A in blood plasma was found after three months of taking antipsychotic drugs [58].

Concerning the use of SGA in other diseases, in particular in multiple sclerosis, all studies agree on the effectiveness of SGA in reducing the severity of symptoms in animal models of multiple sclerosis and experimental autoimmune encephalomyelitis (EAE), delaying the disease onset at the same time as suppressing the production of various pro-inflammatory cytokines. Clozapine demonstrated a similar and even a more intense effect than risperidone, quetiapine, and olanzapine, significantly reducing CD4+ T cell infiltration and activation of myeloid cells, while increasing Treg levels. Clozapine also reduced the level of chemokines responsible for the migration of immune cells to the CNS and caused an increase in the level of dopamine receptors in the brains of mice with EAE [59].

At the same time, it has been reported that antipsychotics are capable of increasing IL-17 levels in in vitro experiments (in stimulated blood samples of healthy women) [60].

An experimental model of schizophrenia has shown an inhibitory effect of many FGAs and SGAs (risperidone, aripiprazole, quetiapine, ziprasidone) on IFN-γ-induced microglial activation in the mouse microglial cell line [61].

Feng et al. studied the possible correlation between the level of inflammatory markers in the blood of patients with schizophrenia and the level of their psychopathological symptoms. Markers of inflammation and psychopathological symptoms were studied in patients with schizophrenia after 3, 6, and 12 months of antipsychotic therapy. A significant decrease in monocyte levels, intercellular adhesion molecules, and adiponectin levels between baseline and 12 months of age was observed. A higher baseline level of IL-6 in the blood predicted a greater decrease in the overall PANSS score after 3 and 6 months, as well as the PANSS subscale for negative symptoms after three months. A higher baseline level of leptin in the blood predicted a greater decrease in the overall score and score on the subscale of negative symptoms of PANSS after six months. During the post-hoc analysis, the associations between baseline IL-6 levels and symptom reduction were strongest in patients receiving SGA ziprasidone or quetiapine. The results obtained provide additional evidence that measuring inflammatory markers in the blood may be important for the clinical management of patients with schizophrenia. In particular, these markers can be helpful in selecting antipsychotic therapy for a more personalized approach to the treatment of patients with schizophrenia [62].

It seems interesting that, due to the established role of neuroinflammation in the pathogenesis of schizophrenia in addition to the immunomodulatory effect of antipsychotics, the potential therapeutic effect of anti-inflammatory drugs in schizophrenia is also being discussed. Jeppesen et al. presented a meta-analysis, according to which the addition of anti-inflammatory drugs to basic antipsychotic therapy reduces the clinical manifestations of schizophrenia (according to the PANSS scale) [55].

CONCLUSION

The data accumulated to date indicate the important role of inflammation in the pathogenesis of schizophrenia. Moreover, the reviewed literature data allow us to assume that in some cases, chronic inflammation, both at the systemic and central nervous system levels, is not only a pathogenetic, but also an etiological factor in schizophrenia. In this regard, anti-inflammatory therapy can be an important component in the management of patients with schizophrenic spectrum disorders. It seems also relevant to analyze the existing classical antipsychotic therapy for its anti-inflammatory effects.

Numerous studies that have studied the effects of first- and second-generation antipsychotics on different groups of patients indicate mainly a common anti-inflammatory vector of action of these drugs. However, there is a significant amount of ambiguous and contradictory data. Hence, further research is needed to elucidate the anti-inflammatory effects of antipsychotics, which may lead to the discovery of new mechanisms of action to affect neuroinflammation by using these drugs more efficiently for therapeutic purposes.

References

1. Huxley P, Krayer A, Poole R, Prendergast L, Aryal S, Warner R. Schizophrenia outcomes in the 21st century: A systematic review. *Brain Behav.* 2021;11(6):e02172. https://doi.org/10.1002/brb3.2172
2. Disease and Injury Incidence and Prevalence Collaborators. Global, regional, and national incidence, prevalence, and years lived with disability for 310 diseases and injuries, 1990-2015: a systematic analysis 1ort he Global Burden of Disease Study 2015. *Lancet.* 2016;388(10053):1545–602. https://doi.org/10.1016/S0140-6736(16)31678-6
3. McCutcheon RA, Reis Marques T, Howes OD. Schizophrenia-An Overview. *JAMA Psychiatry.* 2020;77(2):201–10. https://doi.org/10.1001/jamapsychiatry.2019.3360
4. Orsolini L, Pompili S, Volpe U. Schizophrenia: A Narrative Review of Etiopathogenetic, Diagnostic and Treatment Aspects. *J Clin Med.* 2022;11(17):5040. https://doi.org/10.3390/jcm11175040
5. Kotzeva A, Mittal D, Desai S, Judge D, Samanta K. Socioeconomic burden of schizophrenia: a targeted literature review of types of costs and associated drivers across 10 countries. *J Med Econ.* 2023;26(1):70–83. https://doi.org/10.1080/13696998.2022.2157596
6. Pedraz-Petrozzi B, Elyamany O, Rummel C, Mulert C. Effects of inflammation on the kynurenine pathway in schizophrenia — a systematic review. *J Neuroinflammation.* 2020;17(1):56. https://doi.org/10.1186/s12974-020-1721-z
7. Juckel G, Freund N. Microglia and microbiome in schizophrenia: can immunomodulation improve symptoms? *J Neural Transm (Vienna).* 2023;130(9):1187–93. https://doi.org/10.1007/s00702-023-02605-w
8. Pillinger T, D'Ambrosio E, McCutcheon R, Howes OD. Is psychosis a multisystem disorder? A meta-review of central nervous system, immune, cardiometabolic, and endocrine alterations in first-episode psychosis and perspective on potential models. *Mol Psychiatry.* 2019;24(6):776–94. https://doi.org/10.1038/s41380-018-0058-9
9. Szoke A, Pignon B, Godin O, Ferchiou A, Tamouza R, Leboyer M, et al. Multimorbidity and the Etiology of Schizophrenia. *Curr Psychiatry Rep.* 2024;26(5):253–63. https://doi.org/10.1007/s11920-024-01500-9
10. Vallée A. Neuroinflammation in Schizophrenia: The Key Role of the WNT/β-Catenin Pathway. *Int J Mol Sci.* 2022;23(5):2810. https://doi.org/10.3390/ijms23052810
11. Bechmann I, Galea I, Perry VH. What is the blood-brain barrier (not)? *Trends Immunol.* 2007;28(1):5–11. https://doi.org/10.1016/j.it.2006.11.007
12. Mogensen FL, Delle C, Nedergaard M. The Glymphatic System (En)during Inflammation. *Int J Mol Sci.* 2021;22(14):7491. https://doi.org/0.3390/ijms22147491
13. Mousaviyan R, Davoodian N, Alizadeh F, Ghasemi-Kasman M, Mousavi SA, Shaerzadeh F, et al. H. Zinc Supplementation During Pregnancy Alleviates Lipopolysaccharide-Induced Glial Activation and Inflammatory Markers Expression in a Rat Model of Maternal Immune Activation. *Biol Trace Elem Res.* 2021;199(11):4193–204. https://doi.org/10.1007/s12011-020-02553-6
14. Esslinger M, Wachholz S, Manitz MP, Plumper J, Sommer R, Juckel G, et al. Schizophrenia associated sensory gating deficits develop after adolescent microglia activation. *Brain Behav Immun.* 2016;58:99–106. https://doi.org/10.1016/j.bbi.2016.05.018
15. Xia Y, Zhang Z, Lin W, Yan J, Zhu C, Yin D, et al. Modulating microglia activation prevents maternal immune activation induced schizophrenia-relevant behavior phenotypes via arginase 1 in the dentate gyrus. *Neuropsychopharmacology.* 2020;45(11):1896–908. https://doi.org/10.1038/s41386-020-0743-7
16. Trépanier MO, Hopperton KE, Mizrahi R, Mechawar N, Bazinet RP. Postmortem evidence of cerebral inflammation in schizophrenia: a systematic review. *Mol Psychiatry.* 2016;21(8):1009–26. https://doi.org/10.1038/mp.2016.90
17. van Kesteren CF, Gremmels H, de Witte LD, Hol EM, Van Gool AR, Falkai PG, et al. Immune involvement in the pathogenesis of schizophrenia: a meta-analysis on postmortem brain studies. *Transl Psychiatry.* 2017;7(3):e1075. https://doi.org/10.1038/tp.2017.4
18. Cotel MC, Lenartowicz EM, Natesan S, Modo MM, Cooper JD, Williams SC, et al. Microglial activation in the rat brain following chronic antipsychotic treatment at clinically relevant doses. *Eur Neuropsychopharmacol.* 2015; 25(11):2098–107. https://doi.org/10.1016/j.euroneuro.2015.08.004
19. Holmes SE, Hinz R, Drake RJ, Gregory CJ, Conen S, Matthews JC, et al. In vivo imaging of brain microglial activity in antipsychotic-free and medicated schizophrenia: a [^{11}C](R)-PK11195 positron emission tomography study. *Mol Psychiatry.* 2016;21(12):1672–9. https://doi.org/10.1038/mp.2016.180
20. Iliopoulou SM, Tsartsalis S, Kaiser S, Millet P, Tournier BB. Dopamine and Neuroinflammation in Schizophrenia — Interpreting the Findings from Translocator Protein (18kDa) PET Imaging. *Neuropsychiatr Dis Treat.* 2021;17:3345–57. https://doi.org/10.2147/NDT.S334027
21. Di Biase MA, Zalesky A, O'keefe G, Laskaris L, Baune BT, Weickert CS, et al. PET imaging of putative microglial activation in individuals at ultra-high risk for psychosis, recently diagnosed and chronically ill with schizophrenia. *Transl Psychiatry.* 2017;7(8):e1225. https://doi.org/10.1038/tp.2017.193
22. Bloomfield PS, Selvaraj S, Veronese M, Rizzo G, Bertoldo A, Owen DR, et al. Microglial Activity in People at Ultra High Risk of Psychosis and in Schizophrenia: An [(11)C]PBR28 PET Brain Imaging Study. *Am J Psychiatry.* 2016;173(1):44–52. https://doi.org/10.1176/appi.ajp.2015.14101358
23. Klaus F, Nguyen TT, Thomas M., Liou SC, Soontornniyomkij B, Mitchell K, et al. Peripheral inflammation levels associated with degree of advanced brain aging in schizophrenia. *Front Psychiatry.* 2022;13:966439. https://doi.org/10.3389/fpsyt.2022.966439
24. Ľupták M, Michaličková D, Fišar Z, Kitzlerová E, Hroudová J. Novel approaches in schizophrenia-from risk factors and hypotheses to novel drug targets. *World J Psychiatry.* 2021;11(7):277–96. https://doi.org/10.5498/wjp.v11.i7.277
25. Halstead S, Siskind D, Amft M, Wagner E, Yakimov V, Shih-Jung Liu Z, et al. Alteration patterns of peripheral concentrations of cytokines and associated inflammatory proteins in acute and chronic stages of schizophrenia: a systematic review and network meta-analysis. *Lancet Psychiatry.* 2023;10(4):260–71. https://doi.org/10.1016/S2215-0366(23)00025-1
26. Wang AK, Miller BJ. Meta-analysis of Cerebrospinal Fluid Cytokine and Tryptophan Catabolite Alterations in Psychiatric Patients: Comparisons Between Schizophrenia, Bipolar Disorder, and Depression. *Schizophr Bull.* 2018;44(1):75–83. https://doi.org/10.1093/schbul/sbx035
27. Reale M, Patruno A, De Lutiis MA, Pesce M, Felaco M, Di Giannantonio M, et al. Dysregulation of chemo-cytokine pro-

duction in schizophrenic patients versus healthy controls. *BMC Neurosci*. 2011;12:13.
https://doi.org/10.1186/1471-2202-12-13

28. Boerrigter D, Weickert TW, Lenroot R, O'Donnell M, Galletly C, Liu D, et al. Using blood cytokine measures to define high inflammatory biotype of schizophrenia and schizoaffective disorder. *J Neuroinflammation*. 2017;14(1):188.
https://doi.org/10.1186/s12974-017-0962-y

29. van Rees G, Lago S, Cox D, Tomasik J, Rustogi N, Weigelt K, et al. Evidence of microglial activation following exposure to serum from first-onset drug-naïve schizophrenia patients. *Brain Behav Immun*. 2018;67:364–73.
https://doi.org/10.1016/j.bbi.2017.10.003

30. Cai HQ, Catts VS, Webster MJ, Liu D, O'Donnell M, Weickert TW, et al. Increased macrophages and changed brain endothelial cell gene expression in the frontal cortex of people with schizophrenia displaying inflammation. *Mol Psychiatry*. 2020;25(4):761–75.
https://doi.org/10.1038/s41380-018-0235-x

31. Zhu Y, Webster MJ, Walker AK, Massa P, Middleton FA, Weickert CS. Increased prefrontal cortical cells positive for macrophage/microglial marker CD163 along blood vessels characterizes a neuropathology of neuroinflammatory schizophrenia. *Brain Behav Immun*. 2023;111:46–60.
https://doi.org/10.1016/j.bbi.2023.03.018

32. Mazza MG, Capellazzi M, Lucchi S, Tagliabue I, Rossetti A, Clerici M. Monocyte count in schizophrenia and related disorders: a systematic review and meta-analysis. *Acta Neuropsychiatr*. 2020;32(5):229–36.
https://doi.org/10.1017/neu.2020.12

33. Kübler R, Ormel PR, Sommer IEC, Kahn RS, de Witte LD. Gene expression profiling of monocytes in recent-onset schizophrenia. *Brain Behav Immun*. 2023;111:334–42.
https://doi.org/10.1016/j.bbi.2023.04.019

34. Weber NS, Gressitt KL, Cowan DN, Niebuhr DW, Yolken RH, Severance EG. Monocyte activation detected prior to a diagnosis of schizophrenia in the US Military New Onset Psychosis Project (MNOPP). *Schizophr Res*. 2018;197:465–9.
https://doi.org/10.1016/j.schres.2017.12.016

35. Uranova NA, Bonartsev PD, Androsova LV, Rakhmanova VI, Kaleda VG. Impaired monocyte activation in schizophrenia: ultrastructural abnormalities and increased IL-1β production. *Eur Arch Psychiatry Clin Neurosci*. 2017;267(5):417–26.
https://doi.org/10.1007/s00406-017-0782-1

36. Krause DL, Wagner JK, Wildenauer A, Matz J, Weidinger E, Riedel M, et al. Intracellular monocytic cytokine levels in schizophrenia show an alteration of IL-6. *Eur Arch Psychiatry Clin Neurosci*. 2012;262(5):393–401.
https://doi.org/10.1007/s00406-012-0290-2

37. Nikkilä HV, Müller K, Ahokas A, Rimón R, Andersson LC. Increased frequency of activated lymphocytes in the cerebrospinal fluid of patients with acute schizophrenia. *Schizophr Res*. 2001;49(1–2):99–105.
https://doi.org/10.1016/s0920-9964(99)00218-2

38. Wang C, Zhu D, Zhang D, Zuo X, Yao L, Liu T, et al. Causal role of immune cells in schizophrenia: Mendelian randomization (MR) study. *BMC Psychiatry*. 2023;23(1):590.
https://doi.org/10.1186/s12888-023-05081-4

39. Singh RP, Hasan S, Sharma S, Nagra S, Yamaguchi DT, Wong DT, et al. Th17 cells in inflammation and autoimmunity. *Autoimmun Rev*. 2014;13(12):1174–81.
https://doi.org/10.1016/j.autrev.2014.08.019

40. Ding M, Song X, Zhao J, Gao J, Li X, Yang G, et al. Activation of Th17 cells in drug naïve, first episode schizophrenia. *Prog Neuropsychopharmacol Biol Psychiatry*. 2014;51:78–82.
https://doi.org/10.1016/j.pnpbp.2014.01.001

41. Zheng Y, Zhang Q, Zhou X, Yao L, Zhu Q, Fu Z. Altered levels of cytokine, T- and B-lymphocytes, and PD-1 expression rates in drug-naïve schizophrenia patients with acute phase. *Sci Rep*. 2023;13(1):21711.
https://doi.org/10.1038/s41598-023-49206-x

42. Debnath M, Berk M. Th17 pathway-mediated immunopathogenesis of schizophrenia: mechanisms and implications. *Schizophr Bull*. 2014;40(6):1412–21.
https://doi.org/10.1093/schbul/sbu049

43. Li H, Zhang Q, Li N, Wang F, Xiang H, Zhang Z, et al. Plasma levels of Th17-related cytokines and complement C3 correlated with aggressive behavior in patients with schizophrenia. *Psychiatry Res*. 2016;246:700–6.
https://doi.org/10.1016/j.psychres.2016.10.061

44. Miller BJ, Buckley P, Seabolt W, Mellor A, Kirkpatrick B. Metaanalysis of cytokine alterations in schizophrenia: clinical status and antipsychotic effects. *Biol Psychiatry*. 2011;70(7):663–71.
https://doi.org/10.1016/j.biopsych.2011.04.013

45. Sahbaz C, Zibandey N, Kurtulmus A, Duran Y, Gokalp M, Kırpınar I, Sahin F, Guloksuz S, Akkoc T. Reduced regulatory T cells with increased proinflammatory response in patients with schizophrenia. *Psychopharmacology (Berl)*. 2020;237(6):1861–71.
https://doi.org/10.1007/s00213-020-05504-0

46. Boyko A, Melnikov M, Zhetishev R, Pashenkov M. The Role of Biogenic Amines in the Regulation of Interaction between the Immune and Nervous Systems in Multiple Sclerosis. *Neuroimmunomodulation*. 2016;23(4):217–23.
https://doi.org/10.1159/000449167

47. Sviridova A, Rogovskii V, Kudrin V, Pashenkov M, Boyko A, Melnikov M. The role of 5-HT2B-receptors in fluoxetine-mediated modulation of Th17- and Th1-cells in multiple sclerosis. *J Neuroimmunol*. 2021;356:577608.
https://doi.org/10.1016/j.jneuroim.2021.577608

48. Penedo MA, Rivera-Baltanás T, Pérez-Rodríguez D, et al. The role of dopamine receptors in lymphocytes and their changes in schizophrenia. *Brain Behav Immun Health*. 2021;12:100199.
https://doi.org/10.1016/j.bbih.2021.100199

49. Boiko AS, Mednova IA, Kornetova EG, Gerasimova VI, Kornetov AN, Loonen AJM, et al. Cytokine Level Changes in Schizophrenia Patients with and without Metabolic Syndrome Treated with Atypical Antipsychotics. *Pharmaceuticals (Basel)*. 2021;14(5):446.
https://doi.org/10.3390/ph14050446

50. Sobiś J, Rykaczewska-Czerwińska M, Świętochowska E, Gorczyca P. Therapeutic effect of aripiprazole in chronic schizophrenia is accompanied by anti-inflammatory activity. *Pharmacol Rep*. 2015;67(2):353–9.
https://doi.org/10.1016/j.pharep.2014.09.007

51. Mantere O, Trontti K, García-González J, Balcells I, Saarnio S, Mäntylä T, et al. Immunomodulatory effects of antipsychotic treatment on gene expression in first-episode psychosis. *J Psychiatr Res*. 2019;109:18–26.
https://doi.org/10.1016/j.jpsychires.2018.11.008

52. Lin Y, Peng Y, Zhu C, Su Y, Shi Y, Lin Z, et al. Pretreatment Serum MCP-1 Level Predicts Response to Risperidone in Schizophrenia. *Shanghai Arch Psychiatry*. 2017;29(5):287–94.
https://doi.org/10.11919/j.issn.1002-0829.217093

53. Alvarez-Herrera S, Escamilla R, Medina-Contreras O, Saracco R, Flores Y, Hurtado-Alvarado G, et al. Immunoendocrine Peripheral Effects Induced by Atypical Antipsychotics. *Front Endocrinol (Lausanne)*. 2020;11:195.
https://doi.org/10.3389/fendo.2020.00195

54. Maes M, Bosmans E, Calabrese J, Smith R, Meltzer HY. Interleukin-2 and interleukin-6 in schizophrenia and mania: effects of neuroleptics and mood stabilizers. *J Psychiatr Res*. 1995;29(2):141–52.
https://doi.org/10.1016/0022-3956(94)00049-w

55. Marcinowicz P, Więdłocha M, Zborowska N, et al. A Meta-Analysis 1ft he Influence of Antipsychotics on Cytokines Levels in First Episode Psychosis. *J Clin Med*. 2021;10(11):2488.
https://doi.org/10.3390/jcm10112488

56. Kelly DL, Li X, Kilday C, Feldman S, Clark S, Liu F, Buchanan RW, Tonelli LH. Increased circulating regulatory T cells in medicated people with schizophrenia. *Psychiatry Res*. 2018;269:517–23.
https://doi.org/10.1016/j.psychres.2018.09.006

57. Chen D, Li H, Zhao Q, Song J, Lin C, Yu J. Effect of risperidone treatment on insulin-like growth factor-1 and interleukin-17 in drug naïve first-episode schizophrenia. *Psychiatry Res*. 2021;297:113717.

https://doi.org/10.1016/j.psychres.2021.113717

58. Subbanna M, Shivakumar V, Venugopal D, Narayanaswamy JC, Berk M, Varambally S, et al. Impact of antipsychotic medication on IL-6/*STAT3* signaling axis in peripheral blood mononuclear cells of drug-naive schizophrenia patients. *Psychiatry Clin Neurosci*. 2020;74(1):64–9.
https://doi.org/.1111/pcn.12938

59. Stamoula Ε, Ainatzoglou A, Stamatellos VP, Dardalas I, Siafis S, Matsas A, et al. Atypical antipsychotics in multiple sclerosis: A review of their in vivo immunomodulatory effects. *Mult Scler Relat Disord*. 2022;58:103522.
https://doi.org/10.1016/j.msard.2022.103522

60. Himmerich H, Schönherr J, Fulda S, Sheldrick AJ, Bauer K, Sack U. Impact of antipsychotics on cytokine production in-vitro. *J Psychiatr Res*. 2011;45(10):1358–65.
https://doi.org/10.1016/j.jpsychires.2011.04.009

61. May M, Beauchemin M, Vary C, Barlow D, Houseknecht KL. The antipsychotic medication, risperidone, causes global immunosuppression in healthy mice. *PLoS One*. 2019;14(6):e0218937.
https://doi.org/10.1371/journal.pone.0218937

62. Feng T, McEvoy JP, Miller BJ. Longitudinal study of inflammatory markers and psychopathology in schizophrenia. *Schizophr Res*. 2020;224:58–66.
https://doi.org/10.1016/j.schres.2020.10.003

AUTHORS

Dmitry A. Chugunov, Cand. Sci. (Med.)
https://orcid.org/0000-0001-7173-3373
dr.dmitry.83@gmail.com

Andrey A. Shmilovich, Dr. Sci. (Med.)
https://orcid.org/0000-0002-1060-5076
shmilovich@bk.ru

Daria V. Nikolaeva
https://orcid.org/0009-0008-0113-6555
daniva0103@gmail.com

Tamara V. Yashina
https://orcid.org/0009-0001-0438-4983
toma.yaschina@yandex.ru

Mariya R. Larina
https://orcid.org/0009-0007-6635-6914
mimityan11@gmail.com

Vladimir S. Rogovsky, Cand. Sci. (Med.)
https://orcid.org/0000-0002-3682-6571
qwer555@mail.ru

Anastasia A. Sviridova
https://orcid.org/0000-0003-1086-9052
anastasiya-ana@yandex.ru

COMPARATIVE EVALUATION OF MINION AND NANOPORUS NANOPORE SEQUENCERS IN IDENTIFICATION OF PATHOGEN NUCLEIC ACIDS

Diana A. Grigoryan✉, Ivan F. Stetsenko, Boris S. Gukov, Alina D. Matsvay, German A. Shipulin

Centre for Strategic Planning of the Federal Medical and Biological Agency, Moscow, Russia

Introduction. Nanopore sequencing technologies have become routine methods in science and medicine, being widely used in the study of pathogen diversity and distribution and playing a key role in field epidemiology.

Objective. Comparative evaluation of the functional capabilities of third-generation MinION and Nanoporus sequencers in the detection of pathogens in biological material, including comparison of the as-determined taxonomic composition with the results obtained using the second-generation MiSeq (Illumina) reference platform.

Materials and methods. A total of 138 archival DNA samples with known taxonomic composition (14 families, 20 genus, and 43 species of viral and bacterial pathogens; altogether 169 pathogens) were analyzed. MinION and Nanoporus nanopore sequencers with original R9.4.1 and R10.4.1 flow cells (ONT), as well as the high-performance MiSeq (Illumina) platform were used for preliminary identification of the composition of samples containing different titers of pathogen nucleic acids belonging to various taxonomic groups. Comparative evaluation of the obtained data (number of sequences, average read quality scores (Qscore) for each nucleotide, GC-content of sequences, sequence length distribution, read duplication level) was performed using the MultiQC bioinformatics tool (version 1.20).

Results. The MinION and Nanoporus devices identified 98.8% and 97.6% of pathogens, respectively, including understudied or new viruses. The use of the latest-version flow cell on both devices significantly reduced the share of low-quality reads. The findings demonstrate a high degree of correlation between the results obtained by the second- and third-generation sequencers, which confirms the comparability and interchangeability of these technologies for the purposes of pathogen nucleic acid identification.

Conclusions. The study results demonstrate the potential of MinION and Nanoporus nanopore sequencers for epidemiologic surveillance. These devices are capable of identifying pathogens of different nature with high accuracy and, due to their compactness and portability, facilitating the diagnostics and monitoring of infectious diseases.

Keywords: nanopore sequencing; NGS; Illumina; ONT; Nanoporus; MinION

СРАВНИТЕЛЬНЫЙ АНАЛИЗ НАНОПОРОВЫХ СЕКВЕНАТОРОВ MINION И НАНОПОРУС В ЗАДАЧЕ ИДЕНТИФИКАЦИИ НУКЛЕИНОВЫХ КИСЛОТ ПАТОГЕНОВ

Д.А. Григорян✉, И.Ф. Стеценко, Б.С. Гуков, А.Д. Мацвай, Г.А. Шипулин

Центр стратегического планирования и управления медико-биологическими рисками здоровью Федерального медико-биологического агентства, Москва, Россия

Введение. Технологии нанопорового секвенирования стали рутинным инструментом в науке и медицине, широко применяются в исследовании разнообразия и распространения патогенов, играют ключевую роль в полевой эпидемиологии.

Цель. Проведение сравнительного анализа функциональных возможностей секвенаторов третьего поколения MinION и Нанопорус в задаче выявления патогенов в биологическом материале, включая сопоставление таксономического состава, определенного с их использованием, с результатами, полученными на референсной платформе второго поколения MiSeq (Illumina).

Материалы и методы. Проведено исследование 138 образцов архивной ДНК с известным таксономическим составом (исследованы 14 семейств, 20 родов и 43 вида патогенов вирусной и бактериальной природы, суммарно 169 возбудителей инфекций). В исследовании использовались нанопоровые секвенаторы MinION и Нанопорус с оригинальными проточными ячейками R9.4.1 и R10.4.1 от ONT, а также высокопроизводительная платформа MiSeq от Illumina для предварительной идентификации состава исследуемых образцов, содержащих различные титры нуклеиновых кислот возбудителей инфекций ряда таксономических групп. Сравнительный анализ полученных данных (количество последовательностей, средние показатели качества прочтений (Qscore) для каждого нуклеотида, GC-состав последовательностей, распределение длин последовательностей, уровень дупликаций прочтений) проводился биоинформатическим инструментом MultiQC (версия 1.20).

Результаты. В ходе проведенных исследований на приборах MinION и Нанопорус было идентифицировано 98,8 и 97,6% патогенов соответственно, включая малоизученные или новые вирусы. Применение последней версии проточной ячейки на обоих приборах значительно снизило долю низкокачественных прочтений. Полученные данные продемонстрировали высокую степень корреляции между результатами секвенаторов второго и третьего поколений, что подтверждает сопоставимость и взаимозаменяемость этих технологий в задаче идентификации нуклеиновых кислот патогенов.

Выводы. Результаты исследования демонстрируют потенциал нанопоровых секвенаторов MinION и Нанопорус для применения в эпидемиологическом надзоре. Приборы способны обеспечивать высокую точность идентификации патогенов различной природы и благодаря своей компактности и портативности могут существенно повысить скорость диагностики и мониторинга инфекционных заболеваний.

INTRODUCTION

Sequencing technologies have become routine methods in various areas of molecular biology, due to their capacity to promptly and reliably detect mutations and genetic variations in viruses, identify new pathogens, predict their evolutionary changes, track the dynamics of distribution in populations, and analyze phylogenetic relationships [1–3]. The method of nanopore sequencing was first introduced by Oxford Nanopore Technologies (ONT) in 2014 with the MinION device [4]. This technology possesses a number of unique advantages, which determine its indispensability in modern medicine and science [5]. The ability to sequence long DNA and RNA fragments has made it possible to detect structural variations and epigenetic modifications [6–8]. However, the key advantage of this sequencing method consists in the compactness of nanopore sequencers, their ability to operate by connecting to a laptop USB interface, and low requirements for laboratory equipment. This renders such devices applicable in various conditions, including field studies [9].

Nanopore sequencing technology has already made a substantial impact on various fields of medicine, including diagnosis and treatment of genetic diseases [10, 11], personalized medicine [2, 12], and cancer research [6, 13, 14]. Due to its speed and mobility, nanopore sequencing is a convenient tool for epidemiologic surveillance and outbreak control [9, 15–17]. In particular, during the COVID-19 pandemic, nanopore sequencing played an essential role in rapid identification of virus strains and detection of new genetic variations of pathogens [12, 17, 18]. In addition, this technology has proven to be a reliable alternative to routine methods of sequencing complete virus genomes [15, 19]. These properties are particularly important in the context of global pandemics and outbreaks of new infections, since the promptness of data collection is crucial for the decision-making process.

The Russian market, along with the original third-generation platforms by Oxford Nanopore Technologies, also offers a similarly functional domestic device referred to as Nanoporus. This device is designed for nanopore sequencing using original flow cells by Oxford Nanopore Technologies.

In this work, we carry out a comparative evaluation of the functional capabilities of third-generation MinION and Nanopore sequencers in detecting pathogens in biological material, including comparison of the taxonomic composition identified with their use and the results obtained using the second-generation MiSeq (Illumina) reference platform.

MATERIALS AND METHODS

During two stages of the study, 138 samples of archival DNA from a laboratory collection with known taxonomic composition and different titers of pathogen nucleic acid belonging to different taxonomic groups were analyzed. These included 14 families, 20 genus, and 43 species of pathogens of a viral and bacterial nature, totaling 169 pathogens. Identification of the pathogenic composition of the studied material had been previously performed by high-throughput sequencing on the MiSeq platform (Illumina). Based on the data of local alignment of nucleotide and protein sequences, we analyzed similarity indices with sequences from the database used for taxonomic identification.

The following reagent sets were used during the preparation of amplicon DNA libraries. End Repair of double-stranded DNA fragments and matrix-free adenylation were performed using a NEBNext Ultra II End Repair/dA-Tailing Module reagent kit (New England Biolabs). Adaptor sequence ligation from PCR Barcoding Expansion 1-96 (EXP-PBC096) (ONT) was performed using a Blunt/TA Ligase Master Mix reagent (New England Biolabs). Barcoding of libraries was performed using PCR Barcoding Expansion 1-96 (EXP-PBC096) (ONT). All kits were used according to the manufacturer's instructions.

DNA libraries for sequencing on a R9.4.1 flow cell were prepared using a Ligation Sequencing Kit (SQK-LSK109) (ONT) and then loaded into the flow cell. DNA libraries for sequencing on a R10.4.1 flow cell were prepared using a Ligation Sequencing Kit V14 (SQK-NBD114) reagent kit (ONT) followed by loading into the flow cell. The sequence of sequencing reagents was determined taking technical and methodological considerations into account. At the primary stage of the study, when using the R9.4.1 flow cell for the first time, sequencing was initially performed on the MinION

sequencer to ensure a predictably stable operation of the cell. This order was set to minimize potential risks associated with a possible decrease in the stability or functionality of the cell after its use on the Nanoporus sequencer. At the second step, in order to test the Nanoporus sequencer in terms of its effects on cell functionality for subsequent use in the MinION, sequencing was performed initially on the Nanoporus and then on the MinION.

The detected signal from the devices was recorded using the MinKNOW software version 23.11.4; the basecalling of data in pod5 format was performed by the Dorado software version 7.2.13 (ONT). In order to ensure the correctness of sequencing quality comparison and taxonomic identification by the tested devices, the equal number of reads were selected for each sample representing a random sample generated by the SeqKit bioinformatics tool (version v2.8.0). The quality of reads in fastq format was assessed by using Trimmomatic bioinformatic tools (version 0.32), FastQC (version v0.12.0). Comparative evaluation of the data obtained (number of sequences, average read quality scores (Qscore) for each nucleotide, GC-content of sequences (guanine-cytosine content), sequence length distribution, read duplication level) was performed using the MultiQC bioinformatic tool (version 1.20). Taxonomic identification of the viral composition of the samples was performed using the PathogenID software (FMBA, Russia). As a reference tool for comparing the results of determining the taxonomic composition of samples, the data obtained on the second-generation MiSeq platform (Illumina) were used.

For comparative evaluation of the tested sequencers, the investigated infectious agents were divided into five groups according to their taxonomic identification index (% identity) obtained by high-throughput sequencing.

The following identifiers were assigned to virus groups: Group 1 — 30 pathogens, 100–97% identity, Group 2 — 29 pathogens, 96–94% identity, Group 3 — 39 pathogens, 93–90% identity, Group 4 — 35 pathogens, 89–80% identity, Group 5 — 24 pathogens, 79–71% identity. The presented pathogen groups can be used to simulate the analysis of divergent pathogen groups, new strains, species in particular.

RESULTS

Comparison of data transfer stability and sequencing quality

Using the MinKNOW software, the stability of data transmission from the device to the control computer was assessed. No significant fluctuations and failures in signal transmission, as well as deviations from the uniform distribution of the DNA translocation rate through the pore were registered during the analysis of the graphs obtained from the MinION and Nanoporus devices using the R10.4.1 flow cell (Fig. 1; A2, B2). The graphs of temperature maintenance throughout the entire sequencing process indicated no disturbances in the operation of the sequencers; temperature fluctuations were insignificant and remained within the permissible limits. The corresponding information is presented in Fig. 1; A1, B1.

The quality parameters of reads obtained from both old- and new-type flow cells for MinION and Nanoporus sequencers were compared (Fig. 2). An analysis of the presented graphs revealed an increase in the Qscore parameter, which reflects the accuracy of base identification in the reads, and a decrease in the level of duplications when using a flow cell of the latest R10.4.1 version. All the presented
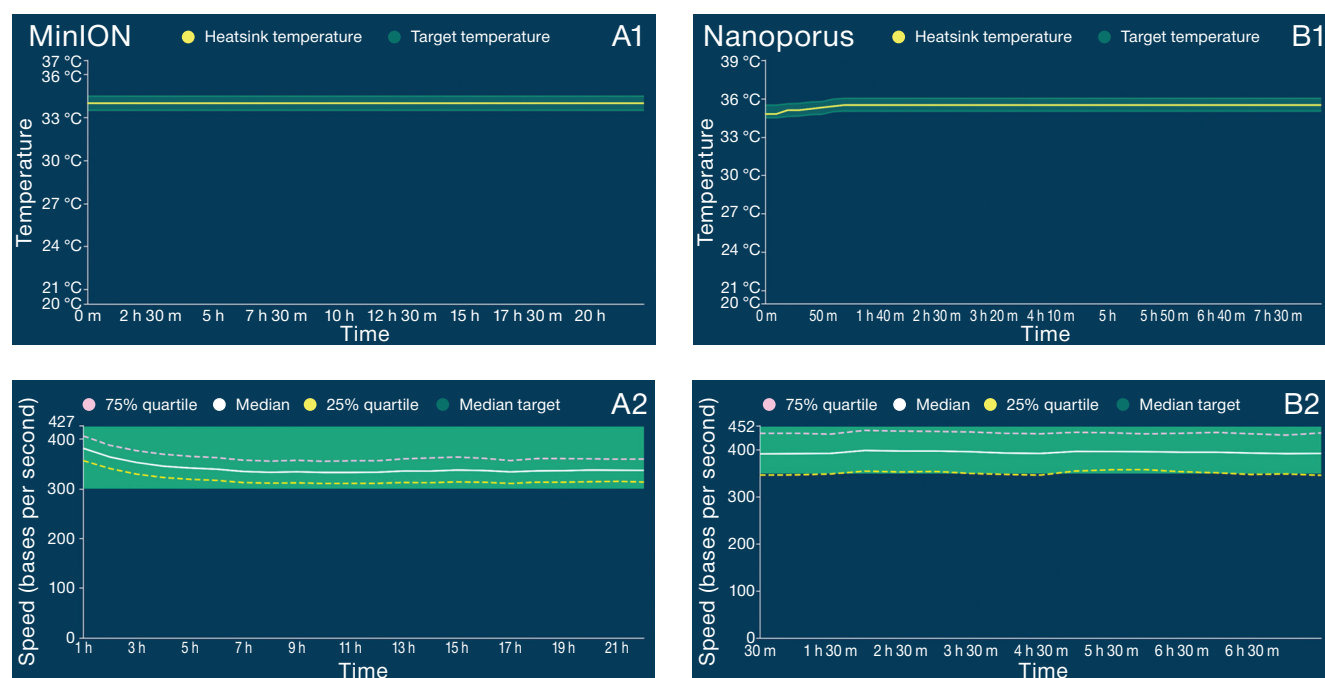
Figure prepared by the authors

Fig. 1. Graphical representation of key parameters of the MinION and Nanoporus sequencers
Note: A1, B1 — maintaining the temperature regime during sequencing; A2, B2 — the rate of DNA translocation through the pore.
The graphs were obtained using the MinKNOW software, version 23.11.4.

metrics for assessing the quality of reads obtained from the two compared nanopore sequencers were also found to be consistent.

Additional indicators of sequencing quality, namely metrics N50, N95, and N5, as well as the percentage of reads with quality above Q20 and Q30 were calculated; the corresponding data are presented in Table 1. A comparative evaluation of sequence percentage with a quality of above Q20 and Q30 found that when using the earlier version of the flow cell (R9.4.1), about 70% of the data demonstrated a quality below Q20 and about 97.3% had a quality below Q30 on both sequencers. At the same time, when the R10.4.1 flow cell of the latest version was used, the proportion of data with a quality below Q20 was less than 55% and below Q30 was less than 76%. There were no significant differences in N50, N95, N5, and the percentage of sequences with a quality above Q20 and Q30 between the two different third-generation devices.

Comparative analysis of the devices in pathogen identification

The studied material contained fragments of pathogen genomes of the following families:

Pseudomonadaceae, Circoviridae, Adenoviridae, Coronaviridae, Orthomyxoviridae, Parvoviridae, Polyomaviridae, Astroviridae*, Caliciviridae, Picornaviridae, Solemoviridae, Hepeviridae, Partitiviridae, Tymoviridae.*

The *Adenoviridae* family included 12 specimens and 5 pathogen species with viral loads ranging from 7.22% to 0.33% of reads per specimen according to high-throughput sequencing data. As a result of processing the data obtained by MinION and Nanoporus devices, the taxonomic composition was confirmed in 11 (92%) and 10 (83%) samples, respectively. The *Circoviridae* family counted 35 specimens and 11 different pathogen species with viral loads ranging from 57.27% to 0.04% of reads based on Illumina
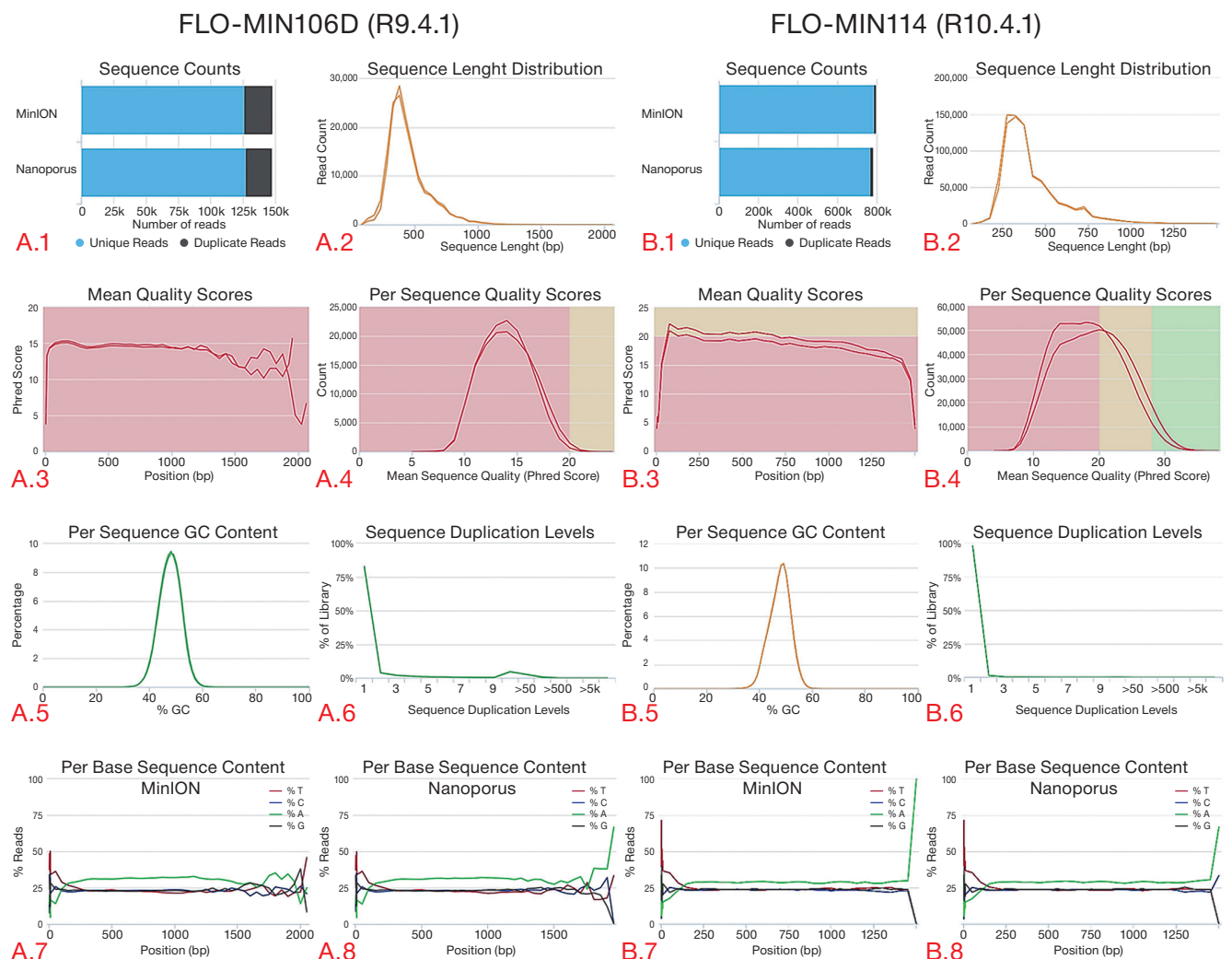
Figure prepared by the authors

Fig. 2. Comparison of quality indicators of reads obtained from MinION and Nanoporus sequencers
Note: graph A.1 — total number of sequences obtained from each device; graph A.2 — distribution of reads by read length; graph A.3 — average read quality values (Qscore) for each nucleotide; graph A.4 — number of reads depending on the quality indicator (Qscore); graph A.5 — GC content in sequences, %; graph A.6 — level of read duplications; graph A.7 — nucleotide composition of reads obtained by the MinION sequencer; graph A.8 — nucleotide composition of reads obtained by the Nanoporus sequencer.
The corresponding data for the R10.4.1 flow cell is shown in graphs B.1–B.8.
The graphs correspond to data recorded using R9.4.1 and R10.4.1 flow cells.
Read quality scores were obtained by the MultiQC bioinformatics tool (version 1.20).

Table 1. Sequencing quality indicators on the original R10.4.1 and R9.4.1 flow cells on the third-generation sequencers: Nanoporus and MinION

Quality assessment parameters	Flow cell R10.4.1, MinION sequencer	Flow Cell R10.4.1, Nanoporus sequencer	Flow cell R9.4.1, MinION sequencer	Flow cell R9.4.1, Nanoporus sequencer
Average read length, units of nucleotides	407.8	417.1	447	435
Maximum read length, units of nucleotides	1500	1500	1399	1388
N50	411	425	454	446
N5	250	256	289	275
N95	900	904	871	860

Table prepared by the authors using their own data

sequencing data. Data from MinION and Nanoporus sequencers resulted in confirmed taxonomic composition in 34 (97%) and 33 (94%) samples, respectively. Although identification of the target pathogen by nanopore sequencers was not performed for 100% of samples containing viruses of these families (*Adenoviridae* and *Circoviridae*), a more detailed virus typing by nanopore data was obtained during alignment of nucleotide sequences to reference databases for a number of samples.

According to the high-throughput sequencing data obtained on the Illumina platform, the *Coronaviridae* family counted 70 samples and 9 different pathogen species with viral loads ranging from 49.52% to 0.15% of reads. The *Orthomyxoviridae* family sample counted 6 samples and 1 species with viral loads ranging from 28.97% to 1.32% of reads. The selection of *Pseudomonadaceae* samples counted 12 samples and 1 species. The test group of the *Parvoviridae* family counted 15 samples and 11 species of pathogens with viral loads ranging from 28.12% to 0.22% of reads. The *Picornaviridae* family counted 4 samples and 4 species of pathogens with viral loads ranging from 11.53% to 0.3% of reads. While the *Astroviridae*, *Caliciviridae*, *Polyomaviridae*, *Solemoviridae*, *Tymoviridae*, *Partitiviridae*, and *Hepeviridae* families counted single specimens, identification of the taxonomic composition of the *Coronaviridae*, *Parvoviridae*, *Picornaviridae*, and *Orthomyxoviridae* families was carried out in 100% of specimens during third-generation sequencing on MinION and Nanoporus devices. A total of 167 (98.8%) and 165 (97.6%) pathogens were identified by the MinION and Nanoporus nanopore sequencers, respectively.

For the most represented virus families, the percentage of reads attributable to the target infectious agent was compared. For a more accessible visualization of the comparison, data were taken on a logarithmic scale and analyzed for three pairs of sequencers: MiSeq and MinION (A), MiSeq and Nanoporus (B), and MinION and Nanoporus (C) (Fig. 3). The plots showed an increase in correlation between sequencing results along with an increase in viral load in the samples, particularly between Nanopore sequencing data at load levels more than two logarithmic units. At low viral loads, deviations were found, particularly between Illumina and third-generation sequencing data.

The Pearson correlation coefficient was calculated to assess the relationship between the percent viral load values on the three devices. An analysis of data collected from both flow cells showed the following results. The correlation coefficient between MiSeq and MinION platforms was $r = 0.567$ ($p \leq 0.05$), indicating a moderate positive relationship. Between MiSeq and Nanoporus, a coefficient of $r = 0.544$ ($p \leq 0.05$) was recorded, also indicating a moderate positive relationship. The highest correlation value was observed between Nanoporus and MinION sequencers, equal to $r = 0.993$ ($p \leq 0.05$), indicating an almost complete correspondence of the results between the two devices.

In the course of the study, groups of infectious agents formed according to the range of taxonomic identity (% identity) were compared according to the average values of taxonomic identification indicators (e-value, % identity, alignment length (nucleotide base pairs), percentage of reads of the target virus) obtained on the tested devices (Fig. 4).

For all presented pathogen groups, the % identity and e-value values obtained on the MiSeq platform were slightly higher than those obtained on nanopore sequencers. At the same time, the index of sequence alignment length showed an inverse relationship. The histograms indicated a high degree of concordance in the detection of infectious agents between the three devices.

To visualize the differences in the reliability of taxonomic identification provided by the tested sequencers, we simulated the variation distribution of viral load and percent identity based on the data obtained from the three devices (Fig. 5). Based on the results of the first stage of the study (95 samples) (A), we observed the following distribution pattern: on the MiSeq platform, the main data cluster was in the range of high identity (90–100%) and medium viral load (2-3 logarithmic units); when using the R9.4.1 flow cell, the MinION platform showed a dense cluster of data in the area of high identity (more than 90%) and a relatively high viral load (2–3 logarithmic units); data from the Nanoporus sequencer were distributed more broadly along the identity axis, however, the main dispersion cluster was also within 90% identity.

The results of the second stage of the study (43 samples suspected to contain nucleic acids of poorly studied pathogens) (B) showed the following data profile. The MiSeq platform revealed a shift in data density towards lower identity and viral load, which is explained by the peculiarities of the tested material. When using the R10.4.1 flow cell, data from the MinION were concentrated in a narrow range of 85% identity and a relatively high viral load

A — Viral load of target pathogens, log of %
MiSeq / MinION

B — Viral load of target pathogens, log of %
MiSeq / Nanoporus

C — Viral load of target pathogens, log of %
MinION / Nanoporus

- Bat coronovirus
- Circovirus
- Alfanfluenzavirus
- Betacoronovirus
- Picornavirus
- Polyomavirus
- Parvovirus
- Alphacoronovirus
- Mastadenovirus

Figure prepared by the authors

Fig. 3. Comparison of the percentage of reads of target pathogens of the most represented families
Note: graph A — MiSeq and MinION sequencers; graph B — MiSeq and Nanoporus sequencers; graph C — MinION and Nanoporus sequencers.
Point on the graphs — one virus under study.
Viral load values are presented on a logarithmic scale.

Figure prepared by the authors

Fig. 4. Comparison of average values of taxonomic identification parameters (pathogen load, % identity, alignment length, e-value) obtained as a result of sequencing on MiSeq, MinION, and Nanoporus sequencers
Note: the analysis was performed based on data obtained from flow cells of the latest two versions.

(2–3 logarithmic units). The Nanoporus sequencer showed a less dense data distribution relative to its counterpart, although demonstrating a comparable viral load.

DISCUSSION

For a long period of time, Oxford Nanopore Technologies (ONT) has been the only developer offering nanopore sequencing solutions. However, over the past year, several similar platforms have entered the market. These include, in particular, the Chinese QNome-3841 and QNome-3841hex sequencers by QitanTech, which have already found application in forensic genetics and full bacterial genome studies [27, 28]; CycloneSEQ by MGI, which has showed significant results in de novo genome assembly, as well as in metagenomic and single-cell sequencing according to a study published by the platform developers [20]. At the time of this research, a comparative evaluation of CycloneSEQ and Gnome with such systems as MinION was not possible due to the recent announcement of the platforms. The Nanoporus Nanopore Sequencer, which is an analog of the well-known MinION

device, was announced in late 2023 and commercialized in early 2024. At the time of preparing this article, we were unable to find any publicly available studies devoted to a direct comparison of the characteristics of these devices; therefore, our conclusions are based purely on our own experimental data.

During testing of the Nanopore sequencer, no violations or abnormalities in operation were detected. The compatibility of the device with the original flow cells of the two latest versions, library preparation kits and software by Oxford Nanopore Technologies was confirmed. The data on the rate of DNA translocation through nanopores did not reveal any signal distortions, indicating that there were no significant deviations from the expected indicators of the quality of information transfer to the control computer. The indicators of temperature maintenance stability by nanopore sequencers showed minimal temperature fluctuations, which is important for stable operation of nanopores, ensuring sequencing accuracy, preventing library degradation, and maintaining optimal conditions for the functioning of enzymes involved in the sequencing process. In the framework of this analysis, the
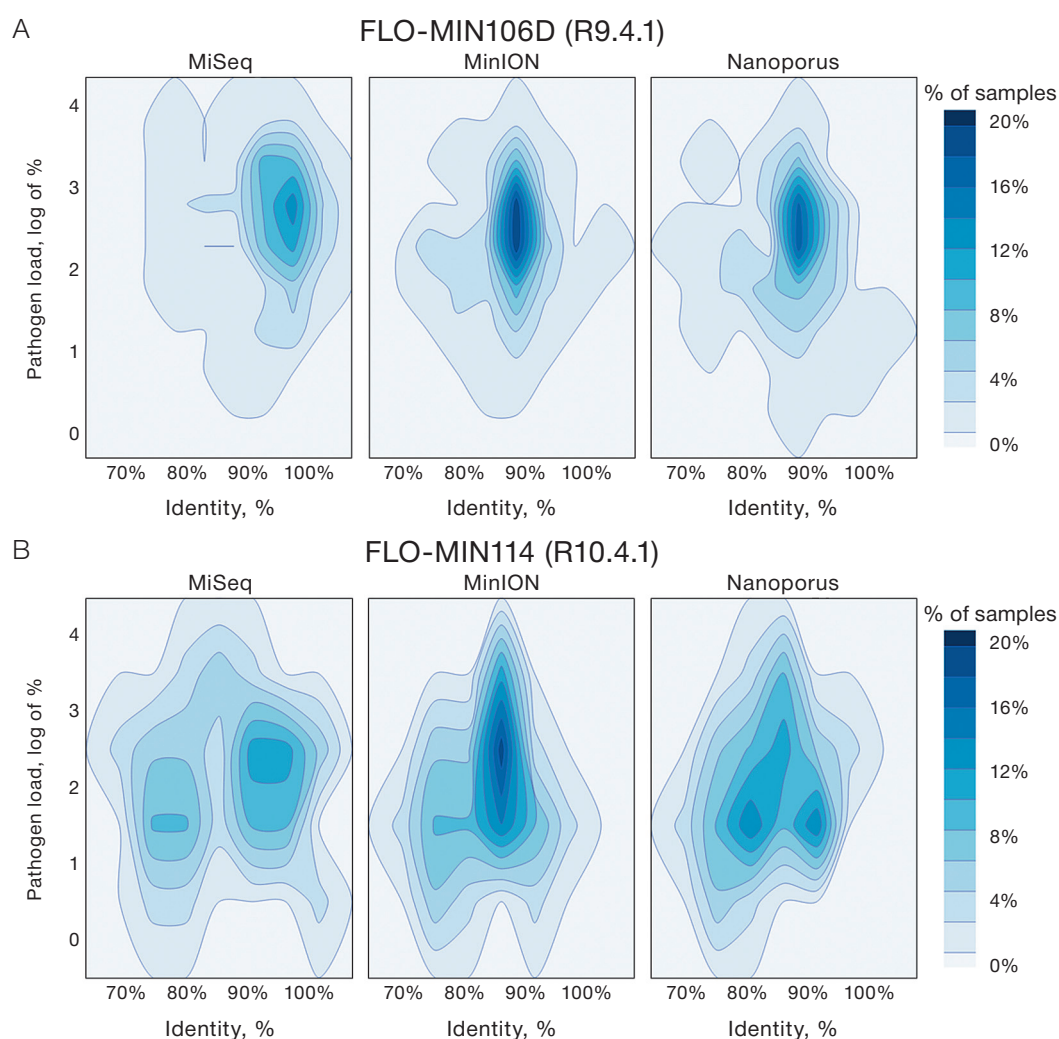
Figure prepared by the authors

Fig. 5. Dispersion distribution of pathogen load and percent identity for data from MiSeq, MinION, and Nanoporus sequencers
Note: graphs correspond to data recorded using R9.4.1(A) and R10.4.1(B) flow cells.

equipment was found to meet the stated characteristics and functional requirements.

An updated R10.4.1 flow cell significantly improves sequencing accuracy and stability, as evidenced by the increase in average Qscore values on both nanopore platforms compared to the previous flow cell version. The existing studies in the field confirm that the latest version of ONT flow cells provides significant improvement in accuracy and quality of reads [21]. According to the data provided by the authors, the percentage of base pairs with Q15 read quality for the R10.4.1 flow cell is six times higher than that for the R9.4.1 version. In the case of bacterial genome assembly, the authors were able to assemble 97% of the genome through the earlier version of the flow cell, and this value increased to 98% in the case of R10.4.1. Our study shows a similar improvement: the proportion of reads with quality below Q20 and Q30 decreases significantly; the proportion of low-quality reads below Q20 decreases from 70% to 55% and below Q30 from 97.3% to 76%. This change indicates an improvement in sequencing accuracy and reliability when using ONT's new V14 chemistry and R10.4.1 flow cells.

Second-generation sequencing is recognized as a highly accurate and reliable method for detecting nucleic acids of infectious agents. Due to its high quality of nucleotide reads, this method can be classified as a leading technology among alternative molecular diagnostic methods [22]. However, nanopore sequencing technology (ONT) offers a number of unique advantages, such as compactness and mobility, thus standing out against the complex optical systems required for second-generation sequencing. These characteristics of ONT allow efficient use of the technology in resource-limited settings and rapid field studies, which is an important factor in the introduction of this method into epidemiologic surveillance processes.

Previous studies demonstrated the potential of ONT as an alternative to high-throughput second-generation platforms. In particular, in a study evaluating the identification of pathogens of bacterial nature using MinION and Illumina sequencers (the type of second-generation devices is not specified), both devices were used to successfully identify species, serotypes, MLST profiles, and subtypes of Shiga-toxin in *Escherichia coli* (STEC) isolates [23]. Another study on the identification of the bacterial composition of a reference sample containing eight different pathogens found that classification performance at the family and genus level prevailed when using MinION. However, at the species level, pathogen identification was found to be more accurate on the MiSeq platform. It is important to note that the R9.4.1 flow cell version was used for MinION [24]. A number of other studies evaluating the efficiency of using different generations of sequencing for

the detection of viral pathogens, in particular, representatives of the genera Alphavirus [25] and Adenovirus [26], also demonstrate only a slight advantage of second-generation platforms in terms of identification quality compared to the results obtained on nanopore sequencers. Our data support the conclusions of the above studies by demonstrating a high correlation between pathogen detection results of different generations of sequencers. The MinION and Nanoporus devices identified 98.8% and 97.6% of pathogens, respectively, of the infectious agents detected by the MiSeq platform. It was also found that an increase in pathogen load in the sample led to an increase in the level of similarity between second- and third-generation sequencing results. A particularly high concordance is noted between the data obtained by MinION and Nanoporus platforms as the average value of pathogen nucleic acid titer in the tested samples is exceeded. In this regard, MinION and Nanoporus can be considered interchangeable in the context of pathogen identification and quantification tasks.

Our study evaluated the ability of nanopore sequencers to detect novel or poorly understood viral variations. The control material under study contained samples for which preliminary identification of pathogen composition using MiSeq platform showed low alignment quality parameters. This may indicate limited representation of these pathogen variations in existing databases or complete absence of information thereon. The analysis of variance distribution and quality parameters for taxonomic identification demonstrated significant alignment between second- and third-generation data. This confirms the capability of MinION and Nanoporus nanopore sequencers to identify previously unknown or poorly studied viruses at a level comparable to high-performance platforms.

CONCLUSION

The Nanopore device demonstrated compatibility with the latest two versions of flow cells, library preparation kits, and software by Oxford Nanopore Technologies. This allows its integration into existing laboratory processes without the need for significant modifications to working protocols. The results of the conducted comparative evaluation confirmed a high level of consistency of pathogen taxonomic identification data obtained using third-generation MinION and Nanopore sequencers with the results provided by the second-generation MiSeq platform. Based on the data obtained, no limitations for the use of MinION and Nanoporus nanopore sequencers in laboratory pathogen detection studies have been identified.

References

1. Brown BL, Watson M, Minot SS, Rivera MC, Franklin RB. MinIONTM nanopore sequencing of environmental metagenomes: a synthetic approach. *GigaScience*. 2017;6(3):gix007. https://doi.org/10.1093/gigascience/gix007

2. Schmidt K, Mwaigwisya S, Crossman LC, Doumith M, Munroe D, Pires C. Identification of bacterial pathogens and antimicrobial resistance directly from clinical urines by nanopore-based metagenomic sequencing. *J Antimicrob Chemother*. 2017;72(1):104–14. https://doi.org/10.1093/jac/dkw397

3. Ciuffreda L, Rodríguez-Pérez H, Flores C. Nanopore sequencing and its application to the study of microbial communities. *Comput Struct Biotechnol J.* 2021;19:1497–511 https://doi.org/10.1016/j.csbj.2021.02.020

4. Jain M, Olsen HE, Paten B, Akeson M. The Oxford Nanopore MinION: delivery of nanopore sequencing to the genomics community. *Genome Biol.* 2016;17(1):239 https://doi.org/10.1186/s13059-016-1103-0

5. Leggett RM, Clark MD. A world of opportunities with nanopore sequencing. *J Exp Bot.* 28 2017;68(20):5419–29 https://doi.org/10.1093/jxb/erx289

6. Ahmed YW, Alemu BA, Bekele SA, Gizaw ST, Zerihun MF, Wabalo EK. Epigenetic tumor heterogeneity in the era of single-cell profiling with nanopore sequencing. *Clin Epigenetics.* 2022;14(1):107 https://doi.org/10.1186/s13148-022-01323-6

7. Searle B, Müller M, Carell T, Kellett A. Third-Generation Sequencing of Epigenetic DNA. *Angew Chem.* 2023;135(14):e202215704 https://doi.org/10.1002/ange.202215704

8. Parker MT, Knop K, Sherwood AV, Schurch NJ, Mackinnon K, Gould PD. Nanopore direct RNA sequencing maps the complexity of Arabidopsis mRNA processing and m6A modification. Wan Y, Hardtke CS. *eLife*. 2020;9:e49658 https://doi.org/10.7554/eLife.49658

9. Quick J, Loman NJ, Duraffour S, Simpson JT, Severi E, Cowley L. Real-time, portable genome sequencing for Ebola surveillance. *Nature.* 2016;530(7589):228–32 https://doi.org/10.1038/nature16996

10. Ameur A, Kloosterman WP, Hestand MS. Single-Molecule Sequencing: Towards Clinical Applications. *Trends Biotechnol*. 2019;37(1):72–85 https://doi.org/10.1016/j.tibtech.2018.07.013

11. Sun X, Song L, Yang W, Zhang L, Liu M, Li X. Nanopore Sequencing and Its Clinical Applications. *Methods Mol Biol Clifton NJ.* 2020;2204:13–32 https://doi.org/10.1007/978-1-0716-0904-0_2

12. Wang M, Fu A, Hu B, Tong Y, Liu R, Liu Z. Nanopore Targeted Sequencing for the Accurate and Comprehensive Detection of SARS-CoV-2 and Other Respiratory Viruses. *Small.* 2020;16(32):2002169 https://doi.org/10.1002/smll.202002169

13. Chen Z, He X. Application of third-generation sequencing in cancer research. *Med Rev.* 21 2021;1:000010151520210013 https://doi.org/10.1515/mr-2021-0013

14. Lau BT, Almeda A, Schauer M, McNamara M, Bai X, Meng Q. Single-molecule methylation profiles of cell-free DNA in cancer with nanopore sequencing. *Genome Med*. 2023;15(1):33 https://doi.org/10.1186/s13073-023-01178-3

15. Faizuloev E, Mintaev R, Petrusha O, Marova A, Smirnova D, Ammour Y. New approach of genetic characterization of group A rotaviruses by the nanopore sequencing method. *J Virol Methods*. 2021;292:114114 https://doi.org/10.1016/j.jviromet.2021.114114

16. Tombácz D, Dörmő Á, Gulyás G, Csabai Z, Prazsák I, Kakuk B. High temporal resolution Nanopore sequencing dataset of SARS-CoV-2 and host cell RNAs. *GigaScience*. 2022;11:giac094 https://doi.org/10.1093/gigascience/giac094

17. Vacca D, Fiannaca A, Tramuto F, Cancila V, La Paglia L, Mazzucco W. Direct RNA Nanopore Sequencing of SARS-CoV-2 Extracted from Critical Material from Swabs. *Life.* 2022;12(1):69 https://doi.org/10.3390/life12010069

18. Gauthier NPG, Nelson C, Bonsall MB, Locher K, Charles M, MacDonald C. Nanopore metagenomic sequencing for detection and characterization of SARS-CoV-2 in clinical samples. *Plos one*. 2021;16(11):e0259712 https://doi.org/10.1371/journal.pone.0259712

19. Ben Chehida S, Filloux D, Fernandez E, Moubset O, Hoareau M, Julian C. Nanopore Sequencing Is a Credible Alternative to Recover Complete Genomes of Geminiviruses. *Microorganisms*. 2021;9(5):903 https://doi.org/10.3390/microorganisms9050903

20. Zhang, JY, Zhang, Y, Wang L, Guo F, Yun Q, Zeng T, Dong Y. A single-molecule nanopore sequencing platform. bioRxiv. 2024;08 https://doi.org/10.1101/2024.08.19.608720

21. Linde J, Brangsch H, Hölzer M, Thomas C, Elschner MC, Melzer F, et al. Comparison of Illumina and Oxford Nanopore Technology for genome analysis of Francisella tularensis, Bacillus anthracis, and Brucella suis. *BMC Genomics*. 2023;24(1):258 https://doi.org/10.1186/s12864-023-09343-z

22. Satam H, Joshi K, Mangrolia U, Waghoo S, Zaidi G, Rawool S, et al. Next-Generation Sequencing Technology: Current Trends and Advancements. *Biology.* 2023;12(7):997 https://doi.org/10.3390/biology12070997

23. Greig DR, Jenkins C, Gharbia S, Dallman TJ. Comparison of single-nucleotide variants identified by Illumina and Oxford Nanopore technologies in the context of a potential outbreak of Shiga toxin–producing Escherichia coli. *GigaScience*. 2019;8(8):giz104 https://doi.org/10.1093/gigascience/giz104

24. Winand R, Bogaerts B, Hoffman S, Lefevre L, Delvoye M, Van Braekel J, et al.Targeting the 16S rRNA Gene for Bacterial Identification in Complex Mixed Samples: Comparative Evaluation of Second (Illumina) and Third (Oxford Nanopore Technologies) Generation Sequencing Technologies. *Int J Mol Sci*. 2020;21(1):298 https://doi.org/10.3390/ijms21010298

25. de Souza LM, de Oliveira ID, Sales FCS, da Costa AC, Campos KR, Abbud A, et al. Technical comparison of MinIon and Illumina technologies for genotyping Chikungunya virus in clinical samples. *J Genet Eng Biotechnol*. 2023;21:88 https://doi.org/10.1186/s43141-023-00536-3

26. Ye F, Han Y, Zhu J, Li P, Zhang Q, Lin Y, и др. First Identification of Human Adenovirus Subtype 21a in China With MinION and Illumina Sequencers. *Front Genet*. 2020 https://doi.org/10.3389/fgene.2020.00285

27. Peng, K., Yin, Y., Li, Y., Qin, S., Liu, Y., Yang, X., Wang, Z., & Li, R. (2022). QitanTech Nanopore Long-Read Sequencing Enables Rapid Resolution of Complete Genomes of Multi-Drug Resistant Pathogens. *Frontiers in microbiology*, *13*, 778659 https://doi.org/10.3389/fmicb.2022.778659

28. Wang, Z., Qin, L., Liu, J., Jiang, L., Zou, X., Chen, X., Song, F., Dai, H., & Hou, Y. (2022). Forensic nanopore sequencing of microhaplotype markers using QitanTech's QNome. *Forensic science international. Genetics*, *57*, 102657 https://doi.org/10.1016/j.fsigen.2021.102657

AUTHORS

Diana A. Grigoryan
https://orcid.org/0000-0001-9763-9879
DGrigoryan@cspfmba.ru

Ivan F. Stetsenko
https://orcid.org/0000-0003-0979-3409
IStecenko@cspfmba.ru

Boris S. Gukov
https://orcid.org/0000-0002-2587-0630
BGukov@cspfmba.ru

Alina D. Matsvay, Cand. Sci. (Biol.)
https://orcid.org/0000-0002-6301-9169
AMatsvay@cspfmba.ru

German A. Shipulin, Cand. Sci. (Med.)
https://orcid.org/0000-0002-3668-6601
Shipulin@cspfmba.ru

DEVELOPMENT AND EVALUATION OF A REAGENT SET FOR QUANTITATION OF MRNA EXPRESSION LEVEL OF CHIMERIC *BCR::ABL1* GENE

Mariia A. Avdonina[1]✉, Natalia G. Kuklina[1,2], Arina A. Glavatskaya[1,2], Vladislav K. Dmitriev[3], Anzhelika S. Chegodar[3], Anastasia M. Danishevich[3], Natalia A. Bodunova[3], Ivan S. Abramov[3], German A. Shipulin[1]

[1] Centre for Strategic Planning, of the Federal Medical and Biological Agency, Moscow, Russia

[2] Izmerov Research Institute of Occupational Health, Moscow, Russia

[3] Loginov Moscow Clinical Scientific Centre, Moscow, Russia

Introduction. Chronic myeloid leukemia is a myeloproliferative disease associated with a t(9;22)(q34;q11) translocation resulting in a chimeric *BCR::ABL1* gene. Molecular genetic studies are used as a diagnostic method and for determination of minimal residual disease by quantification of the mRNA expression level of the chimeric *BCR::ABL1* gene.

Objective. To validate the developed multiplex test system for simultaneous quantitative determination of e13a2 (b2a2) and e14a2 (b3a2) transcripts of translocation p210 in comparison with the analog system registered in Russia.

Materials and methods. In total, 50 peripheral blood samples were used. Of these, 39 belonged to patients diagnosed with CML; 11 blood samples from healthy people were used to confirm analytical specificity. The reagent kit includes the specifically developed primers and fluorescently labeled probes, the concentration of which was selected experimentally, as well as original reagents manufactured by the Centre for Strategic Planning, Federal Medical and Biological Agency (Russia). Statistical analysis was performed using the StatTech v.4.5.0 software (developed by StatTech, Russia). Differences were considered significant at $p < 0.05$.

Results. The conducted analytical and diagnostic characterization of the developed kit showed the following results. The relative sensitivity determined using cell standards was 0.01 %. The reproducible analytical sensitivity was 100 copies/mL (CV = 1.86 %). In analytical specificity testing, the absence of false results was shown. When testing the reagents of the test system on clinical samples, the complete convergence (100 %) with the results obtained using the reference kit was revealed.

Conclusions. Approbation of the developed reagent set showed its sufficiently high analytical sensitivity and diagnostic sensitivity. This set can be used for identification and quantitative determination of the mRNA of the chimeric *BCR::ABL1* gene for the purposes of diagnosis, timely and accurate therapy, and monitoring of minimal residual disease.

Keywords: chronic myeloid leukemia; chimeric *BCR::ABL1* gene; molecular genetic monitoring

РАЗРАБОТКА И ОЦЕНКА НАБОРА РЕАГЕНТОВ ДЛЯ КОЛИЧЕСТВЕННОГО ОПРЕДЕЛЕНИЯ УРОВНЯ ЭКСПРЕССИИ мРНК ХИМЕРНОГО ГЕНА *BCR::ABL1*

М.А. Авдонина[1]✉, Н.Г. Куклина[1,2], А.А. Главацкая[1,2], В.К. Дмитриев[3], А.С. Чегодарь[3], А.М. Данишевич[3], Н.А. Бодунова[3], И.С. Абрамов[3], Г.А. Шипулин[1]

[1] Центр стратегического планирования и управления медико-биологическими рисками здоровью Федерального медико-биологического агентства, Москва, Россия

[2] Научно-исследовательский институт медицины труда им. академика Н.Ф. Измерова, Москва, Россия

[3] Московский клинический научный центр имени А.С. Логинова, Москва, Россия

Введение. Хронический миелолейкоз (ХМЛ) — миелопролиферативное заболевание, ассоциированное с транслокацией t(9;22)(q34;q11), в результате которой образуется химерный ген *BCR::ABL1*. Одним из методов постановки диагноза, а также определения минимальной остаточной болезни является молекулярно-генетическое исследование, а именно количественное определение уровня экспрессии мРНК химерного гена *BCR::ABL1*.

Цель. Апробация разработанной мультиплексной тест-системы для одновременного количественного определения транскриптов e13a2 (b2a2) и e14a2 (b3a2) транслокации p210 в сравнении с зарегистрированным в России аналогом.

Материалы и методы. В качестве образцов использовали 50 проб периферической крови. Из них 39 проб принадлежали пациентам с установленным диагнозом ХМЛ, 11 образцов от здоровых участников использовались для подтверждения аналитической специфичности. В состав набора реагентов входят разработанные праймеры и флуоресцентно-меченые зонды, концентрация которых была подобрана экспериментально, а также оригинальные реагенты производства ФГБУ «ЦСП» ФМБА (Россия). Статистический анализ проводился с использованием программы StatTech v.4.5.0 (разработчик — ООО «Статтех», Россия). Различия считались значимыми при $p < 0,05$.

Результаты. Экспериментальные данные по определению аналитических и диагностических характеристик разработанного набора показали следующие результаты: относительная чувствительность, определяемая с помощью клеточных стандартов, составила 0,01%. Воспроизводимая аналитическая чувствительность составила 100 копий/мл (CV = 1,86%). При проверке аналитической специфичности было показано отсутствие ложноспецифических выходов. При тестировании реагентов тест-системы на клинических образцах было выявлено полное совпадение (100%) с результатами, полученными при использовании аналога зарегистрированного в России набора.

Выводы. Апробация разработанного нами набора реагентов продемонстрировала достаточно высокие показатели аналитической и диагностической чувствительности, что позволит обнаруживать и выявлять количество мРНК химерного гена *BCR::ABL1* как для диагностики, назначения своевременной и точной терапии, так и для мониторинга минимальной остаточной болезни.

Ключевые слова: хронический миелолейкоз; химерный ген BCR::ABL1; молекулярно-генетический мониторинг

✉ Авдонина Мария Алексеевна MAvdonina@cspmz.ru

INTRODUCTION

Chronic myeloid leukemia (CML) is a clonal myeloproliferative neoplasm caused by malignant degeneration of hematopoietic stem cells. This disease is characterized by increased proliferation of granulocytic germ cells without the loss of their differentiation ability, hyperplasia of myeloid tissue, myeloid metaplasia of hematopoietic organs. These disorders are associated with a chromosomal abnormality, i.e., t(9;22)(q34;q11) translocation or the so-called Philadelphia chromosome, as a result of which the chimeric *BCR::ABL1* gene is formed [1]. This fusion is the most common cytogenetic abnormality in adult patients with chronic myeloid leukemia (CML) in 95% of cases, as well as with acute lymphoblastic leukemia (ALL) in 30% of adults and about 5% of children[1] [1].

According to the statistical data for 2022, 1087 new cases of CML were detected in Russia, with about 54% women and 47% men. This nosology is most frequently (in 28.9% of cases) registered in people aged 60–69 years. In 16.5% of cases, CML was detected in people aged 50–59 years and 70–79 years. The incidence of CML in people aged 30–39 years equals about 12% [2].

The mentioned translocation is diagnosed by cytogenetic examination (karyotype) of the bone marrow or molecular cytogenetic examination (FISH method), as well as by determining the quantitative level of expression of *BCR::ABL1* p210 mRNA for e13a2 or e14a2 transcripts.[2]

Modern therapy is aimed at achieving a major molecular response (MMR>3.0), a deep molecular response (DMR≥4.0), as well as at the subsequent prevention of the appearance of tumor clones [3, 4]. Several assessment methods can be used to monitor the response to treatment with tyrosine kinase inhibitors (TKI), such as a complete hematologic response, determined by examining the complete blood count; a partial hematologic response, determined by flow cytometry; and a complete cytological response, evaluated using bone marrow aspirate and biopsy samples based on studying the molecular response using quantitative PCR [5].

PCR is known to be the most sensitive method for assessing minimal residual disease; however, the diversity of reagent kits from different manufacturers results in a high interlaboratory variability in the results obtained. This also leads to inconsistencies in the compared indicators, thus affecting the selection of appropriate treatment tactics. According to the recommendations of the European LeukemiaNet and the National Comprehensive Cancer Network, CML molecular monitoring can be harmonized by monitoring the *BCR::ABL1* mRNA levels using the international scale (IS), which is based on the standardized basic transcript level presented in the International Randomized Study of Interferon and STI571–IRIS [3]. According to the results obtained, this study proposed to evaluate the logarithmic decrease in *BCR::ABL1* (IS ratio) during therapy in comparison with the initial IRIS ratio at diagnosis [6, 7]. To be able to apply this International Scale, each laboratory must calibrate the results obtained using a conversion factor (CF), the numerical value of which must be multiplied by the quantitative indicators obtained in a particular laboratory. In order to determine the CF, which is individual for each laboratory, the World Health Organization has created an international genetic panel for quantification of *BCR::ABL1* transcripts using PCR, containing four different variants (10%, 1%, 0.1%, 0.01%), using the K562 cell line diluted in the cell line, the *BCR::ABL1* merger code [9].

According to the recommendations of International Guidelines for the diagnosis of *BCR::ABL1* mRNA expression and monitoring of minimal residual disease, it is necessary to use the quantitative reverse transcription PCR (RT-PCR) method with a detection sensitivity lower than MO 4.5 (0.0032% IS) [4, 9]. The use of reagents with insufficient sensitivity can lead to incorrect test results and, as a result, premature termination of treatment and further progression of the disease [6]. According to Clinical Recommendations, the procedure for periodic monitoring of expression levels has been define as follows. When the expression level of p210 *BCR::ABL1* mRNA is below the BMO, quantitative real–time PCR is performed every three months. After reaching the BMO, the assay is performed every six

---

[1]   Clinical Guidelines: Management of Chronic Myeloid Leukemia (CML) in adults. C92.1.
[2]   Ibid.

months [10, 11]. In this regard, the development, testing, and implementation into clinical and laboratory practice of domestic highly sensitive specific diagnostic reagent kits for determining the level of *BCR::ABL1* transcripts using PCR present a relevant research task.

In this work, we set out to develop and evaluate a set of reagents for quantitative determination of the mRNA expression level of the chimeric *BCR::ABL1* gene in peripheral blood samples.

MATERIALS AND METHODS

The study included 50 people aged 20 to 80 years, including 28 men and 22 women. The main group consisted of 39 patients with the established clinical diagnosis of CML. In order to validate the analytical specificity for the absence of false positive results, blood samples from 11 apparently healthy individuals, comparable in gender and age with the main group of patients, were used.

Peripheral blood samples were obtained at the Loginov Moscow Clinical Scientific Centre; all the participants were requested to sign an informed consent. Blood sampling was carried out in vacuum tubes with K2 EDTA (China). To confirm the diagnosis of CML and determine the mRNA expression level of the chimeric gene *BCR::ABL1*, a set of reagents was used to detect and quantify the *BCR::ABL1* chimeric gene mRNA (M-bcr variant) and the abl gene mRNA in clinical material by real-time PCR with fluorescence detection AmpliSens® Leukemia Quantum M-bcr-FRT (Central Research Institute of Epidemiology, Russia) according to the manufacturer's instructions.

RNA was isolated using a set of AmpliTest® RIBO-prep reagents (Centre for Strategic Planning, FMBA, Russia) according to the instructions. The efficiency of mRNA isolation was determined using a Qubit 4 fluorimeter (Thermo Scientific, USA).

The developed reagent kit includes specific primers and fluorescently labeled probes, the presence of which allows simultaneous detection of the expression of the chimeric *BCR::ABL1* gene and the *ABL1* gene. The oligonucleotides for detecting chimeric gene expression were selected based on the recommendations of the international group Europe Against Cancer (EAC) in 2003 and allowed the identification of the two most common chimeric transcripts, i.e., e13a2 (b2a2) and e14a2 (b3a2). The control of material collection, RNA isolation, reverse transcription reaction, and PCR was carried out using endogenous internal control, which used specifically selected primers and a probe for the *ABL1* gene.

The concentrations of primers and fluorescently labeled probes were selected experimentally.

The reaction mixture was prepared using the following reagents (manufactured by Centre for Strategic Planning, FMBA, Russia): 5x PCR buffer (5 μL), 10 mM dNTP (0.5 μL), Taq polymerase (0.5 μL), and MMLV revertase (0.25 μL).

PCR amplification conditions were as follows: reverse transcription at 50°C (30 min), preheating at 95°C (15 min), followed by 45 cycles of denaturation at 95°C (10 sec) and annealing at 60°C (60 sec). The fluorescent signal was detected via the FAM and HEX channel.

Interpretation was carried out only for correct results for a negative control sample (NCS) and a positive control sample (PCS) at each setting. Sterile deionized water was used as a NCS; PCS was a mixture of bacteriophage preparations containing sequences of mRNA translocation p210 of the chimeric gene *BCR::ABL1* and mRNA of the control gene *ABL1*.

Plasmids containing mRNA sequences of translocation p210 of the chimeric *BCR::ABL1* gene and mRNA of the control *ABL1* gene with a known concentration were used as calibrators. The concentration of plasmids was measured using the QX200 digital PCR system (Bio-Rad, USA). Plasmids were used in five 10-fold dilutions from about 10 to 1×10^6 copies/mL to determine the linearity and effectiveness of RT-PCR. A single-stage RT-PCR reaction was performed on a DT-96 amplifier (DNA Technology, Russia).

To establish the detection limit for the specificity and sensitivity of the developed kit, RNA isolated from the K562 cell line (*BCR::ABL1* — positive) and HeLa (wild-type samples), as well as samples from CML patients and healthy donors, were used. To determine the relative sensitivity, cellular standards with certain concentrations were prepared, namely 10%, 1%, 0.1%, and 0.01% according to the procedure described by White et al., 2010 [8]. The number of cells was calculated using an automatic Countess II FL Automated Cell Counter (Thermo FS). The resulting standards were calibrated according to the WHO protocol [12].

The relative mRNA expression level of the chimeric *BCR::ABL1* gene was estimated based on calculations for *BCR::ABL1*/ABL1 using the following formula:

$$\frac{BCR::ABL1 \text{ copies number}}{ABL1 \text{ copies number}} \times 100\%.$$

Statistical analysis was performed using the StatTech v.4.5.0 software (developed by Stattech LLC, Russia). Differences were considered significant at $p < 0.05$.

RESULTS AND DISCUSSION

Testing of the reagent kit developed in this study produced the following results. Real-time PCR parameters were as follows: efficiency ranging within 95–105% and the correlation coefficient $r = 0.99$. According to experimental data using cellular standards, the relative sensitivity of the developed set was 0.01%, which corresponds to the level of complete molecular response (CMR)[3]. The reproducible sensitivity for control plasmids and for RNA isolated from K562 cell culture was 100 copies/mL (CV% = 1.86).

Verification of the analytical specificity showed the absence of false positive results when testing samples obtained from healthy patients. During testing, only the internal control signal via the HEX channel was detected; the mRNA detection signal for the chimeric *BCR::ABL1* gene in the FAM channel was absent.

In this study, we analyzed a random sample of peripheral blood samples from patients with the clinical diagnosis of CML. In the main group, mRNA expression of translocation p210 of the chimeric *BCR::ABL1* gene was

---

[3]   Clinical Guidelines: Management of Chronic Myeloid Leukemia (CML) in adults. C92.1.

detected in all 39 samples. The number of positive results was 21 (53.8%) and 18 (46.2%) among men and women, respectively. The incidence of translocation in the age groups of 20–29, 30–49, 50–59, 60–69 and 70–79, and over 80 years comprised 3.2, 12.9, 9.6, 19.3, and 6.4% of cases, respectively, which agrees well with statistical data. The largest number of patients with these changes were registered in the age group of 60–69 and 70–79 years, which is also consistent with statistical data for Russia [2]. Patients under the age of 20 years were not represented due to their limited sample. Morbidity at this age equals about 1% nationwide. CML is equally common in both men and women [13, 14].

The relative expression of the *BCR::ABL1* gene (protein p210, variants b3a2 or b2a2) according to the results of testing in peripheral blood samples of patients with the clinical diagnosis of CML ranged from 2.3% to 100%. The number of copies of the *ABL1* gene ranged from 2200 copies/mL to 17,595,440 copies/mL in the CML group and from 11,675,896 copies/mL to 18,634,577 copies/mL in the control group.

According to the Laboratory Guidelines for the Diagnosis and Treatment of Chronic Myeloid Leukemia (European LeukemiaNet), the minimum number of reference gene transcripts, regardless of whether *BCR::ABL1* is detected or not, should be at least 10,000 ABL1 for MR 4, 32,000 for MR 4.5, and 100,000 for MR 5 in the same volume of cDNA in which the sample is being tested for *BCR::ABL1* [4]. The number of transcripts of the reference gene obtained meets international standards; therefore, the results can be included in clinical reports.

During testing of CML patients, eight samples of IS<1% BCR were identified: ABL1 (MR 2), nine samples of IS<0.1% (MR 3), seven samples of IS<0.01% (MR 4), seven samples of IS<0.0032% (MR 4.5). The object of the study was blood samples from randomized patients. The criterion for inclusion in the main group of patients was the presence of the confirmed diagnosis of CML, established using the AmpliSens® Leukemia Quantum M-bcr-FRT analogue registered in Russia.

Testing of the developed reagent kit on peripheral blood samples with a known level of expression of the chimeric *BCR::ABL1* gene demonstrated their complete agreement with the results obtained using the AmpliSens® Leukemia Quantum M-bcr-FRT reagent kit.

When establishing the diagnosis of CML, molecular genetic analysis (FISH method) is used to identify the chimeric *BCR::ABL1* gene, as well as to determine the expression of *BCR::ABL1* p210 mRNA (quantitative) for chimeric e13a2 or e14a2 transcripts by PCR [15]. This method is also used in assessing the level of response to treatment of patients with tyrosine kinase inhibitors (TKI) and determining the level of minimal residual disease when the number of residual leukemic cells is below the sensitivity level of cytogenetic studies [16].

The current market offers a number of domestic test systems designed to detect the mRNA of the chimeric *BCR::ABL1* gene. These include, e.g., AmpliSens® Leukemia Quantum M-bcr-FRT (Central Research Institute

of Epidemiology of Rospotrebnadzor), ONCOSCREEN 1-1-Q (GenoTechnology), with and without registration certificates: Myeloscreen BCR-ABL (Gene Formula), BCR-ABL1 Mbcr RQ Kit® ("Inogen").

In terms of the number of reproducible copies, the analytical sensitivity of the AmpliSens® Leukemia Quantum M-bcr-FRT kit was twice as low as that of the analyzed kit, amounting to 237 copies/mL vs 100 copies/mL.[4] At the same time, the analysis using the AmpliSens® Leukemia Quantum M-bar-FRT kit involves setting up a reverse transcription reaction initially in isolation, and then performing real-time PCR, which is quite laborious. Unlike the reference kit, the developed kit used a mixture that allows detecting the expression of *BCR::ABL1* p210 mRNA in one tube.

The results of quantification of *BCR::ABL1* mRNA obtained using the kit under study were similar to those recorded using the AmpliSens® Leukemia Quantum M-bcr-FRT kit in all samples. Both sets are capable of identifying at least a 4.5-fold decrease in the IS ratio.

The BCR/ABL MULTITEST kit can be used to simultaneously detect chimeric transcripts p210, p190, and p230 of the *BCR::ABL1* gene using the RT-PCR multiplex format, which is economically feasible during primary screening [17].

In 2019, Kitamura et al. presented a new high-sensitive two-stage reagent kit RT-PCR (Reverse Transcription Polymerase Chain Reaction) with a diagnostic sensitivity of 0.01%, which was determined using the Armored RNA Quant® (ARQ) secondary control panel (Asuragen, Inc., Austin, Texas, USA) [6]. Dubina et al. determined the analytical parameters of the test, in which the specificity should strive for 100%, adequate for the sensitivity level of 3–5 copies of mRNA to the reaction, while the ratio of the *BCR::ABL1* transcript to the normalizer gene should be 0.01% (corresponding to the level of CMR) [18].

In comparison with its analog system, the developed kit has a number of advantages. Firstly, it exhibits higher analytical indicators. Secondly, the use of single-stage RT-PCR significantly reduces the risk of contamination and technical errors during the excavation of reagents and samples, while also reducing the working time of personnel. Finally, the multiplex mixture of specific probes and primers used over two detection channels can significantly reduce the amount of expendable materials used.

Thus, we have succeeded in creating a highly sensitive multiplex test system for simultaneous detection of e13a2 (b2a2) and e14a2 (b3a2) transcripts of the p210 translocation, which also assumes endogenous internal control to assess the correctness of all stages of PCR, including RNA isolation.

CONCLUSION

Quantification and detection of translocation in CML is essential for selecting adequate treatment protocols and monitoring disease recurrence. Sensitive and accurate monitoring of minimal residual disease plays an important

---

4   https://roszdravnadzor.gov.ru/services/misearch

role in managing CML, facilitating the decision-making process concerning treatment cessation and identification of patients at risk of progression. The conducted testing of the developed test system, which makes it possible to detect the p210 transcript of the chimeric *BCR::ABL1* gene, showed a sufficiently high order of diagnostic specificity and sensitivity of the developed set of reagents for

quantitative detection of the level of relative mRNA expression of the chimeric *BCR::ABL1* gene in the blood in order to verify the diagnosis of CML at the level of 100%. The use of endogenous internal control (the *ABL1* gene) made it possible to monitor the main stages of PCR (sample preparation, RNA isolation, reverse transcription, and amplification reactions).

References

1. Ravandi F, Kebriaei P. Philadelphia chromosome-positive acute lymphoblastic leukemia. *Hematol Oncol Clin North Am*. 2009;23(5):1043–63.
https://doi.org/10.1016/j.hoc.2009.07.007
2. Kaprin AD, ed. Malignant neoplasms in Russia in 2022 (morbidity and mortality). M.:NMRRC of the Ministry of Health of Russia; 2023(In Russ.).
3. Etienne G, Guilhot J, Rea D, Rigal-Huguet F, Nicolini F, Aude C, et al. Long-Term Follow-Up of the French Stop Imatinib (STIM1) Study in Patients With Chronic Myeloid Leukemia. *J Clin Oncol.* 2017;35(3):298–305.
https://doi.org/10.1200/JCO.2016.68.2914
4. Hochhaus A, Baccarani M, Silver RT, Schiffer C, Apperley JF, Cervantes F, et al. European LeukemiaNet 2020 Recommendations for Treating Chronic Myeloid Leukemia. *Leukemia*. 2020;34(4):966–84.
https://doi.org/10.1038/s41375-020-0776-2
5. Kantarjian H, Schiffer C, Jones D, Cortes J. Monitoring the response and course of chronic myeloid leukemia in the modern era of BCR-ABL tyrosine kinase inhibitors: practical advice on the use and interpretation of monitoring methods. *Blood*. 2008;111(4):1774–80.
https://doi.org/10.1182/blood-2007-09-110189
6. Kitamura H, Tabe Y, Ai T, Tsuchiya K, Yuri M, Misawa S, et al. A new highly sensitive real-time quantitative-PCR method for detection of BCR-ABL1 to monitor minimal residual disease in chronic myeloid leukemia after discontinuation of imatinib. *PLoS One*. 2019;14(3):e0207170.
https://doi.org/10.1371/journal.pone.0207170
7. Martinez RJ, Kang Q, Nennig D, Bailey N, Brown N, Betz B, et al. One-Step Multiplexed Droplet Digital Polymerase Chain Reaction for Quantification of p190 BCR-ABL1 Fusion Transcript in B-Lymphoblastic Leukemia. *Arch Pathol Lab Med*. 2022;146(1):92–100.
https://doi:10.3390/diagnostics12061305
8. White H.E, Matejtschuk P, Rigsby P, Gabert J, Lin F, Wang YL, et al. Establishment of the first World Health Organization International Genetic Reference Panel for quantitation of BCR-ABL mRNA. *Blood*. 2010;116(22):e111–7.
https://doi.org/10.1182/blood-2010-06-291641
9. Özdemir NZ, Kılıçaslan NA, Yılmaz M, Eşkazan AE. Guidelines for the treatment of chronic myeloid leukemia from the NCCN and ELN: differences and similarities. *Int J Hematol*. 2023;117(1):3–15.
https://doi.org/10.1007/s12185-022-03446-1
10. Kottwitz D, Hadi EH, Amrani E, Cabezas S, Dehbi H, Nadifi S, et al. Evaluation of a novel multiplex RT-qPCR assay for the quantification of leukemia-associated BCR-ABL1 translocation. *Int J Hematol*. 2015;102(3):335–41.
https://doi.org/10.1007/s12185-015-1839-4
11. Franke GN, Maier J, Wildenberger K, Cross M, Giles FJ, Müller MC, et al. Comparison of Real-Time Quantitative PCR and Digital Droplet PCR for BCR-ABL1 Monitoring in Patients with Chronic Myeloid Leukemia Comparative Study. *J Mol Diagn*. 2020;22(1):81–9.
https://doi.org/10.1016/j.jmoldx.2019.08.007
12. International Standard, 1st WHO International Genetic Reference Panel for the quantitation of *BCR-ABL1* translocation NIBSC code: 09/138
13. Winn AN, Atallah E, Cortes J, Deininger MWN, Kota V, Larson RA, et al. Estimated Savings After Stopping Tyrosine Kinase Inhibitor Treatment Among Patients With Chronic Myeloid Leukemia. *JAMA Netw Open*. 2023;6(12):e2347950.
https://doi.org/10.1001/jamanetworkopen.2023.47950
14. Cantoni N, Sommavilla R, Seitz P, Kulenkampff E, Kahn S, Lambert JF, et al. A multicenter real-world evidence study in the Swiss treatment landscape of chronic myeloid leukemia. *BMC Cancer.* 2022;22(1):1192.
https://doi.org/10.1186/s12885-022-10241-y
15. Cross NCP, Ernst T, Branford S, Cayuela J-M, Deininger M, Fabarius A,et al. European LeukemiaNet laboratory recommendations for the diagnosis and management of chronic myeloid leukemia. *Leukemia*. 2023;37(11):2150–67.
https://doi.org/10.1038/s41375-023-02048-y
16. Ryabchikova NR, Minniakhmetov IR, Safuanova GSh, Islamgulov DV, Karunas AS, Khusnutdinova EE. Chronic myelogenous leukemia: molecular monitoring in clinical practice. *Oncohematology*. 2013;8(1):7–16 (In Russ.).
https://doi.org/10.17650/1818-8346-2013-8-1-7-16
17. Gorbenko AS, Stolyar MA, Vasiliev EV, Mikhalev MA, Bakhtina VI, Olkhovik TI, et al. Use of the «BCR/ABL — multitest» kit in the algorithm of laboratory diagnostics of oncohematological diseases: economic aspects. *Clinical laboratory diagnostics*. 2021;66(9):571–6 (In Russ.).
https://doi.org/10.51620/0869-2084-2021-66-9-571-576
18. Dubina MV, Kuevda DA, Khomyakova TE, Tsaur GA, Kutsev SI, Zaritskiy AY. Molecular monitoring of the effectiveness of therapy in patients with chronic myeloid leukemia in Russia. *Journal of Modern Oncology*. 2010;4(12):9–17 (In Russ.).
EDN: NCXVBJ

AUTHORS

Mariia A. Avdonina, Cand. Sci. (Biol.)
https://orcid.org/0000-0002-8605-7432
marysheilaus@gmail.com

Natalia G. Kuklina, Cand. Sci. (Biol.)
https://orcid.org/0000-0002-8255-6226
NKuklina@cspfmba.ru

Arina A. Glavatskaya
https://orcid.org/0000-0001-6223-8258
abessonova1705@gmail.com

Vladislav K. Dmitriev
https://orcid.org/0009-0004-6282-0036
meetyourmeetr1ch@gmail.com

Anzhelika S. Chegodar
https://orcid.org/0000-0001-7753-3698
a.chegodar@mknc.ru

Anastasia M. Danishevich
https://orcid.org/0000-0002-3573-8342
a.danishevich@mknc.ru

Natalia A. Bodunova, Cand. Sci. (Med.)
https://orcid.org/0000-0002-3119-7673
n.bodunova@mknc.ru

Ivan S. Abramov
https://orcid.org/0000-0002-6954-1564
i.abramov@mknc.ru

German A. Shipulin, Cand. Sci. (Med.)
https://orcid.org/0000-0002-9734-0620
shipulin@cspfmba.ru

NGS ANALYSIS OF THE MUTATIONAL PROFILE OF PATIENTS WITH Ph-NEGATIVE MYELOPROLIFERATIVE NEOPLASMS

Anna N. Kirienko[1]✉, Ekaterina V. Motyko[1], Elizaveta V. Efremova[1], Daria V. Kustova[1], Tatyana N. Gert[1], Irina V. Leppyanen[1],
Vasily A. Shuvaev[2,3], Irina S. Martynkevich[1]

[1] Russian Research Institute of Hematology and Transfusiology, Saint-Petersburg, Russia

[2] Russian Medical Academy of Continuous Professional Education, Moscow, Russia

[3] Tsyb Medical Radiological Research Center, Obninsk, Russia

Introduction. The identification of driver mutations in the *JAK2, CALR,* and *MPL* genes is a gold standard approach in the molecular diagnosis of patients with Ph-negative myeloproliferative neoplasms (Ph-MPNs). However, such patients are characterized by a heterogenous genomic landscape. Standard molecular genetic methods cannot be used to identify most somatic mutations, thus failing to provide a comprehensive understanding of the course and prognosis of Ph-MPNs and to confirm the clonality of the disease in patients with triple-negative status. The next generation sequencing (NGS) technology allows simultaneous analysis of an extensive panel of genes and identification of both pathogenic and driver mutations.

Aim. To evaluate the possibility of using NGS to study the mutational status of patients with Ph-negative MPNs and to analyze the effect of identified pathogenic mutations on patient survival.

Materials and methods. The study included 83 patients with polycythemia vera, essential thrombocythemia, and primary myelofibrosis aged from 19 to 85 years (the median onset age of 51 years). For all patients, sequencing was performed using a myeloid panel of 118 genes with an average reading depth of 1000x on MiSeq (Illumina, USA). The clinical significance of the mutations was determined using the COSMIC and Franklin databases. The survival rate was analyzed using the Kaplan–Meyer method followed by assessment of statistical significance using the Cox-Mantel test in the GraphPad Prism 8 environment.

Results. Pathogenic mutations in 23 genes were detected in 39 (46%) patients out of the total cohort of patients. The most frequent mutations were detected in the *ASXL1* gene in 25% of patients, which reduced event-free survival by 50.3% (Me = 7.83 years vs 15.75 years). The pathogenic mutations identified in other genes combined with mutations in driver genes also decreased event-free survival compared to patients with isolated driver mutations. Two or more pathogenic mutations significantly reduced event-free survival compared to patients with only one pathogenic mutation. The NGS method was also capable of identifying pathogenic mutations in 8 out of 10 triple-negative patients studied, thus confirming the clonality of the disease.

Conclusions. The next-generation sequencing (NGS) method using a panel of 118 genes is an effective tool in identifying predictively significant mutations important for selecting the most effective personalized therapy to achieve hematologic response.

Keywords: Ph-negative myeloproliferative neoplasms; next-generation sequencing; pathogenic mutations; event-free survival

ИЗУЧЕНИЕ МУТАЦИОННОГО ПРОФИЛЯ БОЛЬНЫХ Ph-НЕГАТИВНЫМИ МИЕЛОПРОЛИФЕРАТИВНЫМИ НОВООБРАЗОВАНИЯМИ МЕТОДОМ NGS

А.Н. Кириенко[1]✉, Е.В. Мотыко[1], Е.В. Ефремова[1], Д.В. Кустова[1], Т.Н. Герт[1], И.В. Леппянен[1], В.А. Шуваев[2,3], И.С. Мартынкевич[1]

[1] Российский научно-исследовательский институт гематологии и трансфузиологии Федерального медико-биологического агентства, Санкт-Петербург, Россия

[2] Российская медицинская академия непрерывного профессионального образования, Москва, Россия

[3] Медицинский радиологический научный центр имени А.Ф. Цыба, Обнинск, Россия

Введение. Определение драйверных мутаций в генах *JAK2, CALR* и *MPL* является «золотым стандартом» в молекулярной диагностике пациентов с Ph-МПН. Однако геномный ландшафт таких пациентов гетероген, и стандартные молекулярно-генетические методы не позволяют выявить большинство соматических мутаций и тем самым не дают полного представления об особенностях течения и прогнозе Ph-МПН, а также не позволяют подтвердить клональность заболевания у больных с тройным негативным статусом. Метод секвенирования следующего поколения (NGS) дает возможность одновременно провести анализ обширной панели генов и выявить как патогенные, так и драйверные мутации.

Цель. Оценка возможности использования NGS в изучении мутационного статуса пациентов с Ph-негативными МПН и анализ влияния выявленных патогенных мутаций на выживаемость пациентов.

Материалы и методы. В исследование были включены 83 пациента с диагнозами «истинная полицитемия», «эссенциальная тромбоцитемия» и «первичный миелофиброз» в возрасте от 19 до 85 лет (медиана начала заболевания — 51 год). У всех пациентов секвенирование выполнялось с использованием миелоидной панели из 118 генов со средней глубиной прочтения 1000x на приборе MiSeq (Illumina, США). Клиническая значимость мутаций устанавливалась по базам данных COSMIC и Franklin. Для анализа выживаемости использовали метод Каплана — Мейера с оценкой статистической значимости с помощью теста Кокса — Мантела с использованием программы GraphPad Prism 8.

Результаты. Патогенные мутации в 23 генах были выявлены у 39 (46%) пациентов из общего числа больных. Наиболее часто, у 25% пациентов, мутации детектировали в гене *ASXL1*; они снижали бессобытийную выживаемость на 50,3% (Ме = 7,83 года против 15,75 года). Выявленные пато-

генные мутации в других генах сочетанно с мутациями в драйверных генах также ухудшали показатели бессобытийной выживаемости по сравнению с показателями пациентов, имевших изолированные драйверные мутации. Две и более патогенные мутации значимо снижали бессобытийную выживаемость по сравнению с пациентами с одной патогенной мутацией. Методом NGS также удалось выявить патогенные мутации у 8 из 10 исследуемых пациентов с тринегативным статусом и таким образом подтвердить клональность заболевания.

Выводы. Метод секвенирования следующего поколения (NGS) с использованием панели из 118 генов является эффективным инструментом в выявлении прогностически значимых мутаций, важных для подбора наиболее эффективной персонализированной терапии, позволяющей достигать гематологического ответа.

Ключевые слова: Ph-негативные миелопролиферативные новообразования; секвенирование следующего поколения; патогенные мутации; бессобытийная выживаемость

INTRODUCTION

BCR::ABL1-negative myeloproliferative neoplasms (Ph-MPNs) are clonal hematologic malignancies characterized by excessive release of mature myeloid cells into the blood, arising from a mutated hematopoietic stem cell [1, 2, 3]. Classic Ph-MPNs include polycythemia vera (PV), essential thrombocythemia (ET), and primary myelofibrosis (PMF) [4].

Recent advances in molecular genetics have revealed a common trigger mechanism in the pathogenesis of the above diseases. This mechanism is based on constant activation of the Janus kinase (JAK-STAT) signaling pathway in the cell, through which information is transmitted from external chemical signals to the nucleus, resulting in DNA transcription and expression of genes involved in immunogenesis, proliferation, differentiation, apoptosis, and oncogenesis [5]. Constant activation of the JAK-STAT signaling pathway is related to mutations in the *JAK2*, *CALR*, and *MPL* genes, referred to as driver mutations. Detection of mutations in these genes has become an integral part of the modern diagnostic algorithm for patients with MPNs, being included in current clinical guidelines. Deciphering the pathogenetic mechanisms of Ph-MPN development has contributed to the development and introduction into clinical practice of targeted therapy for Janus kinase inhibitors that block the intracellular JAK-STAT signaling system [5].

At the same time, recent studies have revealed the heterogeneity of the genomic landscape of Ph-negative MPNs. Mutations were detected in genes responsible for different functions within the cell, such as epigenetic regulation of DNA methylation (*TET2*, *DNMT3A* and *IDH1/2*), histone/chromatin modification (*ASXL1*, *EZH2*, *SUZ12*), RNA splicing (*SRSF2*, *SF3B1*, *U2AF1*), signal transduction (*SH2B3*, *LNK*, *CBL*, *RAS*, *NF1*) and transcription factors (*TP53* and *RUNX1*), and others [6–9]. Detection of these mutations possesses a diagnostic and prognostic value, allowing the risk of disease progression to be assessed, the most effective treatment tactics to be selected, and the need for hematopoietic stem cell transplantation to be determined. Thus, the next generation sequencing (NGS) method for simultaneous determination of the mutational status of a large number of genes is acquiring particular significance in the diagnosis of *BCR::ABL1*-negative MPNs in patients.

In this study, we aim to evaluate the feasibility of NGS analysis in studying the mutational status of patients with Ph-negative MPNs and to assess the impact of identified pathogenic mutations on patient survival.

MATERIALS AND METHODS

Our study enrolled 83 patients (30 males and 53 females) aged 19 to 85 years (with the median onset age of 51 years) undergoing hospital treatment in St. Petersburg and Moscow, Russian Federation. The diagnosis of Ph-negative MPN was previously established in all patients according to the WHO criteria. Out of them, 47, 15, and 21 patients were diagnosed with PMF, PV, and ET, respectively (Table 1).

All patients had been previously screened for mutations in driver genes followed by detection of mutations in the *JAK2* gene (V617F) in 54 cases (65%), *CALR* in 16 cases (19%), and *MPL* in 3 cases (4%). Nevertheless, these genes were included in the NGS panel of investigational genes for use as internal positive controls. The group of patients with ET and PMF without mutations in any of the driver genes (so-called triple-negative patients) comprised 10 (14.7%) patients of the total sample.

During the follow-up period, 14 patients showed phase transition or leukemic transformation: seven patients diagnosed with PMF showed transformation to Acute Myeloid Leukemia (AML); three patients with ET and four with PV showed transformation to secondary myelofibrosis

(Table 1). DNA isolation from peripheral blood samples was performed with a QIAamp RNA Blood Mini Kit (Qiagen, the Netherlands).

Identification of mutations in *JAK2, MPL, CALR* genes

Mutation in the *JAK2* gene was determined with a reagent kit for detection of V617F G/T mutation in *JAK2* (Janus kinase 2) gene (Syntol, Russian Federation). Mutations in the *CALR* and *MPL* genes were determined by Sanger sequencing using a NANOFOR-05 genetic analyzer (Syntol, Russian Federation). The following primers were used to design DNA fragments:
MPL-F 5'-TAGCCTGGATCTCCTTGGTG-3';
MPL-R 5'-AGAGAGGTGTGACGTGCAGGAAGT-3';
CALR-F 5'-TGAGGTGTGTGTGTGCTCTGCCT-3';
CALR-R 5'-AGAGACATTATTTGGCGCGCGG-3.

Next-generation sequencing

In all patients, sequencing was performed using a targeted exon panel of 118 genes with an average read depth of 1000x on a MiSeq device (Illumina, USA). The independently developed panel included key genes involved in myeloid neoplasms [6–9]. For Illumina sequencing, libraries were prepared from 200 ng of genomic DNA split into 300 bp fragments using a Covaris S2 focused ultrasound system.

Fragmented DNA was transformed into DNA libraries using a KAPA Hyper Prep Kit (Roche, Switzerland). DNA libraries were enriched using a Hyper Cap Target Enrichment kit and a KAPA Hyper Exome Probes kit (Roche, Switzerland) according to the manufacturer's protocol. The MGIEasy Circularization Module V2.0 (MGI, China) was used to prepare DNA libraries. Quantitative analysis of the library was performed on a Quantus fluorimeter with a QuantiFluor® dsDNA System kit (Promega, USA).

The Illumina Sequence Analysis Viewer software was used as the sequencing analysis viewer. The quality of the raw NGS data was assessed using the FastQC software in the Illumina BaseSpace Sequence Hub. Sequencing data were analyzed using a combination of two sequence alignment and variant calling applications also used in Illumina Base eSpace Sequence Hub, DNA Amplicon and Pindel, with a 3% allele frequency detection limit (VAF).

The clinical significance of mutations was determined using the COSMIC, ClinVar and Franklin databases according to the ACMG/AMP criteria. The KEGG database was used for gene function annotation.

The Kaplan–Meier method was used for survival analysis, with statistical significance assessed using the Cox-Mantel test. Statistical analysis was performed using GraphPad Prism 8 (GraphPad Software, La Jolla, CA, USA).

RESULTS

Mutational status of driver genes

At least one of the driver mutations in the *JAK2, CALR* and *MPL* genes was detected in 72 (87%) of the total number

Table 1. Patient cohort description

Main characteristics	Number of patients, *n*
Gender:	
male	30
female	53
Age (Me), yr	19–85 (51)
Diagnosis:	
Primary myelofibrosis (PMF)	47
Polycythemia vera (PV)	15
Essential thrombocythemia (ET),	21
Mutations in driver genes:	
JAK2	54
CALR	16
MPL	3
Triple-negative status	10
Phase transition / Leukemic transformation:	
PMF in acute myeloid leukemia	7
ET in secondary myelofibrosis	3
PV in secondary myelofibrosis	4

Table prepared by the authors using their own data

of patients diagnosed with Ph-negative MPN who participated in the study. This finding is consistent with the data obtained by other molecular methods.

We detected a mutation in the *JAK2* gene (V617F) in 27 (57.5%) patients diagnosed with PMF, a mutation in the *CALR* gene in 12 (25.5%), a mutation in the *MPL* gene in 2 (4.2%) patients. Mutations in driver genes were not detected in 6 (12.8%) patients (the so-called triple-negative status). In all 15 patients with PV, a mutation in the *JAK2* gene (V617F) was detected. In the *JAK2* gene, only mutation in exon 14 (V617F) was detected; mutations in exon 12 were not detected. In the *MPL* gene, mutations were detected only in the W515 position. Two main types of mutations were detected in the *CALR* gene: deletion of 52 nucleotides and insertion of 5 nucleotides.

In the course of the study, 12 (57%) of 21 patients diagnosed with ET had a mutation in the *JAK2* gene (V617F). Mutations in the *CALR* and *MPL* genes were registered in 4 (19%) and 1 (5%) patients, respectively. At the same time, 4 (19%) patients were triple-negative.

Mutation profile of the studied patient cohort

Our NGS study of 118 genes found mutations in 39 (46%) of 83 patients in 23 genes presented in Fig. 1. Moreover, 19 (49%) of 39 patients under observation showed one pathogenic mutation, with two mutations being recorded in 7 (18%) patients and three or more mutations being noted in 13 (33%) patients with Ph-negative MPNs. On average, one pathogenic mutation was detected across the entire cohort.
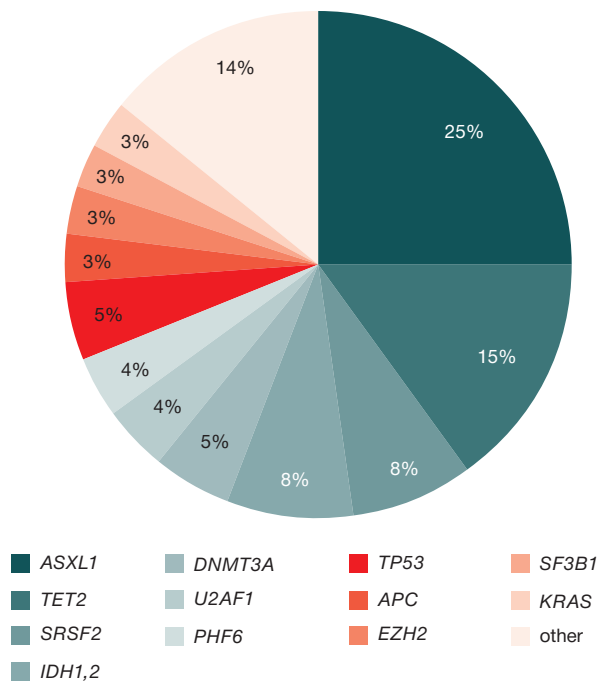
Fig. 1. Mutational profile of 83 patients with Ph-negative myeloproliferative neoplasms

In the analyzed sample of patients, pathogenic mutations were detected most often in the *ASXL1* and *TET2* genes, in 25% and 15% of patients, respectively. Mutations in the *SRSF2* and *IDH1/2* genes were detected in 8% of patients; *DNMT3A* — in 6%; *U2AF1*, *PHF6*, and *TP53* — in 4% each; *APC*, *EZH2*, *SF3B1*, and *KRAS* — in 3% each. Mutations in the *ATRX*, *CBL*, *DDX3X*, *EP300*, *GATA2*, *RUNX1*, *SETBP1*, *SUZ12*, and *ZRSR2* genes were detected only in 1% of patients each (Fig. 1).

Among triple-negative patients, pathogenic mutations were detected in 8 (80%) of 10 patients in seven different genes. In this case, only one mutation was detected in four of them; two patients had two mutations; and two patients had three pathogenic mutations simultaneously. Mutations in two genes combined *SRSF2* and *ASXL1* were detected in four patients with triple-negative status; a mutation in *IDH1* gene was detected in two patients; mutations in the *RUNX1*, *TET2*, *NF1*, and *HRAS* genes were detected in one patient.

Table 2. Functions of the genes identified during NGS analysis

Gene functions	Gene names
Chromatin (histones) modification	*ASXL1, ATRX, EZH2, EP300*
RNA splicing	*SRSF2, U2AF1, SF3B1, PHF6, DDX3X, ZRSR2*
DNA methylation	*DNMT3A, IDH1, IDH2, TET2, SUZ12*
Transcriptional factors	*RUNX1, TP53, GATA2*
DNA replication	*SETBP1, APC*
Signal transmission	*KRAS, CBL*

Table compiled by the authors; annotation of the gene function was carried out using the KEGG database

Fig. 2. Impact of mutations in the ASXL1 gene on event-free survival of patients with Ph-negative myeloproliferative neoplasms. The event was considered to be phase transition, leukemic transformation, or death

Our study established pathogenic mutations in 23 genes, which were further analyzed using the KEGG database to predict the functions of these genes. Most genes (*SRSF2*, *U2AF1*, *SF3B1*, *PHF6*, *DDX3X*, *ZRSR2*) are involved in RNA splicing and DNA methylation (*DNMT3A*, *IDH1*, *IDH2*, *TET2*, *SUZ12*). A smaller number of genes are responsible for chromatin (histone) modification, DNA replication and signaling within the cell; three genes act as transcription factors (Table 2). The limited cohort of the patients included in the study did not allow us to evaluate the impact of each functional group on the prognosis of the disease course or the efficacy of treatment therapy. Nevertheless, the analysis using the KEGG database improved our understanding of the molecular mechanisms underlying Ph-negative myeloproliferative neoplasms.

Genetic markers of leukemic transformation

On average, we detected two pathogenic mutations in 14 patients with phase transition to secondary myelofibrosis or leukemic transformation. Mutations in the *ASXL1* gene were detected in 9 (64%) patients; mutations in the *IDH1/2*, *DNMT3A*, *TET2* genes were detected in 3 (22%) patients; mutations in *SRSF2*, *SF3B1*, *TP53* genes were detected in 2 (14%) patients; mutations in *KRAS*, *SUZ12*, *PHF6* genes were detected in 1 (7%) patient.

Impact of identified mutations on event-free patient survival

Our study showed a significant impact of the gene mutation profile on event-free survival rates of patients. Thus, mutations in the *ASXL1* gene were statistically significantly associated (p = 0.0011) with a decreased event-free survival (median — 11.8 years and 15.75 years) (Fig. 2) in the studied cohort of patients.

An analysis of the data presented in Fig. 3 found that the combination of driver and any of the pathogenic mutations (driver+, pathogenic+ group) was statistically significantly associated with a decreased event-free survival compared to the group of patients with exclusively driver mutations (driver+, pathogenic- group) (median survival of 10 and
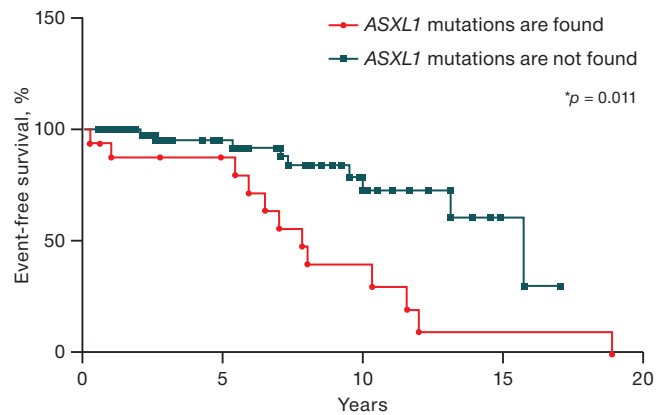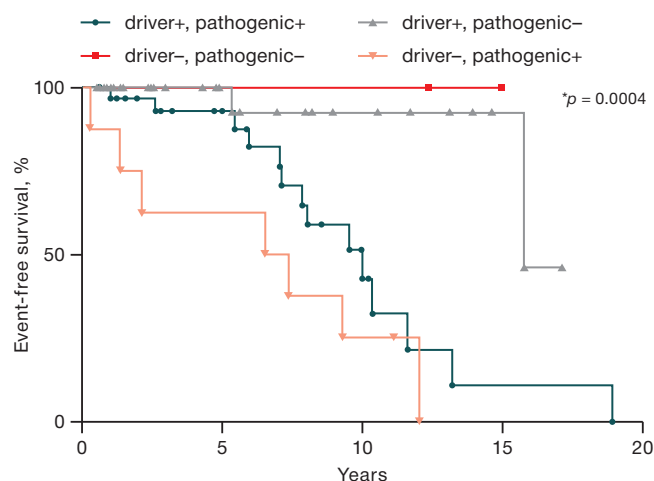
Figure prepared by the authors

Fig. 3. Impact of pathogenic mutations on event-free survival of patients with Ph-negative myeloproliferative neoplasms

Figure prepared by the authors

Fig. 4. Impact of the number of pathogenic mutations on event-free survival of patients with Ph-negative myeloproliferative neoplasms

15.8 years). The worst prognosis was shown for patients with triple-negative status and the presence of at least one pathogenic mutation (driver-, pathogenic+ group) (median survival of 6.9 years). For the group of patients in whom neither pathogenic nor driver mutations were detected (driver-, pathogenic+), the median survival was not reached.

Figure 4 shows that the presence of two or more mutations was also associated with a significantly decreased event-free survival ($p < 0.0001$) (median survival of 7 and 13.17 years) compared to patients with fewer pathogenic mutations. An analysis of NGS data showed that a higher number of pathogenic mutations was associated with a worse survival prognosis.

DISCUSSION

The pathogenesis of Ph-negative myeloproliferative neoplasms is based on mutations in the driver genes, including *JAK2*, *CALR*, and *MPL*. Detection of mutations in these genes is currently the basis of molecular diagnostics in patients with suspected Ph-negative MPNs. Meanwhile, recent studies have shown that the genetic landscape of classical Ph-negative MPNs is not limited only to mutations in driver genes. A significant number of mutations in various genes have been described as pathogenic for Ph-negative MPNs, influencing the phenotype, course, and prognosis of the disease. Rapid and reliable detection of such mutations in a wide range of genes is not possible with routine laboratory methods. In this regard, the NGS method, which detects mutations simultaneously in a large number of genes with high accuracy and sensitivity renders feasible.

At present, both in research and clinical practice, the diagnosis of patients with Ph-negative MPNs by NGS is performed using various personalized and commercial panels of genes [9–12]. In our study, the mutational status of patients with Ph-negative MPNs was investigated for the first time using a personalized panel of 118 genes. This panel includes not only genes associated with Ph-negative MPNs, but also genes with mutations in other types of myeloid neoplasms. Sequencing was performed in 83 Ph-negative
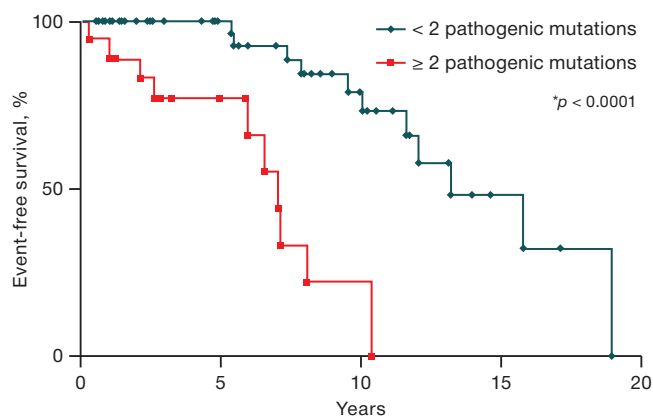
MPN patients. The data analysis showed that mutations in the *JAK2*, *MPL* and *CALR* genes, detected in patients by standard laboratory methods, were successfully detected in our conditions by NGS. This fact indicates the reliability of the obtained sequencing data.

In our study, in addition to driver genes, mutations defined as pathogenic were detected in 23 (20%) genes out of 118 studied; these mutations were found in 39 patients. In comparison with our data, the researchers in [13] analyzed a group of 197 patients by NGS using a targeting panel and found pathogenic mutations in 35% of patients. At the same time, mutations were detected in 27% of genes out of 104 analyzed. The difference in the number of mutated genes (20% and 27%) of the total number of genes can be explained by the different set of genes used in targeting panels of our work and that of Lundberg et al. [13].

The most frequent additional pathogenic mutations in patients with different MPNs are found in the *ASXL1* gene [8]. We also found that 25% of patients had a mutation in this particular gene. The frequency of mutations in the *ASXL1* gene varies in different Ph-negative MPNs. Thus, according to the data presented in [14–19], mutations were found in 23–25% of cases in primary myelofibrosis and in 5–20% cases of essential thrombocythemia. In true polycythemia, the frequency of mutations in the *ASXL1* gene was 3.5–11.8%. In our study, mutations were found in 26.6% of PMF patients, 14.2% of ET patients, and 16% of PV patients.

Two pathways of mutagenesis involving the *ASXL1* gene are proposed in the clonal evolution of MPNs:
- pathogenic mutations may occur as a consequence of driver mutations in the *JAK2* and *CALR* genes in PMF;
- may be the primary triggering event preceding driver mutations [20–22].

Numerous studies showed the effect of mutations in the *ASXL1* gene on general, event-free survival and thrombotic events in patients with Ph-negative MPNs [23, 24]. However, Guglielmelli et al. found that mutations in the *ASXL1* gene reduced overall survival in patients with PMF but not with secondary MF [25]. In addition, *ASXL1* mutations impact the outcome of therapy with targeted drugs and allo-HSCT [26]. Our study showed an association of

dramatic reduction in event-free survival (median survival of 7.83 vs 15.75 years, p = 0.0011) for all patients with and without mutations in this gene.

Advances in genetics and molecular biology in recent years have offered an improved description of the genetic landscape of Ph-negative MPNs and identified genes whose mutations have a negative impact on prognosis. These include *ASXL1*, *EZH2*, *IDH1*, *IDH2*, *SRSF2*, and *U2AF1*Q157. Such mutations, referred to as high-risk mutations, have been included in various prognostic scales. The number of mutations in these genes also affects prognosis, namely, one pathogenic mutation led to a 1.7-fold reduction in the median overall survival of patients, two mutations led to a 4.7-fold reduction compared to patients without mutations in these genes (Me = 12.2 years, Me = 7 years, Me = 2.6 years respectively, p < 0.0001) for patients with myelofibrosis [27]. Our study, based on a panel of 118 genes, showed that not only high-risk mutations affect the survival of patients with MPNs. Indeed, any pathogenic variants in combination with driver genes (p = 0.0004) significantly reduced patient survival, with both the presence of such a variant and their number being important. Patients with two or more mutations demonstrated a significantly decreased event-free survival compared to those with one mutation (p < 0.0001). Thus, when carrying out a diagnosis of Ph-negative MPNs, attention should be paid to analyzing the maximum possible panel of genes, rather than the mutational status of only six genes of high molecular risk.

Recent studies have demonstrated the importance of the NGS method for characterizing the mutational profile of triple-negative patients [28, 29]. Indeed, pathogenic mutations in various genes were detected in 8 out of 10 such patients in our study cohort. The detection of mutations in this group of patients allowed us to confirm clonality and assess the risks of the disease course. It is important to note that the absence of driver and pathogenic mutations in patients with the confirmed diagnosis of Ph-negative MPN allows us to distinguish them into a separate cohort with the most favorable prognosis of the disease course without leukemic transformation [12]. Not all studies, however, identified such a group; thus, Huang et al. identified pathogenic mutations in all 12 patients with triple-negative status [12].

In addition to assessing disease prognosis, NGS is a convenient tool for selecting target genes for targeted therapy, targeting not only driver genes but also genes with different functions (e.g., *IDH1/2* and *EZH2*). Mutations in these genes were also identified in patients from our cohort. The *IDH1/2* genes were mutated in 8% of patients, and *EZH2* in 3% of patients, which is consistent with the data obtained by other researchers using standard molecular methods [8, 30].

Somatic mutations across a wide range of genes were detected in 80% of patients with PMF and 50% of patients with ET/PV, affecting the course and prognosis of the disease [29]. In our patient group, we found pathogenic mutations affecting prognosis in 46% of patients with PMF, including patients with leukemic transformation. Risk factors that increase the likelihood of leukemic transformation include, among others, mutations in various genes: *IDH1*, *IDH2*, *SRSF2*, *ASXL1* in primary myelofibrosis, in *SRSF2*, *IDH2*, or *RUNX1* in polycythemia vera, in *TP53*, *SRSF2*, *EZH2*, *U2AF1*, or *RUNX1* in essential thrombocythemia. At the same time, it was shown that the time to leukemic transformation decreases with the increase in the number of pathogenic mutations in patients with Ph-negative MPNs (p < 0.0001), which agrees with our findings of a greater number of mutations in patients with disease transformation [12].

The detection of driver mutations has been a breakthrough discovery in the diagnosis of myeloproliferative neoplasms, which facilitates determination of the pathogenesis of these diseases. At present, the introduction of NGS analysis is substantially changing the perception and approach to the diagnosis, risk assessment, and treatment of patients with Ph-negative MPNs. Due to the possibility of simultaneous search for mutations in many genes, NGS assists not only in establishing the diagnosis and confirming the clonality of the disease, but also in identifying groups of patients with unfavorable prognosis and increased risk of disease progression and transformation.

CONCLUSION

Thus, the application of NGS technology using a panel of 118 genes in the diagnosis of patients with Ph-negative myeloproliferative neoplasms made it possible to study the mutational profile of the disease, to confirm the clonality of the disease in patients with triple-negative status, and to identify pathogenic mutations significantly affecting the results of patient therapy.

In our study, pathogenic mutations were detected in almost half of patients with Ph-negative MPNs in 23 genes. Reduced event-free survival was shown for patients with a combination of driver and pathogenic mutations. Two or more pathogenic mutations in a single patient reduced event-free survival compared to patients with a single mutation. The most frequent molecular event in Ph-negative MPNs was mutations in the *ASXL1* gene associated with a decreased event-free survival of patients. An integrated approach to the diagnosis of Ph-negative MPNs using modern molecular genetic technologies will make it possible to establish the diagnosis, assess the prognostic features of the disease course, and select the most effective personalized therapy.

References

1. Shuvaev VA, Martynkevich IS, Sidorkevich SV. Mieloproliferative neoplasms. Moscow: Buki Vedi; 2023 (In Russ.).

2. Melikjan AL, Kovrigina AM, Suborceva IN, Shuvaev VA, Morozova EV, Lomaia EG. et al. National clinical guidelines for the diagnosis and treatment of Ph-negative myeloproliferative diseases (polycythemia vera, essential thrombocytemia, primary myelofibrosis) (revision 2020). *Clinical oncogematology.* 2021;14(2):262–98 (In Russ.).
https://doi.org/10.21320/2500-2139-2021-14-2-262-298

3. Spivak JL. Myeloproliferative Neoplasms. *N. Engl. J. Med.* 2017;376:2168–81.
https://doi.org/10.1056/NEJMra1406186

4. Khoury JD, Solary E, Abla O, Akkari Y, Alaggio R, Apperley JF. et al. The 5th edition of the World Health Organization Classification of Haematolymphoid Tumours: Myeloid and Histiocytic/Dendritic Neoplasms. *Leukemia*. 2022;36:1703–19.
https://doi.org/10.1038/s41375-022-01613-1

5. Hu X, Li J, Fu M, Zhao X, Wang W. The JAK/STAT signaling pathway: from bench to clinic. *Signal Transduct Target Ther.* 2021;6(1):402.
https://doi.org/10.1038/s41392-021-00791-1

6. Tefferi A, Lasho TL, Finke CM, Elala Y, Hanson CA, Ketterling RP et al. Targeted deep sequencing in primary myelofibrosis. *Blood Adv*. 2016;30:105–11.
https://doi.org/10.1182/bloodadvances.2016000208

7. Tefferi A, Lasho TL, Guglielmelli P, Finke CM, Rotunno G, Elala Y. et al. Targeted deep sequencing in polycythemia vera and essential thrombocythemia. *Blood Adv*. 2016;22:21–30.
https://doi.org/10.1182/bloodadvances.2016000216

8. Vainchenker W, Kralovics R. Genetic basis and molecular pathophysiology of classical myeloproliferative neoplasms. *Blood*. 2017;129(6):667–79.
https://doi.org/10.1182/blood-2016-10-695940

9. Zuo Z, Li S, Xu J, You MJ, Khoury JD, Yin CC. Philadelphia-Negative Myeloproliferative Neoplasms: Laboratory Workup in the Era of Next-Generation Sequencing. *Curr Hematol Malig Rep*. 2019;14(5):376–85.
https://doi.org/10.1007/s11899-019-00534-8

10. Alduaij W, McNamara CJ, Schuh A, Arruda A, Sukhai M, Kanwar N. et al. Clinical Utility of Next-generation Sequencing in the Management of Myeloproliferative Neoplasms: A Single-Center Experience. *Hemasphere*. 2018;2(3):e44.
https://doi.org/10.1097/HS9.0000000000000044

11. Visani G, Etebari M, Fuligni F, Di Guardo A, Isidori A, Loscocco F. et al. Use of Next Generation Sequencing to Define the Origin of Primary Myelofibrosis. *Cancers (Basel)*. 2023;15(6):1785.
https://doi.org/10.3390/cancers15061785

12. Huang X, Wu J, Deng X, Xu X, Zhang X, Ma W. et al. Mutation profiles of classic myeloproliferative neoplasms detected by a customized next-generation sequencing-based 50-gene panel. *Journal of Bio-X Research* .2020;3(1):13–20.
https://doi.org/10.1097/JBR.0000000000000061

13. Lundberg P, Karow A, Nienhold R, Looser R, Hao-Shen H, Nissen I. et al. Clonal evolution and clinical correlates of somatic mutations in myeloproliferative neoplasms. *Blood*. 2014;123(14):2220–8.
https://doi.org/10.1182/blood-2013-11-537167

14. Shih AH, Abdel-Wahab O, Patel JP, Levine RL. The role of mutations in epigenetic regulators in myeloid malignancies. *Nat Rev Cancer*. 2012;12:599–612.
https://doi.org/10.1038/nrc3343

15. Viny AD, Levine RL. Genetics of myeloproliferative neoplasms. *Cancer J*. 2014;20:61–5.
https://doi.org/10.1016/j.hoc.2020.12.002

16. Milosevic JD, Kralovics R. Genetic and epigenetic alterations of myeloproliferative disorders. *Int J Hematol*. 2013;97:183–97.
https://doi.org/10.1007/s12185-012-1235-2

17. Guglielmelli P, Gangat N, Coltro G, Lasho TL, Loscocco GG, Finke CM. et al. Mutations and thrombosis in essential thrombocythemia. *Blood Cancer J*. 2021;11(4):77.
https://doi.org/10.1038/s41408-021-00470-y

18. Segura-Díaz A, Stuckey R, Florido Y, Sobas M, Álvarez-Larrán A, Ferrer-Marín F. et al. *DNMT3A/TET2/ASXL1* mutations are an age-independent thrombotic risk factor in polycythemia vera patients: an observational study. *Thromb Haemost*. 2024;124(7):669–75.
https://doi.org/10.1055/a-2239-9265

19. Fujino T, Kitamura T. *ASXL1* mutation in clonal hematopoiesis. *Exp Hematol*. 2020; 83:74–84.
https://doi.org/10.1016/j.exphem.2020.01.002

20. Gelsi-Boyer V, Brecqueville M, Devillier R, Murati A, Mozziconacci MJ, Birnbaum D. Mutations in *ASXL1* are associated with poor prognosis across the spectrum of malignant myeloid diseases. *J Hematol Oncol*. 2012;5:12.
https://doi.org/10.1186/1756-8722-5-12

21. Triviai I, Zeschke S, Rentel J, Spanakis M, Scherer T, Gabdoulline R. et al. *ASXL1/EZH2* mutations promote clonal expansion of neoplastic HSC and impair erythropoiesis in PMF. *Leukemia*. 2019;33(1):99–109.
https://doi.org/10.1038/s41375-018-0159-0

22. Svidnicki C, M., De Melo Campos P., Filho A.F., Fujiura L.C., Yoshizato T., Makishima H., et al. Mutations in triple-negative patients with myeloproliferative neoplasms. *Blood*. 2019;134(1):5395.
https://doi.org/10.1182/blood-2019-128764

23. Regimbeau M, Mary R, Hermetet F, Girodon F. Genetic Background of Polycythemia Vera. *Genes*. 2022;13(4):637.
https://doi.org/10.3390/genes13040637

24. Nie YB, Sun M, He CK, Ju MK, Zhou FL, Wu SY. et al. *ASXL1* mutations in Chinese patients with essential thrombocythemia. *Exp Ther Med*. 2015;15(5):4149–56.
https://doi.org/10.3892/etm.2018.5939

25. Guglielmelli P, Coltro G, Mannelli F, Rotunno G, Loscocco GG, Mannarelli C. et al. *ASXL1* mutations are prognostically significant in PMF, but not MF following essential thrombocythemia or polycythemia vera. *Blood Adv*. 2022;6(9):2927–31.
https://doi.org/10.1182/bloodadvances.2021006350

26. Spiegel J, McNamara C, Kennedy J, et al. Impact of genomic alterations on outcomes in myelofibrosis patients undergoing JAK1/2 inhibitor therapy. *Blood Adv*.2017;1(20):1729–38.
https://doi.org/10.1182/bloodadvances.2017009530

27. Guglielmelli P, Lasho TL, Rotunno G, Score J, Mannarelli C, Pancrazzi A. et al. The number of prognostically detrimental mutations and prognosis in primary myelofibrosis: an international study of 797 patients. *Leukemia*. 2014;28(9):1804–10.
https://doi.org/10.1038/leu.2014.76

28. Wu S, Luo P, Yu Y, Xiong B, Wang Y, Zuo X. Next-generation sequencing redefines the diagnosis of triple-negative myeloproliferative neoplasms. *Ann Hematol*. 2022;101(3):705–8.
https://doi.org/10.1007/s00277-021-04561-5

29. Mroczkowska-Bękarciak A, Wróbel T. *BCR::ABL1*-negative myeloproliferative neoplasms in the era of next-generation sequencing. *Front Genet*. 2023;14:1241912.
https://doi.org/10.3389/fgene.2023.1241912

30. Shih A, Abdel-Wahab O, Patel J, Levine R. The role of mutations in epigenetic regulators in myeloid malignancies. *Nat Rev Cancer*. 2012;12(9):599–612.
https://doi.org/10.1038/nrc3343

Authors' contributions. All authors confirm that their authorship meets the ICMJE criteria. The greatest contribution is distributed as follows: Anna N. Kirienko — collection of material, analysis of obtained data, writing and editing of the text; Ekaterina V. Motyko — collection of material, analysis of obtained data, editing of the text; Elizaveta V. Efremova — editing, approval of the final version of the text; Daria V. Kustova — collection of material, analysis of the obtained data; Tatyana N. Gert — collection of material; Irina V. Leppyanen — collection of material; Vasily A. Shuvaev — editing, approval of the final version of the text; Irina S. Martynkevich — research design, editing of the article, approval of the final version of the text.

AUTHORS

Anna N. Kirienko, Cand. Sci. (Biol)
https://orcid.org/0000-0002-2519-306X
kirienkoann@yandex.ru

Ekaterina V. Motyko, Cand. Sci. (Biol)
https://orcid.org/0000-0002-6052-6472
katteerina@mail.ru

Elizaveta V. Efremova
https://orcid.org/0000-0002-2183-5299
liza.goncharova_@mail.ru

Daria V. Kustova
https://orcid.org/0000-0003-4546-5808
dasha_94-07@mail.ru

Tatyana N. Gert
https://orcid.org/0000-0002-2793-452X
tynisa@mail.ru

Irina V. Leppyanen, Cand. Sci. (Biol)
https://orcid.org/0000-0002-2158-0855
leppyanen_irina@rambler.ru

Vasily A. Shuvaev, Dr. Sci. (Med.)
https://orcid.org/0000000335360770
shuvaev77@mail.ru

Irina S. Martynkevich, Dr. Sci. (Biol.)
https://orcid.org/0000-0001-5958-0490
martynkevich@niigt.ru

BIOCOMPATIBLE CHITOSAN- AND STARCH-BASED GELS FOR 3D PRINTABLE INKS

Elena A. Malik[1], Yuliya A. Nashchekina[2], Ilya A. Barsuk[3,4✉], Konstantin P. Golovko[4,5], Viktor N. Alexandrov[4,6], Vladimir Y. Elokhovskiy[7], Vladimir E. Yudin[7]

[1] Peter the Great St. Petersburg Polytechnic University, St. Petersburg, Russia

[2] Institute of Cytology of the Russian Academy of Sciences, St. Petersburg, Russia

[3] Main Military Medical Department of the Ministry of Defense of the Russian Federation, Moscow, Russia

[4] Kirov Military Medical Academy, St. Petersburg, Russia

[5] St. Petersburg State University, St. Petersburg, Russia

[6] St. Petersburg State Pediatric Medical University, St. Petersburg, Russia

[7] Institute of Macromolecular Compounds of the Russian Academy of Sciences, St. Petersburg, Russia

Introduction. Carriers intended for cell culture and transplantation are widely used in modern tissue engineering. The creation of inks for printing such media assumes a wide range of variations in their shape and architecture. Chitosan as a natural polymer is increasingly finding application in various fields of regenerative medicine. Chitosan-based scaffolds are an artificial prototype of the extracellular matrix *in vitro*. The method of 3D printing can be used to bring the structure of such a matrix as close as possible to the properties of native tissues. However, in order to achieve the desired printing quality, the task of developing a chitosan-based ink composition and selecting optimal printing parameters should be solved.

Objective. Development of a biocompatible chitosan-based ink with optimal rheological properties suitable for 3D printing.

Materials and methods. A bioink was manufactured using the chitosan produced by BiologHeppe (Germany) with a molecular weight of 164 kDa and a deacetylation degree of 92.5%. Starch produced by Merck (Germany) was used to modify the bioink. The method of 3D extrusion bioprinting was used to obtain 3D matrices by a 3D bioprinter by Rockit Invivo (Republic of Korea) equipped with the Android OS software. 3D-printed matrices were obtained from a bioink with different chitosan concentrations: 4% and 6%. Cultures of rabbit mesenchymal stem cells were seeded to study the biocompatibility of the printed structures.

Results. The developed chitosan- and starch-based inks demonstrated an increased viscosity of the solution and improved characteristics of the printed designs. The rheological parameters were optimized for printing by increasing the chitosan concentration in the solution up to 6%, as well as by introducing starch at a similar concentration into the solution. An *in vitro* study also showed the biocompatibility of the printed structures with respect to mesenchymal stromal cells.

Conclusions. The developed inks can be used to form scaffolds by 3D printing.

Keywords: bioink; hydrogel; chitosan; starch; biocompatibility; 3D printing

УДК 57.085.2:547.917

БИОСОВМЕСТИМЫЕ ГЕЛИ НА ОСНОВЕ ХИТОЗАНА И КРАХМАЛА В КАЧЕСТВЕ ЧЕРНИЛ ДЛЯ 3D-ПЕЧАТИ

Е.А. Малик[1], Ю.А. Нащекина[2], И.А. Барсук[3,4✉], К.П. Головко[4,5], В.Е. Александров[4,6], В.Ю. Елоховский[7], В.Е. Юдин[7]

[1] Санкт-Петербургский политехнический университет Петра Великого, Санкт-Петербург, Россия

[2] Институт цитологии РАН, Санкт-Петербург, Россия

[3] Главное военно-медицинское управление Министерства обороны Российской Федерации, Москва, Россия

[4] Военно-медицинская академия им. С.М. Кирова, Санкт-Петербург, Россия

[5] Санкт-Петербургский государственный университет, Санкт-Петербург, Россия

[6] Санкт-Петербургский государственный педиатрический университет, Санкт-Петербург, Россия

[7] Институт высокомолекулярных соединений РАН, Санкт-Петербург, Россия

Введение. Носители, предназначенные для культивирования и трансплантации клеток, находят широкое применение в современной тканевой инженерии. Создание чернил для печати таких носителей позволяет в широких пределах варьировать их форму и архитектуру. Хитозан — природный полимер, который уже находит применение в различных областях регенеративной медицины. Скаффолды на его основе являются искусственным прототипом внеклеточного матрикса *in vitro*. Метод трехмерной печати позволит максимально приблизить структуру такого матрикса к свойствам нативной ткани. Однако для улучшения качества печати необходимо как разработать состав чернил на основе хитозана, так и подобрать оптимальные параметры печати.

Цель. Разработка биосовместимых чернил на основе хитозана с оптимальными реологическими свойствами, пригодными для 3D-печати.

Материалы и методы. В исследовании для создания биочернил применялся хитозан фирмы BiologHeppe (Германия) с молекулярной массой 164 кДа и степенью деацетилирования 92,5%. Для модификации биочернил использовали крахмал фирмы Merck (Германия). Для получения

трехмерных матриц применяли метод экструзионной 3D-биопечати. В работе использовали 3D-биопринтер фирмы Rokit Invivo (Республика Корея), в котором установлено программное обеспечение Android OS. 3D-печатные матрицы изготавливали из биочернил с различным содержанием хитозана: 4 и 6%. Для исследования биосовместимости печатных конструкций проводили посев культуры мезенхимальных стволовых клеток кролика.

Результаты. Чернила на основе хитозана и крахмала продемонстрировали увеличение вязкости раствора и наилучшие характеристики напечатанных конструкций. Улучшение реологических параметров, оптимальных для печати, происходит при увеличении концентрации хитозана в растворе до 6%, а также при добавлении в раствор крахмала с аналогичной концентрацией. Исследование *in vitro* также показало биосовместимость напечатанных конструкций по отношению к мезенхимным стромальным клеткам.

Выводы. Разработанные чернила могут быть использованы для формирования скаффолдов методом трехмерной печати.

Ключевые слова: биочернила; гидрогель; хитозан; крахмал; биосовместимость; 3D-печать

INTRODUCTION

Additive technologies, including 3D printing, are driving major innovations in diverse fields of science, including medicine and biology.

Various polymers of natural and synthetic origin are used as printing materials. Such structures can serve as a basis for manufacturing functional 3D fabrics [1]. These biomaterials are referred to as inks that mimic the composition of human or animal body tissues. The advantage of 3D printing consists in the possibility of reproducing the geometry of a 3D structure that is more similar to a natural biological system than an *in vitro* 2D model. The structural similarity of the printed design can lead to more physiologically relevant functional results. No other technology is capable of providing such a level of geometric complexity and similarity to living tissues [2].

3D printing allows 3D volumetric media to be created for use as 3D cell cultures for further transplantation into damaged organs and tissues [2]. The printed designs, together with the cells grown thereon, may serve as tissue models for testing new drugs [3].

The printing parameters can be defined as bioprinter settings (firmware input) that are necessary for an accurate creation of 3D-printed structures. In this sense, only a certain range of values is suitable for 3D printing, with their choice being a key factor in obtaining viable structures. These values depend on the ink composition, which should be carefully selected in each specific case [4].

The main printing parameters include dispenser temperature, substrate temperature, printing speed, and input flow parameters (speed and pressure). Being directly related to the overall 3D printing time, the printing speed (movement across the XY plane) is a highly important parameter. In addition, in the extrusion printing method, the hydrogel flow (thread width) is managed primarily by the printing speed and the retraction speed. The printing speed values used vary from 0.2 to 150 mm/s, ranging within 1–30 mm/s in the majority of cases [4].

The exact dimensions of a 3D-printed structure can be preserved when the input flow is selected correctly, which is indicated as a percentage. This parameter is responsible for the amount of ink being extruded by the printer. Input flow calibration also improves the retraction settings [4].

The main properties of 3D printable inks include strand printability, viscoelastic properties, biodegradability, and cytocompatibility [5]. The 3D matrix should mimic the biological environment and facilitate cell attachment, proliferation, and growth; promote the dispersion of bioactive molecules and growth factors; and contain space for the extracellular matrix [6].

Although both natural and synthetic polymers can be used as inks, the preference is given to natural materials due to their high biocompatibility. At the same time, natural materials may exhibit insufficient mechanical properties [7]. The most commonly used components in ink are chitosan and alginate, followed by gelatin, hyaluronic acid, silk fibroin, and polyethylene glycol [8]. Hydrogels can mimic, e.g., the modulus of elasticity of soft tissues of the human body. For the most durable tissues, such as bones or teeth, other materials are required — thermoplastic polymers with the addition of hydrogels [8].

Chitosan is one of the most promising materials for 3D printing. Chitosan has three types of reactive functional groups: amino groups, as well as primary and secondary hydroxyl groups at C-2, C-3, and C-6 positions, respectively. The positive charge of its functional groups makes chitosan the only positively charged natural polysaccharide. Consequently, chitosan is able to interact with negatively charged biomolecules, lipids, proteins, deoxyribonucleic acid (DNA), and various cellular receptors that trigger a cascade of interrelated reactions in living organisms, which determines its unique characteristics [9]. Among such characteristics of chitosan-based bioink are good

cell–matrix interactions, imitation of the structure of native tissues, creation of a microenvironment for oxygen and nutrient exchange, as well as a favorable immune response after implantation.

According to Huang J. et al., 3D-printed structures showed biomolecular adaptation, stable biocompatibility, and biological activity even after various post-printing modifications [10]. However, chitosan is not devoid of disadvantages, such as a slow gelation rate, sufficient thermal stability, and a low mechanical strength of materials produced on its basis.

It is important to note that the physical stability and mechanical strength of 3D printable inks depend on their viscoelastic properties. The viscoelastic properties of chitosan can be achieved through physical or chemical crosslinking methods, as well as by introducing additional components. Therefore, chitosan is often structurally reinforced with other biopolymers, including polysaccharides. Starch can be used as such a reinforcing biopolymer [11]. Starch consists of carbohydrates, possessing the properties of hydrophilicity, biocompatibility, low cost, good biodegradability, and non-toxicity [12]. Starch consists of a granular form with linear amylose and a large amount of branched amylopectin. The starch structure is semi-crystalline; thus, the addition of a limited amount of water under the action of heat and shear treatment will lead to the destruction of hydrogen bonds. At this stage, the starch will melt, resulting in the formation of a thermoplastic starch. Thus, we assume that the combination of biocompatible and biodegradable biopolymers, such as chitosan and starch, may compensate for the disadvantages of each biopolymer individually and that their combined use will make it possible to obtain inks with optimal characteristics for the formation of carriers with specified structural characteristics by 3D printing. In order to obtain a predictable result, namely matrices with specified structural characteristics, such as the size and height of cells, the optimal ratio of chitosan and starch, as well as optimal printing parameters, should be determined.

In this research, we aimed to develop biocompatible inks with an optimal ratio of chitosan and starch, suitable for 3D printing.

MATERIALS AND METHODS

Chitosan (BiologHeppe, Germany) with a molecular weight of 164 kDa and a deacetylation degree of 92.5% and starch (9005-25-8, HC, Merck, Germany) were used to produce ink compositions.

Table 1. Chitosan and starch calculated concentrations in solutions

Solutions	Chitosan concentration, %	Starch concentration, %
C/S (4/0)	4	0
C/S (6/0)	6	0
C/S (4/4)	4	4
C/S (6/6)	6	6

Table prepared by the authors using their own data

Mesenchymal stem cells (MSCs) obtained from rabbit adipose tissue according to the method [13, 14] and provided by the Center for Cellular Technologies of the Institute of Cytology of the Russian Academy of Sciences were used. Adipose tissue was washed in a phosphate-salt buffer followed by treatment with collagenase. Following collagenase inactivation, the cells were centrifuged. The cells were cultured in a α-MEM (modified Igla medium) nutrient medium with the addition of L-glutamine, 10% bovine fetal serum and antibiotics (100 units/mL) — penicillin, 100 micrograms/mL streptomycin (all Gibco reagents, USA). Cells of 4–9 passages were used in the work.

Preparation method of solutions

The following procedure was used to obtain a matrix based on pure chitosan and chitosan with the addition of starch. Chitosan was mixed with water at room temperature for 15 min on a laboratory mixer (OSC-10L, Russia) at a mixing speed of 1000 rpm to obtain a suspension, which was further supplemented with acetic acid (at a concentration of 97%, 2% of the solution volume), as well as starch at concentrations from 0 to 6%.

The composition was mixed during 1.5 h on a laboratory mixer (OSC-10L, Russia) at a speed of 1000 rpm until chitosan was completely dissolved. Solutions with starch addition were additionally mixed for 15 min at a temperature of 100°C in a water bath to swell the starch. The volume of chitosan, starch, and acetic acid was calculated in mass percentages. The concentration of chitosan and starch in the solution varied. The compositions of the as-obtained solutions are shown in Table 1. The names of the solutions are presented in the C/S (4/0) format, where C is chitosan and S is starch; in parentheses, — chitosan concentration/starch concentration.

Rheology of solutions

The dependence of the shear viscosity of hydrogels on the strain rate was measured on an AntonPaar rheometer (Physica MCR-301 model, Austria) in a cone/plane measuring unit CP25; [d=1 mm] in shear and dynamic modes, in modes of falling and rising strain rates (circular frequency). A viscosity relaxation test was performed at two shear rates of 100 and 0.01 s^{-1}.

3D bioprinting

The method of 3D bioprinting extrusion was used to obtain 3D matrices. We used a 3D bioprinter produced by Rokit Invivo (Republic of Korea) equipped with the Android OS software.

To design a 3D matrix, the Autodesk Fusion 360 software application was used, in which a parallelepiped with sides of 16 mm, 10 mm, and 0.2 mm was created.

To set the 3D printer settings and convert the created model into G-code, we used the NewCreator K.

The printing speed (mm/s) is the linear speed of the printing table. The input flow (%) is the pressure exerted on the gel in the syringe. The selected print options are shown in Table 2.

As a result of 3D bioprinting, volumetric matrices were obtained. Next, they were precipitated in a 10% sodium hydroxide solution for 5 min, after which they were washed with distilled water to remove alkali residues. Subsequently, 96% ethanol was used for additional sterilization, followed by its rinsing with distilled water.

Print quality analysis

The main parameter describing the print quality in this study is strand printability (SP), which is calculated using formula (1):

$$SP = 1 - \frac{D_s - D_{exp}}{D_s},$$

where D_{exp} is the experimental diameter of the printed strips (mm); D_s is the theoretically found standard diameter (mm).

The experimental diameter of the printed fiber was measured in the ImageJ software. Then the strand printability was calculated using formula (1). The print result was considered satisfactory at SP = 1 ± 0.1 [12]. The diameter of the printhead nozzle equal to 0.9 mm was taken as the standard diameter D_s.

D_{exp} measurement was performed 30 times for each sample on different sections of the matrix using the ImageJ software. The diameter values were obtained by comparing the measured value with the reference value.

In vitro cell culture

To study the biocompatibility of the printed structures, rabbit mesenchymal stem cell cultures were seeded onto all printed matrices. To that end, 300 μL of cell suspension with a concentration of 5×10^5 μL^{-1} was added to each Petri dish followed by incubation at 37°C for 40 min. After that, 8 mL of ready-made nutrient medium containing α-MEM nutrient medium (modified Igla medium) with the addition of L-glutamine, 10% bovine fetal serum and antibiotics (100 units/mL) penicillin, 100 μg/mL streptomycin (all reagents — Gibco, USA) was added to each sample.

The cells were cultured under aseptic conditions at a constant temperature of 37°C, 5% CO_2 concentration, and 98% humidity. To analyze the interaction of cells with the matrices, photographs were taken 1 h, 1 day, 3 days, and 7 days after the onset of the study. All experiments were carried out in 3–5 replicates. Lifetime visualization of cells was performed using a Nikon camera (USA); the size scale was 200 μm.

Statistical analysis

Statistical analysis was performed using the Microsoft Excel software; the Student's *t*-test was used to evaluate statistically significant differences between specific samples. The differences were considered statistically significant at $p < 0.05$.

RESULTS AND DISCUSSION

The data on the dynamic viscosity of ink compositions with different concentrations of chitosan and starch demonstrate an increase in the viscosity of the polymer solution

Table 2. Printing parameters for solutions

Solutions	Printing speed, mm/s	Input flow, %
C/S (4/0)	1–5	25–75
C/S (6/0)	1–5	75–125
C/S (4/4)	3–7	125–175
C/S (6/6)	3–7	125–175

Table prepared by the authors using their own data

with an increase in concentrations of chitosan and starch in the solution, which appear quite logical (Fig. 1). Under the transition from a higher shear rate (100 s^{-1}), which simulates the movement of the polymer solution in the nozzle of the extruder, to a lower shear rate (0.01 s^{-1}), which simulates the state of the solution on the table of the printing device, the composition of C/S(6/6) shows the highest ability to restore and preserve the shape of the resulting product.

In the first part of the experiment, the printing speed was varied under a constant input flow. In the second part, the amount of input flow was varied at a constant printing speed.

Figures 2–5 show histograms that were used to visually evaluate the ratio of the standard diameter, i.e., the nozzle diameter (0.9 mm, light columns) to the experimental diameter (bright columns). Histograms with blue columns 2A — with a changing speed, with purple 2B — with a changing input flow. The columns are labeled with the values of the average experimental diameter, taking the error into account. Above the histograms are photos of the studied samples. They were taken from the same height next to the millimeter paper, which makes it possible to estimate the actual dimensions of the matrix and calculate the experimental diameters.

The results obtained show that the most approximate values of the experimental diameter to the standard diameter for a solution with a chitosan concentration of 4% and a starch concentration of 4% (C/S– 4/4) were obtained when the printing speed was set to 3 mm/m, and the input flow was 50%. The relevant data is shown in Fig. 2.

For the C/S (6/0) solution, the exact value of the experimental diameter was achieved only when the printing speed was set to 3–5 mm/s and the input flow was 100%. Similar to the previous case, this range can be considered quite narrow. The corresponding data is shown in Fig. 3.

For the C/S (4/4) solution, a wide range of settings was obtained, at which the experimental diameter was quite close to the standard diameter: 3–5 mm/s at 150% of the input flow and 5 mm/s at 175% of the input flow. The corresponding data is shown in Fig. 4.

The value of the experimental diameter in the C/S sample (6/6) turned out to be the most stable (Fig. 5) when changing the printing parameters. Thus, a sufficiently accurate printing (the proximity of the actual dimensions to the theoretical ones) can be achieved by setting the print speed from 3 to 7 mm/s under an input flow of 125 to 150%.

Table 3 shows the results of calculations of strand printability of all the studied ink compositions.

Values close to 1 ± 0.1 were considered acceptable. In all groups, a decrease in printability to 0.9 was observed with an increase in printing speed or a decrease in input
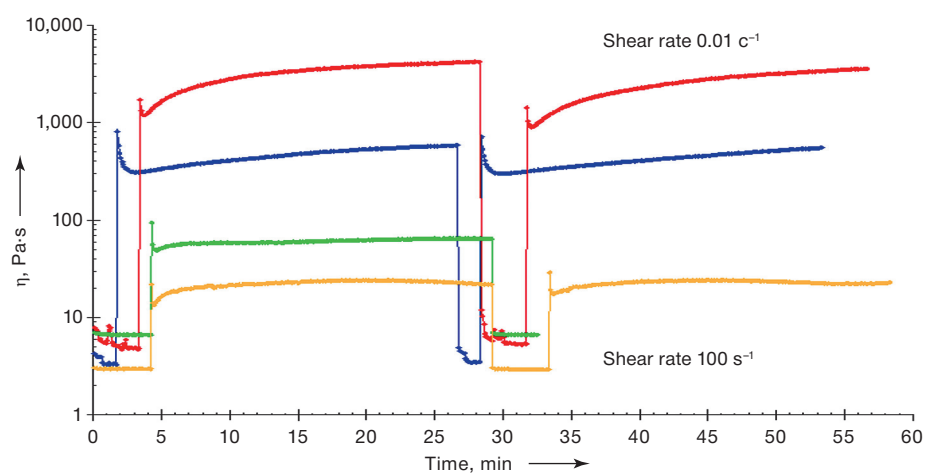
Figure prepared by the authors using their own data

Fig. 1. Dynamic viscosity of hydrogels with different starch–chitosan ratios (X-axis (Time t) — time, min; Y-axis (η) — shear viscosity, Pa·s)
Note: the yellow color of the line is the concentration of 4% chitosan in the solution; the green color of the line is the concentration of 4% chitosan and 4% starch in the solution in a ratio of 1:1; the blue color of the line is the concentration of 6% chitosan in the solution; the red color of the line is the concentration of 6% chitosan and 6% starch in the solution in a ratio of 1:1.
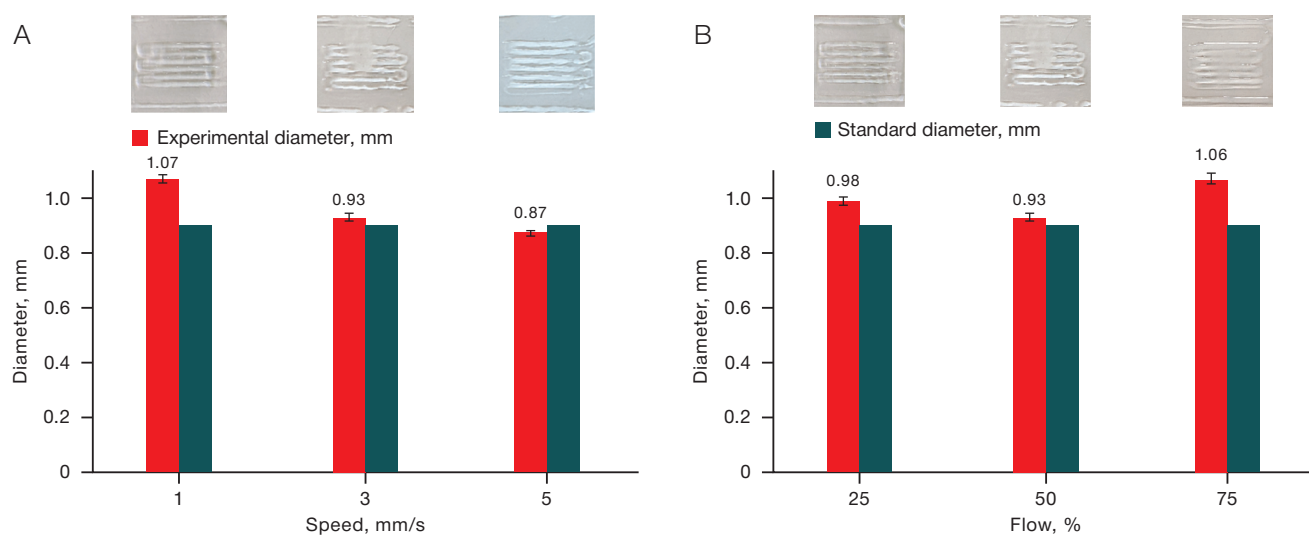
Figure prepared by the authors using their own data

Fig. 2. Effect of printing speed (A) and flow (B) on the printing quality for the C/S solution (4/0)
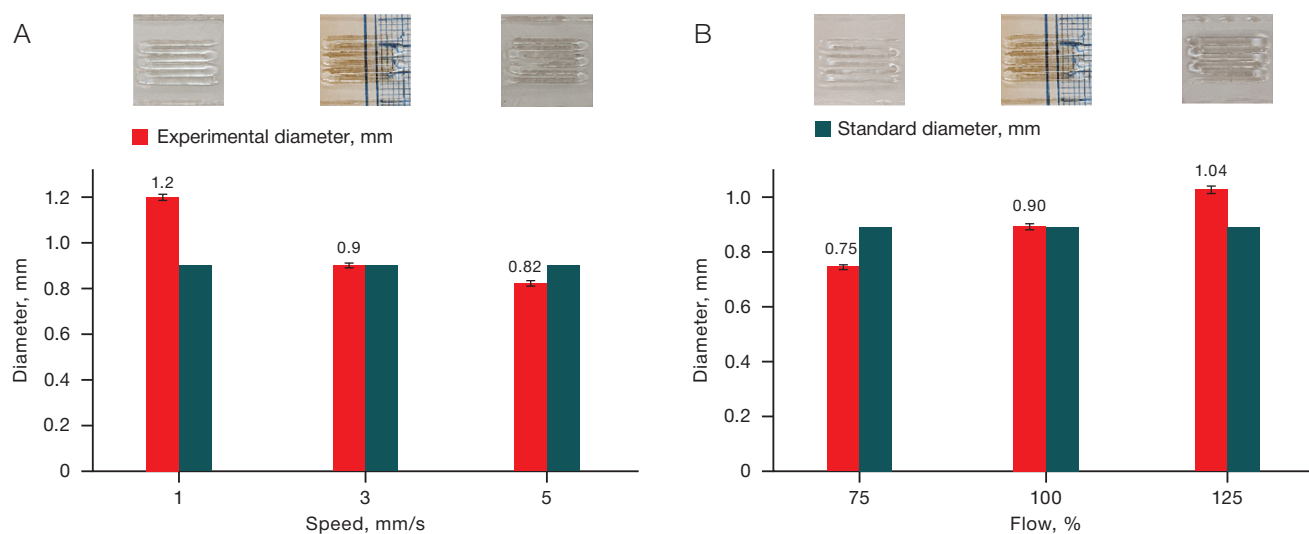
Figure prepared by the authors using their own data

Fig. 3. Effect of printing speed (A) and input flow (B) on the printing quality for the C/S solution (6/0)
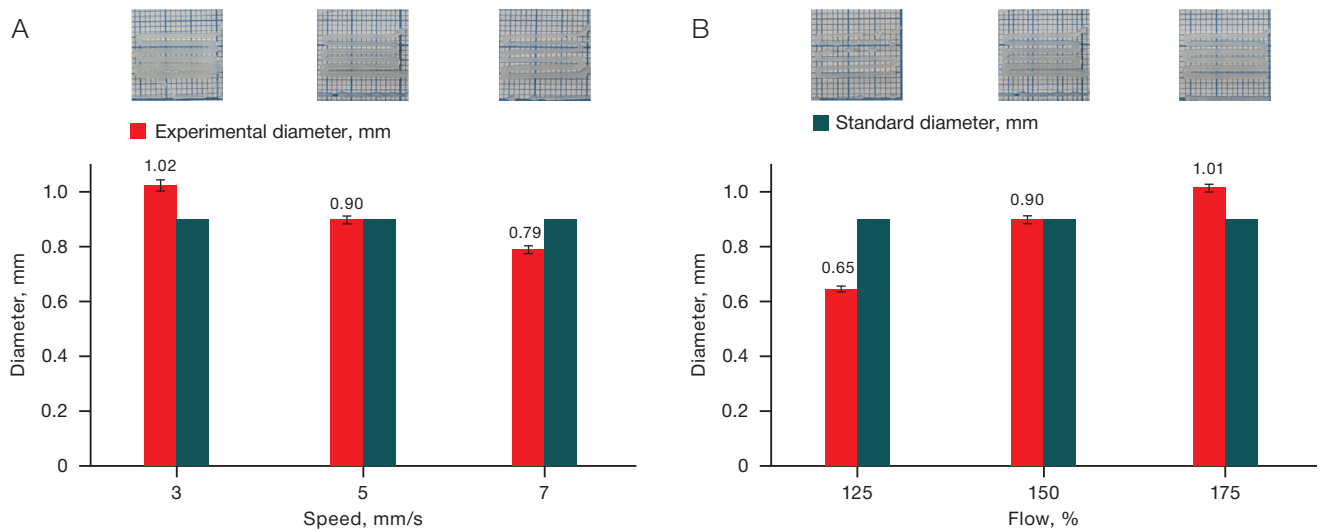
Figure prepared by the authors using their own data

Fig. 4. Effect of printing speed (A) and input flow (B) on the printing quality for the C/S solution (4/4)
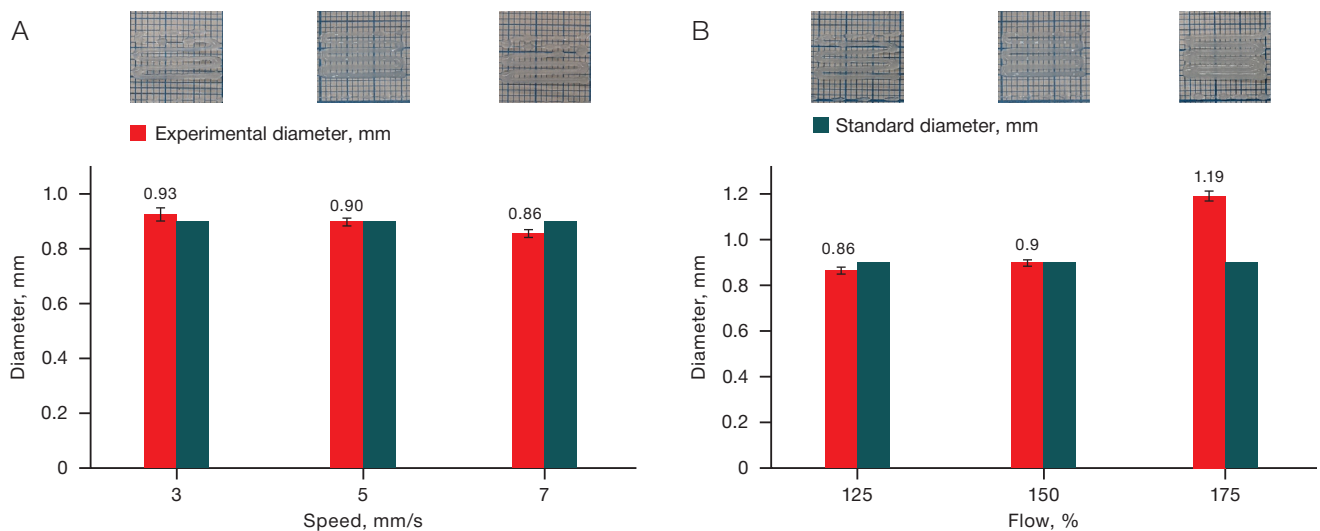
Figure prepared by the authors using their own data

Fig. 5. Effect of printing speed (A) and input flow (B) on the printing quality for the C/S solution (6/6)

flow. In extreme cases, a violation of the integrity of the printed structure was noted. When the printing speed decreases and the input flow increases, the experimental diameter exceeds acceptable values, i.e., the printability value exceeds 1.1. In some cases, strip fusion occurs, which makes it impossible to determine the experimental diameter and printability.

The result can be considered satisfactory when the printing speed is increased to 5 mm/s ($p < 0.01$) with the same value of the input flow. Consequently, a fairly narrow range of settings was observed, at which the experimental diameter is close to the standard diameter.

When setting the value of the input flow to less than the average (25% ($p < 0.001$)), an excess of the experimental diameter over the standard value was recorded, which does not correspond to the results of all other groups. This deviation can be explained by an uneven distribution of bioink over the area of the printed structure due to its poor adhesion to glass.

With an increase in the input flow to 175% ($p < 0.0001$), the experimental diameter exceeds the permissible values (the printed lines are thicker than required).

Thus, the following general conclusion can be drawn. An increase in printing speed and a decrease in input flow leads to a decrease in the thickness of the printed line. The opposite trend was noted under a decrease in printing speed and an increase in input flow.

Printability increases with a simultaneous increase in printing speed and input flow for solutions with a higher viscosity (Fig. 1), such as C/S (4/4) and C/S (6/6). In addition, these solutions are characterized by a wide range of parameters, at which the printability is close to unity. This means that the actual dimensions of the matrices are quite close to the theoretical ones. The use of solutions with a lower density, i.e., C/S (4/0) and C/S (6/0), as bioink requires a more careful selection of printing settings. For such solutions, it was possible to select only one value of the input flow, at which the printability was close to unity.

MSCs were cultured both on the surface of the matrices and next to the printed filaments during the period of seven days.

Figure 6 shows an MSC culture 1 h after seeding. MSCs form aggregates near the C/S (4/0) matrix and on its surface

Table 3. Effect of printing speed and input flow on strand printability for C/S solutions

Solutions	Flow rate, mm/s	Input flow, %	Strand printability
C/S (4/0)	1	50	1.19 ± 0.12
	3	50	1.03 ± 0.13
	5	50	$0.97 \pm 0.10*$
	3	25	1.09 ± 0.13♦
	3	75	1.18 ± 0.14
C/S (6/0)	1	100	1.34 ± 0.12
	3	75	0.84 ± 0.10
	3	125	1.15 ± 0.12
	5	100	0.92 ± 0.10
	3	100	1.00 ± 0.10
C/S (4/4)	5	175	1.13 ± 0.14
	7	150	0.88 ± 0.12
	3	150	1.14 ± 0.15
	5	150	1.00 ± 0.12
	5	125	0.72 ± 0.10
C/S (6/6)	3	150	1.03 ± 0.16
	5	125	0.96 ± 0.13
	5	150	1.00 ± 0.13
	7	150	0.95 ± 0.12
	5	175	1.32 ± 0.16■

Table prepared by the authors using their own data

Note: * — $p < 0.01$; ♦ — $p < 0.001$; ■ — $p < 0.0001$.

(Fig. 6A). Figure 6B demonstrates that the cells are evenly distributed over the surface of the dish, with a small cluster present on the surface of the matrix. The largest number of cells was observed on the C/S matrix (4/4) (Fig. 6), while the cells were concentrated and did not aggregate. In Fig. 6G, an uneven distribution of cells was observed with their high concentration on the surface of the matrix C/S (6/6).

Figure 7 shows photos taken one day after seeding. In Fig. 7A, the cells are spread out on the surface of the dish. Conversely, on the surface of the C/S (4/0) matrix, the cells formed large, loose aggregates. In the case of using the C/S (6/0) matrix (Fig. 7B), a high concentration of cells near the surface was noted. Similar to the previous case, there are significantly fewer cells on the matrix itself. In Fig. 7C, a large number of non-spread cells are observed on the surface of the C/S matrix (4/4). On a Petri dish, the cells are spread out at some distance from the matrix. The C/S matrix (6/6) has a highly heterogeneous structure, as can be seen in Fig. 7D, which makes it difficult to estimate the number of cells. The cell concentration between the printed strips is low.

Figure 8 shows photos taken three days after seeding. In Figs. 8A and 8D, the spread of cells on the Petri dish surface is observed. On the surface of the C/S (4/0) and C/S (6/0) matrices (Figs. 8A and 8B), the cells are seen in low concentrations without spreading out. In Fig. 8C, cells are observed on the surface of the C/S (4/4) matrix in a high concentration. Figure 8D shows that the cells are spread out at a distance from the surface of the matrix C/S (6/0).

Figure 9 shows the results of MSC culture seven days after seeding. Figure 9 (A–C) indicates that the cells are spread out over the Petri dish surface, being adhered tightly to the side surface of the samples. Thus, an assumption can be made about the biocompatibility of the matrices. On the other hand, in Fig. 9D, the cells adhere at a certain distance from the matrix C/S (6/6), which makes this matrix the least preferred for use. The cells do not spread out over the surface of any of the matrices, with their largest number observed on the C/S matrix (4/4). This may indicate a positive effect of starch addition.

CONCLUSION

Our research has shown the possibility of developing effective chitosan- and starch-based inks for 3D bioprinting. An increase in the chitosan concentration in the solution up to
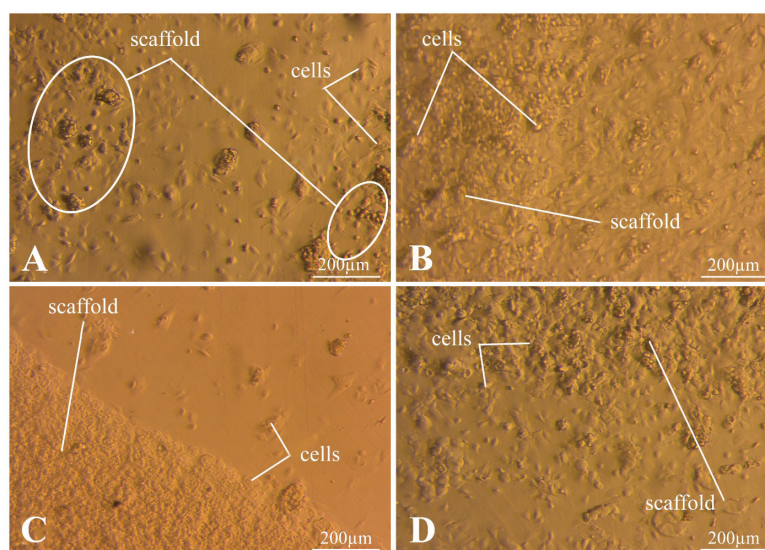
Photos taken by the authors

Fig. 6. Results of MSC culture 1 h after seeding
Note: A — C/S matrix (4/0); B — C/S matrix (6/0); C — C/S matrix (4/4); D — C/S matrix (6/6).
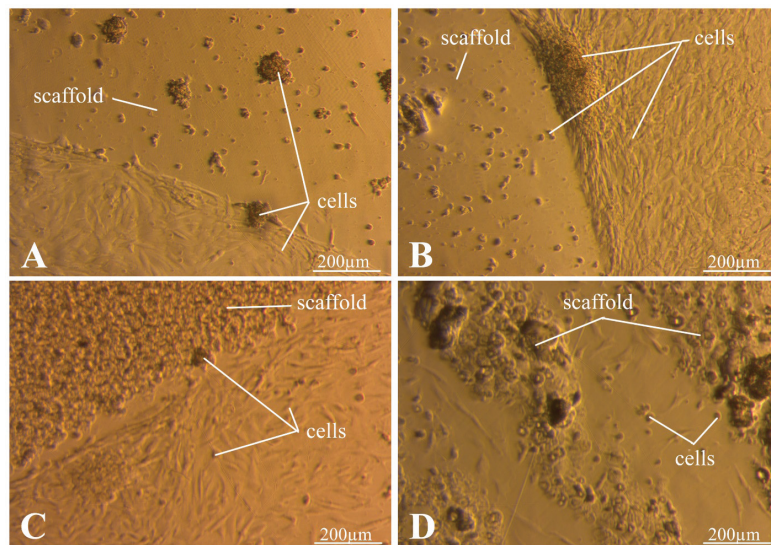
Photos taken by the authors

Fig. 7. Results of MSC culture one day after seeding
Note: A — C/S matrix (4/0); B — C/S matrix (6/0); C — C/S matrix (4/4); D — C/S matrix (6/6).
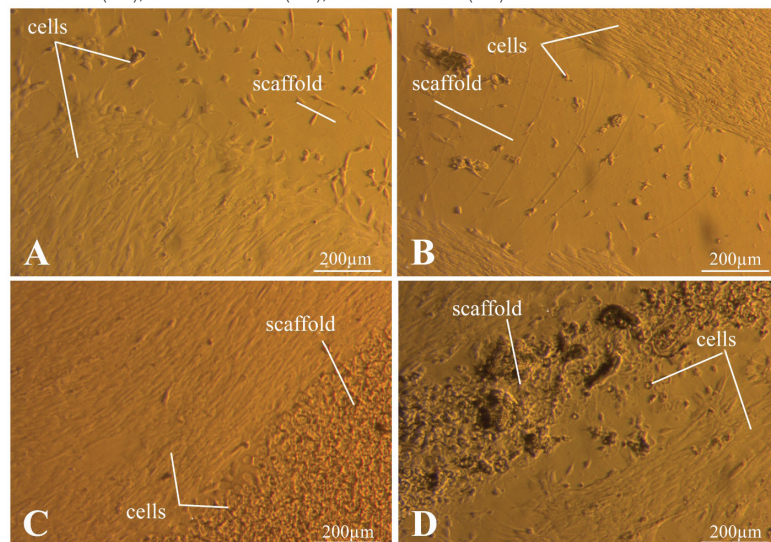
The photos were taken by the authors

Fig. 8. Results of MSC culture three days after seeding
Note: A — C/S matrix (4/0); B — C/S matrix (6/0); C — C/S matrix (4/4); D — C/S matrix (6/6).
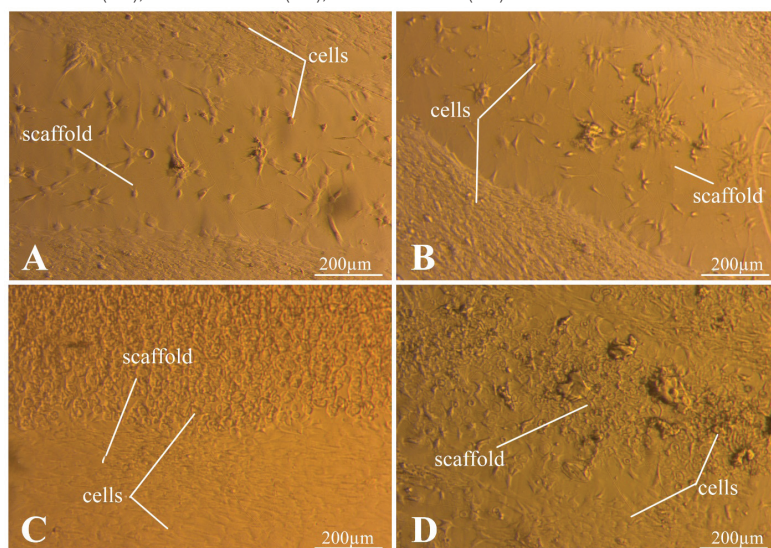
Photos taken by the authors

Fig. 9. Results of MSC culture seven days after seeding
Note: A — C/S matrix (4/0); B — C/S matrix (6/0); C — C/S matrix (4/4); D — C/S matrix (6/6).

6% along with starch addition was shown to increase the dynamic viscosity of the ink, promoting rapid restoration and prolonged preservation of the polymer solution shape after its flowing out of the extruder nozzle. The conducted experiments allowed us to establish optimal printing parameters, including the printing speed and input flow rate, which made it possible to create polymer matrices with tailored structural characteristics. Preliminary *in vitro* experiments demonstrated the biocompatibility of the obtained structures with respect to human mesenchymal stromal cells, which shows the prospects of using such polymer compositions in the development of wound coatings for treating damaged skin.

References

1. Borah A, Kumar DS. Overcoming the barriers of two-dimensional cell culture systems with three-dimensional cell culture systems: Techniques, drug discovery, and biomedical applications. *Biomedical Product and Materials Evaluation*. 2022;7:179–229. https://doi.org/10.1016/B978-0-12-823966-7.00003-7
2. Pai RR, Sekar JA, Ajit S, Velayudhan S, Kasoju N, Kumar A. Three-dimensional bioprinting of tissues and organs. *Biomedical Product and Materials Evaluation*. 2022;5:135–50. https://doi.org/10.1016/B978-0-12-823966-7.00018-9
3. Chircov C, Grumezescu AM. Three-dimensional bioprinting in drug delivery. *Materials for Biomedical Engineering*. 2019;2:19–40. https://doi.org/10.1016/B978-0-12-816913-1.00002-7
4. Mancha Sánchez E, Gómez-Blanco JC, López Nieto E, et al. Hydrogels for Bioprinting: A Systematic Review of Hydrogels Synthesis, Bioprinting Parameters, and Bioprinted Structures Behavior. *Frontiers in Bioengineering and Biotechnology*. 2020;8:776. https://doi.org/10.3389/fbioe.2020.00776
5. Mukherjee P, Rani A, Saravanan P. Polymeric Materials for 3D bioprinting. *3D printing Technology in Nanomedicine*. 2019;4:63–81. https://doi.org/10.1016/B978-0-12-815890-6.00004-9
6. Iordache F. Bioprinted Scaffolds. *Materials for Biomedical Engineering: Hydrogels and Polymer-based Scaffolds*. 2019;2:35–60. https://doi.org/10.1016/B978-0-12-816901-8.00002-X
7. Goel A, Meher MK, Gulati K, Poluri KM. Fabrication of Biopolymer-Based Organs and Tissues Using 3D bioprinting. *3D printing Technology in Nanomedicine*. 2019;3:43–62. https://doi.org/10.1016/B978-0-12-815890-6.00003-7
8. Islam MM, Shahruzzaman M, Biswas S, Nurus Sakib M, Rashid TU. Chitosan based bioactive materials in tissue engineering applications-A review. *Bioactive Materials*. 2020;5(1):164–83. https://doi.org/10.1016/j.bioactmat.2020.01.012
9. Rajabi M, McConnell M, Cabral J, Ali MA. Chitosan hydrogels in 3D printing for biomedical applications. *Carbohydrate Polymers*. 2021;260:117768. https://doi.org/10.1016/j.carbpol.2021.117768
10. Huang J, Fu H, Wang Z, Meng Q, Liu S, Wang H et al. BMSCs-laden gelatin/sodium alginate/carboxymethyl chitosan hydrogel for 3D bioprinting. *RSC Advances*. 2016;6(110):108423–30. https://doi.org/10.1039/C6RA24231F
11. Butler HM, Naseri E, MacDonald DS., Tasker AR, Ali Ahmadi A. Optimization of starch- and chitosan-based bio-inks for 3D bioprinting of scaffolds for neural cell growth. *Materialia*. 2020;(12):100737. https://doi.org/10.1016/j.mtla.2020.100737
12. Ghosh S, Gutierrez V, Fernández C, Rodriguez-Perez M, Viana JC, Reis RL, Mano JF. Dynamic mechanical behavior of starch-based scaffolds in dry and physiologically simulated conditions: effect of porosity and pore size. *Acta Biomaterialia*. 2008;4(4):950–9. https://doi.org/10.1016/j.actbio.2008.02.001
13. Krawczenko A, Klimczak A. Adipose Tissue-Derived Mesenchymal Stem/Stromal Cells and Their Contribution to Angiogenic Processes in Tissue Regeneration. *International Journal of Molecular Sciences*. 2022:23(5):2425. https://doi.org/10.3390/ijms23052425
14. Naghieh S, Sarker M, Sharma NK, Barhoumi Z, Chen X. Printability of 3D Printed Hydrogel Scaffolds: Influence of Hydrogel Composition and Printing Parameters. *Applied Sciences*. 2020;10(1):292. https://doi.org/10.3390/app10010292

Authors' contributions. All authors confirm that their authorship meets the ICMJE criteria. The greatest contribution is distributed as follows: Elena A. Malik — method statement, performance of 3D printing; Yuliya A. Nashchekina — biocompatibility study; Ilya A. Barsuk — laboratory studies; Konstantin P. Golovko — verification of critical intellectual content and final approval for publication of the manuscript; Viktor N. Alexandrov — literature search and review; Vladimir Y. Elokhovskiy — rheological studies; Vladimir E. Yudin — study concept, scientific supervision.

AUTHORS

Elena A. Malik
https://orcid.org/0009-0000-2245-2436
malikalionaa@gmail.com

Yuliya A. Nashchekina, Cand. Sci. (Biol.)
https://orcid.org/0000-0002-4371-7445
nashchekina.yu@mail.ru

Ilya A. Barsuk
https://orcid.org/0000-0002-3728-9966
barsuk20220@gmail.com

Konstantin P. Golovko, Dr. Sci. (Med.), Assoc. Professor
https://orcid.org/0000-0002-1584-1748
labws@mail.ru

Viktor N. Alexandrov, Dr. Sci. (Med.), Professor
https://orcid.org/0009-0001-9229-5293
vnaleks9@yandex.ru

Vladimir Y. Elokhovskiy, Cand. Sci. (Eng.)
https://orcid.org/0000-0001-9123-4926
vladimir.elokhovskiy@gmail.com

Vladimir E. Yudin, Dr. Sci. (Phys.-Math.), Professor
https://orcid.org/0000-0002-5517-4767
yudinve@gmail.com

COMPOSITION ANALYSIS OF PROTEOGLYCANS SYNTHESIZED *IN VITRO* BY CHONDROCYTES OF VARIOUS ORIGINS

Polina A. Golubinskaya, Evgeny S. Ruchko✉, Arina S. Pikina, Igor P. Smirnov, Tatiana V. Vladimirova, Veronika D. Gordeeva, Georgiy P. Arapidi, Artem V. Eremeev

Lopukhin Federal Research and Clinical Center of Physical-Chemical Medicine, Moscow, Russia

Introduction. The use of cellular constructs based on human pluripotent stem cells (hPSCs) is associated with a number of challenges, including the need to standardize methods for cultivating chondrocyte-like hPSCs derivatives to produce a cartilage tissue similar to natural hyaline cartilage. Glycosaminoglycans (GAGs) are the basis of the extracellular matrix (ECM) of cartilage tissue; therefore, a qualitative and quantitative analysis of the GAG composition of cartilage-like tissue engineering structures is an important step in the final assessment of their potential therapeutic effectiveness.

Objective. To determine the composition of GAGs synthesized *in vitro* by chondrocytes of various origins using enzyme-linked immunoassay (ELISA) and liquid chromatography with tandem mass spectrometry (LC–MS/MS), as well as to evaluate the effect of 2D and 3D culturing on their synthesis.

Materials and methods. We analyzed the GAG levels in 2D and 3D tissue-engineered structures obtained from the cartilage tissue of five donors, chondrocyte-like cells differentiated from two hPSC lines. Cellular spheroids were obtained by aggregation in microlunar plates and cultured in mini-bioreactors. The analysis of the GAG content in cell culture samples and spheroids was carried out using ELISA and LC–MS/MS. The Kruskal–Wallis and Dunn tests were used to assess the statistical significance of the differences between the samples.

Results. The ELISA study revealed statistically significant differences ($p < 0.0021$), confirming higher levels of GAGs synthesized in 3D cultures of native chondrocytes compared to 2D cultures (108.67 ng/mL and 1099.87 ng/mL, respectively). The average number of spectra of the chondroitin sulfate proteoglycan 4 protein, determined using LC–MS/MS, was also higher in 3D cultures, amounting to 41.75 spectra compared to 2.24 spectra in 2D culture samples. The levels of aggrecan, biglican, and decorin did not differ between cultures. 3D cultures of chondrocyte-like cells from hPSC showed no significant differences in the content of GAG compared to 2D cultures, which indicates the need to optimize the conditions for their differentiation.

Conclusions. In our study, the composition of the GAGs synthesized *in vitro* by chondrocytes of various origins was determined using ELISA and LC–MS/MS. The the effect of 2D and 3D cultivation on their synthesis was evaluated. The results showed that 3D culture media create favorable conditions for a more complete formation of chondrocytic ECM in native chondrocyte samples. Despite this, the obtained spheroids of chondrocyte-like hPSCs derivatives fail to achieve functional identity with natural cartilage tissue, even after completion of differentiation protocols, thus not representing optimal tissue engineering structures for correcting cartilage defects.

Keywords: chondrocytes; arthritis; extracellular matrix; glycosaminoglycans; hPSCs; differentiation; ELISA; LC-MS/MS

УДК 57.085.23

ОПРЕДЕЛЕНИЕ СОСТАВА ПРОТЕОГЛИКАНОВ, СИНТЕЗИРУЕМЫХ *IN VITRO* ХОНДРОЦИТАМИ РАЗЛИЧНОГО ГЕНЕЗА

П.А. Голубинская, Е.С. Ручко✉, А.С. Пикина, И.П. Смирнов, Т.В. Владимирова, В.Д. Гордеева, Г.П. Арапиди, А.В. Еремеев

Федеральный научно-клинический центр физико-химической медицины имени Ю.М. Лопухина Федерального медико-биологического агентства, Москва, Россия

Введение. Применение клеточных конструкций на основе плюрипотентных стволовых клеток человека (чПСК) связано с рядом трудностей, одной из них является необходимость стандартизации методов культивирования хондроцитоподобных производных чПСК для получения хрящевой ткани, схожей с естественным гиалиновым хрящом. Гликозаминогликаны (ГАГ) — основа внеклеточного матрикса (ВКМ) хрящевой ткани, поэтому анализ качественного и количественного состава ГАГ хрящеподобных тканеинженерных конструкций является важным звеном для итоговой оценки их потенциальной терапевтической эффективности.

Цель. Определить состав ГАГ, синтезируемых *in vitro* хондроцитами различного генеза, с использованием иммуноферментного анализа (ИФА) и жидкостной хроматографии с тандемной масс-спектрометрией (ЖХ-МС/МС), а также оценить влияние 2D- и 3D-культивирования на их синтез.

Материалы и методы. В исследовании анализировали уровни ГАГ в 2D- и 3D-тканеинженерных конструкциях, полученных из хрящевой ткани 5 доноров, хондроцитоподобных клеток, дифференцированных из 2-х линий чПСК. Клеточные сфероиды получали методом агрегации в микролуночных планшетах и культивировали в мини-биореакторах. Анализ содержания ГАГ в образцах клеточных культур и сфероидов проведен с помощью ИФА и ЖХ-МС/МС. Для оценки статистической значимости различий между образцами использовали тест Краскела — Уоллиса и тест Данна.

Результаты. В исследовании с помощью ИФА выявлены статистически значимые различия ($p < 0,0021$), подтверждающие более высокий уровень синтеза ГАГ в 3D-культурах нативных хондроцитов по сравнению с 2D-культурами (108,67 и 1099,87 нг/мл соответственно). Среднее число спек-

тров белка хондроитинсульфат-протеогликана 4, определенное с помощью ЖХ-МС/МС, также было выше в 3D-культурах, составив 41,75 спектра по сравнению с 2,24 спектра в образцах 2D-культур. Уровни аггрекана, бигликана и декорина между культурами не различались. 3D-культуры хондроцитоподобных клеток из чПСК не показали достоверных отличий в содержании ГАГ по сравнению с 2D, что указывает на необходимость оптимизации условий их дифференцировки.

Выводы. В нашем исследовании был определен состав ГАГ, синтезируемых *in vitro* хондроцитами различного генеза, с использованием ИФА и ЖХ-МС/МС, а также оценено влияние 2D- и 3D-культивирования на их синтез. Результаты показали, что 3D-среда культивирования создает условия, способствующие более полноценному формированию хондроцитарного ВКМ в образцах нативных хондроцитов. Однако, несмотря на это, полученные сфероиды хондроцитоподобных производных чПСК не достигают функциональной идентичности с естественной хрящевой тканью, даже после завершения протоколов дифференцировки и не представляют собой идеальные тканеинженерные конструкции для коррекции дефектов хряща.

Ключевые слова: хондроциты; артрит; внеклеточный матрикс; гликозаминогликаны; чПСК; дифференцировка; ИФА; ЖХ-МС/МС

INTRODUCTION

Chronic joint diseases continue to pose a serious challenge to global health. These diseases impose a significant economic burden due to the prevalence and severity of damage to the musculoskeletal system, as well as the costs associated with treatment and related disabilities. In 2019, about 528 million people worldwide suffered from osteoarthritis, which was by 113% more than in 1990 [1]. The clinical potential of chondrocytes derived from the cartilage tissue of patients has long been recognized. Matrix-induced autologous chondrocyte implantation (MACI) is currently the most common method for treating cartilage deficiency and correcting cartilage defects. This therapeutical method was approved by the US Food and Drug Administration (FDA) in 2016 [2].

MACI technique uses autologous chondrocytes isolated from a biopsy of the cartilage tissue of patients, which are cultured on a 3D matrix of a collagen membrane [3]. However, in some cases, such as under a prolonged use of corticosteroids, nonsteroidal anti-inflammatory drugs, or chemotherapy, sufficient amounts of cellular material cannot be obtained, which is the main limitation of this technique. Human pluripotent stem cells, not only being an unlimited source of cellular material but also not requiring painful surgical intervention, represent the next step in the development of cellular technologies [4]. However, a number of problems associated with the hPSCs use remain unresolved, such as the high cost of their culture and differentiation in the chondrocytic direction, the potential risks of an immune reaction to chondrocytes obtained from hPSCs, and the risks of tumorigenicity and oncogenicity of

cell constructs obtained from hPSCs. Progress in solving these problems is inextricably linked to the development of new protocols for differentiation, genetic editing, and culturing of both chondrocytes derived from hPSCs and hPSCs themselves [4].

Cartilage tissue forms on the extracellular matrix (ECM) and a small number of specialized cells known as chondrocytes. The composition and organization of the ECM determine its biomechanical properties. The functional properties of ECM are similar to those of a viscoelastic gel consisting of two main phases: a solid phase comprising collagen fibers, proteoglycans and non-collagen proteins, and a liquid phase consisting of 80% water and electrolytes (Ca^{2+}, K^+, Na^+, Cl^-); the main proteoglycan in cartilage is aggrecan.

Chondrocytes are mechanosensitive cells, whose functional activity depends significantly on the microenvironment [5]. Chondrocytes are located in small cavities referred to as lacunae surrounded by ECM. These structures, known as chondrons [6], form the main structural, functional, and metabolic units of articular cartilage [7] and differ in the composition of collagen fibrils and GAGs. The chondron area is 2–4 μm thick, consisting mainly of proteoglycans and GAGs (perlecan, decorin, biglycan, aggrecan, and hyaluronic acid), as well as type VI collagen [8].

The main proteoglycan of cartilage tissue is aggrecan, which interacts with hyaluronic acid and forms large aggregates that impart shock-absorbing properties to cartilage tissue. A decrease in the content of aggrecan and other proteoglycans in cartilage is associated with the development of osteoarthritis, which leads to deterioration of the mechanical properties of cartilage and disease

progression [9]. At the same time, biglycan and decorin are small leucine-rich proteoglycans (SLRP) that play a key role in maintaining the structure and function of cartilage tissue. They are involved in the regulation of collagen fibrillogenesis by interacting with its fibers and influencing the ECM organization. Dekortin, in particular, binds to type II collagen, regulating the size and shape of collagen fibrils thus maintaining the structural integrity of cartilage. Biglycan also interacts with collagen; however, its functions are more diverse: participation in bone mineralization and regulation of cell growth [10]. Chondroitin sulfate-proteoglycan 4 is a membrane proteoglycan involved in adhesion, migration, and intercellular signaling. Although its role in cartilage tissue remains to be understood, it is assumed to affect the interaction of chondrocytes with ECM, supporting the structure and functionality of cartilage. Chondroitin sulfate-proteoglycan 4, is also capable of regulating cell growth and differentiation, rendering it a promising target for osteoarthritis therapy and cartilage tissue regeneration [11].

Enzymatically isolated chondrocytes can produce a new ECM within a few hours after culture *in vitro*, although no further formation of ECM occurs around the cell [12]. It is believed that the full maturation of ECM takes 2–3 weeks. At the same time, studies have shown that specific conditions are necessary for the full maturation of ECM and the formation of chondrons: the microenvironment and physical factors, such as gravitational and hydrodynamic effects [13], which can be maintained in 3D structures [14]. Spheroidal cell cultures promote improved cell survival and functional activity compared to conventional 2D chondrocyte cultures. These advantages are explained by the ability of 3D structures to more effectively simulate the natural microenvironment, as well as the influence of chemical and physical factors [15]. Conversely, under the conditions of 2D culture, chondrocytes lose their phenotype, demonstrate increased production of type I collagen (associated with fibrous cartilage) and decreased levels of type II collagen (associated with hyaline cartilage), as well as lower levels of GAG. It should be noted that this differentiation phenomenon has not yet been fully studied in chondrocytes obtained from HPSCS.

The GAG composition and content level are the critical characteristics describing the formed chondron. Therefore, when developing cartilage-like tissue engineering structures for regenerative medicine, determining the level of GAG content and composition is essential for assessing the effectiveness and functional activity of the resultant cartilage implant [16]. In addition, the state of chondrocytes and their microenvironment affect the content, properties, and composition of ECM. Chondrocytes obtained from damaged tissues, such as osteoarthritis-affected cartilage, synthesize heparan sulfate with increased sulfation, which is associated with an increased activity of catabolic enzymes such as matrix metallopeptidases (MMP3, MMP13), and a decreased expression of key chondrocyte genes such as type II collagen alpha 1 chain (*COL2A1*), aggrecan (*ACAN*), and SRY-box transcription factor 9 (*SOX9*) [8].

In their study, Lee G. and Loeser R. [12] showed that chondrocytes from the surface and middle/deep areas of cartilage isolated by zonal abrasion exhibit significant differences in GAG content when cultured during the period of four weeks. Hu J. and Athanasiou K. found that chondrocytes from the middle/deep area produced 250% more GAG and collagen in terms of dry weight compared to chondrocytes from the surface area [17]. In addition, chondrocytes of the middle/deep area are capable of forming aggregates and cartilage-like structures, which is favorable for the creation of tissue engineering structures. In another study, Beckers J. et al. [18] found a discrepancy in the synthetic activity of chondrocytes isolated from loaded and unloaded cartilage areas, although these differences decreased when the cells underwent several passaging procedures.

The existing approaches to obtaining cartilage-like cell structures from hPSCs remain to be imperfect, associated with low reproducibility, variability in cell differentiation efficiency, insufficient mechanical strength of the formed tissues, and scaling complexity. GAGs are one of the main components of the ECM of cartilaginous tissue; therefore, a qualitative and quantitative analysis of GAG composition is an important stage in assessing the potential therapeutic efficacy of cartilage-like cellular structures. At the same time, the cultivation conditions that directly affect the resultant GAG content are key to creating effective cellular structures. Cultivation conditions can be modified to obtain tissue samples most similar to hyaline cartilage in their characteristics.

In this study, we aim to determine the composition of GAGs synthesized *in vitro* by chondrocytes of various origins using enzyme immunoassay (ELISA) and liquid chromatography with tandem mass spectrometry (LC–MS/MS), as well as to evaluate the effect of 2D and 3D cultivation on their synthesis.

MATERIALS AND METHODS

Distribution of samples by experimental groups

Samples of the studied cell cultures were divided into groups (Table 1) according to the criteria of cell origin and type of their culture:

1) The group of 2D cultures of native chondrocytes included samples obtained from patients with gonarthrosis and meniscal neuralgia;

2) The group of 3D cultures of native chondrocytes was also represented by samples from patients with similar diagnoses, but grown under 3D culture conditions;

3) The group of 2D cultures of chondrocytes differentiated from hPSCs included samples obtained from the IPSRG4SAb2m c55/1 and IPSRG4S hPSC cell lines;

4) The group of 3D cultures of chondrocytes differentiated from hPSCs also contained samples obtained from the same cell lines, but under 3D cultivation conditions;

5) The control group of hPSCs consisted of IPSRG4S and IPSRG4SAb2m c55/1 cell lines that did not undergo differentiation into chondrocytes.

This sample separation approach enabled a comparative analysis of the effect of different cultivation conditions and cell origin on their characteristics.

Table 1. Distribution of samples into groups for glycosaminoglycan content measurement by ELISA and proteoglycan content measurement by LC-MS/MS

ELISA			LC-MS/MS		
Sample group	Sample number	Cell culture characteristics	Sample group	Sample number	Cell culture characteristics
2D cultures of native chondrocytes	5	Gonarthrosis — 4 Meniscal neuralgia — 1	2D cultures of native chondrocytes	5	Gonarthrosis — 4 Meniscal neuralgia — 1
3D cultures of native chondrocytes	2	Gonarthrosis — 1 Meniscal neuralgia — 1	3D cultures of native chondrocytes	5	Gonarthrosis — 4 Meniscal neuralgia — 1
2D cultures of chondrocytes differentiated from hPSCs	2	the cell line hPSCs IPSRG4SΔb2m cl55/1 the cell line hPSCs IPSRG4S	2D cultures of chondrocytes differentiated from hPSCs	2	the cell line hPSCs 4SΔb2m cl55/1 the cell line hPSCs IPSRG4S
3D cultures of chondrocytes differentiated from hPSCs	2	the cell line hPSCs IPSRG4SΔb2m cl55/1 the cell line hPSCs IPSRG4S	3D cultures of chondrocytes differentiated from hPSCs	2	the cell line hPSCs IPSRG4SΔb2m cl55/1 the cell line hPSCs IPSRG4S
hPSCs control group	2	the cell line hPSCs IPSRG4S the cell line hPSCs IPSRG4SΔb2m cl55/1	hPSCs control group	1	the cell line hPSCs IPSRG4S

Table prepared by the authors using their own data

Obtaining chondrocyte primary culture from donor material and chondrocyte cultivation

Chondrocytes were isolated from biopsies of cartilage tissue of patients who provided their informed consent. Prior to crushing, the cartilage was transferred to a 15 mL tube using a serological pipette and washed once with a Dulbecco's Modified Eagle Medium DMEM (Thermo Fisher Scientific, USA) supplemented with double the amount of penicillin/streptomycin (200 U/mL, PanEco, Russia). The cartilage was then placed in a sterile 60 mm Petri dish and crushed with sterile scissors and a scalpel in the presence of 4 mL of DMEM medium, to which double the amount of antibiotic was also added. The crushed cartilage was washed in 15 mL of the same medium. The cartilage pieces were then incubated for 40 min in a 15 mL tube on a laboratory orbital shaker (Infors HS Celltron, Switzerland) at 37°C with 5% CO_2 using 10 mL of DMEM medium supplemented with double the amount of antibiotic, as well as 10 mg of type IV collagenase (Worthington Biochemical, USA) and 10 mg of type I collagenase (Worthington Biochemical, USA). Following incubation, the cartilage pieces were centrifuged for 5 min at 200 g in a centrifuge (Eppendorf Centrifuge 5804R, Germany). The filler fluid was carefully removed, and the pieces of cartilage were resuspended in DMEM medium and additionally rinsed twice. After that, 10 mL of Dulbecco's Modified Eagle Medium was added to the cartilage with the addition of a 1:1 F-12 nutrient mixture DMEM/F12 (Thermo Fisher Scientific, USA) supplemented with 20% fetal bovine serum FBS (HyMedia, India), 2 mM Glutamax (Thermo Fisher Scientific, USA) and 100 U/mL of penicillin/streptomycin (PanEco, Russia). The pieces were then transferred to a culture vial T-25 cm^2, pretreated with 0.01% gelatin type B solution (PanEco, Russia). Pieces of cartilage were cultured at 37°C with 5% CO_2. The culture was passaged until the cell monolayer reached 70% confluent density; the culture medium was replaced every five days.

Cultivation of human pluripotent stem cells

The IPSRG4S line of induced pluripotent human stem cells was obtained by collaboration of the Cell Biology Laboratory (Lopukhin National Research Center for Biological Medicine, Moscow, Russia) and the Stem Cell Laboratory of the A.I.Virtanen Institute for Molecular Sciences (University of Eastern Finland, Kuopio, Finland) [19]. Later, in the Cell Biology Laboratory of the Lopukhin National Research and Scientific Center of the Russian Academy of Medical Sciences, based on the IPSRG4S hPSC cell line, the IPSRG4SΔb2m cl55/1 hPSC cell line was obtained, in which the beta-2 microglobulin gene was inactivated using CRISPR/Cas9 genomic editing. hPSC was cultured in six-well plates pre-coated with matrigel (BD, USA) on a nutrient medium consisting of mTeSR-1 (STEMCELL Technology, Canada) and Hybris 8 (Paneco, Russia) in a ratio of 1:3.

Differentiation of human hPSCs in the chondrocytic direction

To induce differentiation, hPSCs were cultured in a DMEM/F12 medium (Thermo Fisher Scientific, USA) supplemented with 10% FBS (HyMedia, India), 2 mM Glutamax (Thermo Fisher Scientific, USA), 100 U/mL penicillin/streptomycin (PanEco, Russia), 10 μM kinase-3 glycogen synthase inhibitor CHIR99021 (Miltenyi Biotec, Germany), and 10 nM retinoic acid (Miltenyi Biotec, Germany). The cells were incubated for two days in a CO_2 incubator at 37°C with 5% CO_2. After that, the medium was replaced with a DMEM/F12 medium (Thermo Fisher Scientific, USA) supplemented with 10% FBS (HyMedia, India), 2 mM Glutamax (Thermo Fisher Scientific, USA), 100 U/mL penicillin/streptomycin (PanEco, Russia), 10 ng/mL transforming growth factor β (TGF-β) (Miltenyi Biotec, Germany), 10 ng/mL bone morphogenetic protein-2 (BMP-2) (Miltenyi Biotec, Germany), 2% B27 (Thermo Fisher Scientific, USA), 10 μM ascorbic

acid (Sigma-Aldrich, USA), and 1% insulin solution-Transferrin-selenite (PanEco, Russia). The cells were cultured for two weeks under the same CO_2 incubator conditions. After differentiation, chondrocyte-like derivatives were cultured in a DMEM/F12 medium (Thermo Fisher Scientific, USA) supplemented with 10% FBS (HyMedia, India), 2 mM Glutamax (Thermo Fisher Scientific, USA), 100 U/mL penicillin/streptomycin (PanEco, Russia), 10 ng/mL TGF-β (Miltenyi Biotec, Germany), and 10 ng/mL of BMP-2 (Miltenyi Biotec, Germany).

Preparation of spheroid culture

For the formation of spheroids, chondrocytes were taken, which were on the second passage after isolation of the cell culture from cartilage tissue; chondrocyte-like derivatives of hPSCs were folded into spheroids on the second passage after the onset of the differentiation protocol of hPSCs. By the commencement of chondrocyte differentiation of hPSCs, the IPSRG4S cell line had been located at passage 34, and IPSRG4SΔb2m cells had been located at passage 41. Chondrocyte-like derivatives were removed from six-well plates using 0.05% trypsin solution (Thermo Fisher Scientific, USA), and chondrocytes were removed from T-75 cm^2 culture vials using 0.25% trypsin solution (Thermo Fisher Scientific, USA). The cells were washed of trypsin using a DMEM medium (Thermo Fisher Scientific, USA) supplemented with 10% FBS (HyMedia, India) and centrifuged for 5 min at 200 g. The cells were then transferred to an AggreGell800™ plate (STEMCELL Technology, Canada) at a density of 900,000 to 3 million cells per well and cultured in a DMEM/F12 medium (Thermo Fisher Scientific, USA), supplemented with 10% FBS (HyMedia, India) and 10 μM Rho kinase inhibitor Y27632 (Miltenyi Biotec, Germany), by adding 2 mL of the full medium to the well.

The cells were cultured on an AggreGell800™ plate from 12 h to 24 h. After the incubation period, the spheroids were collected from the wells using a 5 mL serological pipette and transferred to a 15 mL tube. They were allowed to precipitate to the bottom of the tube for 2–3 min, after which the filler liquid was discarded. The spheroids were then placed in a freshly frozen undiluted matrigel (BD, USA). Following 30 min, the spheroids were washed by passive settling in a 15 mL tube or careful centrifugation for 1 min at 300 rpm. Subsequently, the spheroids were transferred to homemade mini-bioreactors, which were low-adhesion Petri dishes with a drop of glue in the center. A detailed protocol for creating mini-bioractors was described in a previous study [20]. The mini-bioreactors were placed on an orbital shaker in a CO_2 incubator. The rotation speed was set to 70–75 rpm. Following 24 h, the medium was replaced. Later, the environment was changed weekly. After transfer to the bioreactors, the spheroids were cultured for two weeks.

Quantitative polymerase chain reaction (qPCR)

To evaluate the expression of chondrocyte markers, a quantitative reverse transcription polymerase chain reaction was performed according to the previously described protocol [21].

For cell lysis in monolayer cultures and spheroids, an RLT buffer (QIAGEN, Germany) supplemented with 10 μL/mL of β-mercaptoethanol was used. Spheroids (3–5 pieces each, depending on the size) and monolayer cell cultures were pipetted in 600 μL of RLT for lysis. The RNeasy Plus Mini Kit (QIAGEN, Germany) was used to isolate RNA, and a solution of DNA was used for purification from genomic DNA (SibEnzyme, Russia). The synthesis of the first cDNA strand was carried out using an MMLV RT kit (Evrogen, Russia) according to the manufacturer's protocol. For qPCR, a reaction mixture was prepared: 5 μL of 5×qPCRmix-HS SYBR (Evrogen, Russia), 0.8 μL of 10 μM primer mixture, 18.2 μL of water, then 1 μL of cDNA matrix was added to the wells of a 96-well plate (SSIbio, USA). Amplification was performed on a CFX96 thermal cycler (Bio-Rad, USA) at 39 cycles. cDNA of IPSC samples was used as a negative control to evaluate the specificity of the reaction. The results were analyzed using Microsoft Excel by the ΔΔCt method.

Measurement of glycosaminoglycan content using ELISA

The GAG content in 2D and 3D chondrocyte culture samples was determined using a Human IGG ELISA Kit (FineTest, China). During the cultivation of chondrocytes, aliquots of the medium were selected for analysis. The samples were stored at a temperature of minus 80°C. Each analysis of a biological sample consisted of two repetitions. The optical density was measured at a wavelength of 450 nm using a Tecan Infinite 200 Pro reader. The standard curve was formed in the Curve Expert Basic software by plotting the dependence of the optical density at $\lambda = 450$ nm of each standard solution on its corresponding concentration. The target concentration of the samples was interpolated from this standard curve.

For ELISA of 2D cell culture samples, 200,000 to 500,000 chondrocyte cells, chondrocyte-like cPSC derivatives, and 1,500,000 cPSC cells were taken. For ELISA of 3D cell culture samples, 700 thousand cells of chondrocyte spheroids, from 375,000 to 1,000,000 cells of chondrocyte-like derivatives of hPSCs and 1,000,000 cells of hPSC spheroids were taken. For data processing, the values obtained for each sample were normalized depending on the volume of the medium in which the chondrocytes were cultured and the number of cells.

Collecting samples for LC–MS/MS

Chondrocytes and chondrocyte-like derivatives from hPSCs were used to create chondrocyte multilayers (2D cartilage-like structures) and 3D spheroids using AggreWell 800™ microlunar plates (STEMCELL Technology, Canada). In addition, 2D and 3D cartilage-like structures were obtained from primary cultures of chondrocytes isolated from patients' donated biological materials. Samples of cell cultures and 3D structures were subjected to trypsinolysis, liquid chromatography was performed using the Dionex Ultimate 3000 system (Thermo Fisher Scientific, USA) followed by mass spectrometric analysis using an Orbitrap Q Exact HF-X system (Thermo Fisher Scientific, USA).

For LC–MS/MS, 1,000,000 cells were taken for the analysis of 2D cultures and 10 spheroids for the analysis of 3D cell cultures. Prior to the procedure, monolayer cultures were washed three times with phosphate buffer to remove the culture medium followed by separation from the culture dish using a Versene solution. After flushing by centrifugation, the filler liquid was removed and the cells were frozen at minus 70°C before the analysis. The 3D structures were similarly washed with phosphate buffer three times by passive sedimentation. The precipitate was then subjected to the final washing procedure before freezing. After sedimentation, the precipitate was transferred for protein composition analysis by the LC–MS/MS method.

Analysis of GAG composition using LC–MS/MS

To destroy cellular structures and isolate proteins, a 10% solution of sodium deoxycholate was added to the samples, adjusting to a final concentration of 1%. A mixture of nucleases was then added to degrade the nucleic acids followed by incubation at 4°C for 30 min. Next, tris(2-carboxyethyl)phosphine (5 mM) and chloroacetamide (30 mM) were added to the solution to restore and alkylate disulfide bonds, after which they were incubated at 80°C for 10 min. The proteins were precipitated with methanol-chloroform; the resulting precipitates were resuspended in 100 μL of Tris-HCl buffer (50 mM, pH 8.5). After that, the protein concentration was determined using a BCA Assay Kit (Thermo Fisher Scientific Inc.). Enzymatic protein cleavage was performed with trypsin (Trypsin Gold, Mass Spectrometry Grade, Promega) in the trypsin ratio:protein 1:50 (% w/w), holding samples at 37°C for 16 h. Proteolysis was stopped by adding trifluoroacetic acid to a concentration of 1%. The peptides were then dried using vacuum concentration (SpeedVac, Thermo Fisher Scientific Inc.) and dissolved in 20 μL of a solution containing 3% acetonitrile and 0.1% trifluoroacetic acid in ultra-high purity (mQ) water. Subsequently, the concentration of peptides was determined using a coloristic method followed by assessing protein concentration using bicynchonic acid (BCA analysis).

A Dionex Ultimate 3000 nano-LC system (Thermo Fisher Scientific, Waltham, MA) with a PicoTips C-18 column (length 10 cm, inner diameter 75 μm, New Objective, USA) filled with Kinetex C18 sorbent (2.4 μm, Phenomenex, Torrence, CA) was used for liquid chromatography. The flow was set at 300 nL/min at 60°C. Buffer A consisted of 0.1% formic acid in LC/MS water, and buffer B consisted of 80% acetonitrile, 0.1% formic acid in LC/MS water. The separation was carried out in a gradient mode, increasing the concentration of buffer B from 3% to 40% for 120 min. Mass spectrometric analysis was performed on an Orbitrap Q Exact HF-X (Thermo Fisher Scientific) instrument with a nanospray source (voltage +2.2 kV, capillary temperature 300°C). MS1 scanning was performed in the range of 350–1500 m/z (resolution 60,000, AGC 3e6, injection time 45 ms). HCD with an energy of 30 eV were used for fragmentation. MS2 scanning was performed in the range of 200–2000 m/z (resolution 30,000, AGC 2e5, injection time 50 ms). The dd-MS2 strategy was used with the selection of the 12 most intense ions (Top12).

LC–MS/MS data analysis

The raw LC–MS/MS data obtained on the Orbitrap mass spectrometer was converted to mgf format data using the MSConvert software with the following command line parameters: "--mgf --filterpeakPicking true". For complex identification of proteins, the obtained results were processed using MASCOT and X! Tandem. Tandem mass spectrometry parameters were analyzed using the UniProt Knowledgebase protein sequence database (human taxon) using the ALANINE algorithm with an error tolerance of 20 ppm to determine the precursor mass and 50 ppm to determine the fragment mass. The search parameters were set as follows: protein hydrolysis by trypsin with one possible missing cleavage site, permanent carbamide methylation modification (C), and variable oxidative modification (M). To compare the identification results obtained using MASCOT and X! Tandem, and the compilation of the final list of identified proteins, the results of both identification algorithms were analyzed in the Scaffold 5 software. This algorithm estimated the local frequency of false positive identifications using a standard protein grouping throughout the experiment. To assess the identification error of peptides and proteins, a threshold level of false identification of less than 5% was selected. Differential gene expression was identified using the R limma programming language package.

Statistical analysis

Statistical analysis of qPCR, ELISA, and LC–MS/MS data was performed using the Bizorender software. The differences between the groups were assessed by the nonparametric Kruskal–Wallis test, which is used for independent samples in which data did not have a normal distribution. When a statistically significant difference was detected ($p < 0.05$), a multiple Dann comparison test was additionally performed for paired comparisons between the groups, which allowed us to adjust the probability of false positive results. The differences at $p < 0.05$ were considered statistically significant, while the following symbols were used to indicate the significance levels: * ($p < 0.05$), △ ($p < 0.01$), ○ ($p < 0.001$). To analyze the qPCR data, the Welch t-test was used, which takes into account differences in standard deviations between two groups of independent samples. The differences were considered significant at a statistical significance level of $p < 0.05$.

RESULTS AND DISCUSSION

Analysis of chondrocyte gene expression

The qPCR method was used to confirm the identity of cell cultures of chondrocytes and chondrocytes obtained from hPSCs by analyzing the expression of key molecular markers characteristic of mature cartilage cells.

The results of qPCR confirmed that cell cultures of native chondrocytes exhibit high expression of specific markers such as aggrecan (ACAN), type II collagen (COL2A1), and transcription factor SOX9, which is a key regulator of chondrogenesis (Fig. 1). The graph shows the relative

expression values of key chondrocyte genes in cell cultures of native chondrocytes and those obtained from hPSCs. The *YWHAZ* reference gene was used to normalize expression levels. The columns on the graph reflect the average values of relative normalized gene expression (ΔΔCt) with an indication of the standard deviation (SD). No significant differences were found between the samples of native chondrocytes and chondrocyte-like derivatives of hPSCs analyzed using the Welch *t*-test. A high level of chondrocyte gene expression indicates the functional maturity of native chondrocyte cell cultures. Chondrocytes obtained from hPSCs also showed a pronounced expression of these markers, which indicates a high degree of their differentiation into cartilage cells similar to native chondrocytes.

Quantitative determination of GAG in chondrocytes of various origins using ELISA

The conducted quantitative analysis of GAG using ELISA revealed that the content of these biopolymers is significantly higher in 3D cultures of chondrocytes compared to those in 2D cultures. In particular, the concentration of GAGs in 3D cultures of native chondrocytes reached 1,099.87 ng/mL, which was significantly higher than the level recorded in 2D cultures (108.67 ng/mL). A similar trend was observed in chondrocyte cultures obtained from hPSCs; however, the GAG content remained lower compared to native chondrocytes, which may indicate the need

for additional optimization of differentiation conditions and prolongation of the cultivation period; the corresponding data are presented in Fig. 2.

The phenomenon of chondrocyte dedifferentiation in 2D conditions is well documented [25, 26]. It was shown that the cultivation of chondrocyte spheroids in 3D media enhances the process of chondrogenic differentiation, allowing for the production of chondrogenic cell constructs without the need for scaffolding or multiple cell passaging [27, 28]. However, a quantitative assessment of the GAG content was not provided in this context.

Gene composition in cultures of chondrocyte cells of various origins

LC–MS/MS analysis was used to explore the ECM composition. Glycosaminoglycans (GAGs) were found to comprise chondroitin sulfate proteoglycan 4 as the main component, the level of which was significantly higher in 3D cultures of native chondrocytes. This indicates favorable conditions for the production of key components for the cartilage matrix. At the same time, the content of other proteoglycans, such as aggrecan, biglycan, and decorin, remained unchanged.

Figure 3 presents the results obtained when investigating the composition of GAGs synthesized in cultures of chondrocytes of various origins using the LC–MS/MS method. The graph shows the quantitative content of various types of GAGs, including chondroitin sulfate-proteoglycan
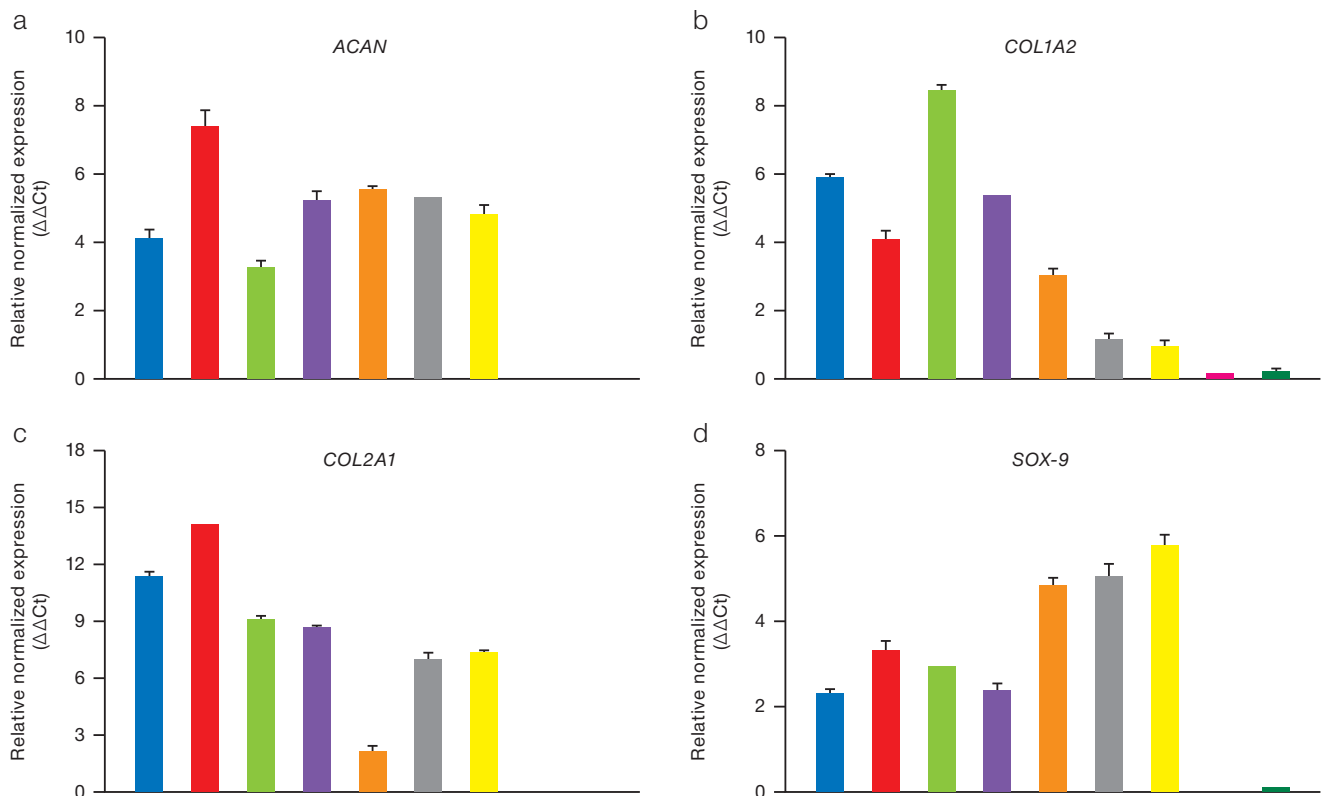
Figure prepared by the authors using their own data

Fig. 1. Relative expression of chondrocyte genes (ΔΔCt), normalized for the *YWHAZ* gene, in 2D samples of chondrocyte cultures of various origins, measured by the qPCR method
Note: a. Aggrecan (*ACAN*); b. Alpha-2 chain of type I collagen (*COL1A2*); c. Alpha-1 chain of type II collagen (*COL2A1*); d. Transcription factor *SOX-9*; color matching in the diagram to the samples under study: blue — chondrocytes of patient 76; red — chondrocytes of patient 75; green — chondrocytes of patient 47; purple — chondrocytes of patient 44; brown — chondrocytes of patient 12; gray — chondrocyte-like cells differentiated from hPSC IPSRG4SΔb2m cl55/1; yellow — chondrocyte-like cells differentiated from hPSC IPSRG4S; purple — hPSC IPSRG4SΔb2m cl55/1; dark green — hPSC IPSRG4S.

Figure prepared by the authors using their own data

Fig. 2. Results of quantitative determination of GAG by ELISA in chondrocyte cultures under 2D and 3D conditions
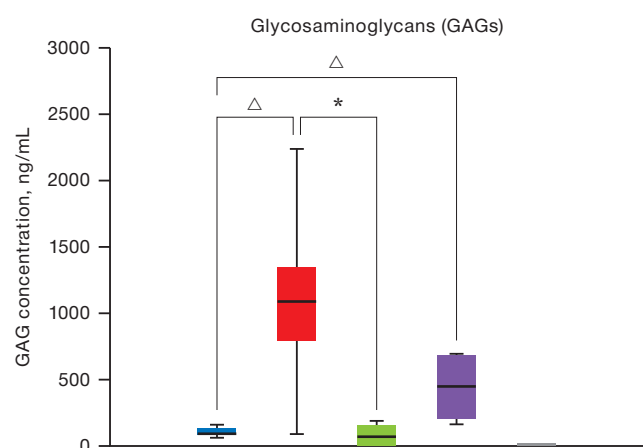**Note:** the colors in the diagram correspond to the studied samples: blue — 2D cultures of patients' chondrocytes ($n = 5$); red — 3D cultures of patients' chondrocytes ($n = 2$); green — 2D cultures of patients' chondrocytes differentiated from hPSC ($n = 2$); purple — 2D cultures of patients' chondrocytes differentiated from hPSC ($n = 2$); gray is the control group of hPSC ($n = 2$); the level of GAG expression in hPSC cultures is zero; levels of statistical significance compared with the control group: * — $p < 0.0332$; △ — $p < 0.0021$.

4, aggrecan, biglycan, and decorin, in 2D and 3D cultures of native chondrocytes and chondrocytes obtained from hPSC. The data is presented as averages with a standard deviation (SD). Significant differences between the groups were assessed using statistical criteria.

The composition of GAGs determined using LC–MS/MS showed an increased level of their content in 3D cultures of native chondrocytes compared to that in 2D cultures (Fig. 3). Chondrocyte spheroids obtained from the biopsies of patients' tissues showed a significantly higher concentration of chondroitin sulfate proteoglycan 4. At the same time, 3D cultures of chondrocyte-like derivatives of hPSC demonstrated a low level of all the studied GAGs, which indicates their immaturity even after differentiation. This limitation can potentially be eliminated by extending the cultivation period and supplementing the medium with factors that stimulate the metabolic pathways of GAG synthesis, such as TGF-β, SOX9, bone morphogenetic proteins, and retinoic acid signaling pathways.

CONCLUSION

In this study, we investigated the composition of GAGs synthesized *in vitro* by chondrocytes of various origins using ELISA and LC–MS/MS and evaluated the effect of
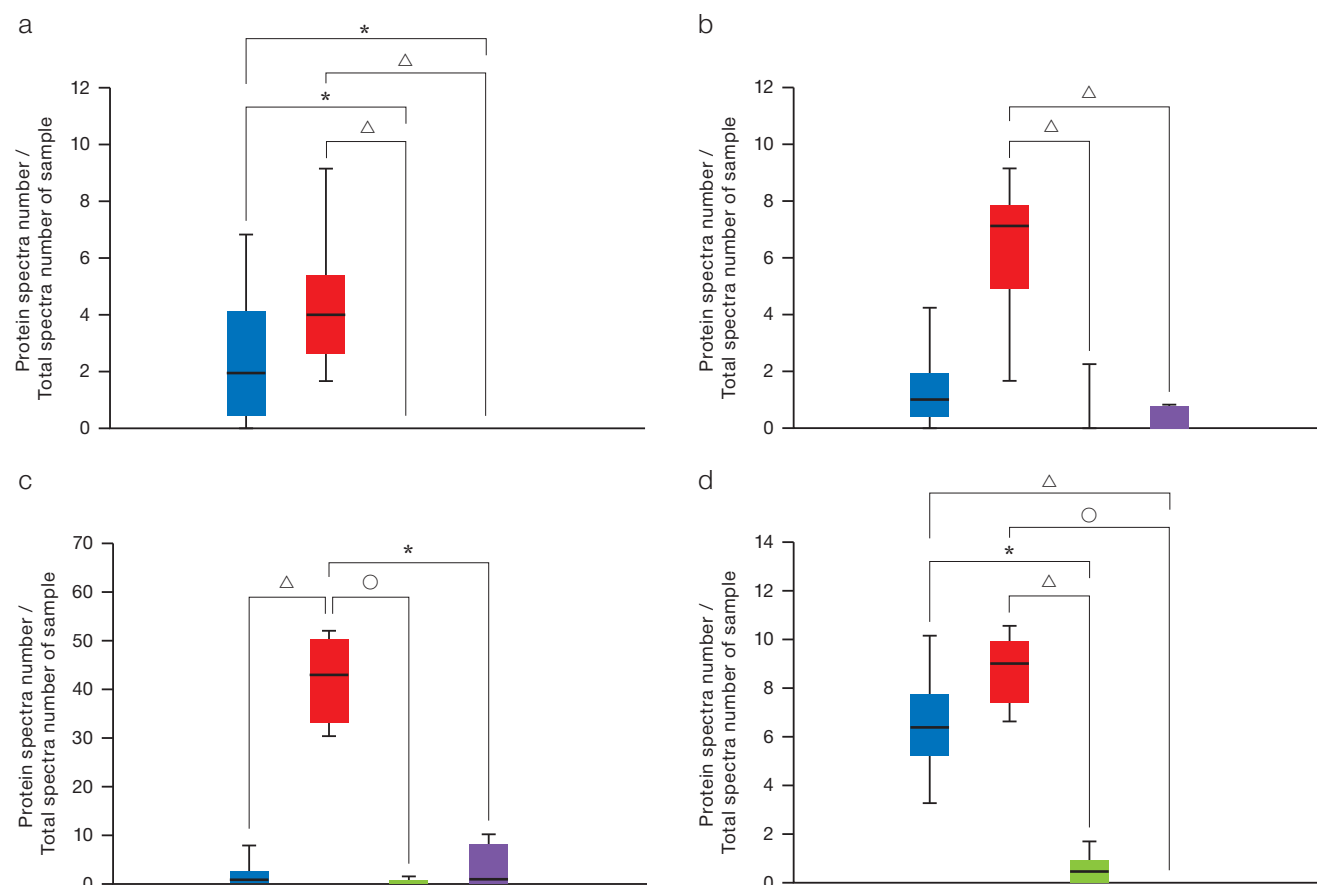
Figure prepared by the authors using their own data

Fig. 3. Composition analysis of GAGs by the LC–MS/MS method
Note: a. Aggrecan; b. Biglycan; c. Chondroitin sulfate proteoglycan 4; d. Decorin; color matching in the diagram to the studied samples: blue — 2D cultures of patients' chondrocytes ($n = 5$); red — 3D cultures of patients' chondrocytes ($n = 5$); green — 2D cultures of patients' chondrocytes differentiated from hPSCs ($n = 2$); purple — 2D cultures of patients' chondrocytes differentiated from hPSCs ($n = 2$); gray — hPSCs control group ($n = 1$); the level of proteoglycan expression in hPSCs cultures is zero; levels of statistical significance compared with the hPSCs control group: * — $p < 0.0332$; △ — $p < 0.0021$; ○ — $p < 0.0001$.

2D and 3D cultivation on their synthesis. According to the results obtained, the conditions of 3D culture are favorable for a more complete formation of chondrocyte ECM in native chondrocyte samples. Nevertheless, the obtained spheroids of chondrocyte-like derivatives of hPSCs fail to achieve functional identity with natural cartilage tissue, even following completion of differentiation protocols, thus not representing optimal tissue engineering structures for correcting cartilage defects. For a more complete maturation in CM and an increase in their potential effectiveness as structures for tissue engineering, longer cultivation in 3D conditions may be required.

References

1. GBD 2019 Diseases and Injuries Collaborators. Global burden of 369 diseases and injuries in 204 countries and territories, 1990-2019: a systematic analysis for the Global Burden of Disease Study 2019. *Lancet*. 2020;396(10258):1204–22. https://doi.org/10.1016/S0140-6736(20)30925-9

2. Carey JL, Remmers AE, Flanigan DC. Use of MACI (autologous cultured chondrocytes on porcine collagen membrane) in the United States: preliminary experience. *Orthopaedic Journal of Sports Medicine*. 2020;8(8):e2325967120941816. https://doi.org/10.1177/2325967120941816

3. Dekker TJ, Aman ZS, DePhillipo NN, Dickens JF, Anz AW, LaPrade RF. Chondral Lesions of the Knee: An evidence-based approach. *Journal of Bone And Joint Surgery*. 2021;103(7):629–45. https://doi.org/10.2106/JBJS.20.01161

4. Ali E, Smaida R, Meyer M, Ou W, Li Z, Han Z, et al. iPSCs chondrogenic differentiation for personalized regenerative medicine: a literature review. *Stem Cell Res Ther*. 2024;15(1):e185. https://doi.org/10.1186/s13287-024-03794-1

5. Li M, Xiao R, Li J, Zhu Q. Regenerative approaches for cartilage repair in the treatment of osteoarthritis. *Osteoarthritis and Cartilage*. 2017;25(10):1577–87. https://doi.org/10.1016/j.joca.2017.07.004

6. Szirmai JA, ed. The concept of the chondron as a biomechanical unit. In F. Hartmann. *Biopolymere und Biomechanik von Bindegewebssystemen*. Heidelberg: Springer-Verlag Berlin; 1974. https://doi.org/10.1007/978-3-642-65963-8_9

7. Wang Q, El Haj A, Kuiper N. Glycosaminoglycans in the pericellular matrix of chondrons and chondrocytes. *J Anat*. 2008;213(3):266–73. https://doi.org/10.1111/j.1469-7580.2008.00942.x

8. Sophia Fox J, Bedi A, Rodeo S. The basic science of articular cartilage: structure, composition, and function. *Sports Health*. 2009;1(6):461–8. https://doi.org/10.1177/1941738109350438

9. Roughley PJ, Mort JS. The role of aggrecan in normal and osteoarthritic cartilage. *J exp ortop*. 2014;1:e8 https://doi.org/10.1186/s40634-014-0008-7

10. Han B, Li Q, Wang C, Chandrasekaran P, Zhou Y, Qin L, et al. Differentiated activities of decorin and biglycan in the progression of post-traumatic osteoarthritis. *Osteoarthritis Cartilage*. 2021;29(8):1181–92. https://doi:10.1016/j.joca.2021.03.019

11. Tang F, Lord MS, Stallcup WB, Whitelock JM. Cell surface chondroitin sulphate proteoglycan 4 (CSPG4) binds to the basement membrane heparan sulphate proteoglycan, perlecan, and is involved in cell adhesion. *J Biochem*. 2018;163(5):399–412. https://doi:10.1093/jb/mvy008

12. Lee G, Loeser R. Interactions of the chondrocyte with its pericellular matrix. *Cells Mater*. 1998; 8:135–49.

13. Vonk L, Roël G, Hernigou J, Kaps C, Hernigou P. Role of Matrix-Associated Autologous Chondrocyte Implantation with Spheroids in the Treatment of Large Chondral Defects in the Knee: A Systematic Review. *Int J Mol Sci*. 2021;22(13):e7149. https://doi.org/10.3390/ijms22137149

14. Prittinen J, Ylärinne J, Piltti J, Karhula S, Rieppo L, Ojanen S, et al. Effect of centrifugal force on the development of articular neocartilage with bovine primary chondrocytes. *Cell Tissue Res*. 2019;375(3):629–39. https://doi.org/10.1007/s00441-018-2938-3

15. Caron MM, Emans PJ, Coolsen MM, Voss L, Surtel DA, Cremers A, et al. Redifferentiation of dedifferentiated human articular chondrocytes: comparison of 2D and 3D cultures. *Osteoarthritis Cartilage*. 2012;20(10):1170–8. https://doi.org/10.1016/j.joca.2012.06.016

16. Study of the composition of glycosaminoglycans synthesized by chondrocytes of different origins *in vitro*. Abstracts of the 77th International School-Conference of Young Scientists «BIOSYSTEMS: Organization, Behavior, Control» Nizhny Novgorod; 2024 (In Russ.). EDN: QOPJWI

17. Hu J, Athanasiou K. Chondrocytes from different zones exhibit characteristic differences in high density culture. *Connect Tissue Res*. 2006;47(3):133–40. https://doi.org/10.1080/03008200600685392

18. Bekkers J, Saris D, Tsuchida A, van Rijen M, Dhert W, Creemers L. Chondrogenic potential of articular chondrocytes depends on their original location. *Tissue Eng*. 2024;20(3–4):663–71. https://doi.org/10.1089/ten.TEA.2012.0673

19. Sodhi H, Panitch A. Glycosaminoglycans in Tissue Engineering: A Review. Biomolecules. 2021;11(1):e29. https://doi.org/10.3390/biom11010029

20. Holmqvist S, Lehtonen Š, Chumarina M, Puttonen K, Azevedo C, Lebedeva O, et al. Creation of a library of induced pluripotent stem cells from Parkinsonian patients. *NPJ Parkinsons Dis*. 2016;2:e16009. https://doi.org/10.1038/npjparkd.2016.9

21. Eremeev A, Belikova L, Ruchko E, Volovikov, E., Zubkova, O., Emelin, A., et al. Brain Organoid Generation from Induced Pluripotent Stem Cells in Home-Made Mini Bioreactors. *J Vis Exp*. 2021;178:e62987. https://doi.org/10.3791/62987

22. Barinova AA, Pikina AS, Golubinskaya PA, Ruchko ES, Yeremeyev AV. *In vitro* assessment of the immunogenicity of chondrocytes derived from B2M knockout-induced pluripotent stem cells. *Extreme Medicine*. 2024;26(1):32–42 (In Russ.). https://10.47183/mes.2024.001

23. Yishan C, Yu Y, Wen Y, Chen J, Lin J, Sheng Z, et al. A high-resolution route map reveals distinct stages of chondrocyte dedifferentiation for cartilage regeneration. *Bone Res*. 2022;10:e38 https://doi.org/10.1038/s41413-022-00209-w

24. Ma B, Leijten JC, Wu L, Kip M, van Blitterswijk CA, Post JN, Karperien M. Gene expression profiling of dedifferentiated human articular chondrocytes in monolayer culture. *Osteoarthritis and Cartilage*. 2013;21(4):599–603. https://doi.org/10.1016/j.joca.2013.01.014

25. Vakhrushev IV, Basok YB, Baskaev KK, Novikova VD, Leonov GE, Grigoriev AM, et al. Cartilage-Specific Gene Expression and Extracellular Matrix Deposition in the Course of Mesenchymal Stromal Cell Chondrogenic Differentiation in 3D Spheroid Culture. Int. J. Mol. Sci. 2024;25:e5695. https://doi.org/10.3390/ijms25115695

26. Yen BL, Hsieh CC, Hsu PJ, Chang CC, Wang LT, Yen ML. Three-Dimensional Spheroid Culture of Human Mesenchymal Stem Cells: Offering Therapeutic Advantages and *In vitro* Glimpses of the In Vivo State. Stem Cells Translational Medicine. 2023; 12 (5):235–44. https://doi.org/10.1093/stcltm/szad011

AUTHORS

Polina A. Golubinskaya, Cand. Sci. (Med.)
https://orcid.org/0000-0002-7414-7326
polinapigeon@gmail.com

Evgeny S. Ruchko
https://orcid.org/0000-0002-1361-666X
ruchkoevgeny@yandex.ru

Arina S. Pikina
https://orcid.org/0000-0002-8967-2318
arina.pikina@yandex.ru

Igor P. Smirnov, Cand. Sci. (Chem.)
https://orcid.org/0000-0003-0402-3392
smirnov_i@hotmail.com

Tatiana V. Vladimirova
https://orcid.org/0009-0001-9266-2065
tat.vlad24@gmail.com

Veronika D. Gordeeva, Cand. Sci. (Biol.)
https://orcid.org/0000-0001-8904-8235
gordeeva.veronika@phystech.edu

Georgiy P. Arapidi, Cand. Sci. (Biol.)
https://orcid.org/0000-0003-2323-1859
arapidi@gmail.com

Artem V. Eremeev, Cand. Sci. (Biol.)
https://orcid.org/0000-0002-3428-7586
art-eremeev@yandex.ru

LUMINESCENT IMMUNOCHROMATOGRAPHY BASED ON Eu³⁺ COORDINATION COMPOUNDS FOR DETECTION OF PATHOGENIC MICROORGANISMS AND BACTERIAL TOXINS

Sergey P. Yarkov✉, Sergey I. Tretyakov, Inessa V. Shilenko, Ekaterina K. Shaulina, Angelina Mandaji, Denis A. Zenkov, Yury N. Ishkov, Konstantin K. Styazhkin

State Scientific Research Institute of Biological Instrumentation, Moscow, Russia

Introduction. Increasing the sensitivity of immunochromatographic assay as an express method for detection and diagnosis of pathogenic microorganisms and toxins is a relevant task with regard to ensuring food safety and population health in general.

Objective. Development of a prototype of a video digital recorder of luminescent immunochromatograms (RLI-Eu³⁺) and luminescent immunochromatographic tests (LICHT) adapted to a device based on microspheres with europium compounds. Comparison of the sensitivity of LICHT and AuNPs-based immunochromatography assay (ICA) tests to increase the sensitivity of the method for detection of pathogenic microorganisms and their toxins.

Material and methods. Submicron polymer microspheres labeled with organic complexes of trivalent europium (Eu³⁺) were used as a luminescent label for immunochromatography. LICHT were recorded using the developed RLI-Eu³⁺ recorder.

Results. The detection threshold of the Eu³⁺ luminescent complex on the immunochromatographic membrane was shown to be 2 pg/mm², with the linearity of the readings ranging within 2–200 pg/mm². The coefficients of variation of the instrument readings in the luminescent complex concentration range of 20–200 pg/mm² and 2–20 pg/mm² were found to be less than 5% and 10%, respectively. Using LICHT and the RLI-Eu³⁺ device, detection thresholds were determined as follows: cholera toxin — 10 ng/mL, staphylococcal enterotoxin type B — 0.5 ng/mL, plague pathogen cells — 1×10^3 cells/mL, anthrax pathogen spores — 5×10^3 spores/mL, Crimean-Congo hemorrhagic fever (CCHF) virus antigens — at a dilution of 1:640,000.

Conclusions. The developed video digital recorder RLI-Eu³⁺ and LICHT based on europium coordination compounds enabled the detection threshold of pathogenic microorganisms and bacterial toxins to be reduced by 20–128 times compared to immunochromatographic tests based on colloidal gold (CG) for the same pathogens.

Keywords: luminescent immunochromatography; video digital recording; submicron polymer particles with europium complexes; cholera toxin; staphylococcal enterotoxin type B; plague pathogen cells; anthrax pathogen spores; CCHF virus antigens

УДК 543.645: 616.931

ЛЮМИНЕСЦЕНТНАЯ ИММУНОХРОМАТОГРАФИЯ НА ОСНОВЕ КОМПЛЕКСНЫХ СОЕДИНЕНИЙ Eu³⁺ ДЛЯ ВЫЯВЛЕНИЯ ПАТОГЕННЫХ МИКРООРГАНИЗМОВ И БАКТЕРИАЛЬНЫХ ТОКСИНОВ

С.П. Ярков✉, С.И. Третьяков, И.В. Шиленко, Е.К. Шаулина, А. Мандажи, Д.А. Зенков, Ю.Н. Ишков, К.К. Стяжкин

Государственный научно-исследовательский институт биологического приборостроения, Москва, Россия

Введение. Повышение чувствительности иммунохроматографического анализа как одного из экспресс-методов индикации и диагностики патогенных микроорганизмов и токсинов актуально для пищевой безопасности и здравоохранения в целом.

Цель. Разработка экспериментального образца видеоцифрового регистратора люминесцентных иммунохроматограмм РЛИ-Eu³⁺ и адаптированных к прибору люминесцентных иммунохроматографических тестов (ЛИХТ) на основе микросфер с соединениями европия, сравнение чувствительности ЛИХТ с ИХА-тестами на основе наночастиц коллоидного золота (НКЗ) для увеличения чувствительности метода и выявления патогенных микроорганизмов и их токсинов.

Материалы и методы. В качестве люминесцентной метки для иммунохроматографии использовали субмикронные полимерные микросферы, меченные органическими комплексами трехвалентного европия (Eu³⁺), ЛИХТ регистрировали с помощью разработанного прибора-регистратора РЛИ-Eu³⁺.

Результаты. Показано, что порог обнаружения люминесцирующего комплекса Eu³⁺ на иммунохроматографической мембране равен 2 пг/мм², линейность показаний наблюдается в диапазоне 2–200 пг/мм². Коэффициенты вариации показаний прибора в диапазоне концентраций люминесцирующего комплекса 20–200 пг/мм² составляют < 5%, в диапазоне 2–20 пг/мм² — менее 10%. С использованием ЛИХТ и прибора РЛИ-Eu³⁺ определены следующие пороги обнаружения: холерного токсина — 10 нг/мл, стафилококкового энтеротоксина типа В — 0,5 нг/мл, клеток возбудителя чумы — 1×10^3 м.к./мл, спор возбудителя сибирской язвы — 5×10^3 спор/мл, антигенов вируса Конго-Крымской геморрагической лихорадки (ККГЛ) — в разведении 1:640 000.

Выводы. Разработанный видеоцифровой регистратор РЛИ-Eu³⁺ и ЛИХТ на основе комплексов европия позволили снизить в 20–128 раз порог обнаружения патогенных микроорганизмов и бактериальных токсинов по сравнению с иммунохроматографическими тестами на основе НКЗ для тех же патогенов.

Ключевые слова: люминесцентная иммунохроматография; видеоцифровая регистрация результатов; субмикронные полимерные частицы с комплексами европия; холерный токсин; стафилококковый энтеротоксин типа В; клетки возбудителя чумы; споры возбудителя сибирской язвы; антигены вируса ККГЛ

INTRODUCTION

Immunochromatographic assay (ICA) in its various schemes is widely used as a rapid clinical and laboratory diagnostic tool for detecting pathogenic microorganisms and toxins in the fields of, inter alia, food safety and environmental monitoring.

Luminescent immunochromatographic assay (LICA) is a versatile rapid diagnostic method (e.g., for detection of specific antibodies to the foot-and-mouth disease virus in blood serum [1]), in which luminescent particles are used to label antibodies. LICA quantifies the blood level of cardiac markers by analyzing the luminescence intensity of a test strip [2, 3]. The advantages of this method include its high reproducibility, sensitivity, and noise immunity against the natural fluorescence of the test sample. LICA is widely used for ensuring food safety [4, 5] and environmental monitoring [6].

In comparison with conventional immunochromatography labels — colloidal gold nanoparticles (AuNPs), LICA provides a two- or threefold increase in sensitivity [7, 8]. A comparison of fluorescent markers with AuNPs-based labels and magnetic nanoparticles in ICA can be found in [9]. Among the luminescent markers used in LICA, polymer microspheres with a diameter of 0.1–0.3 µm stand out. Their surface contains carboxyl groups, which allows covalent bonding with receptor proteins, e.g., immunoglobulins of various classes. When obtaining microspheres during polymerization, organic complexes of trivalent europium are introduced into the reaction environment, such as Eu(DBM)$_3$Phen, (1,10-phenanthroline)-tri- (dibenzoylmethanate) europium; Eu(TTA)$_3$Phen, (2,9-dimethyl-4,7-diphenyl-1,10-phenanthroline-tri-tenoyl triphluoroacetonate) europium in the amount of no greater than 10 wt % [10]. Preparations of such microspheres absorb light in the near ultraviolet band at λ_{max} = 365 nm and fluoresce in the red region at λ_{max} = 615 nm, while possessing a narrow emission peak of fluorescence. Semiconductor diodes, photoelectronic multipliers, and video cameras are used to register the luminescence of the analytical and control zones of immunochromatography (AZ, CZ). The digital video recording (DVR) method of ICA results with various labels has a number of advantages over other design solutions. Thus, the DVR of AuNPs-based tests makes it possible to obtain quantitative data on the content of toxins in dairy products [11].

In this study, we aim to develop a prototype of a video digital recorder for luminescent immunochromatography RLI–Eu³⁺ and luminescent immunochromatographic tests (LICHT) adapted to the device based on microspheres with europium compounds. A comparison of the sensitivity of LICHT and AuNPs-based ICA tests is conducted with the purpose of increasing the sensitivity of the method in identifying pathogenic microorganisms and their toxins.

MATERIALS AND METHODS

In order to obtain conjugates, we used monoclonal antibodies MAB to the B-subunit of the cholera toxin (CT), clone 3D11 (HyTest, Russia); MAB to capsular F1 antigen of the plague pathogen; MAB to anthrax spores, clone SA26; MAB to SEB (staphylococcal enterotoxin B) clone S222 (VNCMDL, Russia); mouse polyclonal immunoglobulins to CCHF (Gamaleya National Research Center for Epidemiology and Microbiology). The same batches of antibody preparations were used to create LICHT and AuNPs-based tests.

The certified CT and SEB preparations, inactivated *Y. pestis* microbial cells (strain EV), inactivated *B. anthracis* cells, strain 942 (State Research Center for Applied Microbiology and Biotechnology), certified sucrose-acetone antigens of the CCHF virus (strain 741), genotype Europe 1 (Gamaleya National Research Center for Epidemiology and Microbiology) were used as analyzed antigens.

The synthesis of antibody conjugates with luminescent microspheres was carried out by covalent binding [12]. 5 µL of suspension of luminescent microspheres (1%, weight/volume) were dispersed in 1.0 mL of MES buffer (0.05 M, pH 6.0) and supplemented with 10 µL EDC and NHS solutions (0.5 mg/mL) to activate the carboxyl groups contained on their surface. The resulting suspension was stirred and shaken on a Vortex-3000 laboratory vortex shaker (Viggens, China) for 20 min at room temperature in the dark followed by centrifugation on a Thermo Scientific SL 4R Plus centrifuge (Thermo Fisher Scientific, USA) at ×9600 g for 15 min; the supernatant was discarded. The precipitate was resuspended in 1.0 mL of phosphate buffer (0.01 M, pH 7.4). Then 100 µL of an antibody solution was added at a concentration of 0.2 mg/mL. The resulting mixture of antibodies and activated luminescent microspheres was continuously stirred for 2 h at room temperature in the

dark. Subsequently, 100 µL of a blocking solution (20% bovine serum albumin BSA) was added to block non-specific binding sites on the surface of the luminescent microspheres; the mixture was kept at room temperature for 1 h. The resulting suspension was centrifuged at 8000 g for 15 min, the supernatant was discarded, and 200 µL of a dispersing solution was added to the precipitate to prevent agglutination of conjugates of luminescent microspheres with antibodies (0.02 M, TRIS-HCl) containing 0.5% (weight/volume) trehalose, 10% (weight/volume) sucrose, 0.5% polyvinylpyrrolidone, 0.1% Tetronic 1307 (S9), 0.05% ProClinTM 300, 1% BSA and 0.1% Tween-20). Prior to application, the solution was stored at 4 °C.

For the formation of the LICHT analytical zone, the following antibodies were used: rabbit polyclonal antibodies to the B-subunit of the cholera toxin; MAB to the capsular F1 antigen of the plague pathogen clone F41F8C9; MAB to anthrax spores clone 278H4A7 (branch of the 48th Central Research Institute of the Russian Ministry of Defense, Kirov); mouse immunoglobulins to CCHF antigens (Gamaleya National Research Center for Epidemiology and Microbiology); MAB to SEB S643 (VNCMDL, Russia) at a concentration of 2.0 mg/mL. The antibodies of the LICHT control zone were goat antibodies to mouse immunoglobulins and goat antibodies to rabbit immunoglobulins (HyTest) at a concentration of 0.1 mg/mL.

A GFCP001000 glass fiber membrane and CFSP203000 and CFSP173000 cellulose membranes (Millipore), cards with TYPE-CNPF-SN12-L2-P25, 10 µ (Mdi, India) nitrocellulose membrane were used to manufacture the LICHT multimembrane composite. The finished test strips were placed in TYPE-Device-1 plastic frames (Mdi, India), the top cover of which was coated with a matte black paint. Prior to application to the glass fiber membrane, the conjugate of microspheres with antibodies was treated with ultrasound on a Labsonic 2000 dispersant (B. Braun, Germany) for 10 s followed by stirring. Then, a storage buffer was added to a concentration of 0.01%. The resulting conjugate was manually applied onto a GFCP001000 (Millipore) fiberglass membrane and dried at room temperature.

A video digital luminescent immunochromatographic analysis was performed using an RLI-Eu^{3+} device at room temperature for 25 min after the introduction of the analyte. The volume of the analyte introduced into the LICHT was 140 µL.

Control samples (CS) intended for studying the analytical characteristics of the recording device were produced in two versions, differing in the range of concentrations of luminescent microspheres in the analytical zone. CSs were immunochromatographic membranes on which a suspension of luminescent microspheres with europium with a linear density of 0.08 µL/mm was applied in strips using an IsoFlowTM dispenser (Imagene Technology Inc, USA). The membranes were dried at room temperature, cut into strips 4 mm wide using a Matrix 2360 programmable guillotine (Kinematic Automation Inc, USA), and placed in rims for multianalytical immunochromatographic elements. A suspension of microspheres at a concentration of 0.01% was used to form a short circuit. Concentrations of microspheres from 0.00005% to 0.01% were used to form the AZ. The area of each zone on the membrane

with luminescent microspheres was 4 mm². In this way, an imitation of LICHT with different luminescence intensities was obtained. CSs were stored in light-proof bags at 4 °C. The following reagents were used in the study: 1% (weight/volume) suspension of carboxylated polystyrene microspheres with a europium complex in deionized water with the addition of 0.05% NaN$_3$ (Bang Laboratories, USA). The average diameter of microspheres was 190 nm. 2-(N-morphino)-ethanesulfonic acid (MES) monohydrate, tris-(hydroxymethylaminomethane) hydrochloric acid (TRIS-HCl) salt, Twen-20 bovine serum albumin (BSA) free of proteases, N-(3-dimethylaminopropyl)-N-ethylcarbodiimide (EDC) hydrochloride, N-hydroxysuccinimide (NHS), sodium hydroxide, ProClinTM-300, glycine, polyvinylpyrrolidone MM 40,000, sodium chloride — all these materials were produced by Sigma-Aldrich. Trehalose-D(+) — dihydrate for biochemistry, hydrochloric acid (chemically pure, C.P.) (Dia-M (Russia), Tetronic 1307(S9), Braveds (China) were used.

Particles with the average diameter of 30 nm were used as a conjugate label for the manufacture of AuNPs-based immunochromatographic tests [11]. The immune components of such tests were identical to those used in LICHT. Multimembrane composites and test manufacturing techniques were similar to LICHT manufacturing techniques. A video digital immunochromatographic Reflex analyzer (Registration certificate for a medical device dated April 26, 2016 No. FSR 2011/11281/, TU9443-001-43312649-2014, Sinteko-Complex, Russia) was used as a digital video recorder (DVR).

The results were processed using the Microsoft Excel 2003 program, the Descriptive Statistics option.

RESULTS

The developed prototype of a video digital recorder of luminescent immunochromatograms RLI-Eu^{3+} consists of a measuring unit and a laptop with a pre-installed software application for monitoring and calculating the obtained results. The appearance of the device is shown in Fig. 1.
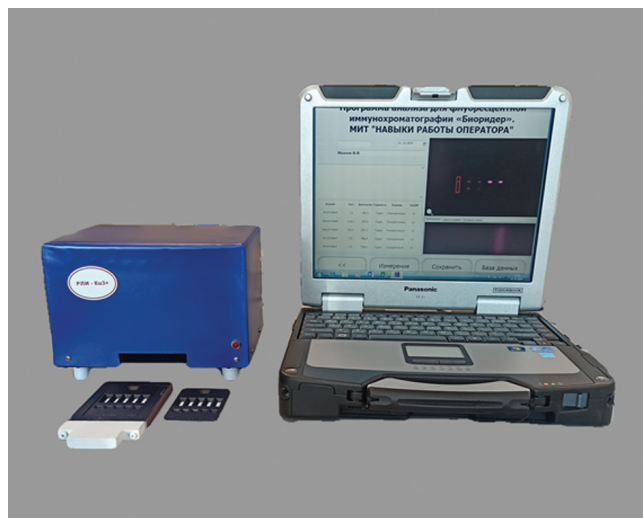

Figure prepared by the author using their own data

Fig. 1. Appearance of the developed luminescent immunochromatography recorder RLI-Eu^{3+}

Table 1. Luminescence intensity in the CS analytical zone as a function of the concentration of the luminescent europium complex on the membrane

Concentration of microsphere suspension during the formation of the analytical zone, %	1×10^{-2}	5×10^{-3}	2.5×10^{-3}	1×10^{-3}	5×10^{-4}	2.5×10^{-4}	1×10^{-4}	5×10^{-5}	0
Concentration of the luminescent europium complex on the membrane, pg/mm^2	200	100	50	20	10	5	2	1	0
Average luminescence intensity, conl. units.	552.3	314	144.3	45.5	44.3	24.4	12.1	3.5	1.06
Standard deviation (SD)	13.0	12.1	5.9	2.3	3.9	2.0	1.2	1.7	0.62
Coefficient of variation (CV), %	2.35	3.9	4.09	5.05	8.80	8.20	9.92	48.57	58.49
Standard error (SE)	4.1	4.0	1.9	0.7	1.2	0.6	0.4	0.5	0.20
Confidence interval (95.0%)	9.3	9.3	4.2	1.7	2.8	1.4	0.9	1.2	0.44

Table prepared by the authors based on their own data

The measuring unit contains a fluorescent light source consisting of two 4 W mercury discharge lamps. The lamp flasks are made of Wood glass, which creates a field of uniform ultraviolet irradiation of immunochromatograms with a maximum wavelength at 365 nm, as well as a lamp power source. A solid-state video camera with a resolution of 1200×1600 pixels and a video shooting speed of 15 frames per sec is also located in the housing of the measuring unit. A SV580 glass luminescence emission filter is installed in front of the camera lens, ensuring a 90% transmission of radiation in the wavelength range from 600 nm to 900 nm. The video camera is connected to a laptop via a USB 2.0 connector. Plastic frames containing LICHT membranes are placed inside the device using a holder. The device allows simultaneous registration of up to five immunochromatograms; however, the possibility of measurement and single tests is also provided.

The images obtained using the device video camera were processed by a fluorescent immunochromatogram analysis software application running in Windows 7, 10.

The device provides calculation of the integral intensity of the LICHT analytical and control zones with automatic correction of the baseline. The criterion for a positive result of DVR analysis was the excess of the luminescence intensity of the analytical zone of the test over the average background value in an idle experiment, taking into account the measurement error with a 95% confidence probability:

$$[X_{mean} - t_s \times SE]_{signal} \geq [X_{mean} + t_s \times SE]_{background}, \qquad (1)$$

where X_{mean} — mean of n-measurements;
t_s — Student's coefficient for *n*-measurements;
SE — standard error mean at 95% confidence level.

The RLI-Eu^{3+} luminescence recorder has the following technical characteristics: weight — 1.64 kg, dimensions — 150×200×170 mm, power supply — 220–240 V, 0.15 A, 50 Hz. Management from an external laptop with Windows 7.10 OS is performed using a specialized software application. The maximum wavelength of exciting light is λ_{ex} = 365 nm; the maximum wavelength of emission is λ_{em} = 615 nm. The detection limit of the luminescent substance on the immunochromatographic membrane is 2.0 pg/mm^2. The number of immunochromatograms in the test frame can vary from one to five. The coefficient of variation of the luminescence intensity readings of the analytical zone of the test in the concentration range of the luminescent complex is 2–20 pg/mm^2 <10%, in the range of 20–200 pg/mm^2 <5%. The linearity of readings ranges within 2–200 ng/mm^2. The operating temperature ranges from 5 °C to 35 °C.

Table 1 shows the results of CS measurements using the RLI-Eu^{3+} instrument in various concentration ranges of the luminescent europium complex in the CS analytical zone.

Table 1 demonstrates satisfactory values of the coefficient of measurement variation (CV) in the range of microsphere concentrations from 20 pg/mm to 200 pg/mm^2, which indicates a high reproducibility of measurement results using the RLI-Eu^{3+} device. Higher values of the coefficient of variation are observed at measuring concentrations <5 pg/mm^2. The detection sensitivity of luminescent microspheres on the membrane surface reaches 1 pg/mm^2, which is 3.5 times higher than the average luminescence values in an idle experiment.

The linearity of instrument readings during measurement is shown in Fig. 2.
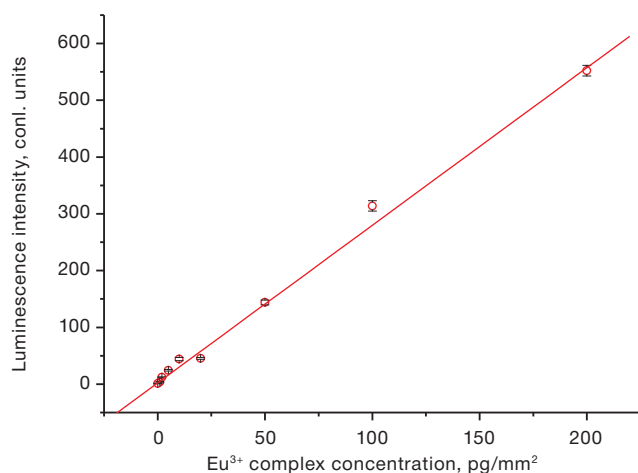

Figure prepared by the author using their own data

Fig. 2. Dependence of the luminescence intensity of the CS analytical zone on the surface concentration of the europium complex on the analytical membrane

A linear regression for the dependence of the luminescence intensity of microspheres on the membrane on the microsphere concentration was constructed using the least squares method using the Origine 6.1 software (OriginLab Corp.). The correlation coefficient of the linear relationship is $R = 0.99$.

Luminescent tests for the immunochromatographic detection of pathogenic microorganisms and toxins were developed in a sandwich format. A detailed description of AuNPs-based immunochromatographic tests in the sandwich format and the analytical procedure for detecting bacterial toxins and spore forms of microorganisms can be found in [13, 14].

During the study, a liquid sample potentially containing pathogenic microorganisms or toxins was applied onto a sample substrate. Under the action of capillary forces, liquid moves through the multimembrane composite. First, the conjugate of microspheres with specific immunoglobulins immobilized on the surface is solubilized. The conjugate of microspheres is luminesced in the red region of the spectrum. In the presence of a detectable antigen in the sample, an antigenic immune complex is formed. This complex moves along the analytical membrane with an excess of conjugate with the flow of liquid. Next, the immune complex is captured on the analytical membrane by specific antibodies in the AZ, forming a sandwich. The unbound conjugate antibodies are captured by antibodies in the CZ of the test strip, which leads to the formation of two luminescent lines. In the absence of an antigen in the sample, an antigenic immune complex is not formed; therefore, the only line visible in ultraviolet light is formed by binding conjugate antibodies and CZ antibodies (antispecific with respect to conjugate antibodies) only in the CZ. The appearance of tests for detecting cells of the vaccine strain of the plague causative agent based on AuNPs and on the basis of luminescent microspheres under ultraviolet irradiation with a wavelength of 365 nm is shown in Fig. 3.

Table 2 shows the detection (LICHT and AuNPs-based immunochromatography) thresholds for various pathogenic microorganisms and bacterial toxins.

Using the example of microorganisms of various taxonomic groups (vegetative and spore forms of bacteria, viruses, and bacterial toxins), Table 2 shows that the use of immunochromatography with conjugates based on microspheres with luminescent labeling of europium compounds provides a much greater sensitivity than the use of tests with AuNPs conjugates. The correctness of the comparison is ensured by using the same batches of antibodies to produce tests based on luminescent antibodies and tests based on colloidal gold nanoparticles. When comparing the sensitivity level, identical antigenic drugs were used.
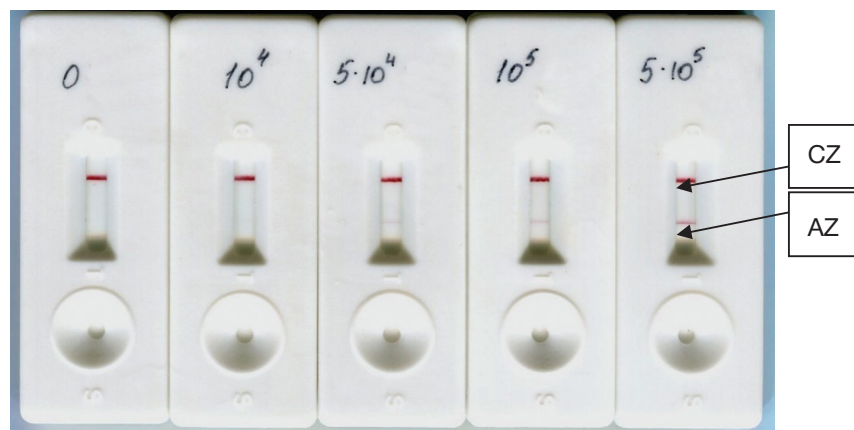
AuNPs-based tests, visible light illumination
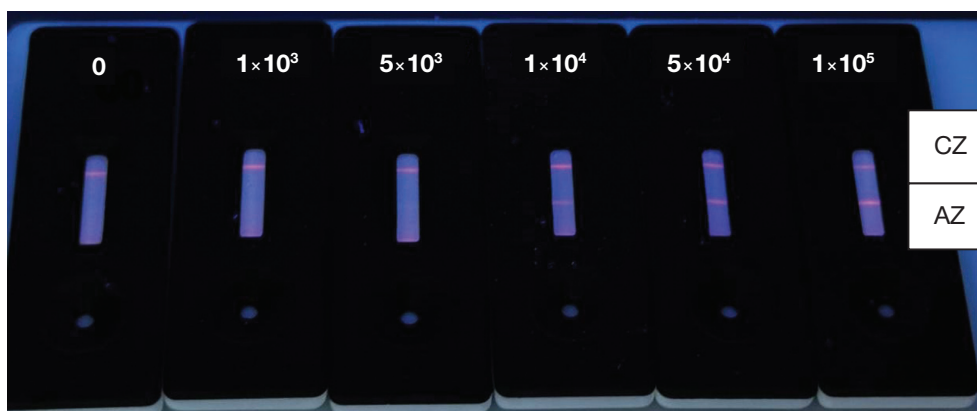
LICHT illuminated with light $\lambda = 365$ nm

Figure prepared by the authors based on their own data

Fig. 3. Appearance of immunochromatograms of *Y. pestis* EV cells.
Note: Arrows and letters indicate the analytical (AZ) and control (CZ) test zones. Concentrations are indicated in cells/mL.

Table 2. Comparative characteristics of LICHT and immunochromatographic tests based on AuNPs in the detection of toxins and pathogenic microorganisms

Analyte	Ratio of the minimum detectable analyte concentrations for different conjugate labels of immunochromatographic tests		
	LICHT based on microspheres with Eu^{3+}complex, luminescence DVR	ICA based on the AuNPs, reflected light DVR	Ratio of LICHT sensitivity to ICA sensitivity
Staphylococcal enterotoxin type B, ng/mL	0.5	30	60
Cholera toxin, ng/mL	10	500	50
Microbial cells of *Y. pestis*, strain EV, mg/mL	1×10^3	5×10^4	50
B. anthracis spores/mL	5×10^3	1×10^5	20
Causative agent of CCHF (dilution of the initial preparation of viral antigens)	1:640,000	1:5000	128

Table compiled by the authors based on their own data

DISCUSSION

The use of digital video recording of immunochromatograms in combination with microspheres containing europium complexes provides a significant gain in ICA sensitivity. This is due to the significant volume of microspheres containing a large number of europium complexes per particle and the photophysical properties of the europium complexes themselves. These compounds are excited by UV light in the near range of 365–370 nm and emit luminescence in the red region.

The significant Stokes shift is due to the processes of excitation of the chelated ligand of the complex and further energy transfer to the $^5D_0$ energy level of the Eu^{3+} ion with subsequent transitions between the $^5D_0 \rightarrow {}^7F_2$ level and light emission in the range of λ = 610–660 nm with a high quantum yield. Practically speaking, this makes it possible to use inexpensive glass filters in the device design to isolate exciting light and emission light, which provides a good contrast between the lines of immunochromatograms and the background. Another advantage of such labels is the small width (<10 nm) of the emission lines and the long luminescence lifetime of microspheres with europium t = 0.43–0.55 ms. The europium luminescent complex isolated in a polystyrene matrix is stable, being protected from exposure to atmospheric oxygen and luminescence-extinguishing substances potentially present in the analyte and buffer solutions used in ICA. However, these compounds are not devoid of drawbacks, since they reduce the quantum yield of luminescence with an increase in temperature. Thus, europium complexes polymerized in films have stable luminescence in the range from –60 °C to +25 °C. When the film is heated to a temperature of above +25 °C, a decrease in the intensity and decay time of luminescence corresponding to the $^5D_0 \rightarrow {}^7F_2$ transition is observed [15]. The effect is reversible; thus, upon cooling, the luminescence intensity is restored. This phenomenon can reduce the sensitivity of LICHT when used in field studies at elevated temperatures.

According to the passport data of the drug, the surface of one microsphere contains up to 353,000 of carboxyl groups with a microsphere average diameter of 190 nm. This allows for effective conjugation of luminescent microspheres with antibody proteins due to the formation of covalent bonds between the amino groups of antibodies and the carboxyl groups of microspheres. The conjugate of microspheres with immunoglobulins has a significant number of antibody valences, which contributes to the effective formation of immune complexes with antigens of bacteria, toxins, and viruses [16].

The use of video cameras as a radiation receiver is also a significant advantage in DVR [17], since the latter have high sensitivity and the ability to change the brightness, contrast, and gamut of the image. These properties of video cameras make it possible to improve the image of immunochromatograms in a wide range of luminescence intensity. In addition, the DVR does not require mechanical drives (actuators) to move immunochromatograms under the beam of exciting light.

We have obtained data on significant differences in the sensitivity of LICHT and AuNPs-based immunochromatographic tests in the detection of toxins and pathogenic microorganisms. The increased sensitivity of detection of microorganisms and toxins in the use of fluorescent tags compared to tests based on AuNPs is primarily due to the higher sensitivity of detection of fluorescent tags compared to the sensitivity of detection of colorimetric tags (AuNPs). An important factor in increasing sensitivity is the greater number of capture antibodies in the immunochromatographic conjugates of luminescent microspheres compared with similar conjugates of AuNPs. This is due to the geometric dimensions of the microparticles: the AuNPs average diameter is 30 nm, compared to the luminescent microspheres average diameter of 190 nm. These factors lead to a more efficient process of immunochromatography and detection results. It should be noted that the preparation of samples for analysis, the procedure for the analysis, and the time of its implementation do not change. Technologically, the production of LICHT and ICA tests based on AuNPs are also similar, with the exception of the conjugate synthesis stage. Therefore, no changes in the technological line of production equipment are required.

The high sensitivity of LICHT is important for the sanitary and hygienic aspect of the use of immunochromatography in general, making it possible to detect lower concentrations of pathogenic microorganisms and toxins in environmental objects, food products, and body fluids. LICHT can be useful for the immunochemical verification of microbial

crops using the conventional microbiological method by reducing the cultivation time, allowing the identification of cells and bacterial toxins across a shorter period of time.

CONCLUSIONS

1. An experimental prototype of a video digital recorder of luminescent immunochromatograms RLI-Eu^{3+} has been developed, where submicron microspheres containing complex compounds of trivalent europium conjugated with specific antibodies are used as a label for immunochromatography.

2. RLI-Eu^{3+} has a sensitivity threshold for the luminescent europium complex of 2 pg of the substance per 1 mm^2 of the immunochromatographic membrane and a linearity in the range of 2–200 pg/mm^2.

3. The coefficient of variation of measurements does not exceed 5% in the concentration range of 20–200 pg/mm^2 and 10% in the range of 2–20 pg/mm^2.

4. LICHT has been developed to detect cholera toxin, staphylococcal enterotoxin type B, plague pathogen cells (vaccine variant EV), anthrax pathogen spores, as well as antigens of the Crimean-Congo hemorrhagic fever pathogen virus. Further studies should address the extension of the LICHT range for the detection of pathogens.

5. The sensitivity of LICHT based on microspheres containing europium complexes during instrument registration is 20–128 times higher than that of immunochromatographic tests based on AuNPs, designed on the basis of the same specific immunoglobulins and analytical membranes.

References

1. Hou FP, Bai MY, Zhang Y, Liu H.Y, Sun SQ, Guo HC. Fluorescent immunochromatographic assay for quantitative detection of the foot-and-mouth disease virus serotype O antibody. *Microchem. J.* 2020; 155:104690.
https://doi.org/10.1016/j.microc.2020.104690
2. Kim TK, Oh SW, Hong SC, Mok YJ, Choi EY. Point-of-Care Fluorescence Immunoassay for Cardiac Panel Biomarkers. *J. Clin. Lab. Anal.* 2014; 28: 419–427.
https://doi.org/10.1002/jcla.21704
3. Gao Y.M., Wei J.C., Mak P.U., Vai M.I., Du M., Pun S.H. Development of a Calibration Strip for Immunochromatographic Assay Detection Systems. *Sensors.* 2016; 16: 1007
https://doi.org/10.3390/s16071007
4. Raeisossadati M.J., Danesh N.M., Borna F., Gholamzad M., Ramezani M., Abnous K., Taghdisi S.M. Lateral flow-based immunobiosensors for detection of food contaminants. *Biosens. Bioelectron.* 2016; 86:235–246
https://doi.org/10.1016/j.bios.2016.06.061
5. Wu Y, Sun J, Huang X, Lai W, Xiong Y. Ensuring food safety using fluorescent nanoparticles-based immunochromatographic test strips. *Trends in Food Science & Technology.* 2021; 118: 658-678.
https://doi.org/10.1016/j.tifs.2021.10.025
6. Sanchis A., Salvador J.P., Marco M.P. Multiplexed immunochemical techniques for the detection of pollutants in aquatic environments. *TrAC Trends Anal. Chem.* 2018; 106: 1–10.
https://doi.org/10.1016/j.trac.2018.06.015
7. Berlina AN, Taranova NA, Zherdev AV, Vengerov YY, Dzantiev BB. Quantum dotbased lateral flow immunoassay for detection of chloramphenicol in milk. *Analytical and Bioanalytical Chemistry.* 2013; 405(14):4997-5000.
https://doi.org/10.1007/s00216-013-6876-3
8. Taranova NA, Berlina AN, Zherdev AV, Dzantiev BB. Traffic light' immunochromatographic test based on multicolor quantum dots for the simultaneous detection of several antibiotics in milk. *Biosensors and Bioelectronics.* 2015; 63:255-261.
https://doi.org/10.1016/j.bios.2014.07.049
9. Yang JC, Wang K, Xu H, Yan WQ, Jin QH, Cui DX. Detection platforms for point-of-care testing based on colorimetric, luminescent and magnetic assays: A review. *Talanta.* 2019; 202: 96–110.
https://doi.org/10.1016/j.talanta.2019.04.054
10. Bajusheva VV, Belozerova OA, Cherednichenko AG. Synthesis and luminescent properties of rare earth metal (rem) complexes with substituted 1,10-phenanthroline and β-diketones. *Advances in chemistry and chemical technology.* 2014; 28(6): 16-18. (In Russ.).
EDN: STFWMN
11. Yarkov SP, Tret'jakov SI, Shilenko IV, Ishkov JuN, Stjazhkin KK. Detection of staphylococcal enterotoxin type B in dairy products by immunochromatography with visual and video digital detection. *Extreme Medicine.* 2023; 3: 86–91 (In Russ.).
https://doi.org/10.47183/mes.2023.039
12. Jiao, X.; Peng, T.; Liang, Z.;Hu, Y.; Meng, B.; Zhao, Y.; Xie, J.;Gong, X.; Jiang, Y.; Fang, X.; et al. Lateral Flow Immunoassay Based on Time-Resolved Fluorescence Microspheres for Rapid and Quantitative Screening CA199 in Human Serum. *Int. J. Mol. Sci.* 2022, 23: 9991-9.
https://doi.org/10.3390/ijms23179991
13. Eremkin AV, Ipatov SS, Kuklina GV, Pechenkin DV, Kytmanov AA, Tihvinskaja OV, Kuznecov SL, Gorshkov A.S., Hapaev NG. Development of enzyme immunoassay systems and immunochromatographic reagent kits designed to detect staphylococcal enterotoxins of types A and B. *Problems of especially dangerous infections.* 2021; 2:94–99 (In Russ.).
https://doi.org/10.21055/0370-1069-2021-2-94-99
14. Yarkov SP, Tret'jakov SI, Shaulina EK, Brovkina AN, Hramov EN. Increasing the sensitivity of immunochromatographic tests to detect the causative agent of anthrax and staphylococcal enterotoxin type B based on silver amplification and instrumental registration. *Extreme Medicine.* 2019; 21(3):455-463. (In Russ.).
EDN: KSFFST
15. Lapaev DV, Zijatdinova RM, Knjazev AA, Galjametdinov JuG, Nikiforov VG, Lobkov VS. The mechanism of thermal quenching of luminescence in a glazed film of the beta-diketonate complex of europium (III). *Bulletin of the Technological University.* 2018;21(4):13-18 (In Russ.).
EDN: XPSTYL
16. Xie QY, Wu YH, Xiong QR, Xu HY, Xiong YH, Liu K, Jin Y, Lai WH. Advantages of fluorescent microspheres compared with colloidal gold as a label in immunochromatographic lateral flow assays. *Biosens. Bioelectron.* 2014; Apr15; 54:262-265.
https://doi.org/10.1016/j.bios.2013.11.002
17. Gupta R, Gupta P, Wang S et al. Ultrasensitive lateral-flow assays via plasmonically active antibody-conjugated fluorescent nanoparticles. *Nat. Biomed. Eng.* 2023; 7: 1556–1570.
https://doi.org/10.1038/s41551-022-01001-1

AUTHORS

Sergei P. Yarkov, Dr. Sci. (Biol.)
https://orcid.org/0000-0003-4644-0485
diasol@dol.ru

Sergey I. Tretyakov, Cand. Sci. (Engin.)
https://orcid.org/0000-0003-2826-9581
14otd@gosniibp.ru

Inessa V. Shilenko, Cand. Sci. (Engin.)
https://orcid.org/0000-0003-0801-6923
14otd@gosniibp.ru

Ekaterina K. Shaulina
https://orcid.org/0009-0008-7522-7775
14otd@gosniibp.ru

Angelina Mandaji
https://orcid.org/0009-0005-4482-3724
14otd@gosniibp.ru

Denis A. Zenkov
https://orcid.org/0009-0001-3209-4940
14otd@gosniibp.ru

Yury N. Ishkov, Cand. Sci. (Engin.)
https://orcid.org/0000-0001-8355-7821
14otd@gosniibp.ru

Konstantin K. Styazhkin, Dr. Sci. (Biol.)
https://orcid.org/0000-0002-9988-2343
director@gosniibp.ru

EFFECTIVENESS OF CONSERVATIVE METHODS FOR PLANTAR FASCIITIS TREATMENT IN ATHLETES

Anton V. Slivin[1,2✉], Valerii V. Karmazin[1], Kirill A. Shlykov[3], Sergey A. Parastaev[1,2]

[1] Federal Research and Clinical Center of Sports Medicine and Rehabilitation, Moscow, Russia

[2] Pirogov Russian National Research Medical University, Moscow, Russia

[3] Osteopathy and Classical Medicine Clinic Osteopolyclinic, Moscow, Russia

Introduction. Plantar fasciitis (PF) is a multifactorial pathology that restricts an athlete's training and competitive activities, leading to premature termination of a sports career in some cases. The search for optimal conservative treatment methods that may improve the overall therapy effectiveness represents an important task of sports medicine.

Objective. Development of a differentiated approach to conservative treatment of athletes suffering from PF, taking the biomechanical features of the disease into account.

Materials and methods. The study involved 82 athletes, including 37 men and 45 women suffering from unilateral PF with a median age of 30 (23; 34) years. The participants were divided into four groups depending on the type of therapeutical action: Group 1 — shock wave therapy (ESWT); Group 2 — vibration therapy combined with myofascial release of the muscles of the posterior thigh and shin; Group 3 — individual orthoses of the feet; Group 4 — a combination of vibration therapy, myofascial release, individual orthoses of the feet. The tested therapeutic measures were assessed by the dynamics of pain syndrome, the results of baropodometry, the severity of tension in the thigh and shin muscles, and changes in the thickness of plantar aponeurosis.

Results. All the studied treatment methods showed varying degrees of effectiveness in reducing pain ($p < 0.001$), reducing the thickness of plantar aponeurosis ($p < 0.05$), normalizing plantar pressure in the posterior and anterior parts of the affected foot ($p < 0.05$), and increasing the postural stability of athletes according to objective indicators ($p < 0.05$). The use of ESWT resulted in the most pronounced reduction in pain. In Groups 2 (vibration therapy and myofascial release) and 3 (individual foot orthoses), a statistically significant decrease in muscle tension in the posterior shin group was observed ($p < 0.05$). In addition, in Group 2, the angle of dorsiflexion of the ankle joint increased significantly ($p < 0.05$). Group 4 (combined treatment) demonstrated the highest level of biomechanical stability.

Conclusions. ESWT demonstrates a high effectiveness in relieving a pronounced acute process. In cases where an athlete experiences some biomechanical disorders or deformities of the foot, orthoses of the feet are advisable. In case of tension of the shin muscles and limitation of dorsiflexion, vibration therapy combined with myofascial release is recommended.

Keywords: plantar fasciitis; sports; shock wave therapy; vibration therapy; foot orthoses; myofascial release; biomechanics

ЭФФЕКТИВНОСТЬ КОНСЕРВАТИВНЫХ МЕТОДОВ ЛЕЧЕНИЯ ПЛАНТАРНОГО ФАСЦИИТА У СПОРТСМЕНОВ

А.В. Сливин[1,2✉], В.В. Кармазин[1], К.А. Шлыков[3], С.А. Парастаев[1,2]

[1] Федеральный научно-клинический центр спортивной медицины и реабилитации Федерального медико-биологического агентства, Москва, Россия

[2] Российский национальный исследовательский медицинский университет им. Н.И. Пирогова, Москва, Россия

[3] Клиника остеопатии и классической медицины «Остеополиклиник», Москва, Россия

Введение. Плантарный фасциит (ПФ) — многофакторная патология, ограничивающая тренировочную и соревновательную деятельность спортсмена, а в некоторых случаях обусловливающая преждевременное завершение спортивной карьеры. Поиск оптимальных методов консервативного воздействия, которые позволят повысить эффективность лечения, является важной задачей спортивной медицины.

Цель. Разработка дифференцированного подхода к консервативному лечению спортсменов с ПФ с учетом биомеханических особенностей заболевания.

Материалы и методы. В исследовании приняли участие 82 спортсмена (37 мужчин и 45 женщин, медиана возраста — 30 (23; 34) лет) с односторонним ПФ, которые были разделены на 4 группы в зависимости от типа терапевтического воздействия: группа 1 — ударно-волновая терапия (УВТ), группа 2 — вибрационное воздействие в сочетании с миофасциальным релизом мышц задней группы бедра и голени, группа 3 — индивидуальные ортезы стоп, группа 4 — комплекс вибрационного воздействия, миофасциального релиза, индивидуальных ортезов стоп. Терапевтические мероприятия оценивались по динамике болевого синдрома, результатам бароподометрического обследования, выраженности напряжения мышц бедра и голени, изменению толщины подошвенного апоневроза.

Результаты. Все исследуемые методы воздействия показали различную степень эффективности в отношении снижения боли ($p < 0,001$), уменьшения толщины подошвенного апоневроза ($p < 0,05$) и нормализации подошвенного давления заднего и переднего отделов пораженной стопы ($p < 0,05$), повышения постуральной устойчивости спортсменов по объективным показателям ($p < 0,05$). Наиболее выраженное снижение болевого синдрома было отмечено при использовании УВТ. В группах 2 (вибрационное воздействие и миофасциальный релиз) и 3 (индивидуальные ортезы стоп) отмечено статистически значимое снижение напряжения мышц задней группы голени ($p < 0,05$); кроме того, в группе 2 значимо увеличивался

угол дорсифлексии голеностопного сустава ($p < 0,05$). Группа 4 (комплексное воздействие), по данным объективных показателей, характеризовалась лучшей биомеханической стабильностью.

Выводы. В купировании выраженного острого процесса высокую эффективность демонстрирует УВТ. При наличии у спортсмена биомеханических нарушений / деформаций стопы целесообразно использовать ортезы стоп, а в случае напряжения мышц голени и ограничения дорсифлексии — вибрационное воздействие в сочетании с миофасциальным релизом.

Ключевые слова: планарный фасциит; спорт; ударно-волновая терапия; вибрационное воздействие; ортезы стоп; миофасциальный релиз; биомеханика

INTRODUCTION

Plantar fasciitis (PF) is an urgent and widespread problem in sports that hinders the training process. Both conservative and surgical methods of treatment can be used to treat this pathology [1]. However, due to the prolonged recovery period and postoperative complication risks, conservative methods are recognized as the first line of therapy in clinical practice [2].

It has been repeatedly noted that the main problem faced by a physician in the treatment of athletes with PF is the low effectiveness of conservative interventions, including insufficient duration of pain relief [3]. Conservative treatment methods widely employ approaches of physical and rehabilitation medicine; however, none of the available PF treatment methods have been supported by convincing scientific evidence [4]. This may be related to biomechanical disorders underlying the development of degenerative changes in plantar aponeurosis, thus resulting in a significant heterogeneity of treatment outcomes.

Despite the wide range of correction methods tested in PF, including athletes, an integrated approach to combining therapeutical measures is yet to be developed. Tools for monitoring the effectiveness of therapeutic effects and tactics for managing athletes with PF should be improved in order to correct not only pain syndrome, but also to prevent disease recurrence.

In this connection, the assessment of disease risk factors and impaired biomechanical patterns is extremely important for PF in general and among athletes in particular [5]. The impact on key steps in the pathogenesis of the disease will make it possible to personalize therapeutical approaches and, accordingly, improve the outcome of therapeutic effects, and reduce the rehabilitation time for athletes.

In this study, we set out to develop a differentiated approach to the conservative treatment of athletes suffering from PF, taking the biomechanical features of the disease into account.

MATERIALS AND METHODS

The study included 82 athletes (37 men and 45 women) representing various sports: athletics, football, basketball, rugby, tennis, handball, volleyball, bobsleigh, fencing, and some others (Fig. 1). The median age of athletes was 30 (23; 34) years. The athletes underwent rehabilitation treatment at the Federal Research and Clinical Center of Sports Medicine and Rehabilitation during the 2023–2024 period.

The criteria for inclusion in the study were: clinical diagnosis of PF with unilateral localization of the process, age from 16 to 50 years, presence of sports qualifications. Criteria for non-inclusion of athletes in the study were: excluded diagnosis of plantar fasciitis, presence of systemic connective
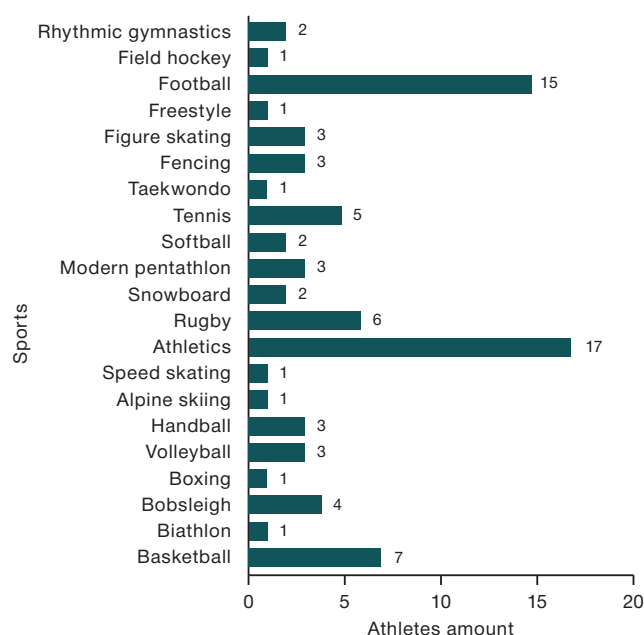

Figure prepared by the authors using their own data

Fig. 1. PF prevalence in various sports in the research sample

tissue diseases, age that does not meet the inclusion criteria (less than 16 years and more than 50 years), inability to perform diagnostic and correction programs due to circumstances beyond their control (severe injuries, diseases, epidemic risks leading to interruption of a sports career), lack of athletic qualifications, refusal to participate in the study. Criteria for exclusion of athletes from the study were: injury to the musculoskeletal system that occurred during the study period, refusal to further participate in the study.

All athletes with PF were divided into four groups depending on the type of therapeutic measures performed:

- Group 1 ($n = 27$) — athletes who were treated with extracorporeal shock wave therapy (ESWT);
- Group 2 ($n = 20$) — athletes who were treated with vibration therapy combined with myofascial release (MFR) of the muscles of the posterior thigh and shin;
- Group 3 ($n = 19$) — athletes who underwent treatment using individual orthoses of the feet;
- Group 4 ($n = 16$) — athletes who were treated with vibration therapy combined with MFR of the muscles of the posterior thigh and shin, as well as with the use of individual orthoses.

Focused ESWT was performed on a BTL-6000 FSWT device (UK) with an energy flow area of 0.65 мJ/mm^2 and a frequency of 4–6 Hz. A course vibration exposure lasting 9–10 days was performed on a Vibrosphere device (Sweden) with a sequential increase in the frequency range from 20 to 45 Hz. The myofascial release of the muscles of the posterior thigh and shin was carried out by athletes independently using a roll with a ribbed surface. For the manufacture of individual orthopedic insoles, Formthotics blanks (New Zealand) were used.[1]

The effectiveness of curative services was assessed by the dynamics of pain syndrome, determined using the Russian version of the Visual Analog Scale Foot and Ankle — VAS FA [6]; the muscle pain in the posterior thigh and shin; evaluation of ankle joint range of motion by the angle of ankle joint dorsiflexion; baropodometry (in static and dynamic tests); and changes in the thickness of the plantar fascia. The muscle tenderness of the posterior thigh and shin was palpated, and the angle of ankle joint dorsiflexion was measured in a supine position with the knee joint extended by goniometry. Baropodometry was performed using the WINTRACK hardware and software complex (Medicaptures, France) according to an algorithm consisting of static and a series of dynamic tests (sagittal, frontal, forefoot lifting and jumping tests) [7]. In addition, changes in the center of pressure (CoP) velocity in the frontal and sagittal planes, as well as the statokinesiogram area, were evaluated: the CoP velocity in the frontal plane was evaluated in the sagittal dynamic test, and in the sagittal plane — in the frontal test; the statokinesiogram area was studied in the jumping dynamic. The thickness of the plantar fascia was determined using magnetic resonance imaging, which was performed on a SIGNA Creator installation 1.5 T (General Electric, USA). The measurement was performed on sagittal sections 1 cm distal to the place of attachment to the calcaneal protuberance. The effectiveness of curative services was evaluated after 7 and 14 days. On day 28 after the completion of curative services,

an additional reassessment of the pain severity was performed. As an additional method for determining the presence and severity of foot pronation, the foot posture was assessed using the FPI-6 scale (Foot Posture Index — 6).

Statistical data analysis was carried out using the IBM SPSS Statistics 23 application software package. To assess the type of distribution of quantitative feature values, the Kolmogorov–Smirnov and Shapiro–Wilk criteria with a critical significance level of 0.05 were used. In the case of differences in the distribution from the normal, nonparametric analysis methods were applied. Descriptive statistics of quantitative data are given in the form of medians and quartiles; descriptions of qualitative features are given in the form of relative frequencies and their confidence intervals. The nonparametric Mann–Whitney U-test was used for comparative intergroup analysis; the Wilcoxon test was used for intragroup analysis. A comparison of discrete quantities was carried out using the χ^2 criterion. The significance level for all calculations of less than 0.05 was taken to be statistically significant.

RESULTS

The largest number of PF cases was observed in athletes involved in athletics, football, basketball, rugby, and tennis (Fig. 1). More detailed information about the study groups evaluated before the onset of curative services is presented in Table 1.

The study did not reveal any statistically significant differences in the sample by age, BMI, and sports experience. An assessment of the pronation degree on the FPI-6 scale found that the foot of athletes with PF was moderately pronated, with all the studied groups of athletes being comparable in this parameter.

Group 1, i.e., the athletes treated with ESWT, showed the lowest angle of ankle joint dorsiflexion, amounting to 15°. This indicates a more pronounced tension of the shin triceps muscle compared to other groups before the onset of curative services.

The analysis of the pain syndrome assessed by VAS FA revealed a statistically significant ($p < 0.001$) decrease in the pain syndrome intensity in all the studied groups in the follow-up period during the intragroup analysis. The corresponding data is shown in Fig. 2. Thus, in Group 1, the athletes reported a decrease in pain by 63%, in Group 2 — by 14%, in Group 3 — by 61%, and in Group 4 — by 18%. In the follow-up observation of athletes with PF, no statistically significant decrease in the VAS FA score was observed 28 days after the completion of therapy, which indicates the stability of the achieved therapeutic effect.

In all the studied groups, an evaluation of the effectiveness of curative services found no statistically significant decrease in muscle tenderness of the posterior thigh group on palpation on days 7 and 14 of therapy compared with the period before the onset of the study. The corresponding data is shown in Fig. 3A.

At the same time, athletes from Groups 2, 3, and 4 showed a statistically significant decrease in tenderness and tension of the posterior shin muscles on palpation after 14 days compared with the period before treatment by

---

[1] Ponomarenko GN, Hajduk AA. The use of individual foot orthoses Formthotics in clinical practice. Guidelines. St. Petersburg; 2015 (In Russ.).

Table 1. Summary of athletes' characteristics in groups before the onset of therapeutical measures

Parameter	Group 1 (n = 27)	Group 2 (n = 20)	Group 3 (n = 19)	Group 4 (n = 16)
Age, years	31 (23; 37)	27.5 (24; 35)	27 (21; 36)	30 (25; 33)
Body mass index, kg/m²	22.1 (21; 23)	21.8 (21; 24)	22.2 (21; 24)	22.8 (21; 25)
Sports experience, years	22 (18; 30)	20 (17; 25)	19 (16; 25)	20.5 (17; 22)
Pronation degree, FPI-6 score	6 (5; 7)	6 (4; 7)	6 (5; 6)	6 (5; 7)
Ankle joint dorsiflexion angle, degree (°)	15 (12; 18)	20 (17; 23)	19 (15; 22)	19 (17; 22)

Table prepared by the authors using their own data

Note: the data is presented as a value median (*Me*) of the lower and upper quartiles *Q* [25–75%].

63%, 59%, and 61%, respectively ($p < 0.05$). The corresponding data are shown in Fig. 3B.

In an intragroup analysis of changes of ankle joint dorsiflexion angle in follow-up (prior to treatment/14 days of treatment), athletes showed a statistically significant increase in the ankle joint range of motion in Groups 2 (vibration therapy and myofascial release) ($p < 0.05$) and 4 (vibration therapy, myofascial release, and individual foot orthoses) ($p < 0.01$) by 15% and 26%, respectively. No statistically significant dynamics was observed in other study groups (Fig. 4).

Table 2 presents the analysis of changes in plantar pressure on the support surface in the anterior and posterior parts of the affected foot before/after treatment according to baropodometry. During corrective actions, athletes in all groups showed normalization of the distribution of plantar pressure in the static test ($p < 0.05$). At the same time, in Groups 1 (ESWT) and 3 (individual orthoses of the feet), an increase in the pressure of the posterior part of the affected foot was detected by 37% and 18%, respectively. At the same time, Groups 2 (vibration therapy and myofascial release) and 4 (vibration therapy, myofascial release, and individual orthoses of the feet), conversely, showed a decrease in plantar pressure by 17% and 13%, respectively, compared to the measurements prior to treatment.

The analysis of baropodometric parameters in dynamic tests in athletes with PF compared before/after treatment (Fig. 5) revealed a decrease in the CoP velocity in both the frontal and sagittal planes, as well as the statokinesiogram area ($p < 0.05$). Thus, in athletes from Group 1, the decrease in CoP velocity in the frontal plane was 31%,

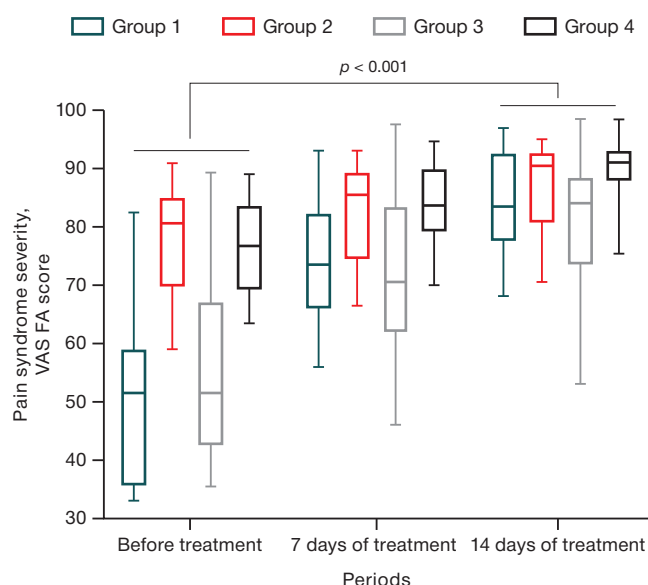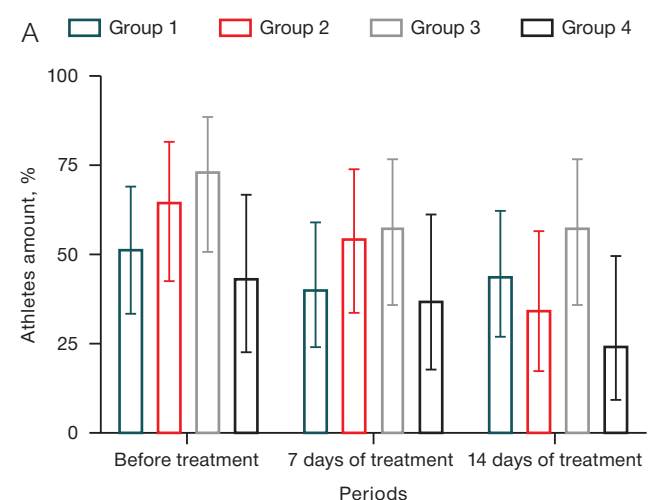Figure prepared by the authors using their own data

Fig. 2. Effectiveness of curative services in athletes with PF by VAS FA pain assessment

Figure prepared by the authors using their own data

Fig. 3. Effectiveness of therapeutic measures in athletes with PF by parameters
Note: A — muscle tenderness of the posterior thigh group; B — muscle tenderness of the posterior shin group.
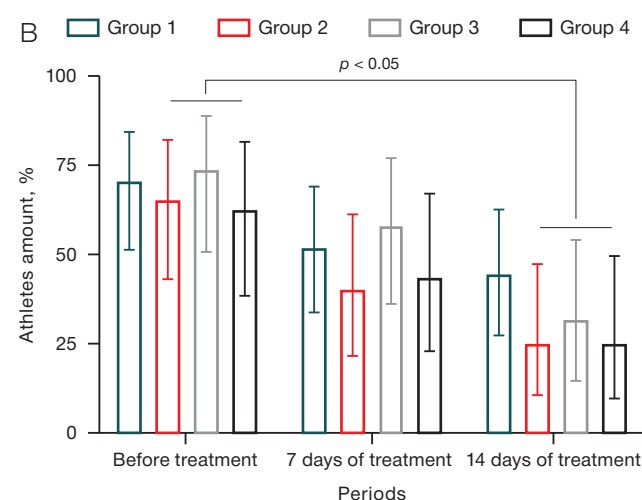
in athletes from Group 2 — 21%, in patients from Group 3 — 26.6%, and in athletes from Group 4 — 39%. At the same time, the decrease in CoP velocity in the sagittal plane in athletes from Group 1 was 29.4%, in patients from Group 2 — 16.6%, in athletes from Group 3 — 27.7%, and in patients from Group 4 — 37%.

There was also a decrease in the statokinesiogram area by 8.7% in athletes from Group 1, in Group 2 — by 12.7%, in Group 3 — by 16.3%, in Group 4 — by 9.2%.

The most pronounced decrease in the CoP velocity was observed in athletes in Group 4 (vibration therapy, myofascial release, and individual orthoses of the feet): by 39% of the CoP velocity in the frontal plane, by 37% of the CoP velocity in the sagittal plane (Fig. 5G). The statokinesiogram area significantly decreased in Group 3 — by 16.3% (Fig. 5B).

Figure 6 shows the results of baropodometry of athletes with PF in follow-up (before treatment/14 days of treatment), reflecting changes in the pressure general vector (PGV) and plantar pressure.

Attention should be drawn to the increase in plantar pressure of the posterior part of the foot in the static test (Fig. 6A), a decrease in the area of PGV distribution and pressure vectors under the feet in the sagittal dynamic test (Fig. 6B), the PGV centralization after curative services in the frontal (Fig. 6C), as well as a decrease in the area of PGV distribution in the jumping dynamic test (Fig. 6D).

The dynamics of changes in the plantar fascia thickness is shown in Fig. 7. In all groups, a statistically significant decrease in the plantar fascia thickness was observed: Group 1 — by 4.8% ($p = 0.001$), Group 2 — by 5.8% ($p = 0.037$), Group 3 — by 8.5% ($p = 0.008$), and Group 4 — by 12.5% ($p = 0.012$). However, in Groups 1 (ESWT) and 2 (vibration therapy and myofascial release), the change in plantar fascia thickness was less pronounced than in athletes from Groups 3 (individual foot orthoses) and 4 (vibration exposure, myofascial release and individual foot orthoses).

Despite statistically significant changes in the plantar aponeurosis thickness, their pronounced character does not point definitely to clinically significant differences (in particular, in Groups 1 and 2).

DISCUSSION

Our study established a statistically significant decrease in pain by VAS FA in all groups of athletes, which generally indicates the effectiveness of PF corrective measures.
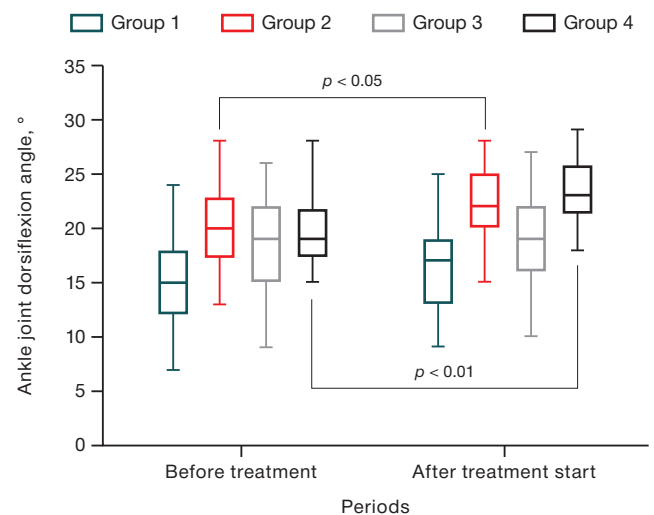

Figure prepared by the authors using their own data

Fig. 4. The effectiveness of curative services in athletes with PF by the ankle joint dorsiflexion angle

Thus, ESWT has been successfully used for PF treatment by some foreign and domestic authors [8, 9]. Mendes et al. reported a positive effect of individual orthopedic insoles in terms of pain reduction in patients with PF [10], which was subsequently confirmed by other authors [11, 12]. Kırmızı et al. noted the effectiveness of a combined therapy with therapeutic exercises and foot orthoses in reducing pain in patients with PF and flat feet [13].

In our research, pain in the muscles of the posterior shin group decreased statistically significantly in the participants of Group 2, whose therapy used vibration and myofascial release, and Group 3, who used individual orthoses of the feet. This fact can be explained by a significant impact of vibration therapy and individual orthoses of the feet on the activation of the internal and external muscles of the foot, thus contributing to their facilitated inclusion in the act of walking. It was previously suggested that the tenderness and tension of the triceps muscle of the shin, mainly its medial head, may be associated with increased stress on the muscle due to compensation for the insufficient function of the external muscles of the foot, in particular the posterior tibial muscle [14, 15]. Moreover, Zhou et al. reported that measures aimed at reducing stiffness and tension in the medial portion of the gastrocnemius muscle could be helpful in reducing the severity of pain in PF patients [15].

The ankle joint dorsiflexion angle increased statistically significantly in Groups 2 (vibration therapy and myofascial

Table 2. Intragroup analysis of changes in plantar foot pressure in athletes with PF in various groups

Athlete groups	Anterior part, %		p	Posterior part, %		p
	before treatment	after treatment		before treatment	after treatment	
Group 1 ($n = 27$)	27 (24; 29)	24 (23; 24)	<0.001	19 (14; 21)	26 (23; 27)	<0.001
Group 2 ($n = 20$)	20.5 (17; 23)	23 (22; 24)	0.001	35 (29; 39)	29 (27; 31)	0.001
Group 3 ($n = 19$)	26 (23; 28)	23 (23; 24)	0.008	22 (18; 29)	26 (25; 27)	0.024
Group 4 ($n = 16$)	21 (19; 24)	23 (22; 24)	0.046	31.5 (29; 37)	27.5 (26; 29)	0.002

Table prepared by the authors using their own data

Note: the data is presented as a value median (*Me*) of the lower and upper quartiles *Q* [25–75%].
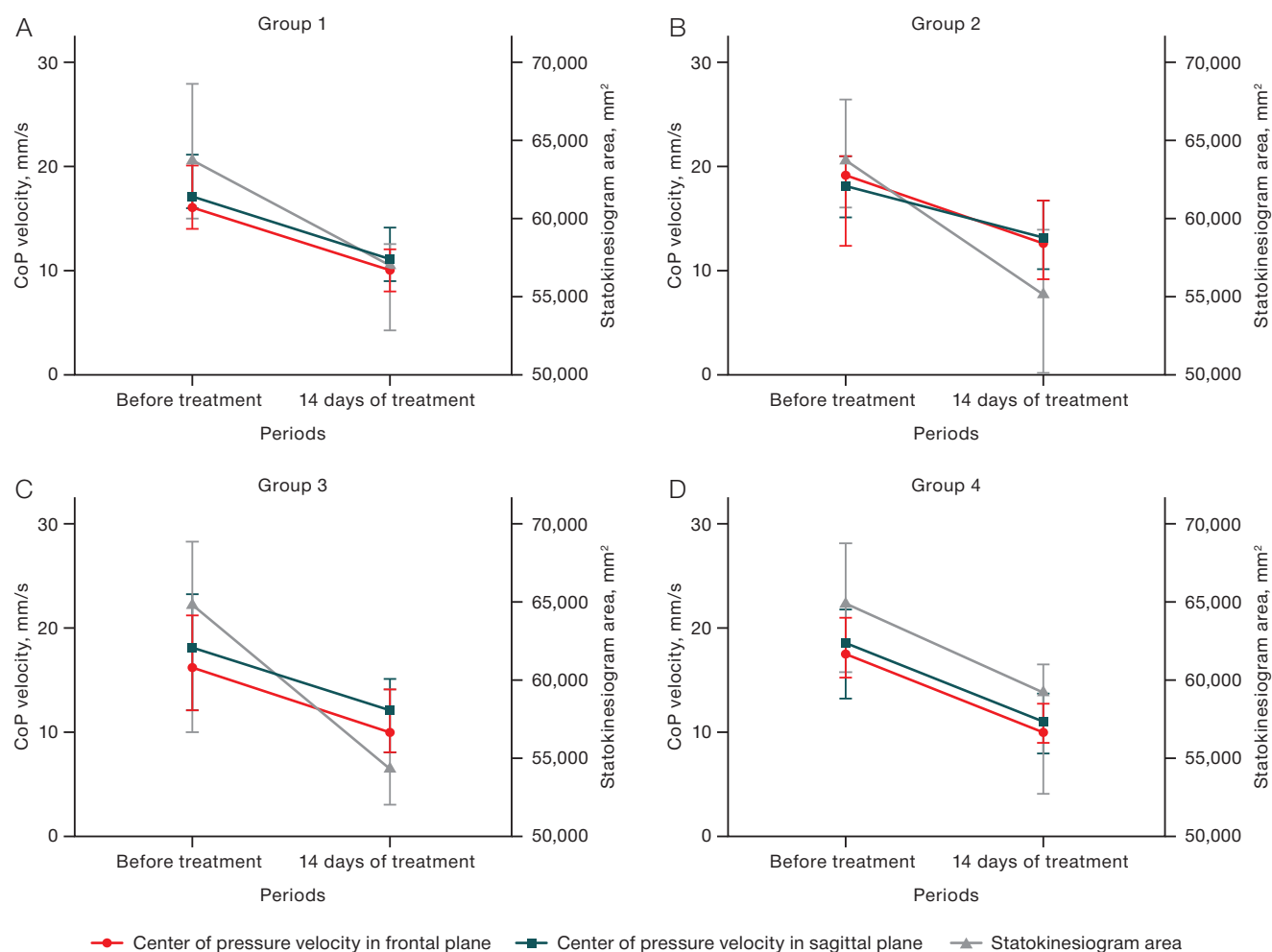
Figure prepared by the authors using their own data

Fig. 5. Changes in baropodometry values in dynamic tests before/after treatment in athletes with PF, depending on the intervention type

Legend for Fig. 5:
- Center of pressure velocity in frontal plane
- Center of pressure velocity in sagittal plane
- Statokinesiogram area
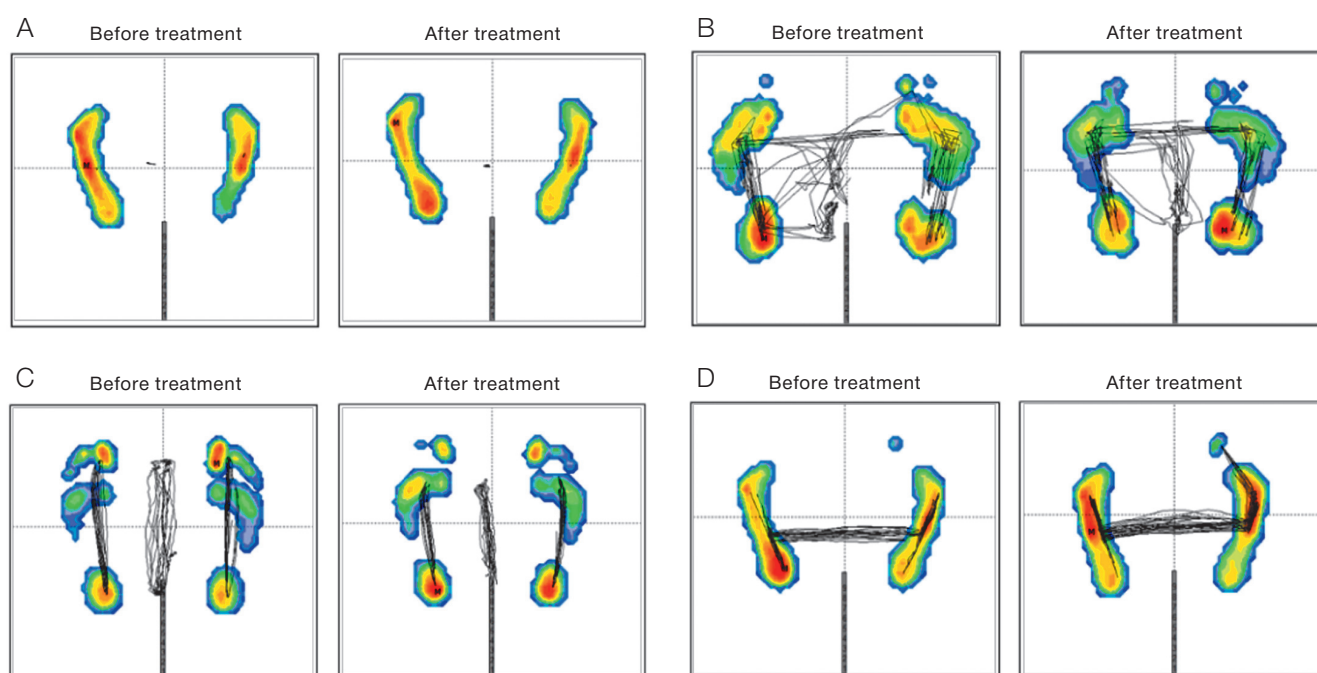

Figure prepared by the authors using their own data

Fig. 6. Baropodometry results of athletes with PF in follow-up
Note: A — in a static test; B — in the jumping dynamic test; C — in the sagittal dynamic test; D — in the frontal dynamic test.

release) and 4 (vibration therapy, myofascial release, and individual orthoses of the feet). This seems logical due to vibration and myofascial effects on the muscles of the posterior shin group, which improve their softness and plasticity. In combination with stretching, these measures allowed the volume of ankle joint posterior flexion to be significantly increased, as previously reported by some authors [15–20]. However, Landorf et al. did not find the aforementioned connection [21].

According to the results of baropodometry in PF, normalization of plantar pressure on the affected foot was noted. Thus, in athletes with low plantar pressure in the posterior part of the foot, it increased to normal values, and in athletes with initially high plantar pressure in the posterior part of the foot, on the contrary, decreased. The redistribution of pressure in the posterior part of the foot was also accompanied by normalization of plantar pressure in the anterior part of both the affected foot and the intact (contralateral) foot, in which plantar pressure had previously been compensationally impaired. In addition to the normalization of plantar pressure, all athletes with PF showed an improvement in both general postural stability and local stability during corrective measures, which were assessed based on the results of dynamic tests. At the same time, in Groups 2 (vibration therapy and myofascial release) and 4 (vibration therapy, myofascial release, and individual orthoses of the feet), a greater decrease in the statokinesiogram area in the jumping test was observed, which may indicate the influence of vibration therapy on the overall postural balance by influencing the proprioceptive apparatus. This fact is particularly interesting concerning the possibility of important effects of the pathobiomechanics of the overlying parts of the organs of support and movement (pelvis) on the underlying ones (feet). A similar effect was previously reported by some authors [22–24].

The plantar aponeurosis thickness tended to decrease in all the studied groups, which indicates a decrease in the fascia edema severity. This, in turn, may reflect a decrease in the load on plantar aponeurosis and a decrease in degenerative-inflammatory changes [25, 26]. The slight decrease in the plantar fascia thickness can be explained by a short follow-up period (14 days), insufficient to identify clear morphological changes accompanying a clinically significant improvement in athletes with PF. At the same time, Drake et al. noted that changes in the plantar aponeurosis morphology may not always correspond to the patient's clinical examination data [27].

In our study, the athlete groups were formed by simple randomization, based on the analysis of changes in the observation dynamics. Therefore, it can be concluded that ESWT allows the most effective relief of severe pain in athletes. In addition, individual orthoses of the feet also show significant effectiveness. However, significant risk factors may also influence the choice of the recommended therapeutic agent [28]. Such factors include flat feet, excessive foot pronation, limited ankle joint dorsiflexion, tension and tenderness of the muscles of the posterior shin group, hammer toe deformity [29–32]. Thus, vibration therapy, myofascial release, and individual feet orthoses showed the most pronounced action on correcting/compensating
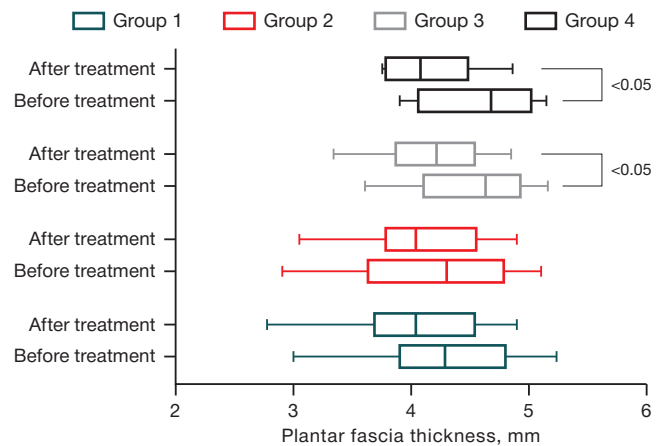

Figure prepared by the authors using their own data

Fig. 7. Plantar fascia thickness before/after treatment in the observation groups

for existing biomechanical risk factors for this disease in athletes. In this connection, it seems advisable to use local treatment methods in the case of an acute process, in order to achieve an anti-inflammatory effect followed by correction of the pathobiomechanics that had triggered the disease. In the case of a sluggish process, correction of impaired biomechanical patterns will not only prevent the development of disease relapses in the future, but also to relieve pain.

Further research should focus on assessing the sustainability of the achieved clinical results in the sports population with a longer follow-up period (12–18 weeks) and the role of therapeutic exercises in preventing possible recurrence of the disease.

CONCLUSION

Our study found that all the therapeutic methods used showed moderate effectiveness in PF treatment in the sports population. The choice of a therapeutic method should be primarily determined by the pain syndrome severity, as well as the foot structural and functional features, identified during a biomechanical examination on a baropodometric platform.

In athletes, the use of a differentiated approach based on a combined therapy aimed at correcting all existing risk factors seems justified. If necessary, ESWT is highly effective for relieving an acute pain syndrome. For achieving good therapeutic effects in the presence of foot deformities, it is advisable to use individual feet orthoses. In the case of limited ankle joint dorsiflexion and muscle tension of the posterior shin group, vibration action in combination with MFR of the muscles of the posterior shin group proves highly effective.

Treatment of athletes with PF is a challenging and lengthy process that does not always result in the resumption of full-fledged sports activities. The use of a combined and algorithmized personalized therapeutic strategy, accounting for significant risk factors for the disease in the sports population, can significantly reduce the duration of rehabilitation treatment for athletes with this pathology, as well as reduce the rate of disease recurrence.

References

1. Trojian T, Tucker AK. Plantar Fasciitis. *Am Fam Physician*. 2019;99(12):744–50
PMID: 31194492

2. Atzmon R, Eilig D, Dubin J, Vidra M, Marom O, Tavdi A, Drexler M, Palmanovich E. Comparison of Platelet-Rich Plasma Treatment and Partial Plantar Fasciotomy Surgery in Patients with Chronic Plantar Fasciitis: A Randomized, Prospective Study. *J Clin Med*. 2022;11(23):6986.
https://doi.org/10.3390/jcm11236986

3. Coppola M, Sgadari A, Marasco D, Danti C, Vitale G, Smeraglia F, Balato G, Bernasconi A. Treatment Approaches for Plantar Fasciopathy in Elite Athletes: A Scoping Review of the Literature. *Orthop J Sports Med*. 2022;10(11):23259671221136496
https://doi.org/10.1177/23259671221136496

4. Wang B, Wang XL, Ma YT, Wu W, Zheng YJ. Evaluation of the efficacy of trigger points combined with extracorporeal shock waves in the treatment of plantar fasciitis: heel temperature and plantar pressure. *BMC Musculoskelet Disord*. 2024 Mar 2;25(1):191.
https://doi.org/10.1186/s12891-024-07296-2
Erratum in: *BMC Musculoskelet Disord*. 2024;25(1):546.
https://doi.org/10.1186/s12891-024-07643-3

5. Pazhooman H, Alamri MS, Pomeroy RL, Cobb SC. Foot kinematics in runners with plantar heel pain during running gait. *Gait Posture*. 2023;104:15-21
https://doi.org/10.1016/j.gaitpost.2023.05.019

6. Kovaleva MA., Mogelnitskiy AS., Belyaev AF. Validation of Russian-language version of Visual Analog Scale Foot and Ankle (VAS FA). *Russian Osteopathic Journal*. 2023;(3):34–45 (In Russ.)
https://doi.org/10.32885/2220-0975-2023-3-34-45

7. Karmazin VV, Slivin AV, Parastaev SA. Plantar pressure distribution features in athletes with plantar fasciitis. *Extreme Medicine*. 2024;26(2):87–93 (In Russ.)
https://doi.org/10.47183/mes.2024.036

8. Belonogov VN, Kireev SI, Kireev SN, Semenov NS. Application of shock wave therapy in the complex treatment of plantar fasciitis. *Saratov Scientific Medical Journal*. 2019;15(4):858–61 (In Russ.)
EDN: LOOVML

9. Vikhlyantsev VA, Kobelev MV, Shapovalova EM. The mechanism of clinical effectiveness of the radial shock wave method in the treatment of plantar fasciitis. *Medical Science and Education of the Urals*. 2020;21(2):84–6 (In Russ.)
https://doi.org/10.36361/1814-8999-2020-21-2-84-86

10. Mendes AAMT, Silva HJA, Costa ARA, Pinheiro YT, Lins CAA, de Souza MC. Main types of insoles described in the literature and their applicability for musculoskeletal disorders of the lower limbs: A systematic review of clinical studies. *J Bodyw Mov Ther*. 2020;24(4):29–36
https://doi.org/10.1016/j.jbmt.2020.06.001

11. Schuitema D, Greve C, Postema K, Dekker R, Hijmans JM. Effectiveness of Mechanical Treatment for Plantar Fasciitis: A Systematic Review. *J Sport Rehabil*. 2019;29(5):657–74.
https://doi.org/10.1123/jsr.2019-0036

12. Lewis RD, Wright P, McCarthy LH. Orthotics Compared to Conventional Therapy and Other Non-Surgical Treatments for Plantar Fasciitis. *J Okla State Med Assoc*. 2015;108(12):596–8
PMID: 26855444

13. Kirmizi M, Sengul YS, Akcali O, Angin S. Effects of foot exercises and customized arch support insoles on foot posture, plantar force distribution, and balance in people with flexible flatfoot: A randomized controlled trial. *Gait Posture*. 2024;113:106–14
https://doi.org/10.1016/j.gaitpost.2024.05.030

14. Dayton P. Anatomic, Vascular, and Mechanical Overview of the Achilles Tendon. *Clin Podiatr Med Surg*. 2017;34(2):107–13
https://doi.org/10.1016/j.cpm.2016.10.002

15. Zhou JP, Yu JF, Feng YN, Liu CL, Su P, Shen SH, Zhang ZJ. Modulation in the elastic properties of gastrocnemius muscle heads in individuals with plantar fasciitis and its relationship with pain. *Sci Rep*. 2020;10(1):2770
https://doi.org/10.1038/s41598-020-59715-8

16. Cheung JT, Zhang M, An KN. Effect of Achilles tendon loading on plantar fascia tension in the standing foot. *Clin Biomech (Bristol)*. 2006;21(2):194–203
https://doi.org/10.1016/j.clinbiomech.2005.09.016

17. Lee SH, Suh DH, Kim HJ, Jang WY, Park YH, Sung HJ, Choi GW. Association of Ankle Dorsiflexion With Plantar Fasciitis. *J Foot Ankle Surg*. 2021;60(4):733–7
https://doi.org/10.1053/j.jfas.2021.02.004

18. Nakale NT, Strydom A, Saragas NP, Ferrao PNF. Association Between Plantar Fasciitis and Isolated Gastrocnemius Tightness. *Foot Ankle Int*. 2018;39(3):271–7
https://doi.org/10.1177/1071100717744175

19. Sullivan J, Burns J, Adams R, Pappas E, Crosbie J. Musculoskeletal and activity-related factors associated with plantar heel pain. *Foot Ankle Int*. 2015;36(1):37–45
https://doi.org/10.1177/1071100714551021

20. Bolívar YA, Munuera PV, Padillo JP. Relationship between tightness of the posterior muscles of the lower limb and plantar fasciitis. *Foot Ankle Int*. 2013;34(1):42–8
https://doi.org/10.1177/1071100712459173

21. Landorf KB, Kaminski MR, Munteanu SE, Zammit GV, Menz HB. Clinical measures of foot posture and ankle joint dorsiflexion do not differ in adults with and without plantar heel pain. *Sci Rep*. 2021;11(1):6451
https://doi.org/10.1038/s41598-021-85520-y

22. Lee JH, Park JH, Jang WY. The effects of hip strengthening exercises in a patient with plantar fasciitis: A case report. *Medicine (Baltimore)*. 2019;98(26):e16258
https://doi.org/10.1097/MD.0000000000016258

23. Lewis CL, Ferris DP. Walking with increased ankle push-off decreases hip muscle moments. *J Biomech*. 2008 Jul 19;41(10):2082–9
https://doi.org/10.1016/j.jbiomech.2008.05.013

24. Mueller MJ, Sinacore DR, Hoogstrate S, Daly L. Hip and ankle walking strategies: effect on peak plantar pressures and implications for neuropathic ulceration. *Arch Phys Med Rehabil*. 1994 Nov;75(11):1196–200
https://doi.org/10.1016/0003-9993(94)90004-3

25. Chimutengwende-Gordon M, O'Donnell P, Singh D. Magnetic resonance imaging in plantar heel pain. *Foot Ankle Int*. 2010;31(10):865–70
https://doi.org/10.3113/FAI.2010.0865

26. Bicer M, Hocaoglu E, Aksoy S, İnci E, Aktaş İ. Assessment of the Efficacy of Extracorporeal Shockwave Therapy for Plantar Fasciitis with Magnetic Resonance Imaging Findings. *J Am Podiatr Med Assoc*. 2018;108(2):100–5
https://doi.org/10.7547/15-106

27. Drake C, Whittaker GA, Kaminski MR, Chen J, Keenan AM, Rathleff MS, Robinson P, Landorf KB. Medical imaging for plantar heel pain: a systematic review and meta-analysis. *J Foot Ankle Res*. 2022;15(1):4
https://doi.org/10.1186/s13047-021-00507-2

28. Tan VAK, Tan CC, Yeo NEM, Zhang M, Mehta KV, Tian RHH, Tan B. Consensus statements and guideline for the diagnosis and management of plantar fasciitis in Singapore. *Ann Acad Med Singap*. 2024;53(2):101–12
https://doi.org/10.47102/annals-acadmedsg.2023211

29. Martinelli N, Bianchi A, Martinkevich P, Sartorelli E, Romeo G, Bonifacini C, Malerba F. Return to sport activities after subtalar arthroereisis for correction of pediatric flexible flatfoot. *J Pediatr Orthop B*. 2018;27(1):82–7
https://doi.org/10.1097/BPB.0000000000000449

30. Pohl MB, Hamill J, Davis IS. Biomechanical and anatomic fac-

tors associated with a history of plantar fasciitis in female runners. *Clin J Sport Med*. 2009;19(5):372–6
https://doi.org/10.1097/JSM.0b013e3181b8c270

31. Bencke J, Christiansen D, Jensen K, Okholm A, Sonne-Holm S, Bandholm T. Measuring medial longitudinal arch deformation during gait. A reliability study. *Gait Posture*. 2012;35(3):400–4

https://doi.org/10.1016/j.gaitpost.2011.10.360

32. Knapik DM, LaTulip S, Salata MJ, Voos JE, Liu RW. Impact of Routine Gastrocnemius Stretching on Ankle Dorsiflexion Flexibility and Injury Rates in High School Basketball Athletes. *Orthop J Sports Med*. 2019;7(4):2325967119836774.
https://doi.org/10.1177/2325967119836774

AUTHORS

Anton V. Slivin
https://orcid.org/0000-0003-2107-6525
anton-slivin@mail.ru

Kirill A. Shlykov
https://orcid.org/0009-0005-0957-1840
kirill@drshlykov.ru

Valerii V. Karmazin, Cand. Sci. (Med.)
https://orcid.org/0000-0002-1971-4420
vkarma@mail.ru

Sergey A. Parastaev, Dr. Sci. (Med.)
https://orcid.org/0000-0002-2281-9936
ParastaevSA@sportfmba.ru

REGIONAL CUTANEOUS BLOOD FLOW IN HEALTHY SUBJECTS UNDER CONDITIONS OF 21-DAY HEAD-DOWN BED REST

Daria V. Pashkova[1✉], Julia A. Popova[1], Andrey A. Fedorovich[1,2], Alexey V. Shpakov[1]

[1] Institute of Biomedical Problems, Moscow, Russia

[2] National Medical Research Center for Therapy and Preventive Medicine, Moscow, Russia

Introduction. Research into the microvasculature as an integral component of the cardiovascular system is particularly relevant in space medicine for identifying adaptive changes to weightlessness and developing new diagnostic criteria for assessing the functional state of an astronaut's body in long-duration space flights.

Objective. To study the process of microcirculation and its regulation in various skin areas in healthy volunteers under conditions of 21-day head-down (–6°) bed rest (HDBR).

Materials and methods. The experiment involved six male volunteers aged 26–34 years. To simulate translocation of liquid media and physical inactivity, the subjects remained in an antiorthostatic position for 21 days. Microcirculation was studied by laser Doppler flowmetry using LAZMA PF portable laser analyzers (SPE "LAZMA" Ltd, Russia). Participant examination was conducted two days prior the onset of the study, on the 3rd, 7th, 15th, 18th, and 20th day of experimental exposure, as well as two days after the completion of HDBR. Statistical data analysis was performed using the Statistica 13.0 software (IBM, USA).

Results. On day 3 of HDBR exposure, a statistically significant decrease in basal perfusion and the amplitude of myogenic oscillations in the skin of the forehead and shin was observed. The analysis of functional tests on the forearm showed a decrease in the respiratory test index by 10.87% throughout the experimental period. On day 3 of hypomobility, a decrease in the venuloarteriolar response by an average of 10.64% and an increase by 91.82% in the capillary blood flow reserve were noted, with the latter persisting throughout the entire exposure.

Conclusions. The effect of HDBR is expressed in a decrease in skin perfusion against the background of increased tone of terminal arterioles and precapillary sphincters in the forehead and lower legs, which may indicate microcirculation shift toward larger vessels. Despite the skin perfusion stability in the forearm area at rest, the conducted functional tests showed the probability of changes in vasomotor function under the action of HDBR.

Keywords: head-down bed rest; cardiovascular system; skin blood flow; laser Doppler flowmetry; blood perfusion; skin blood flow regulation

УДК 612.135+612.014.4

РЕГИОНАРНЫЙ КОЖНЫЙ КРОВОТОК У ЗДОРОВЫХ ОБСЛЕДУЕМЫХ В УСЛОВИЯХ 21-СУТОЧНОЙ АНТИОРТОСТАТИЧЕСКОЙ ГИПОКИНЕЗИИ

Д.В. Пашкова[1✉], Ю.А. Попова[1], А.А. Федорович[1,2], А.В. Шпаков[1]

[1] Институт медико-биологических проблем Российской академии наук, Москва, Россия

[2] Национальный медицинский исследовательский центр терапии и профилактической медицины Министерства здравоохранения Российской Федерации, Москва, Россия

Введение. Исследование микроциркуляторного звена как элемента сердечно-сосудистой системы применительно к космической медицине актуально как для выявления адаптационных изменений к невесомости, так и поиска новых диагностических критериев оценки функционального состояния организма космонавта в перспективе дальних космических полетов.

Цель. Изучение микрокровотока и его регуляции в различных областях кожи у здоровых добровольцев в условиях 21-суточной антиортостатической (–6°) гипокинезии (АНОГ).

Материалы и методы. В эксперименте приняли участие 6 мужчин-добровольцев в возрасте 26–34 лет. Для моделирования транслокации жидких сред и гиподинамии испытуемые находились в антиортостатическом положении в течение 21 сут Микроциркуляцию исследовали с помощью метода лазерной доплеровской флоуметрии с использованием портативных лазерных анализаторов «ЛАЗМА ПФ» (ООО НПП «ЛАЗМА», Россия). Исследование проводили за 2 сут до начала АНОГ, на 3, 7, 15, 18 и 20 сут экспериментального воздействия, а также через 2 сут после окончания АНОГ. Статистический анализ данных проведен с использованием программного обеспечения Statistica 13.0 (IBM; США).

Результаты. Обнаружено статистически значимое снижение базальной перфузии и амплитуды миогенных колебаний в области кожи лба и голени на 3 сут в условиях антиортостатической гипокинезии. Анализ результатов функциональных проб на предплечье показал уменьшение индекса дыхательной пробы на 10,87% на протяжении всего экспериментального периода, снижение венуло-артериолярной реакции на 3 сут гипокинезии в среднем на 10,64% и увеличение на 91,82% резерва капиллярного кровотока на 3 сут, сохраняющееся на протяжении всего воздействия.

Выводы. Эффект воздействия АНОГ выражен в снижении кожной перфузии на фоне увеличенного тонуса терминальных артериол и прекапиллярных сфинктеров в области лба и голеней, что может указывать на распределение микрокровотока в сторону более крупных сосудов. Несмотря на стабильность перфузии в области кожи предплечья в покое, проведенные функциональные пробы показали, что, вероятно, условия АНОГ приводят к изменению вазомоторной функции.

✉ Пашкова Дарья Валерьевна dashapashkova1@yandex.ru

INTRODUCTION

Weightlessness is known to be a significant factor affecting the state of the cardiovascular system (CVS) during space flights (SF). Its effects are mainly caused by blood redistribution toward the cranial direction. In addition, SF conditions trigger such changes in the cardiovascular system as fluid movement from intravascular compartments toward intracellular spaces, a decrease in the total circulating blood volume, myocardial mass loss, decreased vascular resistance, increased venous return, and orthostatic intolerance after returning to gravity [1–2].

The prospects of long-duration space flights, e.g., to the Moon, Mars, etc., with the possibility of landing on their surface poses the challenge of solving arising medical issues without timely support from the Earth. In this connection, assessment of the functional state of the circulatory system at both macro- and micro-levels can provide the necessary information about the overall adaptational capacity of the body and its resilience to external influences. From this standpoint, the microcirculatory bed as the primary element of the cardiovascular system that responds to environmental changes presents particular research interest [3]. The skin is one of the most accessible objects for studying blood microcirculation; however, account should taken of the cutaneous blood flow being directly involved in thermoregulation [4].

According to N. Charkoudian, the skin microcirculation reacts to heat or cold stress [5], while scientific data in available publications may differ due to the variety of methods used to assess the overall thermal effect [6, 7]. Thus, according to Fedorovich et al. [6], a 30-day stay in a hermetic object at a temperature of +30–38 °C and a humidity of 30–50% did not result in an increase in tissue perfusion recorded by laser Doppler flowmetry (LDF) on the forearm. This was explained by the specifics of skin angioarchitectonics and the depth of sensing by measuring equipment. Examination of the skin microcirculatory bed by Yuan et al. using the LDF method in an experiment with 180-day isolation in temperature- and humidity-neutral conditions revealed a decrease in the blood flow response to an acetylcholine test, which indicated the manifestation

of endothelial dysfunction [8]. The study of skin micro-hemocirculation in SF conditions was undertaken in two experiments. In the first study [9], the authors evaluated cutaneous blood flow and endothelium-dependent vasodilation at the forearm level using LDF in combination with acetylcholine iontophoresis during a three-week SF at the Tiangong-2 station in two taikonauts. The authors observed a slight decrease in basal perfusion during and directly after SF, as well as signs of endothelial dysfunction. In the second study [10], conducted on board the ISS with the participation of one space tourist and one professional cosmonaut, a decrease in tissue perfusion and an increase in vascular tone were found on days 2 and 3 of SF in the skin of the first toe and the temporal region of the head. In addition, functional differences were found in the indices of skin perfusion of the upper and lower extremities between the examined astronauts, which the authors attributed to the use of a preventive blood redistribution agent in one of the study participants [10].

The complexity of organizing space experiments and the limited sample of the astronauts being examined, given multicomponent SF factors, impede a comprehensive study of the microcirculatory link and its regulation in these conditions. Earth model experiments can be used to evaluate the effect of weightlessness, including inactivity, lifting of the support load, and redistribution of liquid media in the cranial direction. One of such experiments is head-down bed rest (HDBR) used for modeling the redistribution of body fluids toward the cranial direction.

In this article, we report a study undertaken to investigate microcirculation and its regulation in various areas of the skin in healthy male volunteers under conditions of 21-day head-down bed rest.

MATERIALS AND METHODS

The experiment was conducted on six healthy male volunteers (average age 30.3 ± 5.2 years; weight — 72.8 ± 7.7 kg; height — 177.1 ± 6.3 cm) using a hypogravitation bench at the Institute of Biomedical Problems (Russia). The volunteers were placed in an antiorthostatic position with an angle of inclination of the body relative to the horizon of

–6° without the use of preventive physical exercises and a moderate restriction of motor activity for 21 days. The subjects were verticalized for short-term hygiene procedures (once daily), as well as for passive orthostatic testing (on days 6, 14, and 19) and a lower body negative pressure (LBNP) on day 19. For medical reasons, one of the subjects was allowed to participate in the experiment with restrictions: provided that stress tests, including orthostatic ones, were excluded. A detailed description of experimental conditions can be found in [11].

The method of laser Doppler flowmetry (LDF) was used to assess the state of the skin microcirculatory bed. This method is based on probing the area under study using laser radiation and analyzing the reflected signal from red blood cells moving in the bloodstream. The exclusion criteria for this study of the skin microcirculatory bed (MCB) using the LDF method were: age over 40 years, the presence of additional exposure factors (breathing with hyperoxic mixtures, etc.), the presence of nevi and tattoos in the area of sensor application in the subjects. All six participants in the experiment were included in the study group according to these criteria.

To register microcirculation parameters using the LDF method, three LAZMA PF portable laser analyzers (SPE "LAZMA" Ltd, Russia) with the wavelength of the probing radiation of 850 nm were used. One sensor was placed on the non-dominant arm in the Zakharin–Ged area: along the median line of the forearm, 3–4 cm above the ulnar and radial styloid. The second sensor was placed on the anterior-inner surface in the lower third of the shin. The third sensor was applied on the central area of the forehead (Fig. 1).

The analyzers were fixed using medical tubular elastic bandages. The total examination duration was 45 min. At the first stage, basal perfusion was recorded at rest: the subject was in a relaxed lying position, calmly breathing

Figure prepared by the authors using data from an open online source

Fig. 1. Placement of portable laser analyzers during the study

in a waking state. Following 10 min, functional tests were performed in the forearm area: respiratory and occlusive (venous and arterial) tests. The respiratory test includes a breath-holding maneuver (for 15 sec after rapid deep inhalation through the mouth), allowing assessment of the functional state of sympathetic vasomotor regulation. Venous occlusion was created by increasing pressure in the shoulder cuff to 40 mmHg followed by its maintenance at this level for 2 min. This artificially created an increase in postcapillary pressure, without obstacles to arterial blood flow, to assess the venuloarteriolar constrictor response without involving sympathetic regulation. Arterial occlusion was used to determine the reserve of capillary blood flow, for which pressure was pumped into the shoulder cuff at a level of 30–50 mmHg above the individual systolic pressure and maintained at this level for 3 min, followed by parameter registration in the period of postocclusive hyperemia. The use of these tests allowed us assess the state of the regulation mechanisms of tissue blood flow, as well as the general functional state of the microcirculatory bed in the forearm skin according to the accepted methodology [12, 13].

The Lazma specialized software (SPE "LAZMA" Ltd, Russia) was used to calculate the basal perfusion level (M) in perfusion units (PU), as well as the amplitude–frequency spectrum of blood flow oscillations based on wavelet analysis. Thus, the maximum amplitudes of vasomotion were determined in the appropriate frequency ranges, i.e., Ae, An, Am, Av, Ac (endothelial, neurogenic, myogenic, venular (respiratory), and cardiac components of microvascular tone formation, respectively). When performing functional tests, the following indicators were evaluated: BHI as an index of breath holding test, VAR as an venuloarteriolar response, CFR as capillary blood flow reserve (according to the LDF of the forearm skin).

The microcirculatory bed was examined two days prior to the onset of experimental exposure (background study); on days 3, 7, 15, 18, and 20 during HDBR exposure; as well as two days after the completion of exposure (aftereffect period). The studied parameters were recorded prior to and following the HDBR period in the prone position of the subject (15 min after adaptation to the horizontal position). During HDBR exposure, the participants were examined in an antiorthostatic position. The study prior to and following exposure was performed in laboratory conditions with a constant microclimate: ambient temperature — 24.33 ± 2.58 °C; humidity — 57.83 ± 6.97%; atmospheric pressure — 741.17 ± 16.57 mmHg. Under HDBR conditions, the study was conducted in a room with the following environmental parameters: ambient temperature — 23.36 ± 1.34 °C; humidity — 54.57 ± 3.03%; atmospheric pressure — 744.57 ± 17.08 mmHg.

A statistical analysis of the datasets obtained was carried out using the STATISTICA 13.0 statistical software package (IBM, USA) using principal component analysis and the Wilcoxon criterion [14].

RESULTS

When analyzing the data obtained, the study sample of six people was checked for uniformity using principal
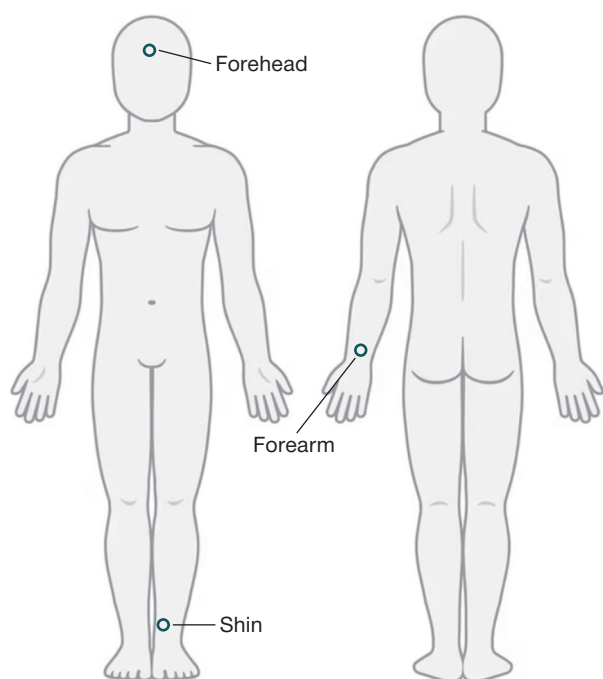
component analysis for all parameters recorded during the experiment. The results obtained recorded the uniformity of the group, with the values not exceeding two standard deviations.

On day 3 of HDBR stay, the conducted statistical analysis revealed a decrease in the basal perfusion level ($p = 0.05$, Wilcoxon criterion) by 32.84% in the forehead skin and 22.52% in the shin skin (Fig. 2). In addition, a decrease in this parameter in the shin skin was noted on days 15 and 18 of exposure, amounting to 31.64% and 34.68%, respectively. This may be related to the cyclogram of the experiment, which included an orthostatic test. It should be noted that, by day 3 of hypokinesia, the participant who was not allowed to undergo an orthostatic test and an LBNP test during the HDBR period, showed a 7.02% decrease in blood perfusion in the forehead skin; during the entire HDBR, the downward trend in this parameter persisted and had reached the maximum difference with the background (34.21%) by day 20 of exposure. It could be assumed that changes in skin perfusion might be associated with temperature changes, since the skin is an essential component of the human thermoregulatory system [4].

In our study, the ambient temperature during the exposure period was kept at 23.36 ± 1.34 °C, being close to the temperature of the laboratory room in which the studies were conducted before and after HDBR (24.33 ± 2.58 °C). In addition, the temperature of the study area was measured using a sensor built into the LDF analyzer, with the parameter remaining around the same level during the entire experiment. The average temperature was 32.88 ± 1.36 °C in the forehead skin and 32.73 ± 1.38 °C in the shin skin. The humidity level in the rooms during the study practically did not differ between sessions: during the procedure, the windows were closed, and the air conditioning system was turned off before (15 min before the start of the measurement) and during the study. Around 15 min before the onset of the experiment, the participants were not covered with a blanket, the examined skin areas were open (freed from clothing) to adapt to environmental conditions. According to subjective feelings, all volunteers felt comfortable in these conditions. Thus, the effect of fluctuations in environmental parameters on our results was minimal.

A decrease in the amplitude of myogenic oscillations by 51.15% and 41.94% was found in both the forehead and shin skin areas at an early stage of the body's adaptation to HDBR conditions (day 3). It should be noted that in the head area, the Am value remained below the background (measured 2 days prior to exposure) and decreased relative to the background by 57.03% on day 7, by 47.23% on day 15, and by 47.71% by day 18 (Fig. 3).

When analyzing the data obtained during functional tests, changes were found in both the VAR during the breath holding test, and in the VAR and CFR during venous and arterial occlusion, respectively (Fig. 4). However, these changes were multidirectional: when the VAR and BHI decreased, the CFR increased throughout the exposure. Moreover, VAR had a reduced value of relative background exposure on days 3 and 15 of HDBR, BHI — throughout the entire exposure.

DISCUSSION

It is known that bed rest models primarily simulate such an effect of weightlessness as the redistribution of body fluids toward the cranial direction. In our series of experiments, part of which was the current study, the authors [11] showed that, due to HDBR exposure, the central hemodynamics showed an average daily decrease in heart rate and blood pressure. Previous studies found a decrease in total peripheral resistance [15] and, concerning the peripheral hemodynamics, a decrease in blood flow in the lower extremities [16].

The results obtained in our study indicate that HDBR conditions with an inclination angle of −6° lead to changes in skin microcirculation, which are manifested in a decrease in basal perfusion in the shin and forehead at an early stage of the body's adaptation (day 3 of exposure).
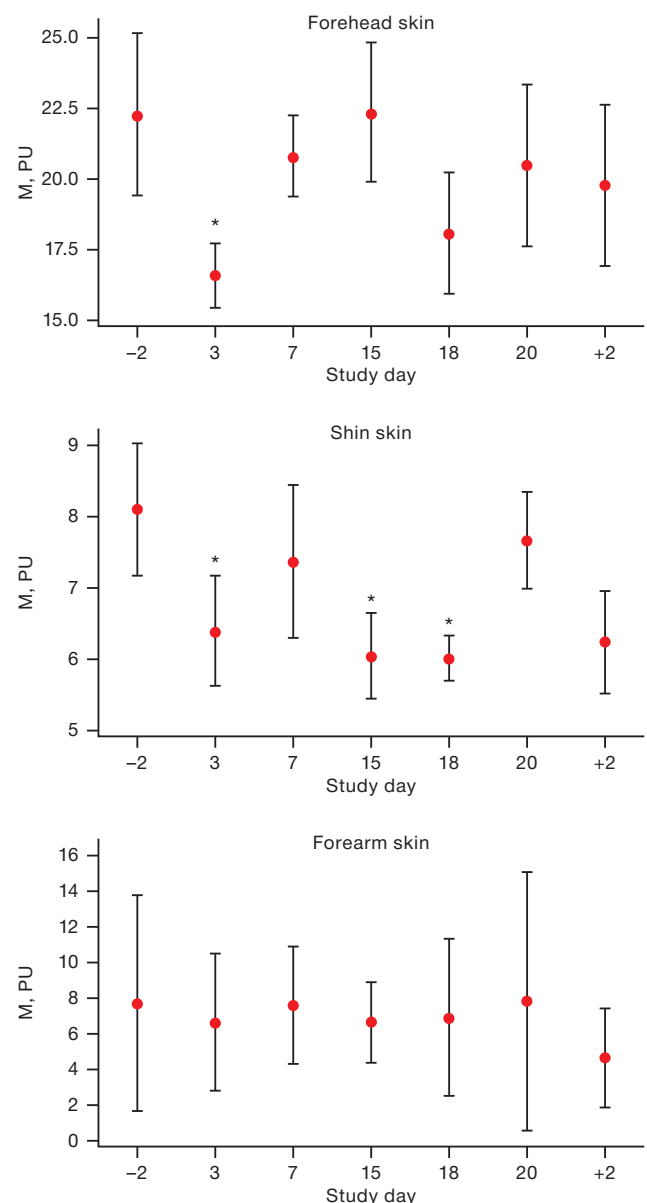

Figure prepared by the authors using their own data

Fig. 2. Basal perfusion changes in HDBR conditions
Note: the graphs show the average values and the interquartile range; on the X-axis: −2 and +2 are the days before and after head-down bed rest; * $p < 0.05$.

Figure prepared by the authors using their own data

Fig. 3. Changes in the amplitude of myogenic oscillations (Am) under the conditions of head-down bed rest.
Note: the graphs show the average values and the interquartile range; on the X-axis: −2 and +2 are the days before and after head-down bed rest; * $p < 0.05$.

Figure prepared by the authors using their own data

Fig. 4. Parameter dynamics of functional tests in the conditions of head-down bed rest
Note: the graphs show the average values and the interquartile range; on the X-axis: −2 and +2 are the days before and after head-down bed rest; * $p < 0.05$.
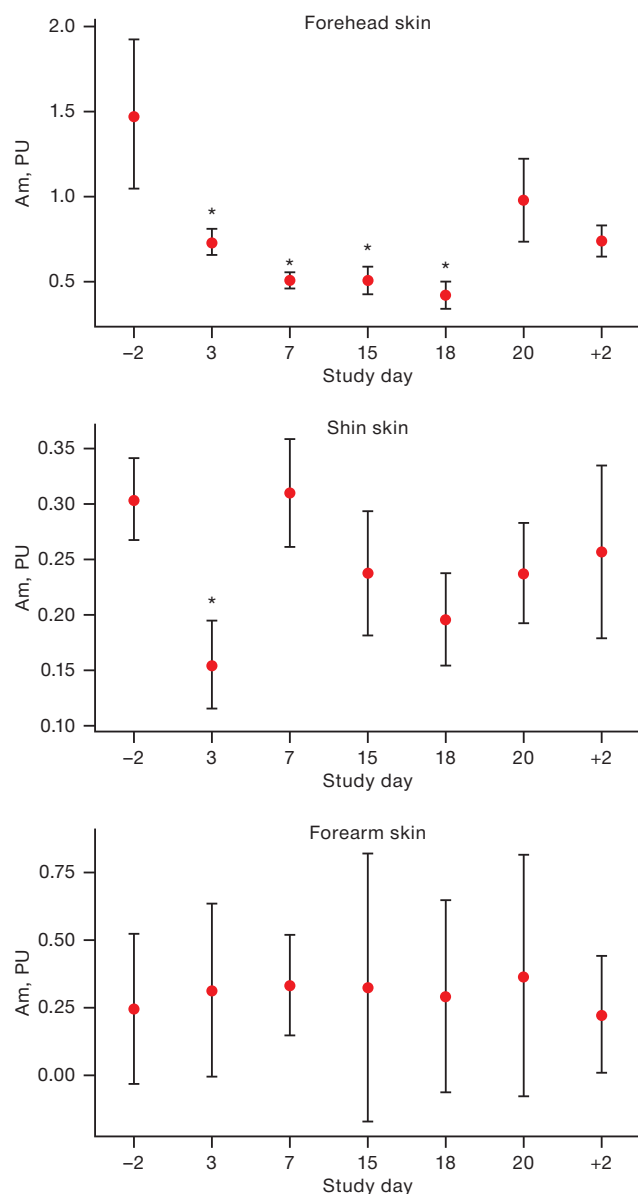
In other words, the changes are unidirectional in both the skin of the lower extremities and the scalp. These data are consistent with the results of a study conducted by Britt et al. [17], who observed a decrease in blood perfusion in the neck area under HDBR conditions.

In an experiment by Kurazumi et al. [18], the subjects briefly placed in an antiorthostatic position demonstrated a decrease in cutaneous blood flow in the cheek area during 10-min antiorthostasis with a body tilt angle of −30°, against which a significant increase in vascular resistance in this area was detected.

In our study, against the background of decreased perfusion, a decrease in the amplitude of myogenic oscillations was noted both in the lower extremities and in the forehead skin. This indicates an increase in vascular tone in the skin microcirculatory bed of these regions. Due to the relatively

increased tone of the arterioles, the microvascular lumen narrows, which reduces skin blood flow in the studied areas. It can be assumed that the decrease in the amplitude of myogenic vasomotions in the forehead skin may reflect protective mechanisms in the basin of the internal carotid artery (including for the capillaries of the brain) from an excessive increase in hydrostatic pressure in conditions of increased arterial blood flow and obstructed venous outflow (myogenic autoregulation of the cerebral vascular bed). It is the myogenic tone that is the last regulatory link at the entrance to the capillary. An increase in the level of tissue perfusion in the forehead skin may be a consequence of activation of other regulatory mechanisms or a contribution to the overall spectral power of the reflected signal of the venular component (venular fullness) against the background of venous outflow difficulty from the head in HDBR

conditions. The restoration of the blood perfusion level in the forehead skin on days 7, 15, and 20 of HDBR back to the initial background level is probably due to the consequence of temporary verticalization of the subjects on the eve of the study session associated with the passive orthoprobe (days 6, 14, and 19) and the LBNP test (day 19).

The detected changes (decreased perfusion and amplitude of myogenic oscillations) on days 3 and 18 may indicate the redistribution of blood from the skin of the shin and forehead into larger vessels against the background of centralization of blood flow. It was previously shown that during space flight conditions, the main volume of extracellular fluid, according to bioimpedance measurements, is observed in the abdominal region [19].

It was found that the changes in skin perfusion in the forehead and lower leg area under HDBR conditions are similar to those recorded in a study of microcirculatory tissue systems by the LDF method on the International Space Station [10]. In comparison with the LDF results under conditions of a three-week SF, indicating a slight decrease in basal perfusion in the forearm skin throughout the flight [20], our study under similar-duration conditions revealed no changes in the LDF parameter in the forearm skin.

Nevertheless, the analysis of the above functional tests showed that HDBR exposure leads to changes in the vasomotor function of the vessels of the forearm skin, which may be indicated by both a decrease in VAR and a decrease in IDP. This, hence, states a decrease in the microvascular response to both types of constrictor stimuli. The steadily reduced value of IDP throughout the entire period of HDBR indicates that the degree of shortening of smooth muscle cells during activation of the sympathetic adrenergic system decreases either due to changes in the sensitivity of myocytes to norepinephrine, or due to increased muscle tone. In this regard, it can be assumed that the tone of myocytes is increased on the forearm (the higher the initial tone, the lower the degree of muscle shortening and, consequently, the lower the amplitude of the recorded signal). However, according to the amplitude-frequency wavelet analysis, we did not register a significant decrease in the amplitude of myogenic vasomitions. The constrictor reaction in venous

occlusion is based on the contraction of precapillary arterioles in response to stretching of myocytes with increasing pressure, initially in the venous region, then in the capillary and in the precapillary (Ostroumov-Baylis mechanism).

The decrease in the VAR index in HDBR conditions can be explained by the obstructed blood flow and free venous flow in the ICR system, which does not have time to fill during two minutes of occlusion. It is also impossible to exclude an increased tone of myocytes in HDBR conditions. An increase in RCC can be considered from the perspective of increasing the sensitivity of smooth muscle cells to the dilatory effect of metabolic products with temporary restriction of blood flow. At the same time, according to some literature data, the reaction to arterial occlusion may indirectly indicate a change in endothelial function [13, 21]. We assumed that the increase in RCC observed in our experiment may indirectly point to a change in endothelial function, since other authors report data on impaired endothelium-dependent vasodilation (in a sample with acetylcholine) in ANH without prophylaxis in both men [22] and women [23].

CONCLUSION

Our study investigated the perfusion dynamics and regulatory mechanisms of vascular tone formation in various skin areas in healthy men under conditions of 21-day HDBR exposure. It has been shown that the skin areas of the forehead and lower extremities respond more strongly to this type of exposure from the skin microcirculation and its regulation. The effect of blood redistribution and physical inactivity is manifested in a decrease in skin perfusion against the background of increased tone of terminal arterioles and precapillary sphincters. Such dynamics may indicate the redistribution of microcirculation toward larger vessels. Despite the stability of perfusion in the forearm skin at rest, the functional tests performed showed the probability of HDBR conditions to invoke changes in vasomotor function.

Further research should address skin microhemodynamics in relation to conditions of actual weightlessness using the HDBR model.

References

1. Egorov AD, Itsekhovskii OG. Study of the cardiovascular system in long-term space flights. *Space biology and aerospace medicine.* 1983;17(5):4–6 (In Russ.).
2. Blaber AP., Goswami N, Xu D. Prolonged unloading of the cardiovascular system during bedrest and spaceflight weakens neural coupling between blood pressure and heart rate. *Acta Astronautica.* 2022;195:567–73.
   https://doi.org/10.1016/j.actaastro.2022.03.009
3. Pizzorni C, Sulli A, Smith V, Lladó A, Paolino S, Cutolo M, Ruaro B. Capillaroscopy 2016: new perspectives in systemic sclerosis. *Acta Reumatol Port.* 2016;41:8–14.
4. Johnson JM, Minson CT, Kellogg DL. Cutaneous Vasodilator and Vasoconstrictor Mechanisms in Temperature Regulation. *Comprehensive Physiology.* 2014;4(1):33–89.
   https://doi.org/10.1002/cphy.c130015
5. Charkoudian N. Skin blood flow in adult human thermoregulation: how it works, when it does not, and why. *Mayo Clin Proc.* 2003;78(5):603–12.
   https://doi.org/10.4065/78.5.603
6. Fedorovich AA, Rodnenkov OV, Ageeva NV, Osyeva MK, Rogoza AN. Parameters of microcirculatory blood flow in human skin under conditions of prolonged thermal stress (model experiment). *Cardiological Bulletin.* 2013;1(20):7–17.
   EDN: RNIWAT
7. McCord GR, Cracowski JL, Minson CT. Prostanoids contribute to cutaneous active vasodilation in humans. *Physiology and Pharmacology of Temperature Regulation.* 2006; 291: R596 – R602.
   https://doi.org/10.1152/ajpregu.00710.2005
8. Yuan M, Custaud MA, Xu Z, Wang, J, Yuan M, Tafforin C, Treffel L, et al. Multi-system adaptation to confinement during the 180-day controlled ecological life support system (CELSS) experiment. *Front. Physiol.* 2019;10:575.
   https://doi.org/10.3389/fphys.2019.00575
9. Lloret J, Arnaud L, Gauquelin G, Ming Y, Yin X, LI Y. Cardiospace French Chinese Cooperation in Gravitational Physiology. *39th ISGP Meeting & ESA Life Sciences Meeting.* Noordwijk; 2019.
10. Dunaev AV, Loktionova JI, Zharkikh EV, Fedorovich AA, Sidorov VV, Vasin AV, Dubinin IV. Investigation of blood microcirculation in microgravity with the use of portable laser

Doppler flowmeters. *Aerospace and environmental medicine.* 2024;58(1):47–54 (In Russ.).
https://doi.org/10.21687/0233-528X-2024-58-1-47-54.10.1016

11. Puchkova AA, Shpakov AV, Baranov VM, Katuntsev VP, Stavrovskaya DM, Primachenko GK, et al. General results of the 21-day head-down bedrest study without the use of countermeasures. *Aerospace and environmental medicine.* 2023;57(4):31–41 (In Russ.).
https://doi.org/10.21687/0233-528X-2023-57-4-31-41

12. Lapitan DG, Rogatkin DA. Functional studies of the blood microcirculation system by laser Doppler flowmetry in clinical medicine: problems and prospects. *The Almanac of Clinical Medicine.* 2016; 44 (2):249–59 (In Russ).
https://doi.org/10.18/786/2072-0505-2016-44-2-249-259

13. Sagaidachnyi AA. Reactive hyperemia test: methods of analysis, mechanisms of reaction and prospects. *Regional blood circulation and microcirculation.* 2018;17(3):5–22 (In Russ.).
https://doi.org/10.24884/1682-6655-2018-17-3-5-22

14. Nosovsky AM, Popova OV, Smirnov YuI. State-of-the art technologies of medical data statistical analysis and methods of graphic presentation. *Aerospace and environmental medicine.* 2023; 57(5):149–54 (In Russ.).
https://doi.org/10.21687/0233-528X-2023-57-5-149-154

15. Grigoriev AI, Kozlovskaya IB. Annual head-down bed rest (HDBT) is a physiological model of interplanetary space flight. Moscow: *Russian Academy of Sciences*; 2018 (In Russ.).
EDN: MWLHGQ

16. Rudenko EA, Baranov MV, Zakharov SYu. Investigation of the parameters of central and peripheral hemodynamics during prolonged stay in conditions of orthostatic and antiorthostatic hypokinesia. *Aerospace and environmental medicine.* 2019;53(7):40–7 (In Russ.).
https://doi.org/10.21687/0233-528X-2019-53-7-40-47

17. Breit, GA, Watenpaugh DE, Ballard RE, Hargens AR. Acute cutaneous microvascular flow responses to whole-body tilting in humans. *Microvascular Research.* 1993; 46:351–8.
https://doi.org/10.1006/mvre.1993.1058

18. Kurazumi T, Kato T, Konishi T, Ogawa Y, Iwasaki K. Alteration in facial skin blood flow during acute exposure to -10 and -30° head-down tilt in young human volunteers *Experimental Physiology.* 2022; 107(12):1432–9.
https://doi.org/10.1113/EP090734

19. Noskov VB, Nichiporuk AI, Vasilyeva GYu, Smirnov YuI. The composition of the human body during prolonged stay in zero gravity. *Aerospace and environmental medicine.* 2015; 49 (1):19–25 (In Russ.).
EDN: TJUDQH

20. Navasiolava N, Yuan M, Murphy R, Robin A, Coupé M, Wang L, Custaud MA. Vascular and Microvascular Dysfunction Induced by Microgravity and Its Analogs in Humans: Mechanisms and Countermeasures. *Frontiers in Physiology.* 2020.
https://doi.org/10.3389/fphys.2020.00952

21. Vlasov TD, Nesterovich II, Shimanski DA. Endothelial dysfunction: from the particular to the general. Return to the «Old Paradigm»? *Regional blood circulation and microcirculation.* 2019;18(2):19–27 (In Russ.).
https://doi.org/10.24884/1682-6655-2019-18-2-19-27

22. Coupé M, Fortrat JO, Larina I, Gauquelin-Koch G, Gharib C, Custaud MA. Cardiovascular deconditioning: From autonomic nervous system to microvascular dysfunctions. *Respiratory Physiology & Neurobiology.* 2009;169S:10–12.
https://doi.org/10.1016/j.resp.2009.04.009

23. Demiot C, Dignat-George F, Fortrat JO, Sabatier F, Gharib C, Larina I, Gauquelin-Koch G, Hughson R, Custaud MA. WISE 2005: chronic bed rest impairs microcirculatory endothelium in women. *American Journal of Physiology-Heart and Circulatory Physiology.* 2007;293(5): H3159-H3164
https://doi.org/10.1152/ajpheart.00591.2007

AUTHORS

Daria V. Pashkova
https://orcid.org/ 0009-0000-8209-4175
dashapashkova1@yandex.ru

Andrey A. Fedorovich, Cand. Sci. (Med.)
https://orcid.org/0000-0001-5140-568X
faa-micro@yandex.ru

Julia A. Popova, Cand. Sci. (Med.)
https://orcid.org/0000-0002-7778-307X
julija.popova@gmail.com

Alexey V. Shpakov, Cand. Sci. (Bio.)
https://orcid.org/0000-0002-0073-2944
avshpakov@gmail.com

CC BY 4.0

Check for updates

LAPAROSCOPIC ACCESS IN TREATMENT OF REPRODUCTIVE SYSTEM DISEASES IN WOMEN WITH MULTIPLE ADHESIONS

Elena A. Soloveva[1✉], Oleg S. Filippov[2,3], Anna P. Uryupina[1], Nina A. Chugunova[1], Daria A. Ivanova[1], Anna M. Utkina[1]

[1] Novorossiysk Clinical Center, Novorossiysk, Russia

[2] Federal Scientific and Clinical Center for Children and Adolescents, Moscow, Russia

[3] Burnasyan Federal Medical Biophysical Center, Moscow, Russia

Introduction. Recent progress in abdominal surgery and operative gynecology has led to a significant increase in the number of patients with postoperative abdominal adhesions. The incidence of adhesions after abdominal surgery reaches 67–95%, a serious health problem. In their presence, any following operations may be associated with an increased risk of intra- and postoperative complications.

Objective. To study the possibility of laparoscopic access and its outcome in the surgical treatment of women with reproductive system diseases concomitant with pronounced abdominal and pelvic adhesions.

Materials and methods. A retrospective analysis of 265 patient medical records was performed. The general group included 91 women who had undergone surgery for diseases of the reproductive system in the setting of pronounced abdominal and pelvic adhesions. The second group (control) comprised 174 patients who had undergone surgery for diseases of the reproductive system and had no adhesions. The average age of the patients in the general and control groups was 47.1 ± 12.8 and 46.5 ± 8.1 years, respectively. The preoperative examination included ultrasonography and dynamic magnetic resonance imaging (MRI) of the abdominal cavity and lesser pelvis. For laparoscopic surgery, a STORZ high-resolution video system (Germany) and a BOWA power plant (Germany), including high-frequency (HF) electric, laser, and argon plasma energy, were used. Statistical data processing was carried out using the Statistica 13 and MS Office Excel software. The result was considered statistically significant at $p < 0.05$.

Results. The conducted comparative analysis demonstrated the possibility of using laparoscopic access for the treatment of women with reproductive system pathologies in combination with pronounced abdominal and pelvic adhesions. The duration of surgery, the volume of blood loss, the severity of pain, the duration of hospitalization, and convalescence had no statistically significant differences between the general ($n = 91$) and control groups ($n = 174$). The absence of differences in the frequency of intra- and postoperative complications proves laparoscopic access to be safe in the setting of severe adhesions. The safety is ensured by preoperative patient preparation and examination, use of necessary modern equipment and tools, surgical skills and experience.

Conclusions. The use of laparoscopic access for performing surgical treatment of patients with reproductive system diseases in combination with pronounced adhesions can be considered as the preferred and safe treatment method.

Keywords: adhesive process; laparoscopy; adhesiolysis; hysterectomy; myomectomy; anti-adhesive barrier

ЛАПАРОСКОПИЧЕСКИЙ ДОСТУП ДЛЯ ЛЕЧЕНИЯ ЗАБОЛЕВАНИЙ РЕПРОДУКТИВНОЙ СИСТЕМЫ ЖЕНЩИН ПРИ ВЫРАЖЕННОМ СПАЕЧНОМ ПРОЦЕССЕ

Е.А. Соловьева[1✉], О.С. Филиппов[2,3], А.П. Урюпина[1], Н.А. Чугунова[1], Д.А. Иванова[1], А.М. Уткина[1]

[1] Новороссийский клинический центр Федерального медико-биологического агентства, Новороссийск, Россия

[2] Федеральный научно-клинический центр детей и подростков Федерального медико-биологического агентства, Москва, Россия

[3] Федеральный медицинский биофизический центр им. А.И. Бурназяна Федерального медико-биологического агентства, Москва, Россия

Введение. Развитие абдоминальной хирургии и оперативной гинекологии определило значительное увеличение числа больных с послеоперационными спайками брюшной полости. Частота встречаемости спаечного процесса после абдоминальных операций достигает 67–95%. Абдоминальные спайки представляют собой серьезную проблему для здоровья. При необходимости повторных операций при наличии спаечного процесса значительно возрастает риск интра- и постоперационных осложнений.

Цель. Изучить возможность и результаты применения лапароскопического доступа при хирургическом лечении женщин с заболеваниями репродуктивной системы в сочетании с выраженным спаечным процессом брюшной полости и малого таза.

Материалы и методы. Проведен ретроспективный анализ 265 историй болезни пациенток. В основную группу была включена 91 женщина, прооперированная по поводу заболеваний репродуктивной системы на фоне спаечного процесса брюшной полости и малого таза. Вторую группу (контрольная) составили 174 пациентки, прооперированные по поводу заболеваний репродуктивной системы и не имеющие спаечного процесса. Средний возраст пациенток основной группы составил $47,1 \pm 12,8$ года, контрольной группы — $46,5 \pm 8,1$ года. Предоперационное обследование включало в себя ультразвуковое исследование и динамическое магнитно-резонансное исследование (МРТ) брюшной полости и малого таза. Для выполнения лапароскопических операций использовали видеосистему высокого разрешения компании STORZ (Германия), энергетическую установку компании BOWA (Германия), включающую электрохирургию высокой частоты (ЭХВЧ), лазерную и аргоноплазменную энергию. Статистическая обработка данных проводилась с использованием программы Statistica 13 и MS Office Excel. Результат считался статистически значимым при $p < 0,05$.

Результаты. Проведенный сравнительный анализ продемонстрировал возможность применения лапароскопического доступа для лечения женщин с патологией органов репродуктивной системы в сочетании с выраженным спаечным процессом брюшной полости и малого таза. Длительность оперативного вмешательства, объем кровопотери, выраженность болевого синдрома, длительность госпитализации и реконвалесценции не имели статистически значимых различий между основной (*n* = 91) и контрольной группами (*n* = 174). Отсутствие различий частоты интра- и послеоперационных осложнений доказывает, что лапароскопический доступ в условиях выраженного спаечного процесса является безопасным, что обеспечивается предоперационными подготовкой и обследованием пациента, применением необходимого современного оборудования и инструментария, оперативными навыками и опытом хирурга.

Выводы. Применение лапароскопического доступа для выполнения оперативного лечения пациенток с заболеваниями органов репродуктивной системы в сочетании с выраженным спаечным процессом может рассматриваться как предпочтительный и безопасный метод лечения.

Ключевые слова: спаечный процесс; лапароскопия; адгезиолизис; гистерэктомия; миомэктомия; противоспаечный барьер

✉ Соловьева Елена Анатольевна solovevaln@inbox.ru

INTRODUCTION

Recent achievements in abdominal surgery and operative gynecology have led to a significant increase in the number of patients with postoperative abdominal adhesions [1]. The development of abdominal adhesions occurs in 67–95% of cases after general abdominal surgery and up to 97% after gynecological surgery with laparotomy access [2, 3]. According to research studies, 63% of the laparotomy access length is involved in the formation of anterior abdominal wall adhesion of the omentum and intestinal loops [4, 5].

According to the International Adhesion Society experts, postoperative adhesions in the abdominal cavity are the most common complication, posing a serious health problem for patients and significantly reducing their quality of life. The most significant consequences of adhesions involve intestinal obstruction (32–85%), female infertility (15–40%), dyspareunia and chronic abdominal pain syndrome (20–50%) [6]. The need for adhesiolysis during subsequent surgical procedures increases the operation duration by an average of 24–50 min. In addition, the risk of iatrogenic intestinal damage, bleeding, and subsequent fistula formation increases, thus lengthening the recovery time. Moreover, repeated laparotomy and adhesiolysis can only worsen the adhesion formation [2, 7–9, 10]. At the same time, according to some authors, laparoscopic adhesiolysis decreased the risk of adhesion recurrence and secondary surgical infections (infectious septic complications, wound infection) [11, 12].

Currently, the efforts aimed at preventing adhesions involve anti-adhesive barriers made of hyaluronic acid and carboxycellulose, thorough hemostasis during surgery, and delicate tissue handling [2, 13–15].

Most publications on the characteristics of adhesions in the abdominal cavity address the features of diagnosis, treatment methods, and analysis of complications of intestinal adhesive obstruction that occur after surgical interventions on abdominal organs [16–18].

Despite the current progress in minimally invasive technologies that have made it possible to minimize the traumatic nature of surgical interventions, the use of modern multimodal postoperative rehabilitation programs and a variety of means and methods aimed at preventing the adhesive process, the results of therapeutic and preventive measures cannot be considered sufficient [6, 19]. The issue of pelvic and abdominal adhesions resulting from surgical interventions on the female reproductive system requires research attention due to its decisive importance for selecting treatment tactics and surgical access.

To date, standardized diagnostic criteria and recommendations for selecting surgical access when treating women with reproductive organ pathologies concomitant with a widespread adhesive process are lacking. This dictates the need to study the technological capabilities of minimally invasive surgery for its further improvement and implementation in gynecological practice.

In this study, we set out to investigate the possibility of using laparoscopic access and its outcome in the surgical treatment of women with reproductive system diseases in combination with pronounced abdominal and pelvic adhesions.

MATERIALS AND METHODS

We carried out a retrospective analysis of 265 records of patients operated at the Gynecological Department of the Novorossiysk Clinical Center for Reproductive System Diseases using laparoscopic access.

The general group included 91 women who had undergone surgery for reproductive system diseases in the setting of pronounced abdominal and pelvic adhesions (grade III–IV according to Blinnikov's scale). The second group

(control) consisted of 174 patients who had undergone surgery reproductive system diseases and had no adhesions or those with a slight degree of its severity (I–II degree according to Blinnikov's scale). The scale is presented in Table 1.

The criteria for selecting patients in the study group were the age of women over 18 years old, reproductive system diseases that required surgical treatment, and abdominal adhesions of varying severity.

In the general group, the average age of the patients was 47.1 ± 12.8 years. In the general group, 55 (60.4%) women were overweight or obese of varying severity with an average BMI of 27.5 ± 5.9 kg/m² (maximum 42.4 kg/m²); 5 (5.4%) patients with morbid obesity with a BMI of more than 40 kg/m² underwent surgery. Body weight deficiency was found in only 1 (1.1%) case. Out of the entire sample, only 30 (32.3%) women were of normal weight.

In the control group of 174 patients, the average age was 46.5 ± 8.1 years. Overweight and obese women prevailed: 113 (64.9%) patients with an average BMI of 30.1 ± 6.7 kg/m² (maximum 52.6 kg/m²), of whom 30 (17.2%) were morbidly obese. Most of the operated patients had a combined gynecological pathology.

The preoperative examination of the patients and operation planning included ultrasonography and dynamic magnetic resonance imaging (MRI) of the abdominal cavity and lesser pelvis. One of the objectives of this study was to determine the presence, localization, and prevalence of the adhesive process, the involvement of the anterior abdominal wall and intestinal loops with the purpose of selecting the safest access to the abdominal cavity (places of insertion of trocar for optics and trocar for instruments).

Abdominal ultrasonography (US) was performed in all patients. Isolated preoperative ultrasonography in obese patients was associated with technical difficulties, which resulted in an objective diagnostic error. In such cases, 16 (17.6%) patients additionally underwent dynamic MRI of the abdominal cavity and lesser pelvis. This group included women with 3–4 obesity grade.

Laparoscopic surgery was performed using a STORZ high-resolution video system (Germany), a BOWA power plant from (Germany), including high-frequency (HF) electric, laser, and argon plasma energy.

A laparoscopic access using 30° anterolateral vision optics provided more reliable information about the condition of the abdominal organs, as well as the presence, localization, and prevalence of adhesions. The volume of dissected splices was determined individually in each case.

In order to prevent damage to internal organs during the introduction of an optical trocar, taking into account ultrasonography and MRI mapping data, in 18 (19.9%) cases

the trocar was installed in an open way along the midline 3–5 cm above the navel; in 9 (9.8%) cases, the optical trocar was not inserted along the classical point of the umbilical region. The Veres needle was not used to create a carboxyperitoneum. To minimize the pathological effect of carboxyperitoneum, abdominal pressure was maintained at a level of 6–8 mmHg.

A combination of various methods and tools was used to dissect the splices: an ultrasonic scalpel (BOWA, Germany), scissors, and mechanical traction. After performing adhesiolysis and gaining access to the pelvic organs, the necessary amount of surgery was performed to solve the set clinical task. To prevent the formation of adhesions in the postoperative period, great importance was given to hemostasis and sanitation of the abdominal cavity. To create an anti-adhesive barrier, an anti-adhesive preparation based on polyethylene oxide and carboxymethylcellulose was injected into the abdominal cavity. Upon the completion of the surgery, the site of the first trocar insertion was examined to ensure the absence of intestinal damage.

A comparative assessment of the results of surgical treatment was carried out by analyzing the duration of surgical treatment, the volume of blood loss, the severity of pain syndrome on the VAS scale, and the duration of hospitalization. In the postoperative period, the classical visual analog pain scale (VAS) was used to assess the pain syndrome [21, 22].

Statistical data processing was carried out using the Statistica 13 and MS Office Excel software. The result was considered statistically significant at p < 0.05.

RESULTS AND DISCUSSION

According to the results obtained, The study found that benign uterine tumor processes prevailed in the general group in 34 (37.4%) cases and in the control group in 86 (49.4%) cases. Benign ovarian neoplasms were registered in 23 (25.3%) patients of the general group and 29 (16.7%) women from the control group. The relevant data is presented in Table 2.

In the general group, 81 (89%) of the patients had previously undergone various surgical procedures on the abdominal and pelvic organs. Only 10 (10.9%) women in this group had no history of any prior surgical procedures. Table 3 shows the types of surgical interventions previously performed in patients of the general group with a pronounced adhesive process. The total number of operations performed was 180, of which 123 (68.3%) were performed for gynecological pathology and 57 (31.7%) operations on

Table 1. Grades of abdominal adhesions by O.I. Blinnikov

Grade I	Local adhesions limited to the postoperative scar area or part of the abdominal cavity, occupying no more than 1/3 of one compartment in the absence of adhesions in other areas
Grade II	Local adhesions in combination with single rare adhesions in other areas
Grade III	Adhesions occupying more than 1/3 of the abdominal cavity
Grade IV	Diffuse adhesions occupying 2/3 of the abdominal cavity

Table prepared by the authors using data from [20]

Table 2. Indication for surgical treatment (*p* > 0.05)

	General group *n* = 91		Control group *n* = 174	
	n	%	*n*	%
Uterine fibroids	34	37.4	86	49.4
Ovarian neoplasms	23	25.3	29	16.7
External genital endometriosis	11	12.1	18	10.3
Chronic inflammatory diseases of the pelvic organs with hydrosalpinxes	8	8.8	7	4.0
Infertility	6	6.6	17	9.7
Pelvic organ prolapse	4	4.4	12	6.9
Atypical endometrial hyperplasia, adenomatosis	2	2.2	5	2.9
Chronic pelvic pain syndrome	3	3	0	0

Table prepared by the authors using their own data

abdominal organs. Previous surgical interventions in the vast majority of 149 (82.8%) cases were performed by laparotomy access. Laparoscopic access was performed only in 29 (16.1%) operations, vaginal access — in 2 (1.4%) operations.

To achieve the clinical task, the patients of the general and control groups underwent various amounts of surgery. Table 4 shows the main types of surgical treatment performed. A large proportion were radical operations, such as radical hysterectomy with appendages or fallopian tubes.

The analysis of the medical records of the patients in both groups found that no damage to the internal organs occurred during the introduction of the trocar for optics and instruments. When comparing the features of the course of surgery and the course of the postoperative period in

Table 3. Total number and types of previous surgical interventions in patients of the general group based on anamnesis data

Surgical interventions	Number of interventions
On the reproductive system organs, in particular:	123
operations on the uterine appendages	43
Caesarean section	38
tubal pregnancy	13
hysterectomy	12
endometriosis	10
myomectomy	5
inflammatory diseases	2
On the abdominal organs, in particular:	57
appendectomy	30
cholecystectomy	9
bowel surgery	6
injuries and traumas of abdominal organs	5
operations for diffuse peritonitis	4
liver surgery	3

Table prepared by the authors using their own data

cases of surgical treatment in patients of the general and control groups, no statistically significant differences were found (Table 5).

Thus, the average duration of surgical intervention increased by 25–40 min in the general group due to the time spent on adhesiolysis. The average volume of blood loss and the hospitalization duration did not differ significantly among the groups. In all cases of surgical intervention, the amount of surgical treatment required by the clinical situation was performed, which additionally confirms the possibility of performing the required amount of surgical intervention in the presence of pronounced adhesions in the abdominal cavity. There were no laparotomy conversions in both groups of patients.

Health promotion in both groups was carried out starting from the first day of the postoperative period; sparing nutrition was organized from the second day. In all patients, intestinal motility was restored on days 1–2.

On the first day after surgery, only 6 (6.6%) patients from the general group rated pain on a scale of 7–8 points. Moderate pain at a level of 5–6 points according to VAS was noted in 38 (41.8%), while a mild pain level of 3–4 points was noted by 42 (46.2%) women. There were no complaints of pain at all in 5 (5.4%) patients from the general observation group. By the third day, all patients had reported a pain level of 2–3 points, which made it possible to cancel the use of painkillers. Similar data were obtained in the control group.

The average duration of hospitalization stay in both groups did not differ statistically, the corresponding data are presented in Table 5. The need to perform adhesiolysis during surgery did not lead to an increase in the postoperative bed day. Significant intraoperative and postoperative complications, such as injury to adjacent organs, bleeding from damaged vessels, and purulent-septic complications in the early and late postoperative periods, were not recorded in both groups. In the general group, in one case, sigmoid colon deserosing occurred without opening the lumen. The defect was sutured laparoscopically and did not affect the course of the postoperative period. During the follow-up year, there were no cases of intestinal adhesive obstruction in both groups of patients.

Table 4. Types of surgical procedures

Types of surgical interventions	General group n = 91		Control group n = 174	
	n	%	n	%
Radical hysterectomy with bilateral oophorectomy	38	41.8	99	55.2
Ovarian neoplasm excision	13	14.3	20	11.5
Adnexectomy	11	12.1	13	7.5
Endometriosis surgery	8	8.7	8	4.6
Myomectomy	7	7.8	20	11.5
Tubectomy	5	5.5	0	0
Dissection of the adhesions (infertility)	5	5.5	4	2.3
Promontofixation using a mesh implant	4	4.4	12	6.9
Scar metroplasty after cesarean section	0	0	1	0.6

Table prepared by the authors using their own data

Table 5. Main indicators of surgical intervention

Parameter	General group	Control group
Average surgery duration, min	107.9 ± 34.38	81.9 ± 25.6
Average volume of blood loss, mL	65 ± 32.5	61.9 ± 29.2
Average hospital length of stay, bed days	5.6 ± 1.8	6.1 ± 1.3
Stay in the intensive care unit 1 day after surgery, number of patients, %	28 (30.8%)	59 (33.9%)
Conversion to laparotomy, %	0	0

Table prepared by the authors using their own data

To date, pronounced adhesions remain a contraindication for selecting laparoscopic access during surgical treatment. It is believed that adhesions impair visualization, increase the risk of damage to the internal organs of the abdominal cavity (intestines, large vessels, etc.), and worsen the outcome of surgical treatment in patients with diseases of the female reproductive system. In addition, the range of noninvasive preoperative diagnostic tools of adhesions is limited, not finding application in routine practice [23, 24].

The development and implementation of standardized diagnostic criteria and surgical tactics for a safer surgical treatment in patients with reproductive system diseases in combination with pronounced abdominal and pelvic adhesions will make it possible to use laparoscopic technologies in larger groups of patients with reproductive system diseases [24–26].

Preoperative mapping of adhesions using ultrasonography and MRI of the abdominal cavity and lesser pelvis with a high degree of probability facilitates the selection of the safest points of trocar insertion into the abdominal cavity. The refusal to use a Veres needle and the direct introduction of the trocar into the abdominal cavity followed by the creation of a carboxyperitoneum does not increase the risk of abdominal organ damage. The use of 30° anterior-lateral vision optics significantly improves visualization in the presence of adhesions. A combination of modern instruments with various types of energy improves the quality of adhesiolysis, reduces the risk of damage to the abdominal and pelvic organs, injury to surrounding tissues, and bleeding. All of the above increases the safety of surgical intervention performed in the setting of adhesions using the laparoscopic method. The presented conclusions are consistent with the literature data [12, 25–27].

The conducted comparative analysis demonstrates the possibility of using laparoscopic access for the treatment of women with reproductive system pathologies concomitant with pronounced abdominal and pelvic adhesions. Laparoscopic access in the setting of pronounced adhesions is a safe choice, which is ensured by preoperative preparation and examination of the patient, the use of necessary modern equipment and tools, the surgical skills and experience of the surgeon.

CONCLUSION

The use of laparoscopic access for performing surgical treatment in patients with reproductive system diseases in combination with pronounced adhesions can be considered as the preferred and safe method of treatment. The use of modern methods of preoperative mapping of adhesions (ultrasonography, MRI) and modern equipment contributes to improving the safety of laparoscopic methods and reducing the risk of intraoperative and postoperative complications.

References

1. Lavreshin PM, Botasheva VS, Gobedzhishvili VV, Kelasov IG. Dynamics of morphologic changes in the peritoneum at its mechanical damage. *Medical Bulletin of the North Caucasus.* 2010;4:59–62 (In Russ.).
   EDN: NBXMFP

2. Catena F, Di Saverio, S, Kelly MD. et al. Bologna Guidelines for Diagnosis and Management of Adhesive Small Bowel Obstruction (ASBO): 2010 Evidence-Based Guidelines of the World Society of Emergency Surgery. *World J. Emerg Surg.* 2011;5:1–24.
   https://doi.org/10.1186/1749-7922-6-5

3. Bezhenar VF, Tsypurdeeva AA, Baylyuk EN. Adhesive disease pelvic organs in gynecological patients: from pathogenesis to prevention. *Oncogynecology.* 2014;(4):68–74 (In Russ.).
   EDN: TDXGYJ

4. Behman R, Nathens AB, Byrne JP, Mason S, Look HN, Karanicolas PJ. Laparoscopic Surgery for Adhesive Small Bowel Obstruction Is Associated With a Higher Risk of Bowel Injury: A Population-based Analysis of 8584. *Patients Annals of Surgery.* 2017;266(3):489–98.
   https://doi.org/10.1097/SLA.0000000000002369

5. Szomstein S, Menzo E, Simpfendorfer C, Zundel N, Rosenthal RJ., Laparoscopic Lysis of Adhesions. *World J Surg.* 2006;30:1–7.
   https://doi.org/10.1007/s00268-005-7778-0

6. Nazarenko AA, Akimov VP, Malyshkin PO. Epidemiology, pathogenesis and prevention of postoperative adhesions in the abdominal cavity. *Bulletin of Surgery named after I.I.Grekov.* 2016; 175(5):114–8 (In Russ.).
   EDN: XBVPAJ

7. Bezhenar VF, Aĭlamazian ÉK, Baĭliuk EN, Tsypurdeeva AA, Polenov NI. Etiology, pathogenesis and prevention of adhesions in surgery of the pelvic. *Russian Obstetrician-Gynecologist Gazette.* 2011;11(2):90–101 (In Russ.).
   EDN: PZAVRV

8. Adamyan LV, Kozachenko AV., Kondratovich LM. Peritoneal adhesions: the history of researh, classification and pathogenesis (a review). *Russian Journal of Human Reproduction.* 2013;(6):7–13 (In Russ.).
   EDN: RZQNGR

9. Lutsevich OE, Akimov VP, Shirinsky VG, Bichev AA. Issues of pathogenesis of adhesive peritoneal disease and modern approaches to its prevention. Literature review. *Moscow Surgical Journal.* 2017; 3:11–26 (In Russ.).
   EDN: YSTFQI

10. Yusubov IA. The role of minimally invasive technologies in the diagnosis and treatment of intestinal obstruction of postoperative adhesive origin. *Siberian Scientific Medical Journal.* 2023;43(4):132–8 (In Russ.).
    https://doi.org/10.18699/SSMJ20230414

11. Sikirica V, Bapat B, Candrilli SD, Davis KL, Wilson M, Johns A. The inpatient burden of abdominal and gynecological adhesiolysis in the US. *Sikirica et al. BMC Surgery.* 2011;11:2–9.
    https://doi.org/10.1186/1471-2482-11-13

12. Zvyagintsev VV, Gorpinyuk VP, Fomov GV et al. Features of laparoscopic operations in patients after abdominal cavity interventions. *Modern problems of science and education.* 2019; (4):128 (In Russ.).
    https://doi.org/10.17513/spno.29013

13. Ahmad G, Kim K, Thompson M et al. Barrier agents for adhesion prevention after gynaecological surgery. *Cochrane Database of Systematic Reviews.* 2020;3(4):CD000475.
    https://doi.org/ 10.1002/14651858.CD000475.pub4

14. Ahmad G, Thompson M, Kim K et al. Fluid and pharmacological agents for adhesion prevention after gynaecological surgery. *Cochrane Database of Systematic Reviews.* 2020;7:CD001298.
    https://doi.org/10.1002/14651858.CD001298.pub5

15. Bondarevsky IYa, Shalmagambetov MS, Bordunovsky VN. The current state of the problem of forecasting and prevention of postoperative peritoneal adhesiogenesis (literature review). Ural Medical Journal. *Ural medical journal.* 2018;1(156):69–78 (In Russ.).
    EDN: YODEDL

16. Shkerdina MI, Antonyan SZh, Zharikov Yu O. Aspects of laparoscopic treatment of patients with adhesive small bowel obstruction (literature review). *Bulletin of surgery named after I. I. Grekov.* 2020;179(2):79–84 (In Russ.).
    https://doi.org//10.24884/0042-4625-2020-179-2-79-84

17. Tarasenko SV, Zaitsev OV, Sokolov PV, et al. Laparoscopic access in the treatment of adhesive small bowel obstruction. *Bulletin of Surgery named after I. I. Grekov.* 2018; 177(2):30–3 (In Russ.).
    https://doi.org/10.24884/0042-4625-2018-177-2-30-33

18. Behman R, Nathens AB, Byrne JP, Mason S, Look Hong N, Karanicolas PJ. Laparoscopic Surgery for Adhesive Small Bowel Obstruction Is Associated With a Higher Risk of Bowel Injury : a Population-based Analysis of 8584 Patients. *Ann. Surg.* 2017;266(3):489–98.
    https://doi.org/10.1097/SLA.0000000000002369

19. Schaefer SD, Alkatout I, Dornhoefer N, Herrmann J, Klapdor R, Meinhold-Heerlein I, Meszaros J, Mustea A, Oppelt P, Wallwiener M, Kraemer B. Prevention of peritoneal adhesions after gynecological surgery: a systematic review. Arch Gynecol Obstet. 2024;310(2):655–72.
    https://doi.org/10.1007/s00404-024-07584-1

20. Ayushinova NI, Shurygina IA, Shurygin MG, Glinskaya EV. Assessment of the severity of the adhesive process in the abdominal cavity. *Siberian Medical Journal (Irkutsk).* 2014;7:10–14 (In Russ.).
    EDN: TQPYQJ

21. Mokhov EM, Kadykov VA, Sergeev AN, et al. Pain assessment scales and features of their application in medicine (literature review). *Verkhnevolzhsky Medical Journal.* 2019;18(2):34–7 (In Russ.).
    EDN: DEYKPY

22. Hawker GA, Mian S, Kendzerska T, French M. Measures of adult pain: Visual Analog Scale for Pain (VAS Pain), Numeric Rating Scale for Pain (NRS Pain), McGill Pain Questionnaire (MPQ), Short-Form McGill Pain Questionnaire (SF-MPQ), Chronic Pain Grade Scale (CPGS), Short Form-36 Bodily Pain Scale (SF-36 BPS), and Measure of Intermittent and Constant Osteoarthritis Pain (ICOAP). *Arthritis Care Res (Hoboken).* 2011;63(11):S240-52.
    https://doi.org/10.1002/acr.20543

23. Ghonge NP, Ghonge SD. Computed tomography and magnetic resonance imaging in the evaluation of pelvic peritoneal adhesions: *What radiologists need to know? Indian J Radiol Imaging.* 2014;24(2):149–55.
    https://doi.org/10.4103/0971-3026.134400

24. Armashov VP, Belousov AM, Vavshko MV, Madrakhimov ShN, Armashov GV, Matveev NL. Is ultrasound diagnosis of peritoneal adhesions possible before abdominal surgery? *Innovative medicine of Kuban.* 2022;(4):75–8 (In Russ.).
    https://doi.org/10.35401/2541-9897-2022-25-4-75-81

25. Lutsevich OE, Gallyamov EA, Popov SV, et al. Features of laparoscopic operations in conditions of adhesive peritoneal disease and the possibility of its laparoscopic treatment and prevention. *Pacific Medical Journal.* 2017;1 (67): 69–73 (In Russ.).
    https://doi.org/10.17238/PmJ1609-1175.2017.1.69-73

26. Di Saverio S, Birindelli A, Broek RT. et al. Laparoscopic adhesiolysis : not for all patients, not for all surgeons, not in all centres. *Updates Surg.* 2018;70(4):557–61.
    https://doi.org/10.1007/s13304-018-0534-4

27. Byrne J, Saleh F, Ambrosini L, Quereshy F, Jackson T D, Okrainec A. Laparoscopic versus open surgical management of adhesive small bowel obstruction: a comparison of outcomes. *Surg Endosc.* 2015;29(9):2525–32.
    https://doi.org/10.1007/s00464-014-4015-7

AUTHORS

Elena A. Soloveva, Cand. Sci. (Med.)
https://orcid.org/0009-0004-9442-8645
solovevaln@inbox.ru

Anna P. Uryupina
https://orcid.org/0009-0008-3348-3631
anna.petra3@mail.ru

Daria A. Ivanova
https://orcid.org/0009-0006-1942-7516
daria.andreevna1995@mail.ru

Oleg S. Filippov, Dr. Sci. (Med.), Professor
https://orcid.org/0000-0003-2654-1334
ilippovolsem@yandex.ru

Nina A. Chugunova
https://orcid.org/0009-0003-3345-579X
nkc@nkc-fmba.ru

Anna M. Utkina
https://orcid.org/0009-0000-1757-0307
annautkina83@gmail.com